



# Rational engineering of self-assembling thermo-sensitive protein complexes and their applications

By

KARIMA TAIBI METRAN

A thesis submitted in fulfilment for the *degree of Doctor of Philosophy*

Royal Holloway University of London  
School of Biological Sciences

Under the supervision of Dr. Mikhail Soloviev

July 2021

## Declaration of authorship

I, Karima Taibi Metran, hereby declare that this thesis and the work presented in it, are entirely my own. Where I have consulted the help of others, this is always clearly stated.

Signed:  \_\_\_\_\_

Date: 28-06-2021



## Abstract

Key aims of this research are to understand fundamental molecular mechanisms underlying the unusual stability of soluble n-ethylmaleimide-sensitive factor attachment-protein receptor (SNARE) proteins and to apply any discoveries to engineer novel self-assembling proteins where their assembly or disassembly could be controlled with externally applied chemical or physical stimuli. SNAREs are a family of membrane proteins responsible for driving membrane fusion in eukaryotic cells. Neuronal SNAREs comprise three proteins, which are referred to as syntaxin, SNAP-25 (which contributes two  $\alpha$ -helices), and Vesicle Associated Membrane Protein (VAMP), also referred to interchangeably as synaptobrevin. These proteins contain SNARE domains, which drive the self-assembly of the three proteins into stable heterotetrameric coiled coil complexes exhibiting extraordinary chemical tolerance to proteases and detergents, and thermoresistance to temperatures of  $\sim 90^{\circ}\text{C}$ . We compiled a database of all SNAREs with elucidated structures obtained from Protein Data Bank, and built a SNARE protein structure compactness analysis tool to analyse their sequences and draw our initial hypotheses about the mechanisms of SNARE assembly. We subsequently used the tool to predict *in silico*, how modifications to the secondary structures of a full-length neuronal SNARE complex (sp. *Rattus norvegicus*) would affect the assembly, and hence the stability of the complex. By virtue of its molecular structure, the individual native SNARE domains exist as fully unfolded polypeptides, which adopt alpha-helical coiled-coil following the assembly. Therefore, circular dichroism (CD) spectroscopy was used as the main method for the experimental evaluation of assembly and stability of the engineered proteins. Where possible other methods were applied, including using native polyacrylamide gel electrophoresis (PAGE), pull down assays and thermal shift assay screen.

A number of peptides were rationally engineered to systematically check key residues predicted to strongly influence complex assembly, stability, and disassembly. Special emphasis was on the development of proteins capable of disassembly in response to small temperature changes within the physiological range and in response to the change in pH. Both of these challenges have been addressed in the course of this research. The newly engineered proteins showed disassembly over an extensive range of  $34 - 83^{\circ}\text{C}$ , displaying the wide potential available for modifying complexes with bespoke stability. New pH sensitive complexes were also engineered with increased sensitivity to high pH (disassembly at pH 8). Furthermore, we explored strategies for nanoparticle-protein conjugation using full-length SNARE complexes, to investigate the applicability of SNARE proteins as potential linkers in delivery devices.

## Acknowledgments

*“Sometimes science is a lot more art than science. A lot of people don’t get that.” – Rick Sanchez*

First and foremost, I must express my deepest gratitude to my supervisor Mikhail Soloviev. With the patience of Job, his incredible wisdom has supported and guided me through this process and for that reason alone; I am ever indebted to him. Special credit goes to my dear friend and colleague Elina Dosadina. Although we knew each other for a relatively brief time, she has made some of the most invaluable contributions to this work, and for that I am extremely appreciative and grateful. With many thanks to another dear friend, Yasmine Al-Saidi, who has been a pillar of support throughout my time at Royal Holloway.

With thanks to my advisor Laurence Bindschedler, who has provided me with objective, constructive advice. In addition, I would like to acknowledge our long-term collaborator Dr. Enrico Ferrari (University of Lincoln) for all his support and instrumental contributions to the project, and his brilliant company and conversation during our visits to the synchrotron. On the subject of the synchrotron, I must give my thanks to Dr. Giuliano Siligardi, a formidable figure at Beamline 23 (B23) at Diamond Light Source (Harwell), for sharing his unparalleled knowledge of the intricacies of synchrotron radiation circular dichroism.

I would like to extend my thanks to BBSRC for funding this studentship, and giving me the opportunity to conduct this research and contribute in any meaningful way to the scientific community, this would not have been possible without them and their support.

Jamila Metran, my exceptionally supportive and patient flatmate, and aunt, thank you for being there for me always. A heartfelt thanks to Miriam and Yusuf (a.k.a. mum and dad) for being a continual source of inspiration and encouragement.

## Table of Contents

<b>Declaration of authorship</b> .....	<b>2</b>
<b>Abstract</b> .....	<b>3</b>
<b>Acknowledgments</b> .....	<b>4</b>
<b>Index of Tables and Figures</b> .....	<b>10</b>
<b>Index of Abbreviations</b> .....	<b>16</b>
<b>1. Introduction</b> .....	<b>21</b>
<b>1.1 A brief history of the discovery of SNAREs</b> .....	<b>21</b>
<b>1.2 SNAREs and their biological role in membrane fusion</b> .....	<b>23</b>
1.2.1 Introduction to membrane fusion and SNAREs.....	23
1.2.2 SNARE proteins .....	24
1.2.3 SNARE-mediated neurotransmitter exocytosis .....	26
1.2.4 Structure and function of other proteins that interact with the SNARE complex .....	30
1.2.5 What is already known about the hierarchy of SNARE complex formation?.....	34
1.2.6 Clostridial neurotoxin (CNT) substrate recognition sites .....	37
<b>1.3 Self-assembling coiled coils</b> .....	<b>38</b>
1.3.1 Molecular structure and geometry .....	38
1.3.2 Matching amino acid properties to positions “ <i>abcdefg</i> ” .....	39
1.3.3 Amino acid properties governing molecular recognition and stability.....	43
<b>1.4 Drug delivery systems</b> .....	<b>46</b>
1.4.1 Coiled coils in drug delivery.....	47
1.4.2 SNAREs in drug delivery .....	49
<b>1.5 Nanoparticle-Protein Conjugation</b> .....	<b>50</b>
1.5.1 Gold Nanoparticles (GNPs).....	51
1.5.2 Magnetic Iron(III) Oxide Nanoparticles (MNPs).....	52
1.5.3 Strategies for protein conjugation/immobilisation .....	54
1.5.4 Obstacles and limitations of protein conjugation .....	55
<b>1.6 Characterisation techniques</b> .....	<b>56</b>
1.6.1 Circular dichroism (CD) spectroscopy .....	56
1.6.2 Pull-down Assay in conjunction with Polyacrylamide Gel Electrophoresis (PAGE) .....	57
1.6.3 FRET-HRM (Förster Resonance Energy Transfer - High Resolution Melt).....	58
<b>1.7 Background on the PDB structures 1N7S, 1L4A and 3B5N</b> .....	<b>60</b>

<b>2. Project Aims and Objectives .....</b>	<b>63</b>
<b>2.1 Aims.....</b>	<b>63</b>
<b>2.2 Objectives .....</b>	<b>64</b>
<b>2.3 Hypotheses .....</b>	<b>66</b>
2.3.1 Hypothesis 1: Hierarchy of assembly .....	66
2.3.2 Hypothesis 2: Specificity of complex .....	66
<b>2.4 Rational design of SNARE peptides: Strategy for modifying Residue Volumes and Ionic Interactions .....</b>	<b>67</b>
<b>3. Materials and methods .....</b>	<b>68</b>
<b>3.1 Materials .....</b>	<b>68</b>
3.1.1 Bioinformatics .....	68
3.1.2 Investigating assembly and stability of truncated SNARE-based peptide complexes.....	68
<b>3.2 Characterising the SNARE proteins using bioinformatics tools .....</b>	<b>70</b>
<b>3.3 Predicting molecular interactions using the SNARE protein structure compactness analysis tool.....</b>	<b>71</b>
3.3.1 Building the SNARE tool.....	71
3.3.2 Integrating “scales” into the tool .....	72
3.3.3 Analysis of the database .....	73
3.3.4 Predicting theoretical pI, salt bridges, buried polar residues and 3D visualisation.....	73
<b>3.4 Rational design of thermosensitive SNARE-based peptides.....</b>	<b>74</b>
3.4.1 Thermal melt of truncated VAMP SNARE complexes using Circular Dichroism.....	74
3.4.2 Profiling residue volume across complex 1N7S .....	74
<b>3.5 Observing assembly of full-length SNARE complex compared to truncated SNARE-based peptide complexes.....</b>	<b>75</b>
3.5.1 CD spectra of control Protein A, full-length SNARE complex and associated controls....	75
3.5.2 CD spectra of full-length SNARE complex and truncated SNARE complexes C04 and C05.....	76
3.5.3 SDS-PAGE of full-length SNARE complex and associated controls.....	76
3.5.4 Testing full-length and truncated SNARE complexes for SDS-stability.....	77
3.5.5 CD spectra of full-length (FL/FL/FL) and truncated SNARE complexes (FL/FL/34 and FL/34/34) .....	77

3.5.6 Preparation of IR-SNAP25 .....	78
3.5.7 Optimisation of buffer conditions for native gels of IR-labelled complexes containing rationally-designed peptides.....	80
3.5.8 Native gels of IR-labelled complexes containing rationally designed peptides .....	80
3.5.9 Observing full-length SNARE complex assembly on nanoparticles using CD spectroscopy .....	81
3.5.10 CD spectra of full-length SNARE complexes conjugated to gold nanoparticles (GNPs)	82
<b>3.6 Thermal and pH stability of the engineered SNARE complexes .....</b>	<b>82</b>
3.6.1 Transformation of BL21 competent <i>E. coli</i> cells .....	82
3.6.2 Expression of GST-SNAP25 fusion protein.....	82
3.6.3 Preparation of GST-SNAP25 on glutathione-agarose beads .....	83
3.6.4 pH-stability pull-down assay .....	84
3.6.5 pH-stability measured using CD spectroscopy for complexes C04, C06, and C0206. ....	85
3.6.6 Thermal melts of full-length (FL/FL/FL) and truncated SNARE complexes (FL/FL/34 and FL/34/34) using CD spectroscopy .....	86
3.6.7 Thermostability pull-down assay .....	87
3.6.8 Thermal stability measured using CD spectroscopy for Salt Bridge study complexes C08, C09, C10, and C11, and compensation study complexes C15, C0315. ....	88
3.6.9 Thermofluor assay: thermal melts of control lysozyme and full-length (CFL) and truncated SNARE complexes (C04 and C05) .....	89
3.6.10 Testing FRET-HRM: Positive control.....	89
3.6.11 Testing FRET methodology using labelled peptides control C04.....	92
<b>4. Characterising the SNARE proteins using existing bioinformatics tools .....</b>	<b>94</b>
<b>4.1 Results .....</b>	<b>94</b>
4.1.1 Amino acid sequence .....	94
4.1.2 Protein topology and conserved domains .....	94
4.1.3 SNARE coiled coil motif.....	96
4.1.4 Post-translational Modifications.....	97
<b>4.2 Discussion .....</b>	<b>99</b>
<b>5. SNARE database and systematic analysis of structural features which affect SNARE complex stability.....</b>	<b>102</b>
<b>5.1 Results .....</b>	<b>102</b>
5.1.1 SNARE database and selection of complexes for analysis.....	102

5.1.2 Hydrophobic Interactions at positions <i>a</i> and <i>d</i> .....	102
5.1.3 Residue volumes .....	104
5.1.4 Buried polar residues at positions <i>a</i> and <i>d</i> .....	105
5.1.5 Long-range ionic attractions and interhelical salt bridges at positions <i>bc</i> and <i>efg</i> .....	105
<b>5.2 Discussion .....</b>	<b>109</b>
<b>6. Rational design of thermosensitive SNARE-based peptides.....</b>	<b>113</b>
<b>6.1 Results .....</b>	<b>113</b>
6.1.1 SNARE stability studies.....	113
6.1.2 Ionic Interactions: Selection of SNARE constituent, sequence length and modifications for peptide candidates .....	117
<b>6.2 Discussion .....</b>	<b>119</b>
<b>7. Investigating assembly of truncated SNARE-based peptide complexes .....</b>	<b>122</b>
<b>7.1 Results .....</b>	<b>122</b>
7.1.1 CD Spectroscopy: control Protein A.....	122
7.1.2 CD Spectroscopy: full-length SNARE complex and associated controls .....	123
7.1.3 Synchrotron Radiation CD Spectroscopy: control truncated SNARE complexes .....	123
7.1.4 Testing full-length and truncated SNARE complexes for SDS-stability.....	124
7.1.5 CD Spectroscopy: control truncated SNARE complexes .....	124
7.1.6 Using native PAGE gels to study the assembly of IR-labelled SNARE proteins complexes and rationally designed peptides .....	125
7.1.7 CD Spectroscopy: full-length SNARE complex assembly on nanoparticles .....	128
<b>7.2 Discussion .....</b>	<b>129</b>
<b>8. Investigating the stability of truncated SNARE-based peptide complexes.....</b>	<b>132</b>
<b>8.1 Results .....</b>	<b>132</b>
8.1.1 Thermostability of control complexes .....	132
8.1.2 Thermostability of complexes from the Residue Volume study.....	133
8.1.3 Thermostability of complexes from the Salt Bridge study .....	135
8.1.4 CD Spectroscopy: thermal melts of control truncated SNARE complexes compared to full-length SNARE complex .....	136
8.1.5 pH-sensitivity of complexes from the pH-sensitivity study.....	137
8.1.6. CD Spectroscopy: pH-sensitivity of complexes from the pH-sensitivity study.....	138

8.2 Discussion .....	139
9. General Discussion and Future Research Developments .....	146
10. Conclusion.....	150
11. References .....	152
12. Tables .....	169
13. Figures .....	178
13.1 Figures in Chapter 1.....	178
13.2 Figures in Chapter 2.....	197
13.3 Figures in Chapter 3.....	198
13.4 Figures in Chapter 4.....	203
13.5 Figures in Chapter 5.....	217
13.6 Figures in Chapter 6.....	226
13.7 Figures in Chapter 7.....	235
13.8 Figures in Chapter 8.....	243
14. Appendix .....	257

## Index of Tables and Figures

### 12. Tables

Table 1	Proposed $\alpha$ -SNAP binding sites on the SNARE complex according to Marz <i>et al.</i> 2003.	169
Table 2	Woolfson and Walshaw's amino acid profile for long parallel two-stranded coiled coils.	170
Table 3	Percentage compositions, and molecular weight, for each of the synaptic proteins obtained using Protparam computational tool from ExPASy	171
Table 4	SNARE-based peptides tabulated with their sequences.	172-173
Table 5	Composition of SNARE complex samples for CD spectroscopy.	174
Table 6	Preparation of 5X stock solutions of buffers A-C.	174
Table 7	Assembly of optimisation samples for native gel containing full-length SNARE complex, BSA and OG, and control IR-SNAP25	174
Table 8	Composition of MNP-SNAREs samples for CD spectroscopy.	175
Table 9	Composition of GNP-SNAREs samples for CD spectroscopy	175
Table 10	Preparation of 100 mM potassium phosphate buffer pH 6-8.	175
Table 11	Preparation of complex on beads (GST-complex) and associated controls for pH-sensitivity pull-down SDS gel.	176
Table 12	Preparation of complex on beads (GST-complex) and associated controls for thermostability pull-down SDS gel.	176
Table 13	Preparation of SNARE complex samples for thermofluor assay.	176
Table 14	Individual components of each sample for fluorescent emission study, and its quantities.	177
Table 15	Preparation of labelled Protein A-IgG complex and associated controls for HRM.	177
Table 16	Preparation of labelled peptides complex and associated controls for HRM.	177

### 13. Figures

#### 13.1 Figures in Chapter 1

Figure 1.1	Early understanding of membrane fusion.	178
Figure 1.2	SNARE fusion machinery as it was understood in 1993.	179



Figure 1.3	SNARE-mediated exocytosis, showing the fusion machinery and heterotypic membrane fusion, as it is currently understood (2020).	180-181
Figure 1.4	Structure of the SNARE-complexin complex elucidated using a combination of X-ray and TROSY-based NMR (PDB: 1KIL).	182
Figure 1.5	Crystal structure of synaptotagmin-1 (PDB ID: 5KJ7).	183
Figure 1.6	Crystal structure of Munc18-1 complexed with syntaxin-1a in its closed configuration (Munc18a-Syx1a PDB ID: 4JEU) (Colbert <i>et al.</i> 2013). Domains	184
Figure 1.7	Crystal structure of the NSF/SNAP/SNARE 20S supercomplex elucidated using single particle cryoelectron microscopy (PDB: 3J96).	185
Figure 1.8	Regions within the SNARE complex that have been identified in the literature as necessary, or unnecessary for binding and assembly.	186
Figure 1.9	Cleavage sites of various clostridial neurotoxins (CNTs) situated on SNARE proteins.	187
Figure 1.10	Helical wheel diagrams depicting a birds-eye view of the helix axis from the N-terminus in a dimeric coiled coil (top) and tetrameric coiled coil (below).	188
Figure 1.11	Potential salt bridge conformations in arginine and lysine.	189
Figure 1.12	Punnett square depicting helical wheel diagrams for the possible spacing and positioning of arginine and glutamate within a monomeric $\alpha$ -helix.	190
Figure 1.13	Schematics of our proposed SNARE-based drug-delivery system, and an example of a simplistic drug delivery system from literature.	191
Figure 1.14	An illustration of the surface plasmon resonance and hypethermia phenomena in gold nanoparticles (Au NPs), and the different types of magnetic rotation and behaviour in magnetic NPs (MNPs).	192
Figure 1.15	Schematic of a circular dichroism (CD) spectrometer.	193
Figure 1.16	Flow-chart schematic depicting the “pull-down” assay methodology, which is conducted in conjunction with Polyacrylamide Gel Electrophoresis (PAGE) to measure the thermostability or pH-sensitivity of the SNARE-based complexes.	194
Figure 1.17	Outline of methodology for observing complex formation, and analysing thermal stability, using a combination of native polyacrylamide gel electrophoresis (PAGE) and real-time HRM (high-resolution melt).	195
Figure 1.18	3D structures of SNARE complexes of interest showing spacefill representations of each heptad in the SNARE motif.	196

## 13.2 Figures in Chapter 2

Figure 2.1	Flow chart summarising the aim and stages defining the project.	197
------------	---	-----

### 13.3 Figures in Chapter 3

Figure 3.1	The SNARE complex database.	198
Figure 3.2	“Scales” in the SNARE database.	199
Figure 3.3	General overview of “Analysis” section of the SNARE database.	200
Figure 3.4	Analysis of single amino acids, and taking moving averages in the SNARE database.	201
Figure 3.5	“Group analysis” section of the SNARE database.	202

### 13.4 Figures in Chapter 4

Figure 4.1	The sequence for each complex, alongside start and stop positions in a range of different scales including PDB scale, our positioning, segments and “4,3-layers” scale.	203-204
Figure 4.2	Hydrophobicity profile overlay for each protein sequence calculated using Kyte and Doolittle’s amino acid hydrophobicity scale and obtained using Protscale (ExpASy).	205
Figure 4.3	TMHMM (CBS) prediction of transmembrane helices	206
Figure 4.4	COILS (ExpASy) output predicting the presence of coiled-coil topologies	207
Figure 4.5	GlobPlot (EMBL) prediction of disorder and globular segments	208
Figure 4.6	Conserved domains obtained from collated from ProtParam (ExpASy), Conserved Domain Database (NCBI) and Globplot (EMBL) using each protein’s swissprot accession number	209
Figure 4.7	X-ray structure of SNARE complex ( <i>Rattus norvegicus</i> ) displaying transmembrane and linker regions (PDB: 3HD7).	210
Figure 4.8	SNARE motif alignment of all the mammalian SNARE proteins collated into the database thus far, showing conservation of residues as predicted by PRALINE.	211-213
Figure 4.9	NetGlycate 1.0 (CBS) prediction of lysine $\epsilon$ -amino acid groups	214
Figure 4.10	NetPhos 3.1 (CBS) prediction of serine, threonine and tyrosine phosphorylation sites	215
Figure 4.11	YinOYang 1.2 (CBS) prediction of O-GlcNAcylated serine and threonine residues	216

### 13.5 Figures in Chapter 5

Figure 5.1	Average hydrophilicity of nonpolar layers of each complex.	217
Figure 5.2	Residue volume of positions <i>a</i> and <i>d</i> in all three complexes ( <i>a</i> ), and in all four helices of complex 1N7S	218
Figure 5.3	Buried polar contacts in <i>a</i> and <i>d</i> layers of 1N7S.	219
Figure 5.4	Theoretical pI of polar segments.	220
Figure 5.5	Predicted interhelical salt bridges, with an O-N distance cut off of 4.0 Å, between the proteins in each complex 1N7S, 1L4A and 3B5N calculated using VMD software.	221-224
Figure 5.6	3D representation of salt bridges of interest created using PyMOL.	225

### 13.6 Figures in Chapter 6

Figure 6.1	Synchrotron Radiation Circular dichroism (SRCD) signal as a function of temperature for SNARE complexes containing a range of different length synaptobrevins.	226
Figure 6.2	Total residue volume (TRV) of each hydrophobic segment in a native full-length SNARE complex motif (PDB ID: 1N7S), with statistical comparators “average” total residue volume, and the deviations associated with it.	227-228
Figure 6.3	Demonstrates amino acid mutations in Brev2-05_27 (B05) that are expected to result in an improvement in thermal and chemical stability.	229-230
Figure 6.4	Demonstrates how selected amino acid mutations made in Brev2-04_34 (B04) are expected to destabilise the complex, and how this can be effectively compensated by corresponding mutations at the same positions in syntaxin.	231-232
Figure 6.5	Mutations in the ionic segments of the SNARE complex follow two streams of interest: pH-sensitivity and salt bridge destabilisation. Note: All positions are given according to Uniprot/PDB scale.	233-234

### 13.7 Figures in Chapter 7

Figure 7.1	Circular Dichroism (CD) spectra of positive control Protein A, full-length SNARE complex, and the separate protein chain components.	235
Figure 7.2	Circular dichroism (CD) spectrum of a full-length SNARE complex, and Synt34 SNARE complexes containing Brev34 (Brev2-04_34) and Brev27 (Brev2-05_27).	236
Figure 7.3	Testing the truncated SNARE complexes for stability in SDS, and comparing with full-length complex.	237

Figure 7.4	Circular dichroism (CD) spectra of Protein A control, full-length SNARE complex (FL/FL/FL), SNARE complexes with truncated synaptobrevin (FL/FL/34), and both truncated synaptobrevin and syntaxin (FL/34/34), as well as HEPES buffer background.	238
Figure 7.5	Results from preparation and purification of infra-red (IR) labelled SNAP-25 ("IR-SNAP25"), and optimisation of IR-SNAP25 concentration and buffer conditions for visualisation on polyacrylamide gel.	239
Figure 7.6	Assembly of all complexes in the Residue Volume study was investigated on native PAGE gels and the results are shown here.	240
Figure 7.7	Assembly of all complexes in the Ionic Interactions study was investigated on native PAGE gels and the results are shown here.	241
Figure 7.8	Circular dichroism (CD) spectra of full-length complex conjugated to magnetic iron oxide nanoparticles (MNP), and gold nanoparticles (GNPs) and associated controls.	242

### 13.8 Figures in Chapter 8

Figure 8.1	Example of typical SDS-gels containing the results from the supernatant product of temperature pull-down assay, which tests for thermal stability in the complexes pertaining to the Residue Volume, and Salt Bridge studies.	243
Figure 8.2	Results from the pull-down "beads" assays testing for relative thermal stability of the control complexes including partially truncated SNARE complexes (i.e. where synaptobrevin alone has been truncated), and SNARE complexes where both syntaxin and synaptobrevin are truncated.	244-245
Figure 8.3	Results from pellet "beads" and supernatant products of temperature pull-down assays, testing for thermal stability in complexes pertaining to the Residue Volume study.	246-247
Figure 8.4	Results from SRCD testing for thermal stability in complexes pertaining to the Compensation study.	248
Figure 8.5	Results from pellet "beads" and supernatant products of temperature pull-down assays, testing for thermal stability in complexes pertaining to the Salt Bridge study.	249-250
Figure 8.6	Results from SRCD testing for thermal stability in complexes pertaining to the Salt Bridge study.	251
Figure 8.7	Circular dichroism (CD) signal as a function of temperature for full-length,	252

and partially truncated SNARE complexes.

Figure 8.8	Example of a typical SDS-gel containing the results of a pull-down assay which tests for pH-sensitivity in the complexes pertaining to the pH-sensitivity study.	253
Figure 8.9	Results from the pull-down assays testing for pH-sensitivity in the complexes pertaining to the pH-sensitivity study.	254
Figure 8.10	Typical SRCD responses to pH by re-engineered complexes C04 and C0206.	255
Figure 8.11	Summary of pH response curves measured for three typical complexes C04, C06, and C0206.	256

#### 14. Appendix

Appendix 14.1	Differentiated thermal melt profiles, from the ROX channel (excitation 586 nm, emission 610/616 nm), of SNARE complexes (all 5 $\mu$ M) including CFL (full-length SNARE complex), C04 (SNARE complex containing truncated Synt1-01_34 and Brev2-04_34), C05 (SNARE complex containing truncated Synt1-01_34 and Brev2-05_27), and control lysozyme (0.1 mg/mL).	257
Appendix 14.2	Outcomes from Protein A labelling, fluorescent emission of IgG-FITC in the presence of labelled Protein A, high-resolution melts of IgG-FITC in the presence of labelled Protein A, and how it differs when commercial IgG-FITC is purified beforehand.	258-259
Appendix 14.3	Results from the high-resolution melt of the labelled peptide complex and controls.	260-261

## Index of Abbreviations

2-ME	<i>2-mercaptoethanol</i>
25C	<i>a.k.a. SNAP-25C - SNAP-25 C-terminal</i>
25N	<i>a.k.a. SNAP-25N - SNAP-25 N-terminal</i>
A	<i>Amps</i>
aa	<i>amino acids</i>
ATP	<i>Adenosine triphosphate</i>
B04	<i>B34/Brev34 - Brev2-04_34 synaptobrevin length 34 aa</i>
B05	<i>B27/Brev27 - Brev2-05_27 synaptobrevin length 27 aa</i>
BoNT	<i>Botulinum Neurotoxins</i>
BrevFluor	<i>BrevFluor34 - Brev2-04_34 labelled with Iodoacetamide-Fluorescein</i>
BSA	<i>Bovine Serum Albumin</i>
C0204	<i>Complex containing Synt1-02_34PH and Brev2-04_34</i>
C0205	<i>Complex containing Synt1-02_34PH and Brev2-05_27</i>
C0206	<i>Complex containing Synt1-02_34PH and Brev2-06_34PH</i>
C0207	<i>Complex containing Synt1-02_34PH and Brev2-07_27PH</i>
C0304	<i>Complex containing Synt1-03_34ST and Brev2-04_34</i>
C0315	<i>Complex containing Synt1-03_34ST and Brev2-15_34ST</i>
C04	<i>or Complex34 - containing Synt1-01_34 and Brev2-04_34</i>
C05	<i>or Complex27 - containing Synt1-01_34 and Brev2-05_27</i>
C06	<i>Complex containing Synt1-01_34 and Brev2-06_34PH</i>
C07	<i>Complex containing Synt1-01_34 and Brev2-07_27PH</i>
C08	<i>Complex containing Synt1-01_34 and Brev2-08_34ST</i>
C09	<i>Complex containing Synt1-01_34 and Brev2-09_34ST</i>
C10	<i>Complex containing Synt1-01_34 and Brev2-10_34ST</i>
C11	<i>Complex containing Synt1-01_34 and Brev2-11_34ST</i>
C12	<i>Complex containing Synt1-01_34 and Brev2-12_27ST</i>

C13	<i>Complex containing Synt1-01_34 and Brev2-13_27ST</i>
C14	<i>Complex containing Synt1-01_34 and Brev2-14_27ST</i>
C15	<i>Complex containing Synt1-01_34 and Brev2-15_34ST</i>
CD	<i>Circular Dichroism</i>
CFL	<i>Full-length SNARE complex</i>
CNT	<i>Clostridial Neurotoxin</i>
Cplx1	<i>Complexin-1</i>
Dab	<i>DABCYL-SE</i>
Dc	<i>Critical Diameter</i>
ddH2O	<i>double-distilled water</i>
DMSO	<i>Dimethyl sulfoxide</i>
EDTA	<i>Ethylenediaminetetraacetic acid</i>
EPR	<i>Enhanced Permeation and Retention</i>
FITC	<i>Fluorescein isothiocyanate</i>
FL	<i>Full Length</i>
FL/34/34	<i>or C04 - Full-length SNAP-25, truncated syntaxin and synaptobrevin length 34 aa</i>
FL/FL/34	<i>or CFL04 - Full-length SNAP-25 and syntaxin, truncated synaptobrevin length 34 aa</i>
FL/FL/FL	<i>or CFL - Full-length complex</i>
FRET	<i>Förster Resonance Energy Transfer</i>
GNP	<i>Gold Nanoparticles</i>
GST	<i>Glutathione S-Transferase</i>
GST-SNAP25	<i>Fusion protein of Glutathione-S-Transferase and SNAP-25</i>
HCl	<i>Hydrochloric acid</i>
HEPES	<i>4-(2-hydroxyethyl)-1-piperazineethanesulfonic acid</i>
HPMA	<i>N(2-hydroxypropyl)methacrylamide copolymer</i>
HRM	<i>High Resolution Melt</i>
IgG	<i>Immunoglobulin G</i>

IgG-FITC	<i>IgG protein linked to Fluorescein isothiocyanate</i>
IPTG	<i>Isopropyl <math>\beta</math>-D-1-thiogalactopyranoside</i>
IR	<i>Infrared</i>
IR-SNAP25	<i>IR-labelled SNAP-25</i>
kV	<i>kilovolts</i>
LB	<i>Luria-Bertani</i>
LCP	<i>Left handed circularly polarised light</i>
LPA	<i>Labelled Protein A</i>
mA	<i>milliAmps</i>
MNP	<i>Magnetic Nanoparticles</i>
MOPS	<i>3-(N-morpholino)propanesulfonic acid</i>
MTX	<i>Methotrexate</i>
MW	<i>Molecular Weight</i>
MWCO	<i>Molecular Weight Cut-Off</i>
NaCl	<i>Sodium chloride</i>
NMR	<i>Nuclear Magnetic Resonance</i>
NMWL	<i>Nominal Molecular Weight Limit</i>
NP	<i>Nanoparticle</i>
NSF	<i>N-ethylmaleimide sensitive fusion protein</i>
OG	<i>Octyl glucoside</i>
PAGE	<i>Polyacrylamide Gel Electrophoresis</i>
PBS	<i>Phosphate Buffered Saline</i>
PCR	<i>Polymerase Chain Reaction</i>
PDB	<i>Protein Data Bank</i>
PEG	<i>Polyethylene Glycol</i>
ph	<i>phonon</i>
PMSF	<i>Phenylmethylsulfonyl fluoride</i>



Q-SNARE	<i>Glutamine-contributing SNARE</i>
qPCR	<i>Quantitative Polymerase Chain Reaction</i>
R-SNARE	<i>Arginine-contributing SNARE</i>
RCP	<i>Right handed circularly polarised light</i>
RPM	<i>Revolutions Per Minute</i>
S01	<i>a.k.a. S34 - Synt1-01_34 or syntaxin length 34 aa</i>
SAR	<i>Specific Absorption Rate</i>
SAXS	<i>Small-Angle X-Ray Scattering</i>
SDS	<i>Sodium dodecyl sulphate</i>
SNAP-25	<i>Synaptosomal-associated protein 25</i>
SNARE	<i>Soluble NSF(N-ethylmaleimide-sensitive factor) Attachment Protein Receptor</i>
SPA	<i>Specific Power Absorption</i>
SPR	<i>Surface Plasmon Resonance</i>
SRCD	<i>Synchrotron Radiation Circular Dichroism</i>
Stxbp1	<i>syntaxin-binding protein 1</i>
SynDab34	<i>a.k.a. SynDab - Synt1-01_34 labelled with DABCYL-SE</i>
SYNT	<i>a.k.a. syn - Syntaxin</i>
Syt1	<i>synaptotagmin-1</i>
t-SNARE	<i>Target-associated snare</i>
TEMED	<i>Tetramethylethylenediamine</i>
TeNT	<i>Tetanus neurotoxin</i>
T <sub>m</sub>	<i>Melting temperature</i>
TROSY	<i>Transverse-Relaxation Optimised Spectroscopy</i>
TRV	<i>Total Residue Volume</i>
UPA	<i>Unlabelled Protein A</i>
UV	<i>Ultra-violet</i>
V	<i>Volts/Voltage</i>

v-SNARE	<i>Vesicle-associated snare</i>
VAMP	<i>a.k.a. brevin, synaptobrevin, brev - Vesicle Associated Membrane Protein</i>
W	<i>Watts</i>
XFEL	<i>X-Ray Free Electron Laser Diffraction</i>
XS	<i>Excess</i>
$\Delta\varepsilon$	<i>Molar circular dichroism or molar ellipticity</i>
$\Delta\sigma$	<i>Predicted deviation</i>
$\lambda_{\text{ex}}$	<i>Excitation wavelength</i>
$\lambda_{\text{max}}$	<i>Wavelength corresponding to the absorbance maximum</i>
$\mu$	<i>Mean</i>
$\sigma$	<i>Standard deviation</i>

# 1. Introduction

## 1.1 A brief history of the discovery of SNAREs

Morphological studies into the secretory pathway led to the hypothesis of a process, occurring via the fission of fused membranes, that enabled secretion granules to eject their contents into glandular lumina (Palade, 1959). This process came to be known as 'membrane fusion'. It consisted of four distinct steps that were carried out with great specificity. First the membranes of the secretion granule and the lumen come into close proximity, the granule fuses with the plasmalemma with remarkable specificity, given that granule is surrounded by a range of other cell membranes at equivalent distances. This fusion stage is also closely followed by the partial elimination, and reorganisation, of membrane layers that results in fission of the two membranes (Palade, 1974). A schematic illustrating these steps can be seen in **Figure 1.1**. Actual existence of endo- and exocytosis processes were recognised and appreciated by cell cytologists well before this point in time, though not specifically referred to with the endo- and exo- prefixes, which were introduced in 1963. It was, however, the illumination of the mechanism of membrane fusion that paved the way for our modern understanding of vesicle fusion and transport.

The challenge thereafter was to elucidate the molecular mechanisms that underpin vesicle fusion, and thus establish the basis for the speed and specificity observed in processes such as neurotransmission. Following successful reconstitution of vesicle transport in cell-free extracts a theory was suggested that membrane fusion must occur in a specific manner (Fries and Rothman, 1980). Subsequent studies implied that the specificity conferred to membrane fusion was of a biochemical nature as opposed to mere physical proximity, since fusion appeared to occur on a random basis when vesicles were given a choice of targets within Golgi populations (Balch *et al.* 1984).

Following successful isolation and identification of N-ethylmaleimide sensitive fusion protein (NSF) (Glick and Rothman, 1987), it was demonstrated that its inactivated form resulted in a build-up of uncoated vesicles on the Golgi membrane, meaning that NSF had a central role in membrane fusion (Malhotra *et al.* 1988). Three other protein factors, already independently characterised in the literature, were found to be involved in the NSF-dependent fusion pathway (Wilson *et al.* 1989). One of these proteins was a cytosolic, soluble NSF attachment protein (SNAP) that was found to be sensitive to proteases and heat (Weidman *et al.* 1989). The other two proteins were an integral membrane receptor exhibiting resistance to Na<sub>2</sub>CO<sub>3</sub> extraction as well as a range of tested proteases (Weidman *et al.* 1989), And finally a third cytosolic, soluble factor with a molecular mass

of approximately 25 kDa whose activity was observed in later stages of vesicle transport suggesting a role in the lead-up towards fusion (Wattenberg and Rothman, 1986). Thus, the discovery of NSF and its associated protein factors heralded the beginning of our current appreciation and understanding of soluble n-ethylmaleimide-sensitive factor attachment-protein receptor (SNARE) proteins.

The activity of a protein partner named  $\alpha$ -SNAP was found to be central to membrane fusion with its main responsibility being to facilitate the binding of NSF to Golgi membranes (Clary *et al.* 1990). A set of temperature-sensitive mutations of a “sec” gene, *sec18*, *sec17*, and *sec22* were found to result in the accumulation of vesicles. The authors concluded that a subsection of sec genes must therefore have vesicle fusion functions (Kaiser and Schekman, 1990).

An evolutionary conserved multisubunit fusion machine located on target membranes was proposed in 1990 (Clary and Rothman, 1990). Subsequently the yeast gene product, *sec17*, was found to be an orthologue of the mammalian  $\alpha$ -SNAP protein. Both proteins are peripheral membrane proteins with similar molecular mass, and similar function in Golgi membranes. Kinetic studies showed that they both appear to act at the same point in the fusion pathway, the *sec17* product complexes with the *sec18* product in a similar fashion to how  $\alpha$ -SNAP binds to NSF, and finally both sets of complexes require a membrane receptor for formation and binding to proceed (Griff *et al.* 1992).

Synaptic proteins that were directly involved in vesicle docking were identified as the key constituents responsible for vesicle-target specificity. Since the proteins were SNAP receptors, they were formally introduced as “SNAREs” (Söllner *et al.* 1993b). Upon formation of a SNAP-SNARE complex, NSF binds stoichiometrically forming a defined fusion particle, NSF then hydrolyses ATP initiating bilayer fusion, and subsequently detaches (Söllner *et al.* 1993a). SNAP-25 protein is located in the presynaptic terminals, and is associated with synaptic membranes, despite lacking hydrophilic sequence characteristic of transmembrane domains (Oyler *et al.* 1989). Palmitoylation at one or more of the four cysteine residues between positions 85 and 92 provides the necessary membrane anchoring of SNAP-25 to the membrane (Hess *et al.* 1992). Vesicle Associated Membrane Protein (VAMP), also referred to interchangeably as synaptobrevin, was found to be mostly cytoplasmic with a single hydrophobic carboxyl-terminal segment anchoring it into the synaptic vesicle membrane (Landis *et al.* 1988). Its role as an essential component in vesicle fusion was determined through its specific proteolytic cleavage by the potent neurotransmitter release inhibitors, tetanus and botulinum B toxins (Schiavo *et al.* 1992). Syntaxin protein is attached to the presynaptic membrane (Bennett *et al.* 1992). A schematic illustrating Söllner’s (1993) understanding of the SNARE complex, and its relationship with the 20S fusion particle, can be seen in **Figure 1.2**.

The SNARE hypothesis that emerged from the early research efforts suggested that the specificity of vesicle transport is due to the presence, recognition and binding of a vesicle-associated SNARE (v-SNARE), acting as a unique marker on a vesicle membrane, and a cognate target-associated SNARE (t-SNARE), acting in the same capacity on a target membrane (Sollner *et al.* 1993b). Binding studies indicated that weak binding between the cytoplasmic domains of VAMP and syntaxin was mediated by SNAP-25. Protein complex formation facilitates the high-affinity docking of VAMP-containing vesicles to the correct target membrane (Pevsner *et al.* 1994).

## 1.2 SNAREs and their biological role in membrane fusion

### 1.2.1 Introduction to membrane fusion and SNAREs

Membrane fusion is an intricately organised, highly coordinated, fundamental process that enables transport processes such as vesicle transport, cellular secretion, and exocytosis to occur with judiciously high specificity. The process of vesicle transport, and by association membrane fusion also, is well conserved in eukaryotes. Furthermore, there is evidence to suggest that the mechanism by which membrane vesicles are released is a universal phenomenon across all branches of life (Deatherage and Cookson, 2012). At the heart of this process are SNARE proteins, which are responsible for mediating vesicular fusion. They are collectively defined by the presence of a 60-70 amino acid long SNARE motif, which upon coming into close proximity with other SNARE motifs, is capable of folding into an amphipathic  $\alpha$ -helix beginning at their N-terminal ends.

Synaptic SNAREs are involved in synaptic transmission and are well characterised. These are: syntaxin-1a, VAMP-2 (also sometimes referred to as synaptobrevin-2s) and SNAP25 protein. Syntaxin-1a and SNAP25 are both Q-SNAREs as a result of a glutamine at position 226 (in the case of syntaxin-1a), and positions 53 and 174 (in SNAP-25), thus syntaxin-1a belongs to the Qa-subgroup of SNAREs, and SNAP25 belongs to the Qb/Qc subgroups (Weimbs *et al.* 1998). VAMP-2 is an R-SNARE as a result of its arginine residue at position 56 (Fasshauer *et al.* 1998). Both Q-SNAREs syntaxin-1a and SNAP25 are located on the presynaptic membrane, syntaxin-1a being anchored in via its transmembrane domain, and SNAP25 associated via palmitoylated cysteine residues situated within the linker joining the two SNARE motifs. The R-SNARE synaptobrevin-2 is anchored into the vesicle membrane via its transmembrane domain (**Figure 1.2**).

## 1.2.2 SNARE proteins

### 1.2.2.1 Location in the body

SNARE proteins describe a diverse family of intracellular proteins involved in targeting of intracellular organelles, and responsible for intracellular membrane fusion. The extensively studied neuronal SNARE protein complex, consisting of syntaxin-1a, SNAP-25, and VAMP-2, is expressed in eukaryotic neurons. It is responsible for mediating neurotransmitter exocytosis at axon terminals, and at neuromuscular junctions (Ramakrishnan *et al.* 2012). The variant syntaxin-3, along with VAMP-2, VAMP-7, and SNAP-25 has also been implicated in dendritic exocytosis in dopaminergic neurons, and hypothalamic neurons (Ovsepian and Dolly, 2011). The process of dendritic exocytosis does not differ significantly from the process at axon terminals, however it has been noted that SNARE inhibitors demonstrate different effects at each of these poles (Ovsepian and Dolly, 2011).

Some SNARE variants have been identified as having no direct involvement in neurotransmitter exocytosis, despite being enriched in brain tissues. An example is SNAP-29, which resides within the presynaptic compartment, and is thought to act a negative modulator of neurotransmitter release by possibly impeding the recycling of SNAREs following fusion (Wang and Tang 2006). Another example is Syntaxin-13, a human syntaxin variant that is localised in endosomes in neurons, that is thought to be involved in regulating glutamate receptor recycling (Wang and Tang 2006). VAMP-7 has been observed in axonal, and dendritic vesicles, as well as in multiple other tissues (Urbina and Gupton, 2020), and is involved in neurite outgrowth (Wang and Tang 2006) (Wojnacki *et al.* 2020). Other SNARE proteins exist outside of the central nervous system, for example SNAP-23, Syntaxin-4, and VAMP-8 catalyse granule fusion and secretion in mast cells (Lorentz *et al.* 2012).

### 1.2.2.2 Structure and function of neuronal SNARE proteins – syntaxin-1a, SNAP-25, and VAMP-2

The main SNARE proteins referred to in this study are the classic neuronal SNAREs (syntaxin-1a, SNAP-25, and VAMP-2), which with the help of a variety of other chaperone proteins including complexin, synaptotagmin, Sec1/Munc-18 (SM) proteins,  $\alpha$ -SNAP, and NSF mediate neurotransmitter exocytosis.

Syntaxins are t-SNARE proteins that are expressed in presynaptic compartments, and have been observed to congregate into membrane microdomains where exocytosis is initiated (Madrigal *et al.* 2019). They are the largest of the SNARE proteins, with the example syntaxin-1a contributing a

molecular mass of 33 kDa to the SNARE complex (*sp. Rattus norvegicus* – uniprot.org/uniprot/P32851). Syntaxin-1a has a transmembrane domain, and a cytoplasmic region that comprises of the SNARE motif, a t-SNARE domain referred to as “H3”, a linker region, and a SynN domain containing the conserved N-terminal domain Habc (see **Chapter 4** and **Figure 4.6** for more on domain structure). Along with syntaxin-12, syntaxin-1 is one of the most abundant Qa-SNARE in humans, and is necessary for axon outgrowth (Urbina and Gupton 2020). Syntaxin-1a and 1b are the main syntaxin isoforms in the brain (Ramakrishnan *et al.* 2012), whilst syntaxin-3 and 3a have been shown to be essential in trafficking membrane proteins in photoreceptors (Kakakhel *et al.* 2020). Syntaxin is known to form a tight complex with another protein called Munc-18 (also referred to as “sec1”), and Munc-13, which both chaperone syntaxin into forming productive membrane-bridging complexes (Hughson, 2013) (Kavanagh *et al.* 2014).

Synaptosomal-associated proteins, such as SNAP-25, are also presynaptic t-SNARE proteins. The “25” in SNAP-25 refers to its molecular mass of 25 kDa (Ramakrishnan *et al.* 2012). The synthesis of SNAP-25 at axonal sites is thought to be an early, and necessary step for the clustering of presynaptic proteins into membrane microdomains, and the development and function of presynapses (Batista *et al.* 2017). SNAP-25 is a cytosolic protein, without a transmembrane domain. It is attached to the presynaptic membrane via palmitoyl side-chains at a cysteine-rich region in between two the coiled coil domains housing the SNARE motifs (see **Chapter 4** and **Figure 4.6** for more on domain structure). SNAP-25 contributes two coiled coils to the SNARE core complex, serves as a site of interaction with other key proteins involved in exocytosis. When bound in a partly assembled SNARE complex with the other SNARE components (syntaxin-1a and VAMP-2), The proximal C-terminal ends of both SNAP-25 and VAMP-2 are clamped by a protein called complexin-1 (also known as “synaphin”). This suppresses zippering of the complex in the absence of an action-potential-induced calcium influx (Antonucci *et al.* 2016). Calcium-dependence of neurotransmitter release is mediated by another interacting protein – a calcium sensor called synaptotagmin (Antonucci *et al.* 2016).

VAMPs (or synaptobrevins), are v-SNAREs found on exocytotic vesicles in the presynaptic membrane. They are the smallest of the three SNARE proteins, with the example VAMP-2 contributing a molecular mass of only 12.7 kDa to the SNARE complex (*sp. Rattus norvegicus* – uniprot.org/uniprot/P63045). VAMP-2 has a transmembrane domain, which is located in the vesicle membrane (Ramakrishnan *et al.* 2012), and a cytosolic region, which contains the SNARE motif capable of interaction with coiled coil domains of SNAP and syntaxin proteins (see **Chapter 4** and **Figure 4.6** for more on domain structure). Co-localised with VAMP-2 on the vesicle membrane is the calcium-sensor synaptotagmin-1 (Hughson 2013), one of the key chaperone proteins involved in neurotransmitter exocytosis. It interacts with the assembled SNARE complex, and is responsible for

accelerating calcium-induced neurotransmitter release. The C-terminal domain of VAMP-2 plays a role in the fusion-pore formation step in neurotransmitter exocytosis (Ngatchou *et al.* 2010) (Han *et al.* 2017) (see **section 1.2.3** and **Figure 1.3** for the steps in neurotransmitter exocytosis). Following stimulation by an influx of calcium, the uncharged VAMP-2 transmembrane domain is drawn into the vesicle membrane, disrupting the bilayer structure, and initiating the fusion-pore formation (Ngatchou *et al.* 2010) (Han *et al.* 2017).

### **1.2.3 SNARE-mediated neurotransmitter exocytosis**

#### *1.2.3.1 Tethering and docking of vesicle*

A note on the terminology “cis” and “trans” in relation to SNARE complexes – a “trans” SNARE complex is a construct where syntaxin and VAMP are situated on different membranes, whereas in a “cis” SNARE complex, all proteins are situated on the same membrane. This is illustrated in **Figure 1.3**.

Tethering is the primary recognition step conferring spatiotemporal specificity to membrane fusion (see **Figure 1.3** panel 1), and the specificity of SNARE assembly is the second step (Koike and Jahn, 2019). Tethering of the vesicle is initiated by tethering factors, which are a large group of homodimeric coiled-coil proteins and multi-subunit tethering complexes (MTCs) that are responsible for tethering vesicles to the target membrane (Hong and Lev, 2014). With their ability to form transient, low-affinity interactions, the coiled coil proteins are expected to be involved in the nascent, and dynamic stages of tethering. MTCs, which have a smaller dynamic range of movement as they are only able to capture vesicles a short distance from the target membrane, are thought to regulate future events, including SNAREpin assembly (Hong and Lev 2014). Rab effectors, of the Ras GTPase superfamily, are an example of a tethering factor that work in tandem with Rab GTPases to mediate mammalian membrane tethering (Mima, 2018). Rab GTPases localise in the cytosol, and act as molecular switches, triggered by the binding of GTP. Once activated in their GTP-bound form, the Rab-GTPases recruit the Rab effector tethering factor to the membrane (Koike and Jahn 2019).

Tethering is followed by the docking, which includes progressive assembly of the four-helical SNARE protein complexes. The starting point is the binding of syntaxin-1a and SNAP-25 in a 1:1 complex on the target membrane (Dawidowski and Cafiso, 2016) (Ma *et al.* 2013). The process begins with syntaxin-1a in its closed state, with the Habc and H3 domains bound together in a conformation that is stabilised by Munc18-1 (Dawidowski and Cafiso 2016) (Rathore *et al.* 2019).



Munc18-1 acts as a chaperone in this way, as it prevents syntaxin-1a from interacting with any other proteins, including aggregating or assembling into the SNARE complex too early (Dawidowski and Cafiso 2016) (Baker and Hughson, 2016). Syntaxin-1a is known to have two distinctive binding modes with Munc18-1, “open” and “closed”, and a change in charge on the syntaxin-1a N-terminal induces a switch of binding modes to “open” (Kavanagh *et al.* 2014). A protein called Munc13 has been implicated in this process, and was reported to accelerate the switch in syntaxin-1a’s conformation to “open”, thus promoting SNARE assembly (He *et al.* 2018). This results in the t-SNAREs binding in the 1:1 complex.

#### 1.2.3.2 Priming

During vesicle docking, SM proteins such as Munc18-1 act as an interface for SNARE assembly, and work in tandem with tethering factors to bring VAMP and its vesicle cargo into molecular contact with the t-SNARE complex (Baker and Hughson 2016). The SNAREs assemble into a metastable parallel four-stranded coiled coil commencing at the membrane distal N-termini of the SNARE motifs and advancing in the direction, but stopping short of, the membrane proximal C-terminal membrane anchors (Wang *et al.* 2016). The assembly occurs via a putative transient, loosely assembled trans-SNARE conformation (Wang *et al.* 2016) (see **Figure 1.3** panel 2a and 2b).

At this stage there is intricate interplay between two regulator proteins, complexin-1 and synaptotagmin-1 (Xu *et al.* 2013). These two proteins ensure that SNARE assembly and resultant membrane fusion only occurs following the calcium ion influx triggered by an action potential (Yoon and Munson, 2018).

Complexin-1, a small cytosolic regulator protein, binds with high-affinity into a groove formed between syntaxin-1a and VAMP-2 in the assembled SNARE complex (Winter *et al.* 2009) (**Figure 1.4**). It has also been observed to bind to the partly-assembled complex prior to fusion pore opening, and thus primes the SNARE complex for subsequent synaptotagmin-1 action (Südhof, 2013). It has also been observed to impede assembly of the SNARE complex at the C-terminal, by clamping the C-terminal of VAMP-2 via its accessory domain. This prevents it from completing SNARE assembly with the t-SNAREs (Bykhovskaia *et al.* 2013) (Maximov *et al.* 2009).

Synaptotagmin-1, a transmembrane protein expressed on the membranes of transport vesicles, comprises of a short N-terminal luminal segment, a transmembrane helix, and an unstructured linker supporting two calcium binding domains referred to as C2A and C2B (**Figure 1.5**) (Baker and

Hughson 2016). The exact mechanism by which synaptotagmin-1 interacts with the SNARE proteins is unknown. Crystal structures resolved of synaptotagmin-1 and a SNARE complex demonstrated an calcium-independent conserved interface between the C2B domain of synaptotagmin-1, and the face of the SNARE complex formed by primarily polar residues on SNAP-25 and syntaxin-1a (Zhou *et al.* 2015).

### 1.2.3.3 Fusion-pore opening and completion

Electrostatic interactions, and the balance between attractive and repulsive forces, play an essential role in the fusion machinery (Ruiter *et al.* 2019). Before an action potential is fired, the balance in these forces keeps the vesicle in the primed state described in **section 1.2.3.2**, even though the SNARE complex is thought to be exerting force on the membranes through its zippering (Ruiter *et al.* 2019).

When an action potential is fired in a presynaptic terminal, the rapid influx of calcium ions through calcium channels in the presynaptic membrane induces membrane depolarisation. Calcium ions bind to the two calcium-binding domains C2A and C2B on synaptotagmin-1, which kick-starts neurotransmitter release. It also causes synaptotagmin-1 to draw the vesicle membrane in close proximity to the target presynaptic membrane via electrostatic interactions, and synchronously abolishes the complexin-1 clamp (Bombardier and Munson, 2015) (see **Figure 1.3** panels 2b – 3b). The energy barrier is lowered by a reduction in electrostatic repulsion, which is overcome when combined with the torque applied by the zippering SNARE complex (Ruiter *et al.* 2019) (Palfreyman and Jorgensen, 2008). The fusion-pore opening is created as a product of this process, and membrane fusion occurs rapidly as a consequence.

In discussion of energy barriers, it is thought that the individual v- and t-SNAREs exist in a thermodynamically metastable state. Upon combining, SNAREs form a highly stable, SDS-resistant SNARE complex, which resides in a lower energy state (Wang *et al.* 2016). This is thought to occur in a stepwise manner whereby the N-terminal domains of the t-SNARE complex initiate assembly of the SNARE complex, then the binding of the VAMP-2 to the middle domain stabilises the C-terminal domains and drives membrane fusion (Zhang *et al.* 2016) (Ma *et al.* 2016). There is a discernible hysteresis in the folding and refolding transition, which is indicative of a kinetic barrier to assembly, meaning it's highly likely to occur via an intermediate structure (Min *et al.* 2013).

The evidence for zippering has been established in structural studies, which have shown that once bound to VAMP-2, the membrane-proximal domain on syntaxin-1a progressively becomes more

ordered. In a study, fragments of syntaxin-1a's SNARE motif deficient in either a C- or N-terminus were studied to gauge their effect on exocytosis. SNARE motif fragments were most effective at inhibiting exocytosis when they contained the N-terminal, regardless of the presence of a C-terminal. Likewise, those containing a C-terminal were only successful at inhibiting exocytosis if they also possessed an N-terminal. These findings were used to support the zipper hypothesis, showing that it is a fundamental component of the fusion mechanism (Matos *et al.* 2003) (Yoon and Munson, 2018).

A number of models of exocytosis at the fusion stage have been published to date, with the two best described modes being “full-vesicle fusion” and “kiss-and-run” (KNR) (Urbina and Gupton 2020) (Shin *et al.* 2020). The full-vesicle fusion model proposes that the fusion-pore opening step is followed by pore dilation, and then collapse of the vesicle membrane into the plasma membrane. This effectively increases the neuronal surface area and fully releases all cargo (Urbina and Gupton 2020). The KNR mode differs in that the fusion pore opens and then subsequently closes with only partial discharge of contents and no expansion of the neuronal surface area (Urbina and Gupton 2020).

Both models occur via a cis-SNARE complex with all proteins situated on the now-fused single membrane (Yoon and Munson, 2018) (**Figure 1.3** panel 3a – 3b). The cis-SNARE complex is highly robust exhibiting both thermal stability and SDS-resistance.

#### 1.2.3.4 Release and recycle

Following fusion completion, the final step in the process is the disassembly of the SNARE complex and recycling of its constituent monomers and the vesicle. Given the stability of the cis-SNARE, disassembly can not happen spontaneously and requires assistance in the form of cytoplasmic proteins  $\alpha$ -SNAP, and the ATPase NSF (Bombardier and Munson, 2015). Disassembly is initiated by the binding of four  $\alpha$ -SNAP proteins, antiparallel to the SNARE complex (Yoon and Munson 2018). It is thought that binding of the first  $\alpha$ -SNAP molecule to the primary binding site on the SNARE complex nucleates binding of the other three  $\alpha$ -SNAP molecules to other weaker binding sites (Ma *et al.* 2016). These  $\alpha$ -SNAP proteins subsequently facilitate the interaction between NSF and the SNARE complex by binding to the N-terminal domains of NSF (Yoon and Munson 2018) (**Figure 1.3** panel 3b). Subsequently NSF binds the complex and catalyses the disassembly via ATP-hydrolysis (Vivona *et al.* 2013).

The structure of the D1 domains within the NSF hexamer has been obtained with ultra-high resolution cryogenic electron microscopy for a range of NSF-containing complexes including: the 20S complex, ATP-bound and ADP-bound NSF (Zhao *et al.* 2015). These reveal a conformational change in its orientation. Comparison of NSF bound to ATP or ADP showed that NSF has a “tight” structure around the SNARE complex when bound to ATP, however it undergoes a conformational change when ATP is hydrolysed to ADP, and adopts a much looser and open orientation. It’s possible that this 'spring-loaded' transition applies rotational forces, which unwind the SNARE complex in a shearing motion (Zhao *et al.* 2015). This immediately releases the SNARE proteins from the 20S complex (**Figure 1.3** panel 4). The instantaneous nature of this discharge prevents reassembly of the SNARE complex within the 20S complex (Yoon and Munson 2018).

Vesicle recycling ends the process, and there are multiple ways in which this can occur, depending on the mode of vesicle fusion observed (see **section 1.2.3.3**). An example of fast vesicle recycling is the kiss-and-run (KNR) mode of fusion, which results in local recycling and reuse of vesicles (Rizo and Südhof, 2012). KNR is favoured where rapid kinetics of recycling are necessary, where there are few vesicles that need to be extensively reused, and where the rate of transmitter discharge needs to be tuned (Urbina and Gupton 2020). An example of where this mode predominates over full vesicle fusion is at photoreceptor ribbon synapses, where it is observed to be convenient in sustaining release (Wen *et al.* 2017).

Slower recycling following full vesicle fusion occurs through an endosomal intermediate, and is dependent on clathrin, a self-assembling protein scaffold that coats the vesicle and is essential in the endocytosis-driven reconstruction and retrieval of the vesicle (Kaksonen and Roux, 2018) (Wen *et al.* 2017) (Rizo and Südhof, 2012). This mode of recycling requires relocation of VAMP, as well as Rab proteins and tethers, back to the donor membrane (Yoon and Munson 2018), which occurs through budding from the plasma membrane (Ungermann and Langosch, 2005) (Ovsepiyan and Dolly, 2011).

#### **1.2.4 Structure and function of other proteins that interact with the SNARE complex**

Complexin-1 (Cplx1) is a high-affinity SNARE complex binding protein that has been experimentally detected alongside syntaxin-1a in a pull down assay (Xue *et al.* 2007). These proteins are known to bind, via their central alpha-helical domain, antiparallel with the SNARE complex in a 1:1 stoichiometry (McMahon *et al.* 1995) (Südhof, 2013) at the groove formed specifically between VAMP-2 and syntaxin-1a, without disrupting the core complex structure (Chen *et al.* 2002). The SNARE-complexin-1 complex structure can be seen in **Figure 1.4**. Complexin’s  $\alpha$ -helix is positioned

anti-parallel to the SNARE complex, with its C-terminus bound to the middle of the groove between VAMP-2 and syntaxin-1a. Complexin interacts directly with the SNARE's central polar layer via a multitude of interactions including hydrophobic, hydrogen-bonding, and ionic interactions. Complexin's N-terminus, on the other hand, is suspended and somewhat exposed with no contact points between itself and the SNARE complex (Chen *et al.* 2002).

Synaptotagmin-1 (Syt1) belongs to the synaptotagmin family of C-terminal type tandem C2 proteins whose principal role is monitoring membrane traffic. Structurally, synaptotagmins typically consist of an N-terminal transmembrane region, which is the location of a VAMP-2 binding site (Fukuda, 2002), a variable linker, and two conserved C-terminal C2 domains designated C2A and C2B, which are capable of binding  $\text{Ca}^{2+}$ . Specifically, the five conserved aspartate residues on C2A are responsible for binding three  $\text{Ca}^{2+}$  ions, while the same aspartates on C2B are capable of binding two  $\text{Ca}^{2+}$  ions (Rizo *et al.* 2006). Synaptotagmin-1's structure can be seen in **Figure 1.5** (Lyubimov *et al.* 2016). Synaptotagmin-1 may play a part in controlling the accessibility of VAMP-2, and therefore regulate SNARE complex formation, or alternatively, VAMP-2's vesicle-targeting signal assists in sorting synaptotagmin-1 into synaptic vesicles (Fukuda, 2002). The C2B  $\beta$ -sandwich also contains a polybasic site, so-called for its patch of up to eight positively charged lysine residues, (Kuo *et al.* 2009) which is the main contact surface for SNARE complexes. This conclusion is supported by mutation data in which the removal of positive charges resulted in no observable membrane tethering (Vennekate *et al.* 2012). On the opposing side is its  $\text{Ca}^{2+}$ -binding site loop, which interacts with phospholipids in a  $\text{Ca}^{2+}$ -dependent manner. Both sites thus allow the protein to simultaneously interact with membranes on either side and facilitating fusion (Rizo and Rosenmund 2008, Dai *et al.* 2007).

Complexin-1 and synaptotagmin-1 work together to control fast  $\text{Ca}^{2+}$ -triggered exocytosis. Complexins have a dual role in fusion; they act as an activator of the SNARE complex, priming it for synaptotagmin action, and also as an inhibitor by way of a clamping mechanism on the partly formed SNARE complex (Südhof, 2013). Their clamping mechanism involves binding a pre-complex consisting of three SNARE motifs (syntaxin-1a and two SNAP-25s), and thus displacing VAMP-2 which remains bound at its N-terminal but flared out and unzipped at its C-terminal (Bykhovskaia *et al.* 2013). Another leading hypothesis suggests that while complexin-1 central helix is bound to one SNARE complex, its accessory alpha-helix reaches away and bridges with second SNARE complex (Kümmel *et al.* 2012). That helix competes with, and eventually displaces VAMP-2 (Kümmel *et al.* 2012). This inhibition thus occurs via a zig-zag topology which sterically hinders complete zippering and provides an additional obstacle to exocytosis (Kümmel *et al.* 2012). Complexin-1 is released as a result of  $\text{Ca}^{2+}$ -triggered displacement by synaptotagmin-1, which binds

simultaneously to both the SNARE complexes and to phospholipids in the bilayer, and induces vesicle fusion (Tang *et al.* 2006).

Deuterium exchange experiments using isolated SNARE complexes showed that a section between residues 42-54 of VAMP-2 (VVDIMRVNVDKVL), which is N-terminal to the polar layer, was highly shielded from exchange suggesting that this area is the site of a number of stable contacts between VAMP-2 and the remaining SNARE complex (Chen *et al.* 2002). When complexin-1 was added to VAMP-2, both ends of the polar layer and indeed beyond the binding region towards the C-terminal membrane anchors, experienced an increase in protection from deuterium, leading to the conclusion that one of complexin-1's roles is to stabilise the interface between VAMP-2 and syntaxin-1a in the SNARE complex (Chen *et al.* 2002). This becomes especially important during membrane fusion, since this very interface is responsible for tolerating the repulsive forces between the synaptic vesicle and plasma membrane. In this capacity, complexin-1 also acts to promote fusion hence 'dual role'.

The three synaptic SNARE proteins also share a common interaction with syntaxin-binding protein 1 (Stxbp1), which belongs to the Sec1/Munc18-like (SM) family of proteins and is more commonly referred to as Munc18-1 or nsec1. These proteins regulate SNARE activity by binding to syntaxin in its open state and assisting it in its conformational change to its closed configuration. Structurally, Munc18-1 is u-shaped, with an interior cavity of approximately 15 Å wide and three domains in total. Domains 1 and 3a are located at the ends of the u-shape forming binding sites for syntaxin-1a. **Figure 1.6** depicts the crystal structure of the binding complex formed between Munc18-1 and syntaxin-1a (Colbert *et al.* 2013). When the two proteins form a complex, the N-terminal Habc domain of syntaxin-1a is extended back onto the SNARE motif preventing SNARE complex assembly and facilitating its transport from the endoplasmic reticulum to the plasma membrane (Yang *et al.* 2000) (**Figure 1.3**).

Syntaxin's N-terminus is the location of a short peptide sequence named the N-peptide, which appears to associate with Munc18-1's domain 1, leading to some hypotheses around its importance in syntaxin-binding and by proxy, SNARE assembly. Data obtained by Burkhardt *et al.* (2008) showed that in the absence of an N-peptide, the Munc18-1-syntaxin-1a complex is capable of binding SNAP-25, suggesting that there is likelihood the N-peptide influences complex conformation. Furthermore, when the N-peptide is intact and bound to Munc18-1, SNARE assembly is prevented. When it is released, SNARE assembly is resumed. These findings suggest that SNARE assembly may include a Munc18-1-syntaxin-1a intermediate, which would then be joined by SNAP-25 and VAMP-2 in an order that remains unresolved (Burkhardt *et al.* 2008). Alternatively,

there is an argument to be made against the idea that the N-peptide influences complex conformation. Evidence from X-ray crystal structures for both a Munc18-1-syntaxin-1a complex with its N-peptide intact and one with it absent, were both revealed to have the same conformation (Colbert *et al.* 2013).

$\alpha$ -SNAP is a constituent of the NSF/SNAP/SNARE 20S supercomplex, a SNARE recycling machine responsible for guiding NSF-mediated SNARE complex disassembly. NSF does not bind SNARE complexes independently and so it is assumed that  $\alpha$ -SNAP acts as an adaptor, facilitating interaction between the two. Specifically, it acts as an adaptor between ATPase and NSF, to aid the fully assembled cis-SNARE in disassembling post-membrane fusion, thereby recycling the SNARE protein constituents (Ma *et al.* 2016). It carries out its function specifically through recognition of the cis-SNARE complex, and is shown not to act on the partially assembled trans-complexes (Zhao *et al.* 2015). It is thought that  $\alpha$ -SNAP recognises the folded C-terminal domain of the SNARE complex when it is bound to NSF, and modulates membrane fusion, bringing about disassembly, by destabilising the linker domain of the SNARE complex (Ma *et al.* 2016).

The crystal structure of the 20S supercomplex can be seen, alongside the isolated SNARE/ $\alpha$ -SNAP complex in **Figure 1.7**. The homomeric hexamer NSF is comprised of six N-terminal domains (N) when ATP-bound, and four when ADP-bound, which is the key contact surface for  $\alpha$ -SNAP-SNARE complex. There are two ATPase domain ring layers designated D1, which is comprised of six such D1 domains and is primarily responsible for ATPase activity, and D2, comprised of six D2 domains and carries out hexamerisation. The transition between ATP and ADP-bound states has been compared to a spring-loaded mechanism in which the compact ATP-bound D1 ring becomes relaxed. The principal differences observed between the ATP- and ADP-bound NSF structures support this model. In the ATP-bound NSF complex, the D2 ring adopts a planar, symmetric conformation, and the D1 ring is resonant of a right-handed 'split washer'. In the ADP-bound NSF state, the D2 ring is asymmetrical with a small gap, and the D1 ring is stretched-out, planar and reminiscent of an open 'flat washer' (Zhao *et al.* 2015). The "washers" in this explanation are references to engineering hardware washers, which are characteristically thin, disk-like plates used as spacers between nuts and bolts.

Structurally,  $\alpha$ -SNAP consists of fourteen  $\alpha$ -helices, nine of which are organized in an antiparallel twisted sheet within the N-terminal domain, and the remaining five forms the C-terminal globular bundle. The majority of the N-terminal domain twisted sheet is arranged in a concave formation, such that the centre face wraps around the SNARE complex's convex surface much like a sheath. The remaining longer edge of the twisted sheet is curved such that it can fit within the narrow grooves between the proteins making up the SNARE complex (Marz *et al.* 2003). Site-directed

mutagenesis on charged residues located across this concave surface led to the conclusion that  $\alpha$ -SNAP contains a conserved diagonal ridge comprising of six basic lysine residues (Lys56, Lys93, Lys94, Lys122, Lys163 and Lys167). Their mutation to alanines resulted in reduced SNARE complex binding to  $\alpha$ -SNAP, and disassembly. The SNARE complex also presents three complementary diagonal bands composed of four to five acidic residues, which are located in close enough proximity to the lysines on  $\alpha$ -SNAP to form salt bridges (Marz *et al.* 2003). These three potential binding sites are detailed in **Table 1**.

The efficiency of  $\alpha$ -SNAP kinetics in facilitating SNARE disassembly on liposomes is approximately 20 times faster than in solution. Such dependence on liposomes was also observed when either VAMP or syntaxin were used for complex incorporation (Winter *et al.* 2009). This negates the supposition that membrane anchors are responsible for this increase in efficiency. The first two helices of the twisted sheet are connected by a hook-like extended loop comprising primarily of hydrophobic amino acids (between residues 27-32). These positions are highly conserved across a number of different SNAPs. Based on the hydrophobicity of this location it can be inferred that this loop may act as a membrane-binding site, augmenting  $\alpha$ -SNAP efficiency in facilitating disassembly. In support of this hypothesis, Winter *et al.* showed that there was no enhanced efficiency of disassembly previously observed in the presence of a membrane, when the entire loop was deleted between residues 1-32 (Winter *et al.* 2009).

### **1.2.5 What is already known about the hierarchy of SNARE complex formation?**

The widely accepted knowledge on the hierarchy of SNARE complex assembly is highly relevant to this project since it ties into one of the hypotheses of this project. It states that SNAP-25 N-terminal preferentially binds to syntaxin in the 1:1 binary complex, and this initiates assembly. This section summarises the current state of the knowledge on this topic, and outlines the regions that have been deemed “necessary” for complex assembly. This information can then be used to inform the rational design process of SNARE-based peptides addressed later on in the project.

The zipper model outlines the argument that complex formation is split into two consecutive steps, beginning with an initial partial trans-SNARE complex forming at the N-terminus, and followed later by coiled coil formation at the C-terminus (Jahn and Scheller, 2006). Multiple studies have established that the interaction between syntaxin and VAMP is very weak, and requires the association of SNAP-25 to enhance binding (Pevsner *et al.* 1994). However interestingly, it has been reported that liposome docking is still possible by this binary interaction between syntaxin and VAMP even in the absence of SNAP-25 (Bowen *et al.* 2004). More importantly, when the local



temperature of the docked liposomes was increased to 37°C using laser illumination, the distribution of SNAP-25-deficient docked liposomes undergoing fusion closely resembled that of SNAP-25-intact docked liposomes. This would indicate that thermally-induced fusion can occur independently of SNAP-25 (Bowen *et al.* 2004).

Although SNARE assembly begins with the 1:1 binary complex between the t-SNAREs syntaxin and SNAP-25, the 2:1 (syntaxin:SNAP-25) ternary t-SNARE complexes might also exist *in vitro*. Such complexes cannot promote fusion *in vivo*. In yeast, the 1:1 binary complexes of Sso1 and Sec9 have been characterised using NMR, which showed that the complex is helical from the N-terminus to approximately two-thirds into the motif, with the remaining C-terminal unstructured and “frayed” (Fasshauer, 2003a). Neuronal SNAREs are more likely to form 2:1 ternary complexes, *in vitro*, between two molecules of syntaxin and one SNAP-25, where one syntaxin takes the place of VAMP. The resulting 2:1 complex will remain unstructured at both ends of helix (Fasshauer, 2003a). It is thought that *in vivo*, either the second syntaxin of the 2:1 ternary complex is displaced by VAMP, or simply that a 1:1 binary complex forms and acts as a receptor site for VAMP (Lou and Shin, 2016).

Studies independently reporting the inhibitory effect of synthetic small peptides patterned after the C- and N-terminal of SNAP-25 on complex assembly and synaptic transmission provide limited insight into which regions are most essential to complex assembly. Comparison between a 20-mer synthetic peptide based on the C-terminal region of SNAP-25 (Ser187-Gly206), and a control peptide composed of the same amino acids but randomly ordered, showed that the inhibition of assembly is sequence-specific. Furthermore, a shortened version of this peptide (Ala195-Lys201) proved to be inactive indicating that peptide length is a factor in determining the efficiency of competition with native SNAP-25 (Gutiérrez *et al.* 1995) (Apland *et al.* 1999). In another similar study, Gutiérrez *et al.* also synthesised a peptide based on the N-terminal of SNAP-25 (Met49-Arg59), and observed no inhibitory effect on synaptic transmission. However in a later study, a synthetic peptide based on a different N-terminal sequence Met1-Ile44 showed inhibition (Blanes-Mira *et al.* 2004). Four peptides were tested (amino acid positions 1-21 (peptide N1), 22-44 (N2), 10-22 (N3), and 26-38 (N4)). The order of inhibition potency (N4>N3>N2>N1) revealed the short region most critical for the assembly as Leu26-Glu38. N-terminal deletion studies of SNAP-25 were consistent with the peptide inhibition experiments, and indicated that the segment containing Met1-Leu21 might be important for the stability of the resulting complex. The regions identified above can be seen in relation to the sequences in **Figure 1.8**. This information is useful for gaining an understanding of the key regions of the motif that are necessary for assembly, and therefore good targets for either maintaining or reducing stability of the complexes. This information can also be

used to inform us where corresponding key regions might occur in the other chains based on the interactions observed within them.

Since both synthetic peptides based on the two domains of SNAP-25 (Met1-Ile44 and Ser187-Gly206) outlined above bind to syntaxin in isolation, the more realistic alternative is that the first two scenarios for the t-SNARE binary complex formation exist in equilibrium, where syntaxin associates with any one of the two domains of SNAP-25. There is an assumption in the literature, that syntaxin's N-terminal domain must be in the open conformation to facilitate the existence of an equilibrium between three different possible configurations (Brunger *et al.* 2009): the first configuration consists of all t-SNARE domains of syntaxin and SNAP-25, the second and third feature syntaxin and either one of the N- or C-terminal domains of SNAP-25 exclusively, with the other domain dissociated (Brunger *et al.* 2009). Furthermore, the absence of the SNAP-25 C-terminal sequence cleaved by botulinum toxin E (positions Ile181 – Gly206) has adverse effects on the formation of the t-SNARE binary complex (Rickman *et al.* 2004). These findings together indicate that both N- and C-terminal domains must be present for the binary complex to form, and they therefore support the associations between syntaxin-SNAP-25 N-terminal domain.

Binding of VAMP to the binary complex (syntaxin:SNAP-25) was also studied using C-terminal and N-terminal fragments of VAMP. All the C-terminal fragments showed faster binding kinetics than the N-terminally extended fragments, indicating that a short N-terminal is satisfactory for fast binding of VAMP (Pobbati, 2006). This is followed by the formation of the initial, partially formed trans-SNARE complex assembled at the N-terminus. The torque produced by the zippering of this trans-SNARE complex delivers the free energy required to overcome the high activation energy barrier to fusion. A kinetic study into the rates of assembly using stopped-flow electron paramagnetic resonance (EPR) revealed that the bulk of the protein complex core in yeast SNAREs is formed in a single kinetic step (Zhang *et al.* 2004), rather than a two-step assembly process as suggested for neuronal SNAREs (Fasshauer 2003). This conclusion is supported by the observation that core SNARE assembly occurred at a faster rate than membrane fusion, prompting the suggestion that assembly and membrane fusion occurs in parallel since core complex formation is expected to be the driving force for membrane fusion.

Though the exact hierarchy of complex formation has not been fully elucidated, it is thought that the initial formation of the binary complex occurs, and the association of the R-SNARE follows this. There are two possible scenarios regarding the order of SNARE motif binding among the t-SNAREs that could be explored: syntaxin could bind to SNAP-25 N-terminal first, then SNAP-25 C-terminal joins up. The order of the SNAP-25 termini could be reversed in that syntaxin associates with SNAP-25 C-terminal first, then SNAP-25 N-terminal joins.

### 1.2.6 Clostridial neurotoxin (CNT) substrate recognition sites

Whilst the SNARE complex remains one of the most thermo- and chemo-resistance protein complexes known to date, it is susceptible to protease cleavage by proteins of the clostridial neurotoxin (CNT) family. This consists of tetanus neurotoxin (TeNT) and botulinum neurotoxins (BoNTs) A, B, C, D, E, F, and G. Vesicle-associated SNARE VAMP is host to four cleavage sites from BoNTs B, D, F, G, and TeNT, which shares the same cleavage site as BoNT B (Schiavo *et al.* 1992), SNAP-25 located on the pre-synaptic membrane features cleavage sites for BoNT A, C, and E, whilst syntaxin, also located on the pre-synaptic membrane, features a single cleavage site for BoNT C (**Figure 1.9**).

BoNT B and TeNT action produces two fragments of VAMP resulting in inhibition of neurotransmission. Though they share the same peptide cleavage site, studies have shown that their action depends on the recognition of differently sized substrates. TeNT recognises a 62-amino acid long fragment corresponding to the hydrophilic core of the SNARE motif of VAMP (Gln33-Lys94). BoNT B is less specific, it recognises a 40-amino acid long peptide fragment Glu55-Lys94 (Foran *et al.* 1994). BoNT D's peptide cleavage site in VAMP was identified as Lys59-Leu60 (Schiavo *et al.* 1993a). Mutagenesis studies focusing on nine specific amino acids (Val39, Val43, Met46, Glu55, Asp57, Gln58, Lys59, Leu60 and Ser61) within a segment of VAMP spanning Val39-Ser61 were found to reduce BoNT D cleavage by up to 33%. The most essential substrate recognition site that permits optimal cleavage appears to cover a cluster between Val39 – Met46 (Sikorra *et al.* 2008). Hydrophobic interactions between BoNT D and VAMP are said to be critical for recognition, and in particular Met46 has been singled out as a vital binding site that expedites the binding of these downstream sites Asn49 and Val53 (Guo and Chen, 2013). BoNT F was found to target the peptide bond between Gln58-Lys59 in VAMP (Schiavo *et al.* 1993b). BoNT F requires a segment spanning Ala21-Asp64 to carry out optimal cleavage, this 44-mer length demonstrates a more taxing specificity compared to BoNT D's 23-mer substrate recognition site (Sikorra *et al.* 2008). BoNT G selectively cleaves the Ala81-Ala82 peptide bond in the C-terminal of VAMP (Schiavo *et al.* 1994). Substrate recognition sites for BoNT G and also BoNT C have not been identified in the literature as of yet.

The t-SNARE syntaxin possesses a single cleavage site specific to BoNT C, which corresponds to the peptide bond between Lys253-Ala254. BoNT C also targets the t-SNARE SNAP-25 between Arg198-Ala199 (Blasi *et al.* 1993). BoNT A and E both target SNAP-25 at bonds located between Gln197-Arg198 and Arg180-Ile181 respectively (Binz *et al.* 1994). A study showed that the small

region Met146-Gly155 was vital for toxin-substrate interaction, since its absence from derivatives did not show any detectable binding (Vaidyanathan *et al.* 2002). Two separate sections, which showed inhibition of BoNT A action, were resolved. These were defined as the active site between Asp193-Met202, and the binding site between Ile156-Ile181, which directly follows the critical region (Met146-Gly155) demarcated by Vaidyanathan *et al.* (Chen and Barbieri, 2006). Structural overlap containing a mixture of salt bridges and hydrophobic interactions between the heavy chain loop of BoNT A and SNAP-25 C-terminal spanning residues Ile156-Asp193 (38-mer length) indicates that this region acts as the key substrate recognition site (S. Chen *et al.* 2007). Bont E was found to target fewer sites, with two regions encompassing residues Ile178-Glu183 in the active site domain, and Met167-Thr173 in the binding domain on SNAP-25 being the most likely substrate recognition zones (Chen and Barbieri, 2006).

### **1.3 Self-assembling coiled coils**

#### **1.3.1 Molecular structure and geometry**

A conventional  $\alpha$ -helix exhibits a structural repeat every 5.4Å along the chain, this is more commonly referred to as its 'pitch'. This is because there are approximately 3.6 amino acids per helical turn, and each residue has a rise of 1.5Å. As a result of this geometry, in an amphipathic protein structure, the hydrophobic side chains must be distributed along the chain in threes, separated from each other by a length of four residues. This 4,3 pattern is known as a heptad repeat, since it is comprised of seven residues. In nature, the most prevalent heptad repeat, suspected to result in the most efficient packing, follows the pattern *abcdefg*, in which a hypothetical protein's side chain residues *a* and *d* are hydrophobic, and the remaining *b,c,e-g* side chains are polar. A coiled coil is a protein structural motif, comprised of two or more right-handed  $\alpha$ -helices coiled together to form a marginally left-handed helical structure,. This motif can be defined by the presence of the aforementioned heptad repeat.

The heptad repeat feature is the stabilising force of the coiled-coil since it is able to efficiently 'bury' the hydrophobic chains of the protein by effectively sandwiching them between the polar ones and thus preventing access of polar water molecules to this hydrophobic core. Interlocking side chains, within the central core of the coiled-coil that result from tandem heptad repeats requires a distortion of the  $\alpha$ -helix, and specifically in the number of residues per helical turn, which is reduced from 3.6 in an average  $\alpha$ -helix, to 3.5 in the coiled coil. An illustration of this can be seen in the helical wheel

diagram in **Figure 1.10**, where the hydrophobic interphase at the centre of the dimeric coiled coil can be seen, alongside the ionic interactions occurring between *e* and *g* outer residues.

### 1.3.2 Matching amino acid properties to positions “*abcdefg*”

#### 1.3.2.1 Positions *a* and *d* are generally inhabited by hydrophobic residues

Assembly of coiled coils involves molecular recognition between two or more  $\alpha$ -helices. Their binding partners and multimerisation properties can be potentially fine-tuned by altering the amino acid sequence. Such motifs are perfect inclusions for self-assembling protein complexes. Different lengths of coiled coils exist in nature. An example of a short-coiled coil would be GCN4 leucine zippers (coiled coil domain length 22 amino acids according to Uniprot P03069) a transcription factor for gene expression. Single-point mutants of the GCN4 proteins have been shown to alter DNA sequence recognition at a specific base pair, which acts as evidence of the existence of direct contacts between individual amino acids and base pairs (Tzamarias *et al.* 1992). Longer coiled-coils are typically observed in organisational or regulatory roles such as golgins (coiled coil domain length 2053 amino acids according to Uniprot Q13439) which mediate membrane tethering (Rose and Meier, 2004), and whose length is interspersed with short breaks that are assumed to confer conformational plasticity (Truebestein and Leonard, 2016). Equally, modifications of the residues within the heptad repeat will also influence molecular recognition and ultimately, coiled coil stability. It was recognised early on that the greater the percentage of hydrophobic residues at positions *a* and *d*, the more stable the coiled coil (Lau *et al.* 1984). Since then, there has been much interest into which residues lend the greatest stability at positions *a* and *d*. Generally, aliphatic hydrophobic residues such as alanine, isoleucine, leucine, methionine and valine are best suited, whilst hydrophobic amino acids containing aromatic side chains such as phenylalanine, tryptophan and tyrosine are all avoided due to their steric hindrance.

One study of particular pertinence is the structure-function analysis of two *d* positions of a leucine zipper in the bZIP domain carried out by Moitra *et al.* In that study, the authors mutated the second and fifth *d* position of a native bZIP protein to seven different amino acids (leucine, methionine, isoleucine, valine, cysteine, alanine and serine) in order to measure the energetic contributions of each, using circular dichroism thermal denaturation. It found the order of decreasing stabilisation to be: Leu>Met>Ile>Val>Cys>Ala>Ser. Leucine is exceptionally stable and suited to the *d* position. When compared to the similarly sized isoleucine, it has been shown to demonstrate up to 2.9

kcal/mol more stabilising energy, and a further 4.6 kcal/mol more stabilising energy than the smaller sized alanine (Moitra *et al.* 1997).

The lower packing energies of the  $\beta$ -branched isoleucine and valine could be attributed to the conformational strain caused by steric clashing between C $\gamma$ 2 methyl groups featured on neighbouring residues of the other helices (Moitra *et al.* 1997). This is because in the *d* position, the C $\alpha$ -C $\beta$  bond is directed towards the neighbouring  $\alpha$ -helix, whilst in the position the C $\alpha$ -C $\beta$  bond points away from the hydrophobic core. This means that  $\beta$ -branched residues are actually more stable in a position than any other residues of similar or superior hydrophobicity (Moitra *et al.* 1997). Supporting this, Wagschal *et al.* reported a stabilising packing effect when leucine was substituted for isoleucine at position *a* in their peptide X19a (Wagschal *et al.* 2008).

Frequency data about the amino acids found within heptad repeats was studied using Walshaw and Woolfson's SOCKET computer programme, designed to recognise the so-called 'knobs-into-holes' side chain-packing characteristic of coiled coils. The study analysed frequency data about the amino acids, and their positions (Walshaw and Woolfson, 2001). **Table 2** summarises the normalised frequencies of occurrence of each amino acid at each heptad position within long parallel two-stranded coiled coils (Walshaw and Woolfson, 2001). Normalisation was carried out by dividing the amino acid profile for long parallel two-stranded coiled coils by the relative frequency of each amino acid in swissprot (Walshaw and Woolfson, 2001). It was observed that the polar asparagine (normalised frequency 4.04), followed by the branched, hydrophobic valine (normalised frequency 3.12) appeared to be most favoured for position *a*, whilst position *d* was most frequently occupied by aliphatic, nonpolar amino acids leucine (normalised frequency 7.61), and methionine (normalised frequency 4.59). The authors also commented that the structures of two- and four-stranded parallel coiled coils are closely related, with the only major difference being the reversal in the *a* and *d* core-packing angles. Core-packing angles are a way of describing the geometry of a knob side-chain with respect to its complimentary hole. It has been used to rationalise the difference between the positions of knob side-chains within different heptad layers in coiled coils with more than two chains. For long parallel two-stranded motifs, these angles were calculated to be 30-35° for *a* layers (parallel packing), and 90-95° in *d* layers (perpendicular packing). In the four-stranded parallel coiled coils, the angles were 80-85° for *a* layers (parallel packing), and 30-35° in *d* layers. In a following study, they shifted focus towards parallel four-stranded coiled coils, reporting that for position *a*, the order of favoured amino acids is: methionine  $\approx$  isoleucine > valine > leucine > alanine, whilst for position *d*, the order is: methionine > isoleucine > glutamine (Woolfson 2005).

An alternative method of increasing the stability by exploiting the heptad repeat is to incorporate unnatural amino acids, which are more hydrophobic than their naturally occurring counterparts. The

substitution of four *d*-position leucines for highly nonpolar fluorinated leucines, 5,5,5-trifluoroleucines in the dimeric coiled coil GCN4-p1d, is a good example of this (Tang *et al.* 2001). The authors of this study reported a considerable rise in stability characterised by increases in midpoint thermal unfolding temperature by 13°C, and free energy of folding by 0.5-1.2kcal/mol in the fluorinated peptide compared to its hydrogenated analogue. Since our aim is to reduce the melting point of the SNAREs, whilst maintaining their specificity, there is a possibility that unnatural amino acids could be used as a negative design principle in the sense that they can be incorporated into key sites to prevent certain interactions and guide assembly in a specific direction. Essentially, this study represents a different avenue towards modulating stability and specificity.

### 1.3.2.2 Positions *b,c,e,f,g* are generally inhabited by polar residues

For positions *b*, *c*, *e*, *f*, and *g*, the polar amino acids that are most favoured in nature and known to promote helical structure include alanine, glutamine, lysine, arginine and glutamate. Glycine and proline are both known to disrupt  $\alpha$ -helical structures, whilst cysteine's propensity for forming disulphide bonds, or otherwise oxidising, means it is also eschewed in coiled coil design (D. N. Woolfson, 2005).

Charged residues, glutamate, aspartate, lysine, arginine, and histidine most commonly occupy positions *e* and *g*, allowing for the formation of intra- and interhelical salt bridges, which for many complexes marks the initial interaction between helices. These interactions then act to guide assembly and further contribute towards the thermal stability of the complex. Polar residues generally occupy the remaining *b*, *c* and *f* positions, which are found at the periphery of the core, in many cases they may also be charged and therefore also can potentially partake in intra- and interhelical salt bridges, or simply hydrogen bonds. The comparative distance and strength limitation of salt bridges compared to hydrogen bonds could possibly have a proportionate influence on the assembly of the SNARE proteins. With their cut-off distance of 4.0 Å, salt bridges are relatively long-distance interactions, whose influence will extend towards the assembly of the complexes. Hydrogen bond strength has been categorised based on distance. Bonds with donor-acceptor distances between 2.2 and 2.5 Å are strong and have a degree of covalency with bond energies of ~40-14 kcal/mol. Longer bonds of 2.5-3.2 Å are moderately strong and mostly electrostatic in nature, with bond energies of ~15-4 kcal/mol. Long bonds of 3.2-4.0 Å are weak electrostatic interactions with energies of <4 kcal/mol (Jeffrey, 1997).

Different geometries of salt bridges are expected according to the amino acid participants, and the distances between them. Arginine, for example, is marginally favoured over lysine, whilst for the

negatively charged residues, glutamate is preferred over aspartate (Huyghues-despointes *et al.* 1993). The preference for arginine may be due to its ability to delocalise the charge onto any of the three nitrogens of the guanidinium group. This means it is capable of forming both side-on and end-on bidentate interactions with acidic amino acid lone pairs in their syn conformation, which are stabilised by the chelate effect due to the resulting six-membered ring formed (see **Figure 1.11**). Of the two conformations, side-on interactions have been shown to form in preference to end-on interactions when the participating amino acids are closely spaced (i.e. a separation of less than 5 amino acids), and are most common within protein folds, whilst end-on interactions are more common in protein-protein interactions (Donald *et al.* 2012). On the other hand, lysine is only capable of forming monodentate salt bridges with acidic residues, and these can be arranged in three different conformations: torsion angle  $180^\circ$ , gauche minus with a torsion angle of  $300^\circ$ , and gauche plus with a torsion angle of  $60^\circ$ . Trans interactions are expected to be preferable to gauche conformations due to the hindrance they present to bond rotation. However in protein-protein interactions, all three conformations occur in almost equal numbers (ratio of the two gauche conformations to trans is  $\sim 2$ ), and gauche conformations are more common than trans at spacings of 5 and below (Donald *et al.* 2012).

Basic and acidic amino acids are of specific importance since inter- and intrahelical salt bridges are the key component of the 'trigger sites', which are partially responsible for mediating stable coiled coil formation. Intrahelical salt bridges can be classified into two groups defined by their "*i to i+x*" spacings. These are: "*i to i+3*" and "*i to i+4*", which are named for the spacing between the starting residue, *i*, and the position of the residue of interest, 3 or 4. Of particular significance are the positions of arginine and glutamate, which have been investigated by Burkhard *et al.* in order to determine the best configuration to optimise salt bridge formation and therefore, improve  $\alpha$ -helical stability. There are four possible combinations of spacing and arginine versus glutamate positioning within the coiled coil, these are named *3RE*, *3ER*, *4RE*, and *4ER*, and they are visually represented in helical wheel diagrams in **Figure 1.12**. Shorter distance between the charged groups of the amino acids corresponds to stronger ionic interactions. Amino acids containing shorter side chains were best suited to position *i*, in an *i+3* spacing, whilst for an *i+4* spacing, longer side chains were more suited to position *i*. Therefore *3ER* and *4RE* arrangements are more energetically favourable than their counterparts (Burkhard *et al.* 2002). However, this conclusion is mostly reflective of monomeric  $\alpha$ -helices, and since the SNARE complex is a tetrameric system, the rules governing stability within interhelical salt bridges are more important.

In the same study, Burkhard *et al.* considered arginine and glutamate amino acids positioned in the *g-e'* interhelical salt bridge arrangement, thus giving rise to the naming convention: *g-e'RE* versus *g-e'ER* (Burkhard, Ivaninskii, and Lustig 2002). Interhelical salt bridges of *d-e'*, *g-a'* and *d-a'* are not



possible due to the hydrophobic nature of amino acids residing in positions *a* and *d*. The *g-e'RE* geometry was found to be the most energetically favourable of these geometries because it allows arginine's longer side chain to angle towards the C terminus. This is consistent with the accepted convention that negatively charged side chains are energetically favourable when oriented towards the N-terminus, and positively charged side chains oriented towards the C-terminus (Burkhard, Meier, and Lustig 2000). Additionally, glutamic acid's side chain is able to pack against the hydrophobic core formed by amino acids in positions *a* and *d*, and finally, all charged groups are conveniently placed for ideal hydrogen bond interactions (Burkhard, Ivaninskii, and Lustig 2002). These conclusions are based solely on the combinations of arginine and glutamate amino acids, however it would not be unreasonable to expect that the essence of these findings can be extrapolated to other amino acids.

### 1.3.3 Amino acid properties governing molecular recognition and stability

The SNARE motif featured exhibited by SNARE proteins takes the form of a parallel heterotetramer, and as such, it is this type of coiled coil that this project will focus on. Building an understanding of the features that underlie the stability and specificity of SNARE coiled coil self-assembly begins with a discussion of the chief properties of the residues that occupy each of the positions (*abcdefg*)<sub>*n*</sub>. These properties include: hydrophobicity, charge, theoretical pI, and residue volume.

Like all coiled coils, the SNARE motif features heptad repeats at the core of its complex, stabilising the resulting helix through van der Waal and hydrophobic interactions. Beyond determining the structure of the protein, the hydrophobic repeats are also partially responsible for the extraordinary thermal and chemical resistance displayed by SNARE proteins. This effect is not unique to SNARE proteins, and can be observed in most coiled coils, Synthetic peptides based on the structure of tropomyosin show that greater hydrophobicity at positions *a* and *d* translated into increased thermal stability, and greater tolerance to high ionic strength and low pH (Lau *et al.* 1984). However, in coiled coils containing multiple periodic hydrophobic 4,3-heptad repeats, coiled coils may slide or stagger, causing one or more helix to shift in register by one or more heptad repeat, an inherent weakness of the periodic nature of  $\alpha$ -helices (Xi *et al.* 2012).

The SNARE core is not solely responsible for the specificity of vesicle fusion as outlined in the 'SNARE hypothesis'. Yang *et al.* analysed the complex-forming potential of five different proteins belonging to the VAMP family, with three members of the syntaxin family, and three members of the SNAP-25 family, and using an SDS-resistance assay. Of the fifteen possible different ternary combinations of mammalian SNAREs tested, twelve formed SDS-resistant complexes proving that

SNARE interactions are decidedly promiscuous (Yang *et al.* 1999). Consistent results were achieved in a similar study of binary interactions between full-length yeast SNAREs, rather than just the isolated core domains tested in the report by Yang *et al.* (Yang *et al.* 1999), showing that yeast SNAREs are also relatively nonspecific (Tsui and Banfield, 2000). SNARE localisation, and specific SNARE interactions with chaperones such as Sec1 and Munc18, have both been offered as possible factors governing the selectivity and specificity of SNARE-SNARE interactions *in vivo* (Brunger, 2006). These studies reveal that SNAREs of different species have the potential to interact with similar affinity and stability as those within a species. They demonstrate the highly conserved nature of the SNARE proteins, and highlights that key interactions such as salt bridges, polar and nonpolar contacts, are also highly conserved at varying degrees across different species.

There must be other mechanisms, aside from the chaperones, that are inherent to the SNARE proteins themselves, conferring the specificity that SNAREs have become known for. Briefly returning to the importance of the nonpolar core, and the heptad repeat that is responsible for its existence, we have established that positions *a* and *d* are most often occupied by nonpolar residues. However, buried polar residues have also been artificially placed in these positions in a number of leucine zippers to observe their effect on coiled coil assembly.

An example would be the coiled coil heterodimer named “Peptide Velcro”, which was designed in a manner analogous to the naturally occurring GCN4 leucine zipper. The GCN4 protein contains a basic region leucine zipper (bZIP), which is a continuous alpha-helix containing repeat leucine residues. Two of the helices form a parallel coiled coil homodimer with a ‘tweezer-like’ appearance that supports its function as a transcription factor by facilitating its binding to the major groove of the DNA binding site (Seroski and Hudalla, 2018).

“Peptide Velcro” comprises of almost identical peptides Acid-p1 and Base-p1 whose only difference is the presence of Glu (Acid-p1) or Lys (Base-p1) at every *e* and *g* position. All *a* and *d* positions feature hydrophobic leucines, with the exception of position 14 of both peptides, which contains a buried polar Asn residue as seen in GCN4 (O’Shea *et al.* 1993). When the Asn residues were mutated for Leu, the peptides preferentially formed a more stable heterotetramer, which appeared to lack any particular structure or helix orientation, showing that the Asn residues play a pivotal role in specifying helix orientation and generally guiding protein folding and assembly towards a unique structure (Lumb and Kim, 1995). Helix orientation was then manipulated by altering the positions of the Asn residues in a manner that ensured polar contact would only occur when the helices were oriented antiparallel to one another (Oakley and Kim, 1998). That study is of vital importance to our prediction of SNARE peptides, since it shows that helix orientation can be determined by a single

interaction, which can be extrapolated further by hypothesising that in fact the structural integrity of the complex could potentially be undermined by one or more of these buried interactions.

This was further expanded on through the investigation of the effect of buried polar residues on oligomeric specificity. Variants of GCN4-p1 were constructed with a single polar residue Asn, Gln, Ser or Thr, at *a* or *d* positions corresponding to the following: Ac-RMKQLEDKVEE-**L**/**X**-LSK-**V**/**X**-YHLENEVARLKKLVGER, where *a* and *d* positions have been outlined, and those that were subjected to mutation are indicated in boldface. It was found that only Asn in the 16a position, and Thr in the 12d position were able to guide assembly towards a unique oligomeric state, all other variants were unsuccessful in this capacity. Specifically, Asn16 is capable of making an asymmetric side chain-side chain hydrogen bond with a neighbouring asparagine in the adjacent chain. The experiments indicated that oligomeric specificity can only be controlled by a select few buried polar residues (Akey *et al.* 2001). Mutation of Asn16 to Lys and Gln in GCN4 produced two very different results, the Asn16Lys mutant formed dimers as expectedly, however the chemically similar Gln mutant unexpectedly formed a mixture of dimers and trimers (Gonzalez *et al.* 1996).

The former studies demonstrate that buried polar residues can be used to modulate specificity, and guide assembly towards a desired structure, but also show that this will occur at the expense of stability. The latter study showed that selectivity is not derived solely from the burial of polar residues, but in fact depends on a much more complex system of cooperating factors including side-chain stereochemistry complementarity, geometry of polar contacts and volume of space occupied by residues. Nevertheless, buried polar residues represent a powerful negative design principle that we may use to destabilise the complex and reduce its melting temperature, whilst still maintaining the specificity of its assembly and also its structural integrity.

When outlining the factors that control specificity or influence structure, residue volumes are often overlooked in favour of a discussion of the more obvious interactions such as salt bridges, hydrogen-bonding and hydrophobic interactions. The first description of leucine zippers found in DNA-binding proteins postulated that the leucines at every seventh position (position *d*) of one chain interdigitated with those in the adjacent chain resulting in a flat “zipper”-like structure (Landschulz *et al.* 1988). This was proven wrong by crystal structures of the leucine zipper GCN4, which showed that in fact the side-chains of hydrophobic residues at every third and fourth position packed side-to-side (O’Shea *et al.* 1991). The purpose of including this study here is to show that while residue volumes are somewhat neglected now that focus has shifted towards hydrophobic and ionic interactions, the very first discussions about coiled coils began by considering the side-chain packing. We expect to observe knobs-into-holes style complementarity when analysing the residue volumes of the SNARE motifs, and we hypothesise that regions exhibiting this complementary side-

chain packing are at least partially responsible for maintaining correct pairing between heptad repeats, and specificity of SNARE assembly. Analysis of residue volumes should also give us an insight into the hierarchy of assembly by revealing which chains would preferentially bind according to their residue volumes.

Salt bridges are a crucial type of interaction that contributes to the specificity and stability of coiled coil assembly. Analysis of charged residues, and their relative positions within the sequences, may be helpful in predicting potential salt bridges within the SNARE complexes. One of our hypotheses is that we expect there to be a pattern of charges, especially at the N-termini of each protein, which has been postulated as the region where the initial interaction of all the chains originates. These charges are expected to act as the impetus that loosely holds the chains in close enough proximity to engage the hydrophobic interactions to form and effectively “zipper” the coils into a coiled coil. Though it is a good starting point, analysis of charged residues alone is a simplistic model for prediction, and could be construed as “superficial” since it doesn’t take into account environmental factors such as the pH of solvent, and ignores the impact that surrounding (assumed to be uncharged) residues may have. To allay these concerns, a more representative property to analyse would be theoretical isoelectric point (pI) of residues. Since salt bridges conventionally form between the polar regions *bc* and *efg*, it would be more applicable to analyse the cumulative theoretical pI of these regions. This would enable us to gain an understanding of which areas along the chains have complementary charges that would facilitate their binding, and thus help us to elucidate the hierarchy of assembly.

## 1.4 Drug delivery systems

Drug delivery systems are formulations or devices that facilitate the delivery of a therapeutic agent (drug) to its site of action in a way that is selective (i.e. little to no interaction with non-target sites) reducing any potential side-effects, enhancing bioavailability to the therapy, and sometimes, allowing for the ability to modulate drug release (Li *et al.* 2019). There are multiple strategies for drug delivery including: stimuli-responsive for controlled release, ligand-mediated (using a ligand to provide the targeting characteristic e.g. antibody-drug conjugates), co-delivery and theranostics (combination therapies, or systems that combine therapy and diagnostic elements), biomimetic delivery (nanosystems that mimic biological systems) among many others (Li *et al.* 2019).

The strategy of most interest and therefore relevance to this study is the stimuli responsive system. This study’s aim is to design and engineer a range of SNARE-like peptide capable of controlled stimuli-sensitive self-assembly and disassembly for the application in a payload delivery device. We

envisage that the peptides will act as a thermally (or potentially pH-sensitive) linker between a payload (drug) and its vehicle (e.g. nanoparticle) (**Figure 1.13a**). We have suggested a very high-level idea of how the delivery mechanism could potentially work in our aim (**section 2.1**). Essentially, we would expect the construct to accumulate in target tissues through the enhanced permeation retention effect, and then the tissue region of interest could be locally heated through electromagnetic induction or near infrared radiation in order to induce metal nanoparticle hyperthermia and initiate complex disassembly, delivering the payload (drug) in a controlled manner (**Figure 1.13a**).

A number of drug delivery system examples discussed in the following sections employ the stimuli-responsive strategy and have been included due to their relevance to this study. Our take on the drug delivery system is entirely unique as none of the literature currently defines a drug-delivery system that incorporates the SNARE tetramer (**section 1.4.2** talks about SNAREs in drug delivery however all examples are dimers based on SNARE sequences).

#### **1.4.1 Coiled coils in drug delivery**

Owing to their remarkable stability and more importantly, their specificity, the potential application of coiled coils in drug delivery has been of increasing interest in the field of nanotechnology. Recognition of said potential has been documented as far back as the mid-nineties. A two-stage targeting and delivery system couriered by chains exhibiting the coiled coil motif (**Figure 1.13b**) has been proposed in (Hodges, 1996). One chain of the reported heterodimeric coiled coil is ligated to a therapeutic drug, and another coil is conjugated to a structure with recognition properties, such as a monoclonal antibody (Hodges, 1996). The latter is administered first to seek the target, and the former is delivered some time later, by virtue of the coiled coil specificity qualities, the two chains dimerise, delivering the drug to the target in a controlled and site-specific manner. One of the key advantages of using coiled coils in drug delivery is that their formation can be easily controlled and modified by changing their composition, and as a result, users can increase or decrease the local drug dosage. In another study, coiled coil mediated drug delivery was used for the treatment of human B-cell lymphoma, to achieve apoptosis in Raji B cells. Using a two-step delivery process, Fab' antibodies were conjugated to one of the peptides of a heterodimeric coiled coil, administered first in order to target CD20 antigens on the B cell surface. The second peptide of the coiled coil was grafted onto a HPMA (N(2-hydroxypropyl)methacrylamide copolymer. Upon interaction, the peptides dimerised, crosslinking the CD20 antigen and inducing apoptosis (Wu, Yang, and Liu 2012).

Heterodimeric pH-sensitive coiled coil peptide sequences based on E3 and K3, has opened up a wealth of possibilities for biomedical applications, due to its unfolding transition, which occurs in the physiological pH range (Apostolovic and Klok, 2008). Oppositely charged residues Glu and Lys incorporated at positions e and g of E3 and K3 respectively, were able to influence the stability and unfolding transition of the resulting coiled coil in a pH-dependent manner. This ionic arrangement is stable at pH 7, however when the pH drops to 5, analysis of sedimentation equilibrium data revealed that E3 appears to form mostly homotrimers, whilst the majority of K3 exist as single peptides, and only a minority population remains of the E3/K3 heterodimers (Apostolovic and Klok, 2008). In a subsequent study, the same group produced K3-containing N-(2-hydroxypropyl)methacrylamide (HPMA) copolymers, which is essentially a polymer backbone functionalised with K3 peptides, and conjugated the cargo, which was the anticancer drug methotrexate (MTX), to E3. This polymer-drug conjugate enters the cell via endocytosis, and is introduced to a new environment complete with a different set of potential stimuli, which can be manipulated to induce release of the cargo. Cytotoxicity experiments carried out on E3-MTX and a range of analogues, compared to non-covalent K3 functionalised copolymers, showed that the copolymers themselves do not appear to be cytotoxic. However, E3-MTX and its analogues all demonstrated concentration-dependent cytotoxicity. Further cytotoxicity studies were conducted on both the E3-MTX polymer conjugate and a modified version, E3-GFLG-MTX, containing a GFLG tetrapeptide spacer, which is liable to cleavage by cathepsin B, a lysosomal enzyme, in the presence and absence of a cathepsin B inhibitor leupeptin. In the presence of leupeptin, both were observed to have similar  $IC_{50}$  values, whilst in its absence, the significance of the GFLG linker became apparent as the  $IC_{50}$  values for E3-GFLG-MTX was lower than E3-MTX. These results indicate that the inclusion of these enzymatically labile linkers of this nature might act to facilitate drug release. It also lends an insight into the intracellular trafficking route, indicating that a proportion of the polymer-drug conjugates must have been transported to the lysosomes (pH~4) (Apostolovic *et al.* 2011).

Such polymer-protein conjugate chemistries involving coiled coils are becoming increasingly attractive for drug delivery systems due to the well-established rules governing coiled coil structure and how they may affect function. This fundamental groundwork allows users inspired by natural proteins, to identify a desirable function or attribute that is linked to a specific motif or domain, and incorporate it into the engineering of de novo peptides for specific applications. The polymer comes with its own advantages; it is most often hydrophilic and so enhances the pharmacokinetics of the conjugate by increasing its solubility. This typically increases blood half-life and bioavailability, improves the stability, reduces the rate of proteolytic degradation, and undesirable immunogenicity, and finally promotes the accumulation of the conjugate within target tissues, such as tumours, through the enhanced permeation and retention (EPR) effect (Chen, Constantinou, and Deonarain

2011, Pechar and Pola 2013). Additionally, the polymers are most often attached to the peptides via noncovalent interactions using non-destructive chemistries. The most exciting achievements demonstrated in the literature above, and in general, are the stimuli-sensitive coiled coils, which are capable of folding and unfolding under differing physiological conditions (Apostolovic and Klok 2008, Hodges 1996, Chao *et al.* 1998). Such coiled coil structures can be custom-made to undergo either transition in a site-specific manner for example, in the acidic, hypoxic environment of a tumour, or where an externally applied laser pulse has elevated the temperature of a tissue. Finally, the inclusion of enzyme-labile linkers and spacers can be used as a means of degrading the delivery vehicle after it has served its function (Yang and Kopecek 2015).

#### 1.4.2 SNAREs in drug delivery

SNAREs have been the focus of a number of synthetic peptide drug delivery vehicles, intended to mimic their fusogenic function. In one such study Zheng *et al.* attempted to mimic the fusion events triggered by the formation of the SNARE complex, using a model system they designed based on the coiled-coil forming peptides K3 ([KIAALKE]<sub>3</sub>), and E3 ([EIAALEK]<sub>3</sub>). These two peptides form a well-characterised parallel heterodimeric coiled coil structure, however when the amino acid sequence of E3 was reversed, exposure to an equimolar quantity of K3 resulted in an antiparallel tetramer coiled coil instead. Although this new coiled coil structure does not permit it to behave in a 'zipper-like' manner, cholesterol-modified K3 and reversed E3 were observed to induce liposome fusion (Zheng *et al.* 2016). Members of the same laboratory were also able to use the same fusion model, employing lipidated coiled coil peptides to induce liposome-liposome fusion, in order to deliver the cytotoxic anticancer drug doxorubicin. If the same heptad peptides, K3 and E3, are arranged into structures containing four identical repeats, the stability of the complex can be increased. Targeting of such stabilised peptides to phospholipid liposome membranes was achieved by attaching a cholesterol moiety connected by a polyethylene glycol (PEG) spacer. Such engineered lipoproteins (CPK<sub>4</sub> and CPE<sub>4</sub>) demonstrated competent coiled coil formation when incorporated into liposome membranes, according to circular dichroism spectroscopic data. Their fusogenicity was confirmed by a lipid-mixing in a fluorescence resonance energy transfer (FRET)-pair based liposome-liposome assay (Yang *et al.* 2016). The effective dosage of doxorubicin is up to 9 µM delivered intravenously into the blood serum of the patient. Using the liposome drug delivery system described above, Yang *et al.* were able to detect HeLa cell viability diminish at concentrations as low as 0.1 nM (IC<sub>50</sub> ~0.01 µM), where free doxorubicin would require concentrations up to 0.1 µM (IC<sub>50</sub> ~5 µM) to have similar efficacy. (Yang *et al.* 2016)

In another study inspired by SNARE proteins, Langosch *et al.* designed synthetic peptides analogous to the transmembrane segments (TMS) of VAMP-2 and syntaxin-1a, which are known to contain dimerisation motifs, and used them to evaluate their efficacy in liposome-liposome fusion. The dimerisation motifs were a group of conserved residues, 6 in the case of VAMP-2 corresponding to the sequence **ILGVICAILLIIVYST** from position 99 to 117, and 5 in the case of syntaxin-1a corresponding to the sequence **IMIIICCVILGIIASTI** from position 267 to 285 (Laage *et al.* 2000). Three positively charged residues flanked the peptides at each terminus. This improved solubility and allowed the peptides to integrate into the liposomal membranes in the correct orientation. TMS-peptides amplify liposome-liposome fusion (Yang *et al.* 2016), however, lacking a cytoplasmic coiled coil domain as in SNAREs, the fusion observed as a result of these peptides most likely proceeds via random collisions rather than the guided juxtaposition of membranes and subsequent reduction in the energy barrier (Langosch *et al.* 2001).

## 1.5 Nanoparticle-Protein Conjugation

This broader scope of this project is envisioned to include conjugation of the SNARE-based coiled-coil forming peptides to nanoparticles, where the resulting complex can act as a therapeutic delivery device in a clinical setting. Nanoparticles are of particular interest as they are able to enter cells through endocytosis, and it has been shown that this movement is not impeded even when the nanoparticles are linked to payloads such as antibodies (Daraee *et al.* 2016).

Thus, the type of nanoparticle to be used, the strategy for nanoparticle-protein conjugation, as well as for assembly and disassembly of the coiled coil once conjugated to the nanoparticle, and finally the limitations of any proposed approach must all be considered. The intended coiled-coil disassembly mechanism involves local hyperthermia, wherein metal nanoparticles act in the capacity of receivers of heat energy when exposed to energy of a specific frequency of electromagnetic radiation. The chief motive for a temperature increase is to induce coiled coil disassembly, however there is the additional advantage of induced apoptosis within the temperature range 41-47 °C in the majority of tissues, effectively expediting a two-pronged attack on diseases like cancer. A further consideration to take into account is just how narrow the desired temperature range is, as temperatures of 50 °C and above are more likely to cause necrosis rather than apoptosis as lipid bilayers are disrupted and proteins denature.

Gold and ferromagnetic iron(III)-oxide are the two materials that are of most interest to this project primarily due to their ability to act as antennas (Chatterjee *et al.* 2011), however also because they are well-characterised materials, and show relatively low toxicity.



### 1.5.1 Gold Nanoparticles (GNPs)

Gold is a particularly attractive material for metal nanoparticles in clinical practice due to their inertness, their compatibility with aqueous solvents (easy phase transfer from organic solvents), and the assumption that they have low long-term toxicity as the majority of studies show nontoxicity after acute exposures for nanoparticles above 4-5 nm (Falagan-Lotsch *et al.* 2016). Furthermore, protein-nanoparticle conjugation is relatively straightforward with GNPs, where surface functionalization with sulphur-containing groups (thiol ligands) is the most frequently explored route (Xiang and Morais, 2014). To this end, thiols (i.e. cysteines) can be incorporated into one end of the coiled coil.

There are a number of examples of successful application of GNP-drug conjugates in cancer therapy. Note that although most of the examples reported here involve cancer therapy, this project does not specifically have any particular therapy application in mind. It is simply reflective of the amount of literature available on that involves nanoparticles in cancer therapies. One instance combined 13 nm GNPs with methotrexate, an anti-cancer agent that restricts growth and reproduction of cancer cells. The GNPs were employed with the aim of increasing retention of methotrexate in the cells, thereby improving its efficacy. Conjugation occurred via the carboxylic acid groups on methotrexate directly to the GNP surface (Chen *et al.* 2007). The study found that accumulation of methotrexate was faster, and greater in concentration, in tumour cells treated with the conjugate than in cells treated with free methotrexate. Moreover, the conjugate showed a stronger cytotoxic effect on tumour cell lines than an equal dose of free methotrexate (Chen *et al.* 2007).

Doxorubicin, another anticancer agent that restricts growth of cancer cells, has also been conjugated to 30 nm GNPs, this time via a pH-sensitive (acid-labile) linker. The conjugate resulted in improved drug accumulation and retention in cancer cells when compared with free doxorubicin. The acidic environment within organelles triggered intracellular release of doxorubicin (Wang *et al.* 2011).

A description of surface plasmons is necessary for the discussion of GNPs' suitability to hyperthermia-driven disassembly approaches and will preface this section. At the simplest level, a plasmon can be defined as a quantum of plasma oscillation (plasma being a state of matter resembling ionised gas). Surface plasmons (SPs) are classified as collective delocalised electron oscillations, existing at the surface of a metal, that have been displaced from their equilibrium

position around the positively charged lattice (Amendola *et al.* 2017). Surface plasmon resonance (SPR) can be achieved by exciting the SPs at a resonant frequency that matches their momentum. At this wavelength, incident light is absorbed and scattered by the SPs, whilst resonant energy is converted to heat (**Figure 1.14a**). This conversion is highly efficient due to the fact that there is low luminescence yield (i.e. the number of photons emitted is less than that absorbed) for plasmon absorption in the visible and near-IR regions. GNPs are highly photostable so will not degrade before conversion can take place, and the rapid heating and cooling dynamics which result in fast relaxation rates of SPR (Qiu and Wei, 2014). **Figure 1.14b** shows the typical sequence of events leading up to hyperthermia, which occur as follows: a laser or pulse fired towards the GNPs is absorbed, exciting the free electrons within the SPs, the resulting heated pulse of electrons cools quickly via electron-phonon interactions caused by collisions with the gold lattice. Phonons are a wave of vibration in a rigid lattice on a quantum level – essentially then, a quantised particle of heat - and therefore any energy exchange between electrons and a lattice is actually due to radiation or adsorption of phonons i.e. “electron-phonon interactions” (Mahan and Plummer, 2000). The heat is subsequently transferred throughout the lattice to the surroundings via phonon-phonon interactions, and is dissipated to the surroundings in the process (Abadeer and Murphy, 2016).

Owing to their surface plasmon resonance, GNPs are often used in photodynamic therapy, where light is used to induce heating either to release a payload or to trigger cellular apoptosis/necrosis at specific sites. In one such study, a photosensitizer (zinc-phtalocyanine) was conjugated to GNPs in combination with an Anti-HER2 monoclonal antibody. The construct was observed to selectively target cancer cells overexpressing the HER2 growth factor cell surface receptor, and when irradiated with visible red light, it produces cytotoxic singlet oxygen (i.e. the active species in photodynamic therapy) triggering apoptosis in breast cancer cells (Stuchinskaya *et al.* 2011).

Although not “traditional” spherical nanoparticles per se, DNA-coated gold nanorods have been used to co-deliver doxorubicin to metastatic breast cancer cells. This is an example of a combination therapy, combining chemotherapy and photothermal ablation. When the nanorods were irradiated with near infrared light, there was a significant temperature increase resulting in the release of doxorubicin. There was also higher cytotoxicity observed when laser irradiation was employed with the doxorubicin-loaded nanorods than with free doxorubicin in breast cancer cells (Wang *et al.* 2014).

### **1.5.2 Magnetic Iron(III) Oxide Nanoparticles (MNPs)**

MNPs are increasingly gaining popularity, including as central components to drug delivery or biosensor devices due to their biocompatibility, robustness, stability in aqueous solutions and ability to induce localised hyperthermia. There are a number of different types of materials for MNPs ranging from the common magnetite iron(III) oxide ( $\text{Fe}_3\text{O}_4$ ) and oxidised form maghemite ( $\gamma\text{-Fe}_3\text{O}_4$ ), to the highly magnetic nickel and cobalt, which are more obscure in biomedical applications owing to their toxicity. MNPs are further categorised based on their relative size, core and if present, the type of coating used.

The following is a brief introduction into how magnetisation at a sub-micron scale works. Magnetisation behaviour is dependent on the number of magnetic domains within a particle, which is dependent on the particle size. Particles with diameters below the critical threshold are categorised as “single-domain”, which means that their magnetic moments align in equal magnitude with an applied magnetic field. Below the superparamagnetism threshold, MNPs exhibit superparamagnetism, which means they retain no net magnetisation in the absence of an applied magnetic field (**Figure 1.14d**).

There are four principle mechanisms for heat-generation in magnetic materials that are subjected to a high-frequency (kHz-MHz) magnetic field; these are eddy currents, hysteresis losses, Brownian, and Néel relaxation. Eddy currents create an opposing magnetic field to the original field, can cause resistive heating in mainly bulk materials, whilst hysteresis, observed in multidomain materials, is where the boundaries between each domain (“domain walls”) shift as the magnetic field changes resulting in a change in the size or number of domains. Whilst dominant in bulk materials, the influence of these mechanisms becomes inconsequential as we approach sub-micron sized particles. The remaining two mechanisms, Brownian and Néel relaxation, which reference the type of rotational mode employed (seen in **Figure 1.14c**), increase in importance as particle size decreases below critical diameter ( $D_c$ ). Néel rotation refers to the rotation of the magnetic moment, in alignment with the orientation of the applied magnetic field, while the particle orientation remains fixed. Thus, Néel relaxation results in the dissipation of thermal energy via reorganization of dipole moments within the material. Conversely, in Brownian relaxation the particle orientation, alongside its magnetic moment, also rotates in parallel with the applied magnetic field, generating heat due to the friction caused by the particle oscillations. The two mechanisms occur concurrently, however unlike Néel relaxation, Brownian relaxation only happens in liquids. Large particles in low viscosity liquids are more influenced by Brownian relaxation, and the converse is true for Néel relaxation (Akbarzadeh *et al.* 2012).

In human imaging, Specific Absorption Rate (SAR) measures the rate of energy absorption by the human body when subjected to a radio frequency electromagnetic field, it can therefore be defined

as the power absorbed per mass of tissue (units are W/kg) (Subramanian and Krishna, 2014). Similarly, the power absorbed by a magnetic nanoparticle per unit mass defines SAR for nanoparticles (Deatsch and Evans, 2014). This is a good indication about the frequency limits required to induce MNP-driven hyperthermia. The theoretical SAR of single-domain magnetite nanoparticles was measured by Deatsch *et al.* according to the Rosensweig model of Brownian and Néel relaxation, in aqueous solution at physiological temperature and field strength of  $25 \text{ kJ/m}^3$ , as a function of particle diameter (limited to a range of 8-20 nm) and the frequency of the applied field (25-300 kHz). Their findings show that larger particles have a maximised SAR (i.e. relaxation time of particle is equivalent to the field frequency which is the “critical frequency”) at lower frequencies. Particles smaller than 14 nm do not reach a maximum SAR at any of the frequencies between 25-300 kHz, falling below the critical frequency of the system, and above 14 nm the SAR becomes independent of frequency (Deatsch and Evans, 2014). In another study of the influence of MNP size and shape on power absorption, an expanded the range of particle diameters were analysed. They showed that at a fixed frequency of 260 kHz the specific power absorption (SPA - similar to SAR and measured in the same units) was maximised at a diameter of 24 nm (137.4 W/g). At the limits 5 nm and 110 nm, however, they showed extremely low SPA values (3.17 and 1 W/g respectively) indicating poor heating efficiency (Gonzalez-Fernandez *et al.* 2009). It is therefore clear that if we wish to maximise heating efficiency, the size limits of MNPs in our study should not exceed 100 nm, and should not go below ~8-10 nm.

### **1.5.3 Strategies for protein conjugation/immobilisation**

There are numerous different protein-nanoparticle immobilisation and conjugation strategies available for use. In order to preserve the coiled coil structure and function, they must be bound to the surface of the nanoparticle using either adsorption or covalent binding techniques as opposed to techniques like entrapment or cross-linking which restrict movement and would likely have a negative effect on coiled coil assembly. The strategies that are most relevant to this project will of course depend on the mutual surface chemistries of the chosen nanoparticle material and the protein itself, and whether coatings or surface modification/functionalization is deemed necessary.

Physical immobilisation makes use of intermolecular forces such as ionic salt bridges and hydrophobic interactions to adsorb the proteins onto the nanoparticle surface. As a passive method it has the advantage of being the easiest, most accessible strategy that requires little or no manipulation, however the disadvantage is that it is nonspecific and so its difficult to control where and how the protein binds. Chemical, or covalent immobilisation is where the surface chemistry of the nanoparticle has been manipulated, usually by coating it in a material that has reactive

functional groups. Iron(III) oxide NPs in an aqueous environment have hydroxyl groups on their surfaces, which alone have the potential to weakly interact with amino or carboxyl groups on the protein (Cornell and Schwertmann, 2006). It is preferable, however, to “activate” these hydroxyl groups using silanisation. Here, silane agents with variable R-groups react with the hydroxyl groups on the MNPs via their methoxy group forming strong and stable Si-O bonds. Subsequently, the reactive functional groups in the variable R-group will form strong covalent bonds with the protein, effectively immobilising it to the MNP (Wu, He, and Jiang 2008). The silane coating not only maintains most of the physical characteristics of uncoated MNPs, but also has the additional advantage of high saturation magnetisation, and improved dispersity (Wahajuddin and Arora, 2012). Saturation magnetisation is the point at which an external magnetic field cannot increase magnetisation of the sample any more, and a higher saturation limit is more desirable as it is an indicator of enhanced magnetism.

#### **1.5.4 Obstacles and limitations of protein conjugation**

One of the difficulties anticipated for protein conjugation will be controlling which parts of the protein come into contact with the NP. There is a potential loss of protein structure and function if it adsorbs to the NP indiscriminately and resultantly becomes disordered. The most realistic prospect for protein-nanoparticle interaction is the formation of a corona across the surface area of the nanoparticle. Depending on the strength of interaction and reversibility, and therefore the exchange rate, of binding this corona can be described as hard (irreversible binding or slow exchange rates) or soft (fast exchange rates). Furthermore, agglomeration of protein-NPs can also reduce protein function by inducing conformational changes. Thus, an additional obstacle is maintaining tight control over the colloidal stability of solutions containing protein-NPs in order to prevent situations wherein agglomeration, aggregation, or gravitational precipitation become favourable events. The latter can be avoided by using smaller sized nanoparticles. Agglomeration, and to a lesser extent aggregation, can be prevented using a roster of different methods such as ultrasonic energy (to be used with caution as it could potentially disrupt protein structure in the process), surfactants, polymer coatings and dispersion media.

Coating with biocompatible polymers such as dextran or polyethylene glycol (PEGylation) is a very common practice, not only does it reduce agglomeration, it improves general dispersity and blood circulation time ensuring that the protein-NP conjugates have ample time to accumulate in target tissues through the EPR effect (Yallapu *et al.* 2011). An appropriate case study for looking at the positives of coatings on modulating NP properties is the following by Yallapu *et al.* Here, Iron(III) oxide core NPs coated in a formulation consisting of  $\beta$ -cyclodextrin and pluronic polymer were

loaded with curcumin (a model anticancer drug). The majority of the curcumin was loosely held in the cyclodextrin layer by hydrophobic interactions, and exhibited a bi-phasic release profile. This led to an initial burst-like release of surface bound curcumin, followed by sustained release of curcumin encapsulated deeper in the polymer matrix. Hyperthermia was achieved by subjecting the NPs to an alternating 300 kHz magnetic field. The  $\beta$ -cyclodextrin and pluronic polymer formulation coating showed a superior hyperthermia performance compared to a simple cyclodextrin coating, or no coating at all, with excellent heating effects reaching temperatures of  $\sim 65$  °C within 15 minutes of exposure (ca.  $\sim 60$  °C for the cyclodextrin coating and 50 °C with no coating) (Yallapu *et al.* 2011). A disadvantage of coating is that it is likely to have an impact on heat propagation out of the particles, and so adversely affect hyperthermia, reducing its efficiency and driving down the SAR. This was experimentally observed in a study of the influence of MNP size and shape on power absorption, where silica-coated  $\text{Fe}_3\text{O}_4$  NPs were found to have lower specific power absorption (SPA) values compared to naked  $\text{Fe}_3\text{O}_4$  NPs. The thickness of the  $\text{SiO}_2$  shell was found to have a strong influence on the SPA mechanism by hindering the heat outflow (Gonzalez-Fernandez *et al.* 2009). It would be favourable to avoid coating by exploring other conjugation strategies however, in the event that coating becomes necessary for surface functionalization it is evident that a compromise must be struck between that and maximising heating efficiency.

## 1.6 Characterisation techniques

### 1.6.1 Circular dichroism (CD) spectroscopy

Circular dichroism spectroscopy is a highly sensitive technique that measures the circular dichroism of chiral molecules over a range of wavelengths. Briefly, circular dichroism shows the differential absorption of left- and right-handed circularly polarised light. A light beam is passed through a polariser causing its electric field to oscillate sinusoidally in a single plane. Plane polarised light is equivalent to a vector sum of two circularly polarised beams, of which one rotates clockwise (right-handed) and another anticlockwise (left-handed), when viewed down the axis of propagation. Different protein secondary structures (ordered helices, sheets, turns, random coils) interact with the polarised light differently, producing signature spectra that act as the basis for secondary structure analysis (Greenfield, 2007). In this way, it can be used to qualitatively, and quantitatively study protein secondary structure and conformational behaviour as a function of temperature, solvent composition, pH, and ligand binding interactions among other variables. A detailed diagram of a CD spectrometer can be seen in **Figure 1.15**.

### 1.6.2 Pull-down Assay in conjunction with Polyacrylamide Gel Electrophoresis (PAGE)

A pull-down assay is a convenient method of measuring protein-protein interactions, and therefore has been described as a variant of affinity-based purification. A protein is immobilised on a solid support, and this construct acts as "bait" to which other proteins of interest, or "prey", may bind depending on their mutual affinity. Glutathione-S-transferase (GST) protein tags are used for purification of recombinant fusion proteins and for pull-down analyses. Both applications take advantage of the strong affinity of GST to glutathione, which is usually immobilised on solid support, for example agarose beads. GST protein tag is recombinantly fused with the protein of interest (hence "GST-fusion protein"). It improves recombinant protein solubility and folding, and normally does not affect protein function. GST fusion protein pull-down assays have been a popular technique used to elucidate the role of SNARE proteins in membrane fusion, and specifically to determine the existence of protein-protein interactions between SNARE proteins and other accessory proteins involved in membrane fusion such as Munc18 (Rehman *et al.* 2014), and Snapin (Mistry *et al.* 2007).

Pull-down assays were used as preliminary experiments to identify optimum conditions for the CD measurements. They have been used in this study to characterise the thermostability, and pH-sensitivity, of a number of mutated SNARE complexes of interest. In this way, we were able to generate a preliminary set of results to decide which complexes would be suitable for more precise methods available to us, for e.g. synchrotron radiation circular dichroism. It was also used to narrow down the temperature and pH ranges to be tested. A flow-chart schematic of the method used in this study can be seen in **Figure 1.16**. Cell lysate containing GST-SNAP25 fusion protein is immobilised on glutathione-agarose beads, which act as the "solid support". This is mixed with an excess of mutated syntaxin and VAMP synthetic peptides, and incubated overnight at 4°C to allow complex assembly to occur. The complex-on-beads is washed and split into tubes ready for incubation at different temperatures or pH. Following treatment, the supernatant is collected, a denaturing SDS-loading buffer is added, and the sample is dehydrated to prepare it for SDS-PAGE. The supernatant will contain the proportion of peptide that was freed during complex disassembly as a result of treatment.

The pellet is washed, and the same denaturing SDS-loading buffer is added to the pellet. The SDS-loading buffer breaks the interactions holding any remaining complexes together, and severs the bonds between the solid support and GST-SNAP-25. This frees the peptide that remained bound to the solid support because of high complex stability during treatment. SDS-PAGE using commercial 4-20% SDS-gradient gels is conducted for both the "beads" and "supernatant" products of the pull-down assay. Densitometry analysis is conducted on a set of peptide bands from either syntaxin or

VAMP depending on which is most visible. The peptide band density is plotted as a function of a temperature, and the melting temperature ( $T_m$ ) is calculated by finding the mid-point of the highest and lowest peptide band densities. Appropriate controls for this type of SDS-PAGE experiment includes GST-SNAP25 fusion protein immobilised on the beads, and the individual SNARE components i.e. syntaxin and VAMP synthetic peptides, and to a lesser extent it might include GST alone, GST on beads and beads alone. We have used this approach to test for pH and thermal sensitivity of our synthetic SNARE complexes (see **section 8.1**), with the controls employed being GST-SNAP25 and the individual synthetic peptides.

There are two “products” obtained from a pull-down – the solid beads product and the supernatant product (**Figure 1.16**). In terms of the thermostability of the complexes, different trends are expected for each pull-down product. Both products should show a sigmoidal pattern, however the beads product should show the greatest peptide band density at lower temperatures where more complex (and therefore peptide) should have remained bound to the solid support, and the lowest peptide band density at higher temperatures where the complex is likely to have denatured and less peptide is bound to the solid support. The converse is expected for the supernatant product, which contains the peptide released from the solid support. Therefore, at lower temperatures there should be less peptide as the complex is more stable, and as temperature increases, the complex unfolds releasing more peptide into the supernatant, which corresponds to a rise in peptide band density at higher temperatures.

### **1.6.3 FRET-HRM (Förster Resonance Energy Transfer - High Resolution Melt)**

FRET (Förster Resonance Energy Transfer) is also a technique frequently used for detecting protein-protein interaction. It describes a mechanism by which energy is transferred between two different fluorophores, a donor, and an acceptor, which could be two different fluorescent labels for the protein pair of interest. The donor and acceptor are chosen such that the donor’s emission wavelength, and the acceptor’s excitation wavelength overlap. The donor is excited by light of a wavelength corresponding to its energy gap, and as the two labelled proteins come into close (binding) proximity, rather than emit fluorescence, the donor instead transfers energy to the acceptor through non-radiative dipole-dipole coupling. This excites the acceptor, which may emit fluorescence, or in the case of a quencher, simply absorbs the energy and does not emit. This is illustrated in the Jablonski diagram in **Figure 1.17a**, which outlines the electronic transitions occurring between the donor and acceptor (which, in line with our proposed methodology, is shown as a quencher). The efficiency of FRET is wholly dependent on the distance between donor and acceptor, given as  $R$ , and since the mechanism is based on dipole-dipole coupling, it follows that



efficiency will reduce at a rate of  $1/R^6$ . FRET is most commonly coupled with confocal microscopy to image fluorescence from protein-protein interactions both *in vitro* and *in vivo*, as shown in this *Methods* study, which outlines how FRET can be used to determine how colocalised proteins interact (Kenworthy, 2001).

High Resolution Melting is used widely in real-time PCR applications to measure  $T_m$  of the amplified double-stranded DNA (Wittwer, 2009). HRM detects  $T_m$ , which depends on the sequence amplified. Whilst the detection is based on measuring fluorescence, the fluorescence nature and methods may vary. A common approach is to use double-stranded DNA-specific fluorescent dye, such as SYBRGreen. Alternatively, a range of FRET-based approaches can be used, such as TaqMan “reporter” and “quencher” dye combination. The former approach is clearly unsuitable for studying proteins, but FRET based approaches would be. However, the attachment of dyes will obviously be different for the TaqMan strategy.

Whilst a few reports have shown that FRET can be coupled with high-resolution melt (HRM) analysis performed using real-time PCR instruments for the detection of specific analytes, such as the detection and differentiation of *Plasmodium* species (Safeukui *et al.* 2008), there is currently no published data wherein HRM has been coupled with FRET technology for the purposes of characterising protein-protein interactions. HRM is a technique that has been ostensibly designed for the analysis of DNA melting following qPCR amplification. We have used a qPCR instrument, and PCR equipment to carry out HRM

We propose that the protein-protein interactions that occur as a consequence of SNARE complex assembly can be effectively characterised by FRET-HRM. The strategy for this method is illustrated in **Figure 1.17**. Essentially, the two SNARE proteins, VAMP and syntaxin, which are the subject of truncation and mutation, will be conjugated to the FRET donor fluorescein ( $\lambda_{em}$  512), and FRET acceptor DABCYL ( $\lambda_{abs}$  range 346-489). As an aside, it is noted that the match between the emission (fluorescein) and absorbance (DABCYL) is not ideal. For FRET to occur the absorption spectrum of the quencher and the emission, fluorescence spectrum of the donor should overlap. The relative efficiency of FRET will depend on the size of the spectral overlap integral, and the concentration of both the donor and the acceptor. Complex assembly is allowed to proceed between the labelled proteins and SNAP-25, following which the complex is subjected to HRM. Initially, at low temperatures whilst the complex remains stable, there should be low fluorescence as the distance between fluorescein and the quencher DABCYL results in highly efficient FRET. As temperature increases, the complex should begin to unfold, and fluorescence should increase proportionally, indicating FRET becoming inefficient due to the increasing distance between fluorescein and the quencher DABCYL. The melting temperature, defined as the point at which 50%

of the protein is unfolded, can be used as a measure of the stability of the complex. Native polyacrylamide gel electrophoresis (PAGE) can be used as an independent method to confirm complex assembly and disassembly.

## 1.7 Background on the PDB structures 1N7S, 1L4A and 3B5N

Protein Data Bank (“PDB” – accessible from rcsb.org) is an online archive of 3D structures of biological molecules including proteins. Having access to a protein’s 3D structure can be particularly helpful in analysing sequence, conformation, and spacefill. We have chosen to focus on three such PDB structures, referred to as 1N7S, 1L4A, and 3B5N. These were chosen on the basis of their differing thermostability. They were subsequently analysed to uncover patterns in the hydrophobicity, residue volume, and theoretical pI that would reveal how their thermostability is governed by their physicochemical properties. **Figure 1.18** shows their 3D structure, as well as the 3D structure of the heptad slices that make up their SNARE motifs.

1N7S is a C-terminally truncated neuronal rat (*Rattus norvegicus*) SNARE complex, consisting of the t-SNAREs syntaxin and SNAP-25 N- and C-terminal domains, and the R-SNARE VAMP (Ernst and Brunger, 2003). It has been truncated from Trp89 of the C-terminal of VAMP, and similar truncations at the same relative position on the other chains were carried out. Consequently, approximately one  $\alpha$ -helical turn was removed from syntaxin and VAMP C-termini. The melting temperature of the resulting ‘micro-SNARE’ complex was determined to be 89 °C, which is 5 °C less than minimal, and N-terminally truncated SNARE complexes whose melting temperature is 94 °C under native conditions (Ernst and Brunger, 2003). In SDS-denaturing conditions they observed a ~20-23 °C reduction in stability, with a drop in melting temperature to 37 °C compared to minimal and N-terminally truncated SNAREs who remained stable until 60 °C (Ernst and Brunger, 2003). This complex will be referred to as the ‘standard’ to which the other two complexes will be compared.

1L4A is originally a squid (*Loligo pealei*) neuronal-complexin-SNARE complex (Bracher *et al.* 2002). The SNARE complex comprises of the squid neuronal proteins syntaxin, SNAP-25 N- and C-terminal domains, and VAMP. The PDB happens to contain a complexin, whose structure is known. It binds to SNAREs but it has no known effect on the thermostability of the SNARE complex, and therefore its presence should not affect the validity of any subsequent analysis conducted on the complex. Between hydrophobic layers -6 and 0 (ionic layer), 1L4A shares a high degree of sequence conservation and amino acid identities with the analogous rat SNARE complex. However, in spite of this, 1L4A exhibits a lower melting temperature of 73 °C under native conditions (Bracher

*et al.* 2002). This is attributed to the greater flexibility observed at the termini of the chains, especially from layer -7 towards the N-terminal, and from layer +1 towards the C-terminal, which in turn is hypothesised to be an energy-economising adaptation of the cold-blooded squid in a cold habitat. There is said to be tight, well-defined packing between the hydrophobic layers -7 and +1, however extending from +1 to the C-terminus, the structure begins to deviate from that of the rat, and loses definition in the packing (Bracher *et al.* 2002).

Finally, 3B5N is a yeast (*Saccharomyces cerevisiae*) plasma membrane SNARE complex (Strop *et al.* 2008). It comprises of t-SNAREs Sso1p, which is a syntaxin homologue, the SNAP-25 homologue Sec9 homology domain 1 (H1) and Sec9 homology domain 2 (H2), and the R-SNARE Snc1p, which is a VAMP homologue. The yeast SNARE has a markedly reduced stability compared to its rat and squid analogues, is not SDS-resistant, and its melting temperature was recorded as 55 °C (Strop *et al.* 2008).. Like 1L4A, 3B5N also exhibits some flexibility with a greater degree of helical bending observed close to the ionic layer. This is assumed to be the result of a glycine to glutamine (Gln225) substitution in Sso1. The authors suggest that this bent conformation is a consequence of the Sso1 backbone being driven back 1.0-1.7 Å away from the ionic layer avoiding a steric clash with the ionic layer glutamine Gln468 in Sec9 H1 (Strop *et al.* 2008).. However, unlike 1L4A, thermal stability studies on a Q225G mutant of Sso1 revealed that this helical bending does not destabilise the complex (Strop *et al.* 2008). The mutation Q225G introduced glycine, the smallest of the amino acids (no side chain) instead of the glutamine into Sso1p. The glutamine side chain of the yeast protein would normally face inward the assembled coiled-coil. Therefore, the Q225G mutant will result in an extra "empty" space inside the assembled helix and therefore is likely to cause a small reduction in the tightness of the fit. It was therefore expected that the Q225G mutation should form a complex with a reduced bend at the ionic layer. Instead, the mutation decreased the thermal stability of the complex. This indicates that the more pronounced bending angle of Sso1 is not destabilising (Strop *et al.* 2008).

The loss in stability has been attributed to the presence of at least three water-filled cavities in close proximity to the ionic layer. At the -2 hydrophobic layer, Met167 in neuronal SNAP-25 C-terminal is substituted for Thr615 in Sec9 H2. Threonine's smaller side-chain allows water to penetrate, and then hydrogen bond with Thr615 and Thr461, at the centre of the complex (Strop *et al.* 2008). A second water-filled cavity occurs between layers -4 and -5, caused by the replacement of hydrophobic Val36, in neuronal VAMP-2, and Ile157, in neuronal SNAP-25 N-terminal, to the hydrophilic Thr39, in Snc1p, and Ser605 in Sec9 H2 (Strop *et al.* 2008). Finally, there was the appearance of a likely partially filled cavity between layers +5 and +6, caused by the substitution of Met71 in SNAP-25 N-terminal, to Asn486 in Sec9 H1. The substitution resulted in the observation of two distinct asparagine conformers in one of the three complexes characterised, which indicates

loose packing (Strop *et al.* 2008). Mutation studies to systematically remove the cavities showed an overall increase in melting temperature of 6.7 °C (Strop *et al.* 2008).

## 2. Project Aims and Objectives

### 2.1 Aims

The key aim of this project is to develop a fundamental understanding of the molecular mechanisms underpinning SNARE complex assembly and stability.

A brief description of SNAREs follows to give context to the aims and objectives: SNAREs are a family of membrane proteins responsible for driving membrane fusion in eukaryotic cells. They are capable of self-assembling into incredibly stable heterotetrameric coiled coil complexes comprising of three proteins. In neuronal SNAREs, these three proteins are referred to as syntaxin, SNAP-25 (which contributes two  $\alpha$ -helices), and synaptobrevin (sometimes referred to as VAMP, or shortened to brevin). The SNARE complex has exhibited extraordinary tolerance to a number of chaotropic agents and proteases, as well as chemoresistance to detergents such as SDS, and thermoresistance to temperatures as high as  $\sim 90$  °C, and finally, such self-assembling coiled coil systems as that demonstrated by SNAREs, have already shown excellent promise as part of drug-delivery systems.

Thus, we have been inspired by their architecture and action, and aim to engineer a range of SNARE-like peptides capable of stimuli-sensitive assembly and disassembly, but which do not interact with native SNAREs. This is for the expressed purpose of reducing potential interference with the exocytosis machinery, for example in molecular payload-delivery to intracellular compartments. Our approach for the payload delivery mechanism begins with the design and engineering of the intended SNARE-inspired peptides. Two of the principle limitations encountered when using SNARE proteins in their natural states as part of payload (drug) delivery systems, is that firstly, they have a tendency to interfere with native SNAREs, and hence, exocytosis, and secondly, once formed, the coiled coil complex is too stable to disassemble by thermal or chemical means. As a result, it will be necessary to first study the structural features, and how they influence the SNAREs' molecular recognition and fusogenicity. Then isolate and modify the sequences responsible for these functions to a sufficient degree, to avoid interference with native systems, but also to trigger disassembly in a narrow physiological temperature and pH range.

We envisage these modified peptides playing the part of a thermally sensitive linker between a payload (drug) and its vehicle (e.g. a metal nanoparticle “antenna”) (**Figure 13**). It will accumulate in target tissues through the enhanced permeation retention effect, and then the tissue region of interest would be locally heated through electromagnetic induction or near infrared radiation in order

to induce metal nanoparticle hyperthermia and initiate complex disassembly, delivering the payload (drug) in a controlled manner.

## 2.2 Objectives

There are five distinct stages that define this project, and they are described briefly as follows:

1. to create a comprehensive database of all existing native SNARE complexes, and separately, a database of complexes where protein structure is known,
2. to design and build a computer-based tool to allow systematic analysis, and possible quantitative characterisation of the elements of SNARE structures which have an effect on SNARE assembly or stability,
3. to rationally design a range of self-assembling SNARE-like peptides with adjusted amino acid sequences to experimentally prove the stability changes we have predicted,
4. to rationally design a range of self-assembling SNARE-like peptides capable of controlled stimuli-sensitive self-assembly or disassembly,
5. to explore applications of these peptides for nanoparticle-driven conjugation that allow protein-protein interaction and complex formation to occur, and to test the resulting nanoparticle-peptide conjugate's propensity to disassemble under the influence of a selected stimulus.

**Figure 2.1** summarises our approach in a flow-chart format.

In order to develop our understanding of SNARE protein assembly, we have outlined a bioinformatics approach towards building up a relatively small database of known SNAREs, and will subsequently study their molecular biology, protein sequences, and structures trying to identify key domains and features that influence assembly and disassembly. This process involves the use of a number of existing bioinformatics including protein structure visualisation and sequence alignment software.

Stability and affinity will be analysed using pull-down assay in conjunction with Polyacrylamide Gel Electrophoresis (PAGE), FRET-HRM (Fluorescence Resonance Energy Transfer High Resolution Melt), and CD (Circular Dichroism) spectroscopy (**Figure 1.17**). Whilst full length native SNAREs are stable under SDS-PAGE conditions (Ferrari *et al.* 2012), truncated SNARE complexes are not (**Figure 7.3**). Therefore, native PAGE analysis is the preferred method to see whether the peptide candidates assembled, and to assess complex stability. Native electrophoresis does not disrupt protein-protein interactions in SNAREs. Another important reason for using native PAGE is that separation is no longer based on the molecular weight of the proteins, but also on the protein

charge under the pH conditions of the electrophoresis. Protein charge depends on the protein pI. The key advantage of the native gel is that even if the mass change caused by the complex formation is too small to detect based on the protein mobility, the likely change of the protein complex pI might be able to change the protein mobility in the native PAGE substantially. The assembly of the SNARE complex, whether full length or partially truncated, changes the pI as well as the density of protein packing in the assembled complex and therefore fully assembled SNARE complex is distinguishable from free SNAP-25.

Pull-down assay in conjunction with SDS-PAGE can divulge quantitative information on the assembly of these peptides through densitometry analysis of peptide bands. This will be supported by the use of FRET-HRM. FRET-HRM is expected to allow real-time recording of assembly and disassembly. Melting temperature ( $T_m$ ) can be used to characterise thermal stability. Circular Dichroism (CD) spectroscopy remains the ultimate tool in our studies. SNAREs, only exist in a fully folded coiled coil conformation when fully assembled. Therefore, CD can confirm assembly by visualising and quantifying the coiled coil. CD can also be used to test the stability of the resulting protein-protein complexes using a thermal melt to yield a melting temperature ( $T_m$ ), and van't Hoff enthalpy ( $\Delta H_{VH}$ ).

There are many variables to consider for nanoparticle-protein conjugation, namely, which nanoparticle will be most suitable for both protein immobilisation, and inductive heating. Metal nanoparticles, and particularly gold nanoparticles, are an obvious choice with the availability of sulphur chemistries to use for conjugation, however there is a number of other nanoparticles, for example Iron(II,III) Oxide nanoparticles, which come functionalised with amino- and, or, carboxyl-groups that will be worth investigating. Different diameters will surely affect the capacity for inductive heating, whilst surface chemistries can be exploited to decrease the propensity for agglomeration.

There are a number of other techniques that may be useful for either characterisation or confirmation of protein phenomena throughout the stages of this process. Fluorescence spectroscopy in conjunction with a thermal shift assay (also known as “thermofluor assay”) provides a suitable method of quantifying the change in thermal denaturation of a protein. In the presence of a native protein, a dye known as SYPRO ORANGE is quenched, and as local temperature is elevated, the protein unfolds and the environmentally sensitive dye binds to exposed hydrophobic regions and fluoresces. Melting temperature can then be calculated from a melt curve using a Boltzmann fit. Similarly, we could develop a reporter system in which peptides with intrinsic fluorescence, or FRET-based fluorescent probes, are incorporated into the termini of our SNARE-like peptides. As the proteins assemble into the parallel coiled coil, the fluorescent peptides are brought into close enough proximity to undergo Förster resonance energy transfer (FRET). Protein-

protein interactions may be tracked and their affinity kinetics can be quantitatively assessed using surface plasmon resonance (SPR), a label-free technique used to measure parameters such as equilibrium association or dissociation constants. It does so by directing polarised light at the interface between a glass prism, whose surface is covered in conductive gold film, and immobilised with one protein, and a flowing sample containing the complimentary protein, and then subsequently measuring the refractive index of the resulting excited plasmons.

## **2.3 Hypotheses**

### **2.3.1 Hypothesis 1: Hierarchy of assembly**

It has been previously established that assembly of the SNARE complex is initiated at the N-terminal, and involves a 1:1 binary complex between syntaxin and SNAP-25, with synaptobrevin binding last (Yoon and Munson, 2018). Although this knowledge is in place, the hierarchy of assembly has not yet been fully elucidated since it is not currently known yet, which of SNAP-25's  $\alpha$ -helices bind to syntaxin first. We hypothesise that the syntaxin binds preferentially to SNAP-25 N-terminal, and they come into close proximity due to long-range ionic attraction at the N-terminal region of both helices.

### **2.3.2 Hypothesis 2: Specificity of complex**

Moreover, we hypothesise that the specificity of complex assembly and its stability are not governed by the presence of the ionic layer alone, but also by complementary residue volumes that permit a single arrangement of helices. The ionic layer might prevent frame shifts by effectively “centering” the complex around this single, uncharacteristically ionic layer among the otherwise hydrophobic repeats. We postulate that the residue volumes in each segment interlock “knobs-into-holes” style, so if one imagines two chains, when a residue in one of the chains is large, the corresponding position in the second chain must be small to accommodate both residues in the same location. This contributes to the specificity of the chain assembly. If, for example, there was a frame shift, at another location the large residue may be faced with a similarly large residue and the steric clash would prevent the chains from assembling into a stable complex.

Tight packing is expected along the entirety of the SNARE motif, if not the entire complex. It is therefore reasonable to expect that the general volumes of individual heptad slices (slice refers to the entire heptad layer consisting of abcdefg amino acids) should be consistently similar from the



start to the end of the SNARE motif. This would mean that there should be regularity in volume of the coiled coil, and that feature is one of the driving factors that confers the fidelity of SNARE-binding, and to an extent, thermal stability to the SNARE complex.

## **2.4 Rational design of SNARE peptides: Strategy for modifying Residue Volumes and Ionic Interactions**

There are two streams of interest in terms of the rational design process for the thermosensitive, self-assembling SNARE-based peptides. The first is concerned with residue volume, and how it can be used to influence complex stability, and the second focuses on ionic interactions, and how they can be used to strengthen or weaken complex stability, as well as playing a role in recognition. Our design process for each stream is quite distinctive. For the residue volumes, a quantitative approach using SNARE protein structure compactness analysis tool, has been employed to help define target residues or positions that can be modified to influence complex stability. Such analysis is completely novel, and the tool was created as part of this research project (see **section 3.3** for more information). Ionic interactions, which are known to affect stability of protein complexes (Chao *et al.* 1998), were considered separately. With ionic interactions, a more logical, qualitative approach has been employed to introduce pH-sensitivity by mutating key positively charged residues, and investigate the significance of a set of existing salt bridges on complex stability by introducing ionic repulsion.

Unlike the residue volume study, ionic interactions will be studied using qualitative analysis based on data generated from bioinformatics and 3D modelling. Whilst the overall aim is to investigate the hypothesis that SNARE assembly is initiated by long-range ionic interactions, and that complex stability is supported by the formation of salt bridges, the experiments designed for this investigation follow two different themes. The first theme aims to explore the possibility of introducing pH-sensitivity to the SNARE complex by mutating key positively charged residues, which participate in salt bridges, with pH-sensitive histidine residues. Furthermore, it is anticipated that knowledge will be gained regarding the extent to which these salt bridges contribute to the stability, and ultimately initiation of SNARE complex assembly. The second theme deals directly with salt bridges present in the native complex. The aim of this study is to explore importance of a number of existing salt bridges on the stability of the complex, but the approach is slightly different. It is thought that introducing ionic repulsion by mutating at least one residue in a salt bridge pair will weaken or break the salt bridge, thus destabilising the complex.

### 3. Materials and methods

#### 3.1 Materials

##### 3.1.1 Bioinformatics

UniprotKB database (Uniprot, <http://www.uniprot.org/>)

ScanProsite (ExPASy) (ScanProsite ExPASy, <https://prosite.expasy.org/scanprosite/>)

PRALINE multiple sequence alignment tool (PRALINE IBIVU, <http://www.ibi.vu.nl/programs/pralinewww/>)

ProtParam (ProtParam ExPASy, <https://web.expasy.org/protparam/>)

ProtScale (ProtScale ExPASy, <https://web.expasy.org/protscale/>)

NetGlycate 1.0 (NetGlycate 1.0 CBS, <http://www.cbs.dtu.dk/services/NetGlycate/>)

NetPhos 3.1 (NetPhos 3.1 CBS, <http://www.cbs.dtu.dk/services/NetPhos/>)

YinOYang 1.2 (YinOYang 1.2 CBS, <http://www.cbs.dtu.dk/services/YinOYang/>)

TMHMM v 2.0 (TMHMM v 2.0 CBS, <http://www.cbs.dtu.dk/services/TMHMM/>)

COILS (COILS ExPASy, [https://embnet.vital-it.ch/software/COILS\\_form.html](https://embnet.vital-it.ch/software/COILS_form.html))

GlobPlot (GlobPlot v2.3 EMBL, <http://globplot.embl.de>)

Conserved Domain Database (Conserved Domain Database NCBI, <https://www.ncbi.nlm.nih.gov/Structure/cdd/cdd.shtml>)

STRING database (STRING Consortium, <https://string-db.org/>)

Protein Data Bank (Protein Data Bank RCSB, <https://www.rcsb.org/>)

Swiss-PdbViewer (Swiss-PdbViewer v4.1 SIB, <https://spdbv.vital-it.ch/>)

Protein-protein blast (NCBI, <https://blast.ncbi.nlm.nih.gov/Blast.cgi?PAGE=Proteins>)

Excel (Microsoft Office)

PyMOL (PyMOL, <https://pymol.org/2/>)

Cn3d (Cn3d, <https://www.ncbi.nlm.nih.gov/Structure/CN3D/cn3d.shtml>)

##### 3.1.2 Investigating assembly and stability of truncated SNARE-based peptide complexes

Proteins including GST, SNAP-25, GST-SNAP-25, VAMP55, VAMP54, VAMP2, truncated VAMP 25, 27, 34, and 45 were kindly provided by our collaborator Dr. Enrico Ferrari (University of Lincoln). For synthesis of GST-SNAP25, SNAP-25 recombinant protein was encoded in a pGEX-KG vector as a Glutathione-S-Transferase (GST) C-terminal fusion protein, with a thrombin cleavage site at

the N-terminal. Dr. Enrico Ferrari of University of Lincoln also provided this pGEX-KG-SNAP25 plasmid. BL21 competent cells were a gift to Elina Dosadina from Professor Simon Cutting (Royal Holloway, University of London). Isopropyl b-D-1 thiogalactopyranoside (IPTG) was purchased from Thermo Fisher. Peptides (outlined with sequences in **Table 4**) were ordered from Synpeptide Co. Ltd (Shanghai, China). Other proteins used included Anti-Human IgG (whole molecules)-FITC produced in rabbit, Bovine Serum Albumin (BSA), Protein A, and lysozyme, all from Sigma. Mini-Protean® Electrophoresis System, Mini-Protean TGX precast gradient gel (4-15%) and the Precision Plus Dual Colour Standard molecular weight ladder were obtained from Biorad and TruPage 4-20% gradient precast SDS-gel was obtained from Sigma. Gels were visualised using Odyssey CLx scanner imaging system (Li-Cor Biosciences). Zeba Spin desalting columns 7 kDa MWCO were obtained from Thermoscientific, whilst Amicon ultra-0.5 mL centrifugal filter units of 10, and 30 kDa NMWL and Millipore Amicon Ultra 15 mL centrifugal filters 100 kDa MWCO were obtained from Merck. Pierce™ glutathione-agarose resin was obtained from Thermofisher. Scientific. Gold nanoparticles (20 nm diam.) and amino-reactive magnetic nanoparticles (iron(II,III) oxide composition, N-hydroxysuccinimide ester functionalised surface, 5 nm diam.) were sourced from Sigma. CF790 succinimidyl ester, DABCYL-SE (SE: succinimidyl ester), and 5-(Iodoacetamido)fluorescein were all obtained from Sigma-Aldrich. We carried out HRM using Rotor-Gene Q (Qiagen) real-time quantitative PCR instrument. It collects fluorescent signals with high optical and thermal precision ( $\pm 0.02$  °C resolution, and  $\pm 0.5$  °C accuracy), and the HRM channel is wide with a source 460 nm, and detector 510 nm, that accommodates the FRET dye pair, donor fluorescein ( $\lambda_{em}$  512 nm), and acceptor DABCYL ( $\lambda_{abs}$  range 346-489 nm), selected for our methodology. We also conducted thermal melts on a StepOnePlus real-time qPCR instrument, with the following settings: melt curve with standard ramp speed, and continuous mode was selected, the heating profile was defined as 25-4°C at 100% rate, 4-99°C at a rate of 1% set to collect data in the “ROX” (excitation 586 nm, emission 610/616 nm) filter channel during this ramp. Data was normalised and differentiated by the StepOnePlus software. Synchrotron Radiation Circular Dichroism (SRCD) was performed using a nitrogen-flushed Module X end-station spectrophotometer at B23 Synchrotron Radiation CD Beamline at the Diamond Light Source (Oxfordshire). Other CD experiments were conducted using a PiStar-180 CD stopped-flow spectrometer. The settings used for each CD instrument varied depending on the experiment, and these are specified in the relevant methodology.

All other chemicals were sourced from Sigma-Aldrich (now Merck), unless specified otherwise. This applies to all subsequent method sections.

### 3.2 Characterising the SNARE proteins using bioinformatics tools

The collection of known mammalian SNARE proteins was collated using the SWISS-PROT database within UniprotKB. An advanced search for “syntaxin”, “VAMP”, and “snap25” was conducted, with taxonomy selected as “eukaryota” and “mammalia”, and only SWISS-PROT reviewed proteins were accepted.

Rat neuronal synaptic SNARE proteins were selected as the model complex since this is one of the most widely studied organisms in the realm of SNARE proteins. The evidence for this can be found in the SNARE database tool outlined in **section 3.3.1**, where of the 26 elucidated SNARE complex structures, 13 were of *Rattus norvegicus* neuronal SNAREs.

A primary search in the UniprotKB database (Uniprot, <http://www.uniprot.org/>) using the keywords: “syntaxin-1a”, “VAMP-2” and “SNAP-25” was conducted, and the results were subsequently filtered to only include SWISS-PROT reviewed proteins, and finally the taxonomy was set to *Rattus norvegicus* for all three proteins. ScanProsite (ExPASy) (ScanProsite ExPASy, <https://prosite.expasy.org/scanprosite/>) was used to scan the Prosite collection of motifs in order to confirm the location of the SNARE motif within the SNARE proteins. The proteins’ accession codes (syntaxin-1a: P32851, SNAP-25: P60881, VAMP: P63045) were submitted and the tool was conducted at high sensitivity. Subsequently, all ‘SNARE proteins’ within the database that did not contain a SNARE motif were manually removed. The SNARE motifs sequences were manually converted to FASTA input and submitted for alignment using PRALINE multiple sequence alignment tool (PRALINE IBIVU, <http://www.ibi.vu.nl/programs/pralinewww/>), with settings kept at default.

The proteins’ amino acid composition, instability index and topological features were ascertained by entering their Swiss-Prot accession numbers into ProtParam (ProtParam ExPASy, <https://web.expasy.org/protparam/>). ProtScale (ProtScale ExPASy, <https://web.expasy.org/protscale/>) was used to determine the hydrophobicity profiles for each protein based on the amino acid scale determined by Kyte and Doolittle, once again by entering their accession numbers. The location of glycation sites was predicted using NetGlycate 1.0 (NetGlycate 1.0 CBS, <http://www.cbs.dtu.dk/services/NetGlycate/>), phosphorylation sites were predicted using NetPhos 3.1 (NetPhos 3.1 CBS, <http://www.cbs.dtu.dk/services/NetPhos/>), O-GlcNAcylation sites were predicted using YinOYang 1.2 (YinOYang 1.2 CBS, <http://www.cbs.dtu.dk/services/YinOYang/>), and the locations of transmembrane helices were predicted using TMHMM v 2.0 (TMHMM v 2.0 CBS, <http://www.cbs.dtu.dk/services/TMHMM/>), in all cases the FASTA sequence for each protein was input and generic settings were used. The tool COILS (COILS ExPASy, [https://embnet.vital-it.ch/software/COILS\\_form.html](https://embnet.vital-it.ch/software/COILS_form.html)) was used to predict

the number and positions of coiled-coil topologies, in all cases the proteins' accession numbers were entered rather than the FASTA sequence, otherwise generic settings were used. To investigate the disorder and globularity, as well as predict domains, the protein FASTA sequences were entered into GlobPlot (GlobPlot v2.3 EMBL, <http://globplot.embl.de>), with Russell-Linding propensities selected. Conserved domains were ascertained using the Conserved Domain Database (Conserved Domain Database NCBI, <https://www.ncbi.nlm.nih.gov/Structure/cdd/cdd.shtml>), by entering the proteins' accession numbers and all settings kept generic. Protein-protein interaction networks were mapped using STRING database (STRING Consortium, <https://string-db.org/>). In all cases, the protein name was entered and the organism was selected. Protein crystal structures were obtained using Protein Data Bank (Protein Data Bank RCSB, <https://www.rcsb.org/>), viewed, and superficially modified using Swiss-PdbViewer (Swiss-PdbViewer v4.1 SIB, <https://spdbv.vital-it.ch/>).

### **3.3 Predicting molecular interactions using the SNARE protein structure compactness analysis tool**

#### **3.3.1 Building the SNARE tool**

A database was compiled containing all SNARE proteins that are known to assemble into complexes, with either elucidated complex structures obtained from the Protein Data Bank (Protein Data Bank RCSB, <https://www.rcsb.org/>), or mined from the literature. The criteria of selection is that they must be proven to form a complex, the complex must be a tetrameric coiled coil, and it must contain SNARE proteins, although not necessarily in the QabcR format containing only syntaxin, SNAP-25 and VAMP, for example, it could be two syntaxin proteins binding to SNAP-25.

In order to build a database of known SNARE proteins with PDB (protein databank) structures, the key word "snare complex" was entered into the protein databank website search bar (Protein Data Bank RCSB, <https://www.rcsb.org/>), the results were filtered for mammalian and the results were saved as a custom report showing datablock name, chain I.D. Pfam accession code, Pfam I.D. Pfam description, sequence, and Uniprot accession code. This yielded 43 different PDB entries associated with SNARE complexes.

In order to ensure that only proteins with SNARE motifs were included in the database, these 43 entries were filtered using the Pfam I.D. and description from the PDB report, as well as the ScanProsite tool (ScanProsite ExpASY, <https://prosite.expasy.org/scanprosite/>). Their sequences

were manually entered into ScanProsite, 10 at a time, to scan them against the PROSITE collection of motifs. The results, in the form of a PROSITE “name of motif”, “start position” and “stop position” were entered into the PDB report. All tetrameric SNARE complexes following the conventional QabcR format with three T\_SNARE and one V\_SNARE PROSITE-defined motif were highlighted as priority and use to form the initial database. This consisted of 22 unique PDB I.D.s. two further PDB I.D.s, 1HVV and 1JTH, who were defined by PROSITE as containing four T\_SNARE motifs and no V\_SNARE motif were also included but highlighted as “odd cases” that do not follow convention.

Since 24 PDB I.D.s is too small a sample size, we sought to increase the database by adding SNAREs that have been characterised in the literature. Two of these new entries were non-mammalian PDBs 1L4A (*Loligo pealeii*), and 3B5N (*Saccharomyces cerevisiae*), and these were used for subsequent analysis described in this review. 37 new entries were added on the basis of either: literature searches for characterised SNARE complexes in other organisms or non-traditional tetrameric SNAREs that do not follow QabcR convention, and based on speculation where a characterised complex was used to find corresponding proteins in a different organism. These 37 entries do not have PDB I.D.s. The final number of complexes in the database was 63. The complexes were arranged in the database in the order: syntaxin, SNAP-25 N-terminal, SNAP-25 C-terminal and VAMP-2.

In order to align the sequences, the PDB I.D.s of all those with elucidated structures, and their corresponding uniprot accession codes were used as the input for a protein-protein blast (NCBI, <https://blast.ncbi.nlm.nih.gov/Blast.cgi?PAGE=Proteins>). The full sequence was retrieved from the blast, and entered into the database. The motif was then selected from this sequence in the Excel (Microsoft Office) database. **Figure 3.1** shows the layout of the database, and describes each component.

### 3.3.2 Integrating “scales” into the tool

**Figure 3.2** shows the layout of the “Scales” section of the database. Column A corresponds to all 20 natural amino acids, and a further “amino acid” given the symbol “X” which is used as a prop to signify the absence of an amino acid when positions selected by the user exceeds the length of the actual sequence. This column is used as an index for the amino acids in the selected sequences of the database, allowing them to be matched to their corresponding score in a selected scale, which is returned in the “Analysis” section of the database spreadsheet. This process is called “index-match” in Excel. The scales in this section, as shown in **Figure 3.2**, include: hydrophilicity (Kyte, J. Doolittle, 1982), approximate charge of amino acids at physiological pH, average mass of amino

acids, residue volumes (Zamyatnin, 1984), average volume buried (Richards 1977, Baumann, Frommel, and Sander 1989), van der Waals volume (Darby and Creighton, 1993).

### 3.3.3 Analysis of the database

**Figure 3.3** shows the general overview of the “Analysis” section of the database. **Figure 3.4** specifically deals with the details of individual amino acid, and averaging amino acid data analysis.

The scale is selected by inputting the column it corresponds to. Columns AA to DV follow the same format as columns AA to DV in the database, however they contain formula that index-matches the amino acids they correspond to, with scores from the scale chosen. Only sequences that have been selected in the “database” page of the spreadsheet will return values in these rows. Individual amino acid data is returned as an output in rows 2-6. Row 2 is an average of all the scores at each position across the entire four-helical complex, whilst rows 3-6 refer to single helices only i.e. row 3 will only take an average of the score for syntaxin at each position in columns AA to DV. A moving average can be taken to simplify analysis; this requires a window size to be selected from a choice of 1,3,5,7, and 9. The results are returned in rows 9-13 titled “A.A. RANGES’ DATA”, where once again the top row refers to an average of the scores for the entire four-helical complex, and rows 10-13 refer to an average of the scores for single helices at the column position indicated.

**Figure 3.5** focuses on group analysis of nonpolar and polar segments. Group analysis is conducted slightly differently to the protocol described above, since it refers to grouped segment of amino acids in the complexes. Nonpolar segments “a” and “d” of the selected complexes are simply averaged at every position they occur in. Polar segments “bc” and “efg” of the selected complexes are first averaged at each position they occur in, i.e. a column referring to a particular “b” position is averaged across all the complexes that have been selected, then an average of the entire layer (“bc” or “efg”) is taken.

### 3.3.4 Predicting theoretical pI, salt bridges, buried polar residues and 3D visualisation

Theoretical pI of each polar layer “bc” and “efg” was calculated using ProtParam (ProtParam ExPASy, <https://web.expasy.org/protparam/>). Since there is a minimum of five amino acid residues required to complete the calculation, each “bc” layer was input alongside four glycine residues (in the format GG**BC**GG), and each “efg” layer was input alongside six glycine residues (GGG**EF**GGG). Salt bridges for PDBs 1N7S, 1L4A and 3B5N were predicted using VMD

(Humphrey *et al.* 1996), using the default oxygen-nitrogen cutoff 4.0 Å. PyMOL (PyMOL, <https://pymol.org/2/>) was used to visualise the salt bridges, and subsequently calculate the distances between the participating residues. PyMOL was also used to find polar contacts between residues of interest and other atoms excluding solvent. Cn3d (Cn3d, <https://www.ncbi.nlm.nih.gov/Structure/CN3D/cn3d.shtml>) was used to visualise the residues in selected segments with the side chains in stick format, and partial backbone down in spacefill format. The results of these experiments can be seen in **Figures 5.4 – 5.6**.

### **3.4 Rational design of thermosensitive SNARE-based peptides**

#### **3.4.1 Thermal melt of truncated VAMP SNARE complexes using Circular Dichroism**

SNARE complexes containing full-length or truncated VAMP (lengths 25, 27, 34, 45 and 54 (FL)) were prepared at a final concentration of between 10 – 16.7 µM, and volume 60 µL, from distilled water (27.5 µL), SNAP-25 (25 µL, 24 µM), syntaxin (7 µL, 111 µM), and truncated VAMP peptide (0.5 µL, 2 mM in DMSO) They were incubated for 1 h at room temperature. Samples containing truncated peptide were diluted 1:4 before conducting the thermal melt. The baseline was prepared from buffer (320 µL, 20 mM HEPES, 100 mM NaCl, pH 7.3), DMSO (5 µL), and deionised water (275 µL), and was diluted 1:4 before conducting the thermal melt. Samples (60 µL) were transferred to a 0.2 mm pathlength cuvette. Scans were conducted across an absorbance range of 180-260 nm, with a temperature profile 20-95 °C in 17x 5 °C steps. To plot the melting curve, molar circular dichroism ( $\Delta\epsilon$ ) at 222 nm was plotted as a function of temperature. The 222 nm wavelength corresponds to the alpha-helical trough. The melting temperature was identified as the temperature at which 50% of the complex had unfolded. Synchrotron Radiation Circular Dichroism (SRCD) was performed using a nitrogen-flushed Module X end-station spectrophotometer at B23 Synchrotron Radiation CD Beamline at the Diamond Light Source, Oxfordshire, UK. The result of this experiment can be seen in **Figure 6.1**.

Dr. Enrico Ferrari (University of Lincoln) is acknowledged for his contribution towards the experiments, which ultimately produced the data in this figure, including providing the recombinant full-length proteins.

#### **3.4.2 Profiling residue volume across complex 1N7S**

The sequences “syntaxin-1a”, “SNAP-25 N-Terminal”, “SNAP-25 C-Terminal”, and “VAMP-2”, from the SNARE complex corresponding to PDB 1N7S were selected in the SNARE database tool. The



residue volume scale was selected from the “Analysis” section of the tool. From the output, only the hydrophobic segments “a” and “d” from positions 15 to 67 for each of the four proteins were selected, and plotted on a graph against segment position. The sum of four residues (from each of the four proteins) per hydrophobic segment was calculated, this was referred to as the total residue volume (TRV), and was plotted on the graph. The average of all the TRVs within the region of interest was calculated, and this was plotted. The 1x and 2x standard deviations were calculated by adding and subtracting 1x, and 2x, the standard deviation of the TRVs within the region of interest, to and from, the average. Predicted deviation was calculated in the following way: the standard deviation of the hydrophobic segment residue volumes within the region of interest (i.e. from positions 15 to 67) of each of the four SNARE proteins was calculated separately, and the resulting values were input into **equation (1)**. This procedure was repeated for all other residue volume profiles. The result of this experiment can be seen in **Figure 6.2**.

$$\Delta\sigma \text{ TRV} = \sqrt{(\sigma \text{ TRV syn})^2 + (\sigma \text{ TRV 25N})^2 + (\sigma \text{ TRV 25C})^2 + (\sigma \text{ TRV brev})^2} \quad (1)$$

### 3.5 Observing assembly of full-length SNARE complex compared to truncated SNARE-based peptide complexes

*Note: Full peptide sequences can be seen in Table 4, which outlines peptide abbreviations, sequences, and the complexes they take part in.*

#### 3.5.1 CD spectra of control Protein A, full-length SNARE complex and associated controls

Protein A was prepared at a final concentration of 20  $\mu\text{M}$ , and volume  $\sim 200 \mu\text{L}$ , from buffer (197  $\mu\text{L}$ , 5 mM HEPES, 25 mM NaCl, pH 7.4), and Protein A (3.6  $\mu\text{L}$ , 50 mg/mL, sourced from Sigma catalog no. P7837). The full-length SNARE complex was prepared at a volume of 150  $\mu\text{L}$ , from buffer (18  $\mu\text{L}$ , 20 mM HEPES, 100 mM NaCl, pH 7.4), SNAP-25 (48  $\mu\text{L}$ , 25  $\mu\text{M}$ ), Syntaxin (48  $\mu\text{L}$ , 36  $\mu\text{M}$ ), and VAMP55 (36  $\mu\text{L}$ , 53  $\mu\text{M}$ ). Individual protein “associated controls” including SNAP-25, Syntaxin and VAMP55, were prepared at a final concentration of 8  $\mu\text{M}$  in buffer (20 mM HEPES, 100 mM NaCl, pH 7.4), then this was diluted 4x in distilled water. The following CD settings were used for all samples detailed in this subsection. A sample volume of 40  $\mu\text{L}$  was transferred to a clean 0.2 mm round cell. Scans were conducted across an absorbance range of 180-260 nm, with an increment of 80 nm, pathlength 0.2 mm, slit size 1 mm, and integration time 1 s. Synchrotron Radiation Circular Dichroism (SRCD) was performed using a nitrogen-flushed Module X end-station

spectrophotometer at B23 Synchrotron Radiation CD Beamline at the Diamond Light Source, Oxfordshire, UK. The results of this experiment can be seen in **Figure 7.1**.

Dr. Enrico Ferrari (University of Lincoln) is acknowledged for his contribution towards the experiments, which ultimately produced the data in this figure, including providing the recombinant full-length proteins.

### **3.5.2 CD spectra of full-length SNARE complex and truncated SNARE complexes C04 and C05**

Full-length SNARE complex was prepared at a final concentration of 6  $\mu\text{M}$ , and volume 200  $\mu\text{L}$ , from buffer (145  $\mu\text{L}$ , 10  $\mu\text{M}$  HEPES, 10 mM NaCl, pH 7.3), SNAP-25 (58  $\mu\text{L}$ , 13  $\mu\text{M}$ ), syntaxin (36  $\mu\text{L}$ , 35  $\mu\text{M}$ ), and VAMP54 (11  $\mu\text{L}$ , 114  $\mu\text{M}$ ). Complex was mixed, and incubated at room temperature for 2.5 h. Truncated SNARE C04 was prepared at a final concentration of 6  $\mu\text{M}$ , and volume 200  $\mu\text{L}$ , from buffer (104  $\mu\text{L}$ , 10  $\mu\text{M}$  HEPES, 10 mM NaCl, pH 7.3), SNAP-25 (92  $\mu\text{L}$ , 13  $\mu\text{M}$ ), Synt1-01\_34 (1.2  $\mu\text{L}$ , 2 mM) and Brev2-04\_34 (2.4  $\mu\text{L}$ , 2 mM). Truncated SNARE C05 was prepared at a final concentration of 6  $\mu\text{M}$ , and volume 200  $\mu\text{L}$ , from buffer (104  $\mu\text{L}$ , 10  $\mu\text{M}$  HEPES, 10 mM NaCl, pH 7.3), SNAP-25 (92  $\mu\text{L}$ , 13  $\mu\text{M}$ ), Synt1-01\_34 (1.2  $\mu\text{L}$ , 2 mM), and Brev2-05\_27 (2.4  $\mu\text{L}$ , 2 mM). Truncated complexes were mixed, and incubated at room temperature for 3 h, and then a further 1.5 h on ice. CD sample volume was 150  $\mu\text{L}$ , and CD was conducted on a PiStar-180 CD stopped-flow spectrometer, across an absorbance range of 185-260 nm, with a 2 sec time per point, a bandwidth of 4 nm, and 3-5 repeats per scan. The results of this experiment can be seen in **Figure 7.2**.

Elina Dosadina is acknowledged for conducting the experiment and generating the data presented here, and Dr. Enrico Ferrari (University of Lincoln) is acknowledged for arranging access to instrument, contributing towards the experimental design and providing the recombinant full-length proteins.

### **3.5.3 SDS-PAGE of full-length SNARE complex and associated controls**

Full-length complex was assembled as follows: PBS (7.4  $\mu\text{L}$ ), syntaxin (3.1  $\mu\text{L}$ , 35  $\mu\text{M}$ ), SNAP-25 (8.5  $\mu\text{L}$ , 13  $\mu\text{M}$ ), VAMP54 (1  $\mu\text{L}$ , 114  $\mu\text{M}$ ), and left to incubate 5 h at 4  $^{\circ}\text{C}$ . The sample was subsequently split into 2x 10  $\mu\text{L}$ , and SDS-loading buffer (2.5  $\mu\text{L}$ ) was added to both aliquots. One aliquot was labelled “DC – denatured complex”, and heated in a thermocycler to 70  $^{\circ}\text{C}$  for 10 min. Control proteins syntaxin, SNAP-25 and VAMP54 were prepared in the same manner, but substituting all other protein for PBS to a volume of 20  $\mu\text{L}$ . A 15% acrylamide gel was prepared from distilled water (1.65 mL), acrylamide/bisacrylamide (3.75 mL, 30%, 0.8% w/v), TRIS (1.95 mL, 1.5

M, pH 8.8), SDS (75  $\mu$ L, 10%), ammonium persulphate (75  $\mu$ L, 10%), and TEMED (7.5  $\mu$ L). Once the gel had set, the samples (10  $\mu$ L) were loaded onto the gel, alongside the marker ladder (5  $\mu$ L, Precision Plus Dual Colour Standard, Biorad). SDS-PAGE was conducted at 170 V, 29 mA for 40 min in ice. The gel was stained with Coomassie blue dye for 15 sec in microwave, and then left on rocker for 15 min, and destained using destain solution (25% methanol, 10% acetic acid, 65% distilled water) for 2 h. The gel was visualised using Photosmart 1200 photo scanner (Hewlett Packard). The results of this experiment can be seen in **Figure 7.3a**.

#### **3.5.4 Testing full-length and truncated SNARE complexes for SDS-stability**

Samples from **section 3.5.2** (stored at -20 °C) were the subject of this gel. The gel samples were prepared in the following way: full-length complex CD sample (30  $\mu$ L) was mixed with SDS-loading buffer (10  $\mu$ L), C04 CD sample (32  $\mu$ L) was mixed with SDS-loading dye (8  $\mu$ L), C05 CD sample (32  $\mu$ L) was mixed with SDS-loading buffer (8  $\mu$ L), and SNAP-25 (16  $\mu$ L, 6  $\mu$ M) was mixed with SDS-loading buffer (4  $\mu$ L). The complex samples were each split 2x 20  $\mu$ L, and one aliquot of each was denatured at 90 °C for 5 min in a thermocycler. The samples (20  $\mu$ L), and a marker ladder (3  $\mu$ L, Precision Plus Dual Colour Standard, Biorad) were loaded onto the precast gradient gel (Mini-Protean TGX 4-15%, Biorad), and electrophoresis was conducted at 120 kV, 20 mA, 5W for 1.5 h in Tris-Glycine-SDS running buffer. The gel was stained in Coomassie blue dye for 15 sec in microwave, then left at room temperature for 15 min, and destained in distilled water, before visualising using Odyssey CLx imaging system (Li-Cor Biosciences). The results of this experiment can be seen in **Figure 7.3b**.

Elina Dosadina is acknowledged for conducting the experiment and generating the data presented here.

#### **3.5.5 CD spectra of full-length (FL/FL/FL) and truncated SNARE complexes (FL/FL/34 and FL/34/34)**

Samples including FL/FL/FL (full-length SNARE complex), FL/FL/34 (SNARE complex with truncated VAMP “Brev2-04\_34”), FL/34/34 (SNARE complex with both truncated syntaxin “Synt1-01\_34”, and VAMP “Brev2-04\_34”) were assembled at final concentration of 3  $\mu$ M, and a final volume of 200  $\mu$ L, in accordance to **Table 5**. The samples were incubated at room temperature for 2 h.

The complexes were subject to a buffer exchange to remove the excessive salt in the recombinant proteins, and the DMSO in the peptide-containing samples to improve sample quality for CD

spectroscopy. Buffer exchange was conducted using Zeba Spin desalting columns (7 kDa MWCO, 2 mL, Thermoscientific), following the protocol provided by the product. The column was centrifuged at 1000x g for 2 min to remove the storage buffer. HEPES (1 mL, 10 mM) was added to the column, and it was centrifuged at 1000 g for 2 min to wash it. This was repeated 2 further times (3 washes in total). The columns were placed in fresh falcon tubes, and the sample (0.2 mL) was added. It was centrifuged at 1000 g for 2 min to recover the sample (~200-240  $\mu$ L). This was repeated for each sample.

An initial HEPES background (0.2 mL, 10 mM) was conducted followed by the Protein A control (0.2 mL, 0.05 mg/mL in 10 mM HEPES), and then the three SNARE samples (0.2 mL, ~3  $\mu$ M), all of which had the HEPES background auto-subtracted. The CD settings were as follows: 185-260 nm, 0.5 step, 2 sec time per point, autoPM (photomultiplier) monochromator set to 260 nm wavelength, a bandwidth of 4 nm), 5 scan repeats per sample. CD was conducted on a PiStar-180 CD stopped-flow spectrometer. The resulting data was subsequently averaged over a window length of nine values to improve the signal-to-noise ratio, and normalised to facilitate comparison. The results of this experiment can be seen in **Figure 7.4**.

Lauren Nelless is acknowledged for preparing and conducting the Protein A control experiment. Elina Dosadina is acknowledged for her guidance in using the instrument, and Dr. Enrico Ferrari (University of Lincoln) is acknowledged for arranging access to instrument, contributing towards the experimental design, and providing the recombinant full-length proteins.

### **3.5.6 Preparation of IR-SNAP25**

#### *3.5.6.1 Labelling SNAP-25 with infrared (IR) label CF790*

IR-labelled SNAP-25 was prepared by incubating CF790 (25  $\mu$ L, 1 mg/mL in DMSO) and SNAP-25 (~200  $\mu$ L, 0.32 mg/mL), for 1 h at RT in the dark. Ethanolamine (5  $\mu$ L, 16 M) was added to the solution to block all free amino groups, and this was incubated for a further 1 h at RT. Labelling was confirmed by running 10% SDS-PAGE on 2  $\mu$ L IR-SNAP25 with SDS- loading buffer (5  $\mu$ L) using settings 0.15 kV, 18 mA, 5 W for 1.5 h. This was visualised using Odyssey Clx scanner imaging system (Li-Cor Biosciences).

#### *3.5.6.2 Purification of IR-SNAP25*

Buffer (450  $\mu$ L 100 mM sodium bicarbonate with 0.05% OG pH 7) was added to 2x 50  $\mu$ L aliquots of impure IR-SNAP25 (~0.28 mg/mL). One aliquot (500  $\mu$ L) was transferred to a 10 kDa filter unit (Amicon ultra-0.5 mL centrifugal filter) and spun at 6000 RPM for 20 min to collect the initial flow-through (300  $\mu$ L). A further 300  $\mu$ L buffer was added to the unit and it was spun at 7000 RPM for 20 min. This washing process was repeated three times, collecting ~300  $\mu$ L each time. The sample (100  $\mu$ L) was recovered from the unit at the end of the last wash, 300  $\mu$ L buffer was added to the unit and spun at 9000 RPM for ~5 min to recover excess sample left in the filter. The second aliquot (500  $\mu$ L) was transferred to a 30 kDa filter unit (Amicon ultra-0.5 mL centrifugal filter), and the same procedure was repeated except the centrifuge settings were 4000-5000 RPM for 10 min per spin. A 100  $\mu$ L aliquot was taken from the initial flow-through and washings for each filter unit, and these samples were heated at 95 °C to reduce their volume to ~10  $\mu$ L. An SDS-gel (12%) was prepared from ddH<sub>2</sub>O (2.4 mL), acrylamide/bisacrylamide (3 mL, 30%, 0.8% w/v), TRIS (1.95 mL, 1.5 M, pH 8.8), SDS (75  $\mu$ L, 10%), APS (75  $\mu$ L, 10%), and TEMED (7.5  $\mu$ L). Samples for SDS-PAGE were as follows:

- IR-SNAP25 purified with 30 kDa filter size,
- IR-SNAP25 purified with 10 kDa filter size,
  - both were prepared by adding 10  $\mu$  L sample (~0.35  $\mu$  g) to 5  $\mu$  L 4X SDS-containing loading buffer
- impure IR-SNAP25 prepared by adding 1  $\mu$  L sample (~0.28  $\mu$  g) to 9  $\mu$  L buffer, and 5  $\mu$  L 4X SDS-containing loading buffer
- initial flow-through from 10 kDa filter size,
- initial flow-through from 30 kDa filter size,
- washings from 10 kDa filter size,
- washings from 30 kDa filter size,
  - flow-through and washings were prepared by adding ~10  $\mu$  L from the dehydrated 100  $\mu$  L sample to 5  $\mu$  L 4X SDS-containing loading buffer.

A Precision Plus Dual Colour Standard (Biorad) molecular weight ladder (5  $\mu$ L) was also applied to the gel. Electrophoresis was conducted at room temperature for ~47 min with the following settings: 170 V, 29 mA, 5 W, using TRIS/glycine running buffer. The gel was visualised in 700 nm and 800 nm channels, with the Odyssey CLx scanner (Li-Cor Biosciences). The results of this experiment can be seen in **Figure 7.5a**.

### 3.5.7 Optimisation of buffer conditions for native gels of IR-labelled complexes containing rationally-designed peptides

5X stock solutions of buffers A-C containing final concentration of BSA (1-0.01 mg/mL), OG (0.1%), HEPES (16 mM), and NaCl (80 mM) were prepared according to **Table 6**.

Full-length SNARE complex was prepared from IR-SNAP25 (11.2  $\mu$ L, 1.41  $\mu$ M, final concentration = 0.7  $\mu$ M), syntaxin (8.6  $\mu$ L, 35  $\mu$ M, final concentration = 13.3  $\mu$ M), and VAMP (2.8  $\mu$ L, 114  $\mu$ M, final concentration = 14.1  $\mu$ M). This was kept at RT for 2.5 h. It was then diluted into stock solutions CFL A-C (containing IR-SNAP25 final concentration 3.2  $\mu$ g/mL – 0.2  $\mu$ g/mL) in the following manner: CFL A (3.2  $\mu$ g/mL) was prepared from 17.1  $\mu$ L full-length SNARE complex with 7.8  $\mu$ L ddH<sub>2</sub>O, CFL B (0.8  $\mu$ g/mL) was prepared from 4.2  $\mu$ L full-length SNARE complex with 20.7  $\mu$ L ddH<sub>2</sub>O, CFL C (0.2  $\mu$ g/mL) was prepared from 1.2  $\mu$ L full-length SNARE complex with 23.7  $\mu$ L ddH<sub>2</sub>O. A diluted stock solution of IR-SNAP25 (D) was prepared from IR-SNAP25 (1  $\mu$ L, 0.035 mg/mL) with ddH<sub>2</sub>O (3  $\mu$ L).

Native PAGE samples were assembled as indicated in **Table 7**, in the order of buffer first, then CFL master mix, and finally, adding SDS-free loading buffer (composition 62.5 mM TRIS pH 6.8, 10% glycerol, 0.05% Bromophenol Blue) last. Sample 10 was prepared directly from IR-SNAP25 (1.41  $\mu$ M), and not any stock solution. All samples (15  $\mu$ L) were loaded onto the native mini-Protean TGX pre-cast 4-15% gradient gel (Biorad), alongside a Precision Plus Dual Colour Standard molecular weight ladder (5  $\mu$ L). Electrophoresis was conducted at room temperature for ~1 h 23 min, using TRIS/glycine running buffer, with the following settings: 120 V, 30 mA, 4 W for 13 min, then current was changed to 20 mA for the remainder of the time. The native gel was visualised using Odyssey Clx scanner (Li-Cor Biosciences). The results of this experiment can be seen in **Figure 7.5b**.

### 3.5.8 Native gels of IR-labelled complexes containing rationally designed peptides

*Note: This method was used for all IR-labelled complexes containing rationally designed peptides (0.241 mM, 1 mg/mL in DMSO) on native gradient gels. This encompasses **Figures 7.6** and **7.7**. In addition, the marker bands in the native gels are not labelled with molecular weight because mobility depends on protein charge and the hydrodynamic radius of the protein, not molecular weight alone.*

IR-SNAP25 stock was prepared from 10X Buffer B (36  $\mu$ L), ddH<sub>2</sub>O (169.2  $\mu$ L) and IR-SNAP25 (33.6  $\mu$ L, 0.035 mg/mL). Samples for native PAGE were prepared as follows: IR-SNAP25 stock (20.6  $\mu$ L), syntaxin of interest (1  $\mu$ L, 1 mg/mL), and VAMP of interest (1  $\mu$ L, 1 mg/mL). They were incubated at 4°C overnight. After incubation, 4X-loading buffer (7.4  $\mu$ L, composition 62.5 mM TRIS

pH 6.8, 40% glycerol, 0.05% Bromophenol Blue) was added to each sample. All samples are split into 2x15  $\mu$ L aliquots. One aliquot of the complex mixes was heated at 95°C for 15 min, then it was loaded onto the gel (denatured “D” control). The remaining aliquots were loaded onto the gel with no further treatment (native complex). The native gel used was a native mini-Protean TGX pre-cast 4-15% gradient gel (Biorad), and a Precision Plus Dual Colour Standard (Biorad) molecular weight ladder (5  $\mu$ L) was also loaded onto each gel. Electrophoresis was conducted in an ice-water bath for ~1.5 h using TRIS/glycine running buffer with the following settings: 120 V, 35 mA, 5 W. The gel was visualised in 700 nm and 800 nm channels, and densitometry analysis was conducted on Odyssey CLx scanner (Li-Cor Biosciences).

### **3.5.9 Observing full-length SNARE complex assembly on nanoparticles using CD spectroscopy**

Amino-reactive magnetic nanoparticles (10 mg, iron(II,III) oxide composition, N-hydroxysuccinimide ester functionalised surface, 5 nm diameter, sourced from Sigma catalogue no. 747440) were cross-linked with GST (40  $\mu$ L, 111  $\mu$ M) in sodium phosphate (100  $\mu$ L, 100 mM, pH 6.5) for 1-2 h at room temperature, then 24-48 h at 4 °C. MNPs were cross-linked with GST-SNAP25 (100  $\mu$ L, 36  $\mu$ M) in sodium phosphate (100  $\mu$ L, 100 mM, pH 6.5) for 1-2 h at room temperature, then 24-48 h at 4 °C. Sodium azide was added to 0.02% final concentration. Both samples were purified to remove excess protein using Millipore Amicon Ultra 15 mL Centrifugal Filters with 100 kDa MWCO (Merck). Each sample (150  $\mu$ L) was diluted to a volume of 5 mL in a filter unit, and centrifuged at 5000x g for 3 min. This was repeated six times with 5 mL each time, and in the final round, the particles were maintained at a volume of 1 mL. In parallel, a master mix of synt/vamp was prepared containing VAMP54 (18  $\mu$ L, 114  $\mu$ M), syntaxin (57  $\mu$ L, 35  $\mu$ M) in sodium phosphate (85  $\mu$ L, 10 mM) to a final concentration of 12.5  $\mu$ M, and volume 160  $\mu$ L. Samples for CD were prepared according to **Table 8**. The amount of MNPs in each sample was calculated such that the final absorbance was 0.05. The samples were assembled at a final volume of 50  $\mu$ L, and were diluted to the CD sample volume 300  $\mu$ L with 250  $\mu$ L distilled water. They were incubated for 2 h at room temperature. Scans were conducted across an absorbance range of 185-260 nm, with an increment of 75 nm, pathlength 10 mm, slit size 0.5 mm, and integration time 1 s. Synchrotron Radiation Circular Dichroism (SRCD) was performed using a nitrogen-flushed Module X end-station spectrophotometer at B23 Synchrotron Radiation CD Beamline at the Diamond Light Source, Oxfordshire, UK. The results of this experiment can be seen in **Figure 7.8a**.

### 3.5.10 CD spectra of full-length SNARE complexes conjugated to gold nanoparticles (GNPs)

Gold nanoparticles (20 nm diameter, Sigma) were diluted 1:2 in distilled water. Samples GNP, GNP-GST and GNP-GST-SYNT were prepared according to **Table 9**, and incubated for 2 h at room temperature. CD spectroscopy was conducted on these samples using a sample volume of 100  $\mu$ L, across a wavelength range of 180-260 nm, with an increment of 80 nm, pathlength 1 mm, slit size 1 mm, and integration time 1 s. A master mix of SNAP-25 (6  $\mu$ L, 25  $\mu$ M), and VAMP55 (4  $\mu$ L, 53  $\mu$ M) was prepared, and 10  $\mu$ L was added to each of the samples GNP, GNP-GST, and GNP-GST-SYNT. These were incubated for 3 h at room temperature. GST baseline was GST (100  $\mu$ L, 0.04 mg/mL) alone. CD spectroscopy was subsequently conducted on these samples using the same parameters and procedure as previously described. Synchrotron Radiation Circular Dichroism (SRCD) was performed using a nitrogen-flushed Module X end-station spectrophotometer at B23 Synchrotron Radiation CD Beamline at the Diamond Light Source, Oxfordshire, UK. The results of this experiment can be seen in **Figure 7.8b**.

## 3.6 Thermal and pH stability of the engineered SNARE complexes

### 3.6.1 Transformation of BL21 competent *E. coli* cells

*Note: This protocol has been adapted from the original protocol, which was written and carried out by Elina Dosadina.*

BL21 competent cells (50  $\mu$ L) were thawed on ice for 30 min, followed by the addition of the pGEX-KG-SNAP25 plasmid (50-200 ng). This was mixed by gentle pipetting, and incubated on ice for 30 min. The sample was heat-shocked by incubating in a water bath at 42°C for 45 s, then transferred to ice for 2 min. SOC medium (500  $\mu$ L) was added to the sample, and it was then incubated at 37°C in a shaker-incubator for 1 h. Aliquots (60, 80, 100, 150  $\mu$ L) of the bacterial culture were plated out onto LB-agar (LB: Luria-Bertani) plates containing ampicillin (final concentration 100  $\mu$ g/mL), the plates were inverted and incubated at 37°C.

### 3.6.2 Expression of GST-SNAP25 fusion protein

*Note: This protocol has been adapted from the original protocol written by Elina Dosadina. This procedure was carried out by Elina Dosadina with the aim of optimising the conditions for the expression of GST-SNAP25 fusion protein, which is not one of the aims of this project and hence, the results have not been discussed in this thesis, and nor is there a Figure to go with this method. This author however, subsequently used the resulting GST-SNAP25 fusion protein produced by Elina Dosadina using this method for the purposes of the pull-down assay.*



2xYT medium (25 mL, 16 g/L tryptone, 10 g/L yeast extract, 5 g/L NaCl) was mixed with ampicillin (50  $\mu$ L, 50 mg/mL), and then inoculated from a single colony of transformed BL21 competent cells expressing GST-SNAP25. The bacterial culture was incubated overnight at 37°C in a shaker incubator at 200 RPM. Following this, fresh 2xYT medium (80 mL) was mixed with ampicillin (200  $\mu$ L, 50 mg/mL), and inoculated with the bacterial culture (800  $\mu$ L). This was incubated at 30°C for 3.5 h, until OD<sub>600</sub> reached 0.6. Bacterial culture (40 mL) was transferred to a sterile flask, and IPTG (40  $\mu$ L, 100 mM) was added to induce protein expression. Induced bacterial culture (3x10 mL) was transferred to three separate sterile flasks. Non-induced bacterial culture (3x10 mL) was also transferred to another three separate sterile flasks. A pair of induced and non-induced bacterial culture flasks were incubated at 37°C for 4 h, the second pair at 32°C for 8 h, and the third pair at 27°C for 24 h. Following incubation, each bacterial culture was centrifuged at 3000x g for 20 min. The pellets were frozen at -20°C overnight, then resuspended in ice-cold PBS (phosphate buffered saline) buffer (500  $\mu$ L), mixed with lysis buffer (500  $\mu$ L, 20 mM Tris, 0.1% TritonX-100, 1 mg/mL lysozyme, pH 7.5), and incubated on ice for 30 min. The samples were subjected to 5 cycles of low-amplitude sonication (10 s) on ice with rest intervals of 30 s in between. The sonicated samples were centrifuged for 20 min at 3000x g, then analysed with a 12% SDS-PAGE. Samples for SDS-PAGE were incubated at 90°C for 5 min with 4X-loading buffer (62.5 mM TRIS pH 6.8, 40% glycerol, 0.05% Bromophenol Blue). A Precision Plus Dual Colour Standard (Biorad) molecular weight ladder (5  $\mu$ L) was also loaded onto the gel. Electrophoresis was conducted at room temperature for ~1.5 h using TRIS/glycine SDS running buffer with the following settings: 180 V, 20 mA, 5 W. The gel was visualised on Odyssey CLx scanner (Li-Cor Biosciences). Samples were then combined together by filtering through a 0.2  $\mu$ m filter into a single tube.

### **3.6.3 Preparation of GST-SNAP25 on glutathione-agarose beads**

*Note: This protocol has been adapted from the original protocol written by Elina Dosadina. Elina Dosadina carried out this procedure, and this author subsequently used the resulting “glutathione agarose-GST-SNAP25 beads” produced by Elina Dosadina using this method for the purposes of the pull-down assay.*

Washing buffer (1 mL, 0.1X PBS, 0.1% OG, 1 mM EDTA, 1 mM PMSF) was added to agarose-glutathione resin (250  $\mu$ L, “Pierce” by Thermofisher), and centrifuged at 2000 RPM for 1 min. The supernatant was discarded, and the process was repeated 2 further times. Lysis buffer (1 mL, PBS, 0.1% TritonX-100) was added to the washed agarose-glutathione resin, and centrifuged at 2000 RPM for 1 min. Again, the supernatant was discarded and the process was repeated 2 further times. Following this, lysis buffer (1 mL) was mixed with the resin, and to this suspension, bacterial lysate containing expressed GST-SNAP25 (2 mL) was added. The mixture was incubated at 4°C

overnight, with constant agitation. The resin containing the bacterial lysate was centrifuged at 2000 RPM for 1 min, and a sample of the supernatant was saved for SDS-PAGE analysis. Lysis buffer (1 mL) was added to the resin pellet, incubated for 10 min at 4°C with agitation, then centrifuged at 2000 RPM for 1 min. This washing procedure was repeated 3 times, and a sample of supernatant was saved for SDS-PAGE analysis each time. The resin was washed in the same manner, this time with storage buffer (0.1X PBS, 0.1% octylglucoside, 1 mM EDTA, 1 mM PMSF), however centrifugation time was increased to 3 min. After the third and final wash, the storage buffer was added up to 1 mL of the total volume. 4X-loading buffer (62.5 mM TRIS pH 6.8, 40% glycerol, 0.05% Bromophenol Blue) was added to the SDS-PAGE samples, and they were incubated at 90°C for 5 min. To enable protein quantification, BSA SDS-PAGE samples were prepared at a final mass of 0.5, 1, 5, 10 and 20 µg, and run concurrently with the samples from this procedure. A 12% SDS-gel was prepared, and a Precision Plus Dual Colour Standard (Biorad) molecular weight ladder (5 µL) was loaded onto the gel. Electrophoresis was conducted at room temperature for ~1.5 h using TRIS/glycine SDS running buffer with the following settings: 180 V, 20 mA, 5 W. The gel was visualised using Coomassie Brilliant Blue staining, and densitometry analysis was conducted on Odyssey CLx scanner (Li-Cor Biosciences). The lysate product “glutathione agarose-GST-SNAP25 beads” was shown to have a concentration of 0.4 mg/mL based on the density of the GST-SNAP25 band in proportion to the BSA bands. It was stored at -20°C.

### 3.6.4 pH-stability pull-down assay

Potassium phosphate buffer (200 mM) with pH 6-8 was prepared according to **Table 10**, and then diluted 1x to a concentration of 100 mM and volume 1 mL. A sample of glutathione agarose-GST-SNAP25 beads (50 µL, 0.4 mg/mL, 8.19 µM, referred to as GST-SNAP25 beads or “beads”) was centrifuged at 3000 RPM for 2 min. The storage buffer was removed from the beads, and buffer (300 µL, 16 mM HEPES, 0.1 mg/mL BSA, 0.1% OG) was added. This washing procedure was repeated five times. After the final centrifugation step, buffer (100 µL) was added to the beads and a 90 µL aliquot was made for the complex, and the remaining 10 µL of beads was kept for the GST-SNAP25 control.

**Table 11** indicates the preparation of the complex on the beads, and the associated controls. Following overnight incubation at 4°C, the complex-on-beads was washed thrice using buffer (300 µL, 16 mM HEPES, 0.1 mg/mL BSA, 0.1% OG), and after the final centrifugation step, buffer (280 µL, 16 mM HEPES, 0.1 mg/mL BSA, 0.1% OG) was added to the beads. On ice, 3x90 µL aliquots were made (beads were resuspended well between aliquots) and labelled “pH 6”, “pH 7” and “pH 8”. The excess buffer was removed and replaced with 90 µL of a 10-fold dilution of the potassium

phosphate buffer (final concentration = 10 mM) of interest as indicated by their label. The complex was incubated for 1 h at room temperature. Following incubation, the samples were centrifuged at 2500 RPM for 2 min. The excess buffer was removed, and the pellet was resuspended with 3  $\mu$ L 2X-loading buffer (31.25 mM TRIS-HCl, 5% v/v glycerol, 1% w/v SDS, 0.025% w/v Bromophenol Blue, 5% v/v 2-mercaptoethanol). All samples were heated at 80 °C for 20 min. The SDS-gel used was a 4-20% gradient pre-cast gel (TruPAGE, Sigma), and a Precision Plus Dual Colour Standard (Biorad) molecular

weight ladder (3  $\mu$ L) was also loaded onto each gel. Electrophoresis was conducted in an ice-water bath for ~1 h using MOPS/SDS running buffer (0.5 M MOPS, 0.5 M TRIS, 34.65 mM (1%) SDS, 10.25 mM EDTA) with the following settings: 150 V, 50 mA, 9 W. The gel was visualised using Coomassie Brilliant Blue staining, and densitometry analysis was conducted on Odyssey CLx scanner (Li-Cor Biosciences). The data for each complex was normalised against the density value obtained for pH 7, then normalised against the density values obtained for the appropriate control complex. The results of this experiment can be seen in **Figure 8.8** and **8.9**.

### **3.6.5 pH-stability measured using CD spectroscopy for complexes C04, C06, and C0206.**

Potassium phosphate buffer (200 mM) with pH 6 was prepared according to Table 10. Each master sample (C04, C06 and C0206) comprised of:

- Potassium phosphate buffer (46  $\mu$  L, 200 mM),
- Synt1-01\_34 (7  $\mu$  L, 10 mg/mL) for C04 and C06, and Synt1-02\_34PH (7  $\mu$  L, 10 mg/mL) for C0206
- SNAP-25 (70  $\mu$  L, 0.545 mg/mL),
- VAMP peptide (7  $\mu$  L, 10 mg/mL) – VAMP peptide would have been Brev2-04\_34 for C04, Brev2-06\_34PH for C0206 and C06.

The master samples were incubated in the fridge (4°C) for 12 h. Buffer exchange was carried out on Zeba Spin desalting columns (7 kDa MWCO, 2 mL, Thermoscientific), using the same protocol as outlined in section 3.5.5. Buffer used for the exchange was potassium phosphate buffer pH 6 (5 mM), and the volume of each master sample (C04, C06 and C0206) was adjusted to final volume of 140  $\mu$ L using 5 mM potassium phosphate buffer. For CD spectroscopy, there were to be 7 points per sample, corresponding to pH 6.0, 6.5, 7.0, 7.5, 8.0, 8.5, and 9.0. The CD spectroscopy samples for pH 6.0 – 8.5 were therefore prepared using 20  $\mu$ L of the master sample mix, and 20  $\mu$ L potassium phosphate buffer (200 mM) prepared at the desired pH, largely in accordance with Table 10, with minor pH adjustments made. For pH 9, a carbonate/bicarbonate solution was prepared

from Na<sub>2</sub>CO<sub>3</sub> (0.2 M, 0.5 mL), NaHCO<sub>3</sub> (0.2 M, 4.5 mL), and pH adjusted to 9.0. Then 20 µL of this buffer was mixed with 20 µL of the master sample mix.

Concentration of the samples was measured in mg/mL using IMPLM NanoPhotometer P330, using 3 µL of sample solution, and a path length of 1 mm. The absorbance was set to 0.3, and the readings were averaged across all pH values within one preparation. Molecular weight of 34,000 was used for the complex when calculating concentration. The following concentrations were obtained:

- C04 = 0.210 mg/mL
- C06 = 0.152 mg/mL
- C0206 = 0.205 mg/mL

Scans were conducted across an absorbance range of 185-260 nm, with an increment of 75 nm, pathlength 10 mm, slit size 0.5 mm, and integration time 1 s. Synchrotron Radiation Circular Dichroism (SRCD) was performed using a nitrogen-flushed Module X end-station spectrophotometer at B23 Synchrotron Radiation CD Beamline at the Diamond Light Source, Oxfordshire, UK. The results of this experiment can be seen in Figure 8.10 and 8.11.

Dr. Enrico Ferrari (University of Lincoln), Dr Giuliano Siligardi (Diamond UK), and Dr Mikhail Soloviev (RHUL) are acknowledged for their contribution towards the experiments, including providing the recombinant full-length protein (EF), setting up the SRCD spectrometer (GS) and experimental design (EF, MS) which ultimately generated the data in this figure.

### **3.6.6 Thermal melts of full-length (FL/FL/FL) and truncated SNARE complexes (FL/FL/34 and FL/34/34) using CD spectroscopy**

This experiment uses the SNARE complex samples FL/FL/FL, FL/FL/34, and FL/34/34 prepared in **section 3.5.5**. The thermal melt protocol was the same for each SNARE sample. CD was conducted on a PiStar-180 CD stopped-flow spectrometer that was connected to a water bath, which heats the sample chamber. The CD settings were entered into the software as follows: 210-260 nm, 0.5 step, 1 sec time per point, autoPM (photomultiplier) monochromator, a bandwidth of 4 nm, 1 scan per temperature point. An initial HEPES background (0.2 mL, 10 mM) was conducted, and following this, the SNARE sample was injected (0.2 mL, ~3 µM). All subsequent scans of the SNARE sample(s) had the HEPES background auto-subtracted. The water bath was programmed to heat to a temperature of ~95°C, and the CD scans, which took approximately 2 min each, were manually conducted as the temperature increased at an approximate rate of ~1.3-2.3 °C/min. The

CD signal between wavelength 230-222 nm corresponded to one of the  $\alpha$ -helical troughs, and this region was averaged to produce the data for the graph. This data was subsequently averaged over a window length of 5 values to further improve the signal-to-noise ratio. The results of this experiment can be seen in **Figure 8.7**.

Elina Dosadina is acknowledged for her guidance in using the CD instrument, and Dr. Enrico Ferrari (University of Lincoln) is acknowledged for arranging access to instrument, contributing towards the experimental design, and providing the recombinant full-length proteins.

### 3.6.7 Thermostability pull-down assay

A sample of glutathione agarose-GST-SNAP25 beads (~125  $\mu$ L, 0.4 mg/mL, 8.19  $\mu$ M, referred to as GST-SNAP25 beads or “beads”) was centrifuged at 3000 RPM for 2 min. The storage buffer was removed from the beads, and buffer (300  $\mu$ L, 16 mM HEPES, 0.1 mg/mL BSA, 0.1% OG) was added. This washing procedure was repeated five times. After the final centrifugation step, buffer (100  $\mu$ L) was added to the beads and a 90  $\mu$ L aliquot was made for the complex, and the remaining 10  $\mu$ L of beads was kept for the GST-SNAP25 control.

**Table 12** indicates the preparation of the complex on the beads, and the associated controls. Following overnight incubation at 4°C, the complex-on-beads was washed thrice using buffer (300  $\mu$ L, 16 mM HEPES, 0.1 mg/mL BSA, 0.1% OG), and after the final centrifugation step, buffer (490  $\mu$ L, 16 mM HEPES, 0.1 mg/mL BSA, 0.1% OG) was added to the beads. On ice, 7x70  $\mu$ L aliquots were made (beads were resuspended well between aliquots) and labelled with temperatures 4, 25, 45, 55, 65, 75 and 85°C, and then incubated at their labelled temperature for 20 min. Following incubation, the samples were centrifuged at 2500 RPM for 2 min. The supernatants were collected in separate labelled tubes, ~3  $\mu$ L 2X-loading buffer (31.25 mM TRIS-HCl, 5% v/v glycerol, 1% w/v SDS, 0.025% w/v Bromophenol Blue, 5% v/v 2-mercaptoethanol) was added, and the samples were dehydrated to ~10-12  $\mu$ L at 99°C.

Cold buffer (100  $\mu$ L) was added to the pellets, and it was kept on ice for 5 min. Then the excess buffer was discarded, and the pellets were resuspended in 3  $\mu$ L 2X-loading buffer. All samples were heated at 80 °C for 20 min. The SDS-gel used was a 4-20% gradient pre-cast gel (TruPAGE, Sigma), and a Precision Plus Dual Colour Standard (Biorad) molecular weight ladder (3  $\mu$ L) was also loaded onto each gel. Electrophoresis was conducted in an ice-water bath for ~1 h using MOPS/SDS running buffer (0.5 M MOPS, 0.5 M TRIS, 34.65 mM (1%) SDS, 10.25 mM EDTA) with the following settings: 150 V, 50 mA, 9 W. The gel was visualised using Coomassie Brilliant Blue

staining, and densitometry analysis was conducted on Odyssey CLx scanner (Li-Cor Biosciences). The results of this experiment can be seen in **Figure 8.1-8.4**.

### **3.6.8 Thermal stability measured using CD spectroscopy for Salt Bridge study complexes C08, C09, C10, and C11, and compensation study complexes C15, C0315.**

A master mix (222  $\mu$ L) of SNAP-25 (71  $\mu$ L, 0.545 mg/mL), Synt1-01\_34 (4  $\mu$ L, 10 mg/mL), and deionised water (147  $\mu$ L) was prepared. The samples for CD spectroscopy were prepared as follows, and then incubated at room temperature for 6 h.

- C04: 53  $\mu$ L master mix + 1  $\mu$ L Brev2-04\_34
- C05: 53  $\mu$ L master mix + 1  $\mu$ L Brev2-05\_27
- C08: 53  $\mu$ L master mix + 1  $\mu$ L Brev2-08\_34ST
- C09: 53  $\mu$ L master mix + 1  $\mu$ L Brev2-09\_34ST
- C10: 52  $\mu$ L master mix + 1  $\mu$ L Brev2-10\_34ST
- C11: 52  $\mu$ L master mix + 1  $\mu$ L Brev2-11\_34ST

Samples C15 and C0315 were prepared from a different master mix (164  $\mu$ L), comprising of SNAP-25 (54  $\mu$ L, 0.545 mg/mL), and deionised water (110  $\mu$ L). The samples for CD spectroscopy were prepared as follows, and then incubated at room temperature for 5 h.

- C15: 52  $\mu$ L master mix + 1  $\mu$ L Synt1-01\_34 + 1  $\mu$ L Brev2-15\_34ST
- C0315: 52  $\mu$ L master mix + 1  $\mu$ L Synt1-03\_34ST + 1  $\mu$ L Brev2-15\_34ST

Following incubation, all samples were purified using Zeba Spin desalting columns (7 kDa MWCO, 2 mL, Thermoscientific), using the same protocol as outlined in **section 3.5.5**. Scans were conducted across an absorbance range of 185-260 nm, with an increment of 75 nm, pathlength 10 mm, slit size 0.5 mm, and integration time 1 s. Synchrotron Radiation Circular Dichroism (SRCD) was performed using a nitrogen-flushed Module X end-station spectrophotometer at B23 Synchrotron Radiation CD Beamline at the Diamond Light Source, Oxfordshire, UK. The results of this experiment can be seen in **Figure 8.4 and 8.7**.

Dr. Enrico Ferrari (University of Lincoln), Dr Giuliano Siligardi (Diamond UK) and Dr Mikhail Soloviev (RHUL) are acknowledged for their contribution towards the experiments, including providing the recombinant full-length protein (EF), setting up the SRCD spectrometer (GS) and experimental design (EF, MS) which ultimately generated the data in this figure.

### **3.6.9 Thermofluor assay: thermal melts of control lysozyme and full-length (CFL) and truncated SNARE complexes (C04 and C05)**

*Note: The results from this study can be seen in the Appendix 14.1.*

A master mix of full-length SNARE complex (8  $\mu$ M, 35  $\mu$ L) was prepared from full-length recombinant proteins syntaxin (8  $\mu$ L, 35  $\mu$ M), SNAP-25 (21.5  $\mu$ L, 13  $\mu$ M), VAMP54 (2.5  $\mu$ L, 114  $\mu$ M), and buffer (3  $\mu$ L, 180 mM HEPES, 900 mM NaCl, 1% OG, pH 7.0). SNARE “C04” master mix (8  $\mu$ M, 35  $\mu$ L) was prepared from Synt1-01\_34 (1.2  $\mu$ L, 241  $\mu$ M), full-length recombinant SNAP-25 (21.5  $\mu$ L, 13  $\mu$ M), Brev2-04\_34 (1.2  $\mu$ L, 241  $\mu$ M), and buffer (11.1  $\mu$ L). SNARE “C05” master mix (8  $\mu$ M, 35  $\mu$ L) was prepared from Synt1-01\_34 (1.2  $\mu$ L, 241  $\mu$ M), full-length recombinant SNAP-25 (21.5  $\mu$ L, 13  $\mu$ M), Brev2-05\_27 (1.2  $\mu$ L, 241  $\mu$ M), and buffer (11.1  $\mu$ L). They were incubated for 3 h at room temperature. A 50X SYPRO Orange stock was prepared from SYPRO Orange (1  $\mu$ L, 5000X in DMSO, Sigma-Aldrich), ddH<sub>2</sub>O (9  $\mu$ L), and then a further 10X dilution was made by diluting 4  $\mu$ L of this stock in 36  $\mu$ L ddH<sub>2</sub>O. The SNARE complex thermofluor assay samples (5  $\mu$ M) “CFL”, “C04” and “C05” were all prepared in 0.2 mL sample tubes in the same manner according to **Table 13**, and then they were spun down at high speed, and transferred to 0.1 mL white-opaque multiwell plate wells.

Controls containing lysozyme (0.1 mg/mL in 0.03X PBS, 10X SYPRO Orange, total volume 50  $\mu$ L, Lysozyme from Chicken Egg White, Sigma), and IgG (0.2 mg/mL in 0.03X PBS, 10X SYPRO Orange, total volume 50  $\mu$ L, Anti-Human IgG produced in rabbit, Sigma-Aldrich) were prepared, and conducted alongside the SNARE complexes. The samples were loaded onto the multiwell plate, and it was sealed with optically clear film. The thermal melt was conducted on a StepOnePlus real-time qPCR instrument with the following settings: melt curve with standard ramp speed, and continuous mode was selected, the heating profile was defined as 25-4°C at 100% rate, 4-99°C at a rate of 1% set to collect data in the “ROX” (excitation 586 nm, emission 610/616 nm) filter channel during this ramp. Data was normalised and differentiated by the StepOnePlus software.

Elina Dosadina is acknowledged for her contribution towards optimising the conditions for the control lysozyme, which ultimately were used for the SNARE complexes also.

### **3.6.10 Testing FRET-HRM: Positive control**

*Note: The results from this study can be seen in the Appendix 14.2.*

#### **3.6.10.1 Labelling of positive control Protein A with DABCYL-SE**

Protein A labelling reactions were assembled in the following manner: Protein A (20  $\mu$ L, 1 mg/mL) was added to sodium bicarbonate (4  $\mu$ L, 1M, pH 8.5), and DABCYL-SE (1 mg/mL) was added to this in the quantities 0, 2, 5, 15, and 2  $\mu$ L for samples Dab-0,1,2,3,x respectively. Deionised water was added to bring the total volume of solution to 40  $\mu$ L. The samples were mixed, covered in foil and incubated at room temperature for 1 h, then 4 °C overnight. Following this, ethanolamine (5  $\mu$ L, 0.5 M) was added to each of the labelling reactions to block any unincorporated dye, and this was incubated at room temperature for 30 min. Reaction mixtures Dab-0,1,2 and 3 (45  $\mu$ L) were transferred to an Amicon ultra-0.5 mL centrifugal filter (NMWL 10 kDa, Merck), and ~350  $\mu$ L of sodium bicarbonate (100 mM) was used to wash out the reaction tubes, and this was also transferred to the filter units. The units were centrifuged at 9000 RPM for 34 min, reducing the volume inside the centrifugal to 60  $\mu$ L, the initial filtrate (~340  $\mu$ L) was transferred to tubes labelled "filtrate 1". The samples were washed 3 times with ~350  $\mu$ L sodium bicarbonate (100 mM) at 9000 RPM for ~40-50 min each time. Finally, the samples were recovered by centrifuging at 5000 RPM, 4 min, the inside of the filter units was washed with ~345  $\mu$ L sodium bicarbonate (100 mM), and centrifuged at same speed and time. This was added to the sample to make a total volume of 400  $\mu$ L. Sodium bicarbonate (355  $\mu$ L, 100 mM) was added to Dab-X to bring the total volume to 400  $\mu$ L. Absorbance of DABCYL in the samples Dab-1,2,3 and Filtrate Dab-1,2,3 (200  $\mu$ L each) was measured using a spectrophotometer (LKB Biochrom) in 15 mm UV-cuvettes at a wavelength of 450 nm, with Dab-0 acting as the reference, and sensitivity mode 0-1 Abs.

#### *3.6.10.2 Fluorescent emission of labelled Protein A and IgG samples*

IgG-FITC (0.01-0.02 mg/mL) was prepared by adding buffer (294  $\mu$ L) to a 1.5 mL tube, followed by 6  $\mu$ L IgG-FITC (0.5-1 mg/mL). The contents were mixed and put on ice. Unlabelled Protein A (70  $\mu$ L, 5 mg/mL) was prepared by adding 35  $\mu$ L Protein A (10 mg/mL) to 35  $\mu$ L buffer. A 100-fold dilution of unlabelled Protein A (100  $\mu$ L, 0.05 mg/ml) was prepared by adding 1  $\mu$ L Protein A (5 mg/mL) to 99  $\mu$ L buffer. Solutions were prepared in parallel according to **Table 14**. They were given 40 min at room temperature to incubate. Following this, the emission was measured using a spectrophotometer (LKB Biochrom) in 15 mm UV-cuvettes at the emission settings 500-600 nm,  $\lambda_{ex}$  480, slit size  $\pm$ 10 nm, scan speed 100 nm/min.

#### *3.6.10.3 Labelled Protein A – IgG complex assembly for HRM*

IgG-FITC (50  $\mu$ L, 0.01-0.02 mg/mL) was prepared by adding buffer (49  $\mu$ L) to a 1.5 mL tube, followed by 1  $\mu$ L IgG-FITC (0.5-1 mg/mL). The contents were mixed and put on ice. Unlabelled Protein A (10  $\mu$ L, 5 mg/mL) was prepared by adding Protein A (5  $\mu$ L, 10 mg/mL) to 5  $\mu$ L buffer.



Solutions are prepared in parallel, with components added in accordance to **Table 15** - in the order of buffer, IgG-FITC, Dab-3, unlabelled Protein A - directly to 0.1 mL strip tubes, and mixed with pipette. They were incubated at room temperature for 1 h.

#### *3.6.10.4 High Resolution Melt (HRM) of labelled Protein A – IgG complexes*

HRM was conducted on a Rotor-Gene Q (Qiagen) real-time quantitative PCR instrument. Samples were set inside the 72-well rotor, with the remaining positions balanced with empty tubes. “Empty run” was selected, and the sample volume was set to 20  $\mu$ L. The acquisition channel was set as HRM (high resolution melt, source = 470 nm, detector = 510 nm), and the gain for the HRM channel was optimised at 25 °C according to sample IgG-FITC. Optimised gain was 0 for HRM. A melt step was inserted with a temperature profile of 25- 99C, at a rate of 1 degree per 60 sec (1 °C/min), and included 90 sec of pre-melt conditioning.

#### *3.6.10.5 Purification, fluorescence and of IgG-FITC*

IgG-FITC (10  $\mu$ L, 0.5-1 mg/mL) was diluted in 90  $\mu$ L buffer, and the resulting solution was separated into 2x 50  $\mu$ L aliquots and labelled “P – purified” and “U – unpurified”. A Micro Bio-Spin 30 chromatography column was sharply inverted several times to resuspend the settle gel, the tip was snapped off and it was placed in a 2.0 mL waste tube. The cap was removed and the excess packing buffer was drained by gravity and discarded. The column was centrifuged for 2 min at 1000x g (5000 RPM) to remove remaining packing buffer, which was discarded. Sodium bicarbonate/BSA buffer (500  $\mu$ L, 100 mM sodium bicarbonate/0.1 mg/mL BSA) was applied to the column, and it was centrifuged at 5000 RPM for 1 min to remove buffer, which was discarded. This was repeated four times to achieve >99.8% buffer exchange (according to Biorad protocol). The column was placed in a clean collection tube and “P” sample (50  $\mu$ L) was applied to the centre. It was centrifuged at 5000 RPM for 4 min to collect the purified sample. The sample volume at the end was ~76  $\mu$ L. Both samples were brought to 100  $\mu$ L by the addition of 24  $\mu$ L, and 50  $\mu$ L sodium bicarbonate/BSA buffer respectively. They were transferred to 15 mm cuvettes and fluorescent emission was measured for each one with the emission settings 500-600 nm,  $\lambda_{ex}$  480 nm, slit size  $\pm$ 10 nm, scan speed 100 nm/min. After fluorescence was measured, 100% glycerol (100  $\mu$ L) was added to each 100  $\mu$ L sample.

#### *3.6.10.6 HRM of purified IgG-FITC samples and samples containing 2-fold labelled Protein A*

Concentration of IgG-FITC in the purified sample was estimated to be 0.009 mg/mL. Samples were prepared according to **Table 15**, whilst samples containing 2-fold labelled Protein A were also prepared in the same manner, but double the volume of Dab-3, with adjustments made to the volume of buffer to compensate. They were given 1 h at room temperature to incubate. HRM proceeded according to the same protocol from **section 3.6.10.4**. Gain was optimised against sample IgG-FITC, and was 0.

### **3.6.11 Testing FRET methodology using labelled peptides control C04**

*Note: The results from this study can be seen in the **Appendix 14.3**.*

#### **3.6.11.1 Labelling Synt1-01\_34 with DABCYL-SE – SynDab34**

Distilled water (15  $\mu$ L), sodium bicarbonate (5  $\mu$ L), Synt1-01\_34 (10  $\mu$ L, 0.241 mM, 1 mg/mL), and DABCYL-SE (20  $\mu$ L, 2.732 mM, 1 mg/mL) were added to a labelled tube. This was incubated for 2 h at room temperature. Tris-HCl (1M, 50  $\mu$ L, pH 8.0) was added to the reaction mixture to block excess amino groups, and this was incubated for 1 h at room temperature. Following this, sodium bicarbonate (400  $\mu$ L, 100 mM) was added to give a final peptide concentration 0.001 mg/mL, 0.241  $\mu$ M, with ~20 XS dye to peptide.

#### **3.6.11.2 Labelling Brev2-04\_34 with Iodoacetamido-Fluorescein – BrevFluor34**

Distilled water (30  $\mu$ L), sodium bicarbonate (5  $\mu$ L), Brev2-04\_34 (10  $\mu$ L, 0.241 mM, 1 mg/mL), and iodoacetamido-fluorescein (5  $\mu$ L, 9.709 mM, 5 mg/mL) were added to a labelled tube. This was incubated for 2 h at room temperature. Sodium bicarbonate (50  $\mu$ L, 100 mM) was added to the reaction mixture (this is not a blocking step, it's to match the incubation time and volume of SynDab), and this was incubated for 1 h at room temperature. Following this, sodium bicarbonate (400  $\mu$ L, 100 mM) was added to give a final peptide concentration 0.001 mg/mL, 0.241  $\mu$ M, with ~20 XS dye to peptide.

#### **3.6.11.3 Labelled peptides purification process**

Reaction mixtures SynDab and BrevFluor (400  $\mu$ L) were transferred to an Amicon ultra-0.5 mL centrifugal filter (NMWL 3 kDa), and the remaining 100  $\mu$ L of unpurified mixture was set aside. The filter units were centrifuged at 9000 RPM for 1 h and ~320-330  $\mu$ L initial flow-through was collected. Approximately the same amount of buffer (320-330  $\mu$ L) was added to the filter units, pipetted

carefully on the sides to dislodge remnants of dye, and the process was repeated three times to yield three wash fractions. The final purified fraction was diluted to 400  $\mu$ L with sodium bicarbonate (100 mM) and transferred to a fresh tube. The absorbance was recorded at 450 nm for SynDab, and 485 nm for BrevFluor, for the unpurified fraction, initial flow-through, the three subsequent washes, and the final purified fraction. Sodium bicarbonate (100 mM) was used as a reference. Fluorescent emission was recorded for BrevFluor unpurified fraction, initial flow-through and final purified fraction using the settings 500-600 nm, fixed excitation 480 nm, slits  $\pm$  10 nm, scan speed 100 nm/min.

#### *3.6.11.4 HRM of C04 and associated controls*

Samples were prepared according to **Table 16**, and allowed to incubate for 1 h at room temperature. HRM proceeded according to the same protocol from **section 3.6.10.4**. Gain was optimised against sample 3 (BrevFluor alone), and was -2.67.

## 4. Characterising the SNARE proteins using existing bioinformatics tools

### 4.1 Results

#### 4.1.1 Amino acid sequence

Synaptic SNARE proteins syntaxin-1a, VAMP-2, and SNAP-25 are the most pertinent to this study since they have undergone the most rigorous characterisation in comparison to others. This study will favour SNARE proteins belonging to the organism *Rattus norvegicus*, unless otherwise stated. Each protein's accession code, full sequence and total number of amino acids was obtained using the Uniprot website and the results are presented in **Figure 4.1**. With the exception of SNAP-25, which exists as two isoforms SNAP-25b and SNAP-25a, the rest of the proteins do not exhibit alternative splicing. Syntaxin-1a is the longest protein with 288 amino acids whilst VAMP-2 is less than half the size at 116 amino acids long. A closer look at their amino acid percentage compositions (ProtParam, ExPASy) in **Table 3** reveals that VAMP-2 is primarily comprised of non-polar, non-charged aliphatic amino acids alanine, isoleucine, and leucine (12.9, 8.6 and 8.6% respectively) suggesting that it could be a significantly hydrophobic protein. Likewise, Syntaxin-1a also holds a large quantity of isoleucine (10.4%), however it additionally possesses noteworthy amounts of negatively charged, polar acidic amino acids glutamic acid and aspartic acid (12.2 and 7.6% respectively) as well as post-translational modification targets such as serine (9%) and lysine (8%). The amino acid compositions of both isoforms of SNAP-25 are mostly in agreement with the exception of their asparagine quantities (isoform 2 has a greater percentage). Comparable to syntaxin-1a, both isoforms contain large amounts of polar, negatively charged aspartic acid and glutamic acid (9.2% and ~11% respectively), and like VAMP-2, they have reasonable amounts of non-polar, neutral amino acids such as alanine (7.8%) and leucine (7.8%). Finally, both SNAP-25 and syntaxin-1a sequences hold a large proportion of arginine, a positively charged amino acid that acts as a hydrogen-bond donor, contributing to SNAP-25's overall hydrophilic nature.

#### 4.1.2 Protein topology and conserved domains

ProtScale (ExPASy) was used to predict the hydrophobicity profile of the synaptic proteins, and the results from this tool can be seen in **Figure 4.2**. VAMP-2 and syntaxin-1a both display similar patterns of hydrophobicity, with the C-terminal exhibiting a peak scoring approximately 4 on the scale in both cases. There is some contrast to be observed between the two patterns however, with

VAMP-2 displaying a much broader profile in comparison to syntaxin-1a's sharper peaks and troughs however, this is most likely to be a result of the difference in sequence length. The aforementioned C-terminal peak suggests a transmembrane domain occurring in this region for both proteins. SNAP-25 presents the least amount of hydrophobicity with a reasonably consistent pattern suggesting that this is a cytosolic protein with no transmembrane anchors.

TMHMM (CBS) was used to predict the presence of transmembrane regions within proteins, and more specifically, to confirm the presence of C-terminal transmembrane anchors in syntaxin-1a and VAMP-2, and the absence of any transmembrane regions within SNAP-25. The results in **Figure 4.3** with syntaxin-1a displaying a transmembrane helical domain between residues ~266-287 and the sequence preceding it ~1-265 located in the cytosol. VAMP-2 also exhibits a helical transmembrane between residues 93-115, the preceding N-terminal portion is cytosolic. The full length of SNAP-25 is predicted to be entirely extra-cytosolic, presenting no transmembrane regions at all.

It was evident based on ProtParam features (ExpASy) that coiled-coil topologies were present in all three proteins and so the next logical step was to confirm their presence and determine their number and location within the sequences using COILS (ExpASy). **Figure 4.4** displays the outputs for each of the proteins syntaxin-1a, VAMP-2, and SNAP-25. Syntaxin-1a presents two coiled-coils in its N-terminal with probabilities greater than 0.5 and one further down in the C-terminal with a much lower probability, VAMP-2 shows only one coiled-coil closer to its C-terminal, and finally, SNAP-25 displays three coiled-coils, two in close proximity within the N-terminal domain and an isolated coiled-coil further down in its C-terminal.

Further analysis into the disorder and globular segments, using the bioinformatics tool GlobPlot (EMBL) was carried out, and the results can be viewed in **Figure 4.5**. Syntaxin-1a was predicted to contain small regions of disorder flanking the sequence between positions 9-20 and 280-288, with the majority indicating globular topology. The transmembrane region predicted by TMHMM was corroborated in this tool's output within the same specified region, and two other named regions including: synN, a conserved N-terminal domain containing Habc, between positions 25-146, and a target SNARE coiled coil between positions 187-254. These are assumed to be conserved domains and will be covered in more detail later. VAMP-2 demonstrated a minority region of low-complexity disorder, with low-complexity defined as regions lacking amino acid diversity, and this was indicated by the white-line peak between positions 1-28, with the remaining majority between 29-113 predicted to be globular. VAMP-2 also contained a coiled-coil region located between residues 59-79 and the expected transmembrane domain between 93-115. SNAP-25 displayed a region of

disorder between residues 3-8, with the majority of the sequence predicted as globular, and showed two target SNARE coiled coil regions between 14-81 and 135-202.

Developing a deeper understanding of the named regions in GlobPlot necessitated the use of a combination of tools including the Conserved Domain Database (CDD) (NCBI) and ProtParam features section (ExPASy). From the collective information obtained, a schematic displaying the domains and their positions was devised and this can be seen in **Figure 4.6**. CDD confirms the presence of a synN domain in syntaxin-1a, and goes on to detail three features of this particular domain which include: an interdomain interaction site that is responsible for interacting with the t-SNARE domain, otherwise referred to as 'H3' mentioned previously, nSec1 interaction sites, and a linker region connecting Habc with H3 of syntaxin. The SNARE motif occurs at positions 191 to 259 and contains three features outlined as: a heterotetramer interface that acts as a polypeptide-binding site, the zero layer, which is defined as the polar interaction between the arginine of the R-SNARE VAMP2 and the glutamine of Q-SNAREs (i.e. syntaxin-1a in this case), and finally, a Munc18 interface polypeptide-binding site. VAMP-2's SNARE motif is similar to syntaxin-1a since it contains both a zero layer and a heterotetramer interface polypeptide-binding site, it does not however contain a Munc18 interface region. SNAP-25 contains two SNARE motifs flanking the sequence, one located in the N-terminal between 10-82 and the other in the C-terminal between 143-201.

Target membrane associated SNAREs syntaxin-1a and SNAP-25 both contain t-SNARE coiled-coil homologies, the latter comprising two such domains, while the vesicle-associated VAMP-2 contains a corresponding v-SNARE coiled-coil homology between 59-79, corroborating the output from COILS. Membrane-associated SNAREs syntaxin-1a and VAMP-2 also include a helical transmembrane anchor for type IV membranes, both located in the proteins' C-termini. Being a non-transmembrane protein, SNAP-25 instead contains a cys-rich region between 85-92 corresponding to the sequence CGLCVC PC. As aforesaid, these cysteines are the subject of palmitoylation, which tethers SNAP-25 to the membrane. The elucidated crystal structure for the SNARE complex, encompassing its helical membrane extension can be seen in **Figure 4.7**. Syntaxin-1a and VAMP-2 displayed helical continuity throughout their structures including the transmembrane and linker regions.

#### **4.1.3 SNARE coiled coil motif**

The SNARE protein family is distinguished by the distinctive evolutionarily conserved  $\alpha$ -helical motif of approximately 70 amino acids in length they all share in common. This can be observed in

**Figure 4.8**, where the SNARE motifs located within the database of identified and reviewed SNARE proteins (collated from Uniprot as of 2016), have been aligned and the conservation of residues has been predicted by PRALINE. The motifs for the synaptic proteins syntaxin-1a, VAMP-2, and SNAP-25, arrange in a parallel, heterotetrameric coiled coil. This complex is extremely stable, exhibiting thermal resistance to temperatures up to ~90 °C, as well as chemical resistance to a number of destructive methods including SDS-denaturation, protease digestion, and finally biological resistance to clostridial neurotoxin cleavage among many others (Hayashi *et al.* 1994). According to our PRALINE prediction, the SNAREs in our database sample contain relatively well-conserved hydrophobic residues in the *a* and *d* positions of their heptad repeats (**Figure 4.8**). This is judged by the consistency scores for *a* and *d* positions being ~6 and upwards, of particular importance is the highly conserved (consistency score 10) glutamine residue occupying the “central” *d* position in all Q-SNAREs (hence their classification as such), whilst the corresponding residue in the same position in the R-SNARE, VAMP-2, is accordingly arginine (**Figure 4.8**). These residues make up a polar, ionic layer at the core of the coiled coil.

#### 4.1.4 Post-translational Modifications

Lysines are a common site for glycation, a non-enzymatic modification process in which  $\epsilon$ -amino acid groups present on lysine residues react with carbonyl groups on reducing sugars. The final products of glycation reactions are AGEs (advanced glycation end products), which accumulate and cause long-term detrimental effects for proteins (Johansen *et al.* 2006). NetGlycate 1.0 (CBS) was employed to predict lysine  $\epsilon$ -amino acid group targets for glycation and the results are found in **Figure 4.9**. With its greater percentage composition of lysine, syntaxin-1a accordingly possessed a greater number of positive glycation sites whose potential exceeds the threshold. These sites were mostly concentrated towards the beginning of the sequence. This was to be expected since the authors of this tool have acknowledged that the majority of glycosylated lysines are typically found at the N-terminal. In contrast, VAMP-2 and SNAP-25b (isoform 1) were found to have only 2-3 positive sites found in the middle and towards the end of the sequence – a marked difference to syntaxin-1a. In statistical terms, glycation is more likely to affect longer proteins, and as it is a cumulative process, its effects will only be observed in proteins that possess longer biological half-lives. It is difficult to determine the lifetime of syntaxin-1a within the body, however we can estimate that according to its high instability index of 48.79 (Protparam, ExPASy), glycation is unlikely to have a significant effect on its mechanism of action.

The final targets of post-translational modification covered in this study are the residues that are subject to phosphorylation: serine, threonine, and tyrosine. NetPhos 3.1 (CBS) was the tool used to

predict the phosphorylation sites for the aforementioned residues within the synaptic proteins, and the results can be seen in **Figure 4.10**. Syntaxin-1a maintains the largest number of phosphorylation sites, which is found to be in accordance to its percentage composition compared to the other proteins. The majority of residues with a phosphorylation potential exceeding the threshold was found to be serines in all proteins, however syntaxin-1a holds a sizeable amount of threonine targets too. Within syntaxin-1a, the majority of phosphorylation targets were observed in the middle and towards the end of the sequence, starting at position ~55 and most densely populated until ~260, where ProtParam (ExpASy) predicts there to be a large number of helices and turns.

VAMP-2 exhibits the least phosphorylation sites with only three substantially surpassing the threshold with scores above 0.7 and one with a score of ~0.6, these are located at residues: Thr35 corresponding to the sequence RLQQTQAQV and predicted to be a target of DNAPK, ser61 corresponding to the sequence DQKLSELDD and predicted to be targeted by CKII, ser75 corresponding to QAGASQFET and predicted to be targeted by ATM, and Thr79 corresponding to SQFETSAAK which is predicted to be targeted by PKC.

A competing post-translational modification process called O-GlcNAcylation also targets serine and threonine residues. This describes the addition of an N-acetylglucosamine group to a serine or threonine via a O-glycosidic linkage. Since O-GlcNAcylation typically occurs at the same sites as recognised phosphorylation sites, it was appropriate to investigate the possibility of this in the SNARE proteins. YinOYang 1.2 (CBS) was the tool used to predict O-GlcNAcylated serine and threonine residues within syntaxin-1a, VAMP-2 and SNAP-25b (isoform 1), and the results can be viewed in **Figure 4.11**. Syntaxin-1a was not predicted to have any sites of significance and similarly SNAP-25 only yielded two sites with low probability scores. In contrast, VAMP-2 presented a number of sites with varying probability however; the two most notable sites were Thr7 and Thr35, with the latter referred to above as a predicted site of phosphorylation by DNAPK.

Sumoylation describes a type of post-translational modification similar to ubiquitination, where a Small Ubiquitin-like Modifier (SUMO) protein is covalently bound to other proteins to alter their function. The primary target residue for sumoylation is lysine which are most often located in consensus sites expressed as  $\Psi$ -K-x-D/E, where  $\Psi$  refers to a large hydrophobic residue, K is the lysine, x refers to any amino acid and D/E refer to the acidic residues glutamate and aspartate. Using the tool Sumoplot™ (Abgent), the presence or absence of sumoylation target sites were predicted for syntaxin-1a, VAMP-2 and SNAP-25. Only syntaxin-1a yielded a single high-probability, positive result, which was situated at residue Lys204 corresponding to group RHSEI IKLE NSIRE.



## 4.2 Discussion

The small flanking regions of disorder predicted in syntaxin-1a, between residues 9-20 and 280-288, have been recognised in a structure determination study using X-ray diffraction data by Misura *et al.*, which detected the presence of disordered regions between 1-26 and 249-267 (Misura *et al.* 2000), and an older study by Fernandez *et al.* using NMR spectroscopy, which in turn established the positions of these unstructured regions to be between 1-26 and 147-180 (Fernandez *et al.* 1998). Whilst there is some discrepancy between the prediction and the two literature reports regarding the latter region of disorder, all are in agreement regarding the former N-terminal region, which happens to be the location of the Habc domain.

It has long been observed that there is a correlation between the activation of protein kinases at the presynaptic membranes and transmitter release (Malenka *et al.* 1986) and since SNAREs are responsible for mediating the vesicular fusion that results in transmitter release, it is a realistic assumption that phosphorylation plays an important part in the biochemical pathway preceding these events.

Upon investigation into the experimentally determined phosphorylation sites within syntaxin-1a, it was found that positions Thr21 and Ser14 act as phosphorylation targets for casein kinase I (CKIa) and II (CKII) respectively. Located at the N-terminal, the authors of this study assert that the CKII phosphorylation enhances syntaxin-1a's ability to bind to synaptotagmin and the additional phosphorylation at Ser14 may serve to regulate this interaction. Furthermore, the product of Ser14 phosphorylation has also been shown to favour association with SNAP-25 (Dubois *et al.* 2002). Another study has determined Ser188 as another site of Ca<sup>2+</sup>-dependent phosphorylation, this time by death-associated protein (DAP), with the result being a substantial reduction in syntaxin-1a binding to the membrane fusion regulator Munc18-1 (Tian *et al.* 2003). Now, it is known that unlike VAMP-2 and SNAP-25 where the majority of the chain-length is involved in SNARE complex formation, only the C-terminal third of the cytoplasmic section of syntaxin-1a, where ser188 is located, is implicated in complex formation (Kee *et al.* 1995).

Elucidation of the N-terminal domain structure of syntaxin-1a revealed an independently folded domain between positions 27-146, containing a three-helix bundle named Habc since it consists of segments Ha, Hb and Hc (Fernandez *et al.* 1998). The boundary at which the second and third helices (Hb and Hc) meet displayed a highly conserved sequence found within plasma membrane syntaxins only and plays a critical role in regulating exocytosis. It does so by associating with the SNARE-forming segment, known as H3, in a closed configuration, and preventing syntaxin-1a from

assembling into the SNARE complex by making it unavailable to interact with VAMP-2 and SNAP-25 (**Figure 1.3**). Importantly, there is a flexible linker region located between the N-terminal domain and the C-terminal transmembrane region at positions 145-188, which becomes structured when syntaxin-1a is bound to Munc18-1 and so, is believed to play an imperative role in the formation of the open versus closed configuration (Margittai *et al.* 2003). Since this phosphorylation target is located at the end of the linker, it may be the stimulus driving the conformational changes observed in syntaxin-1a and as a result, influencing its binding to Munc18-1 (Tian *et al.* 2003). On another note, electron paramagnetic resonance spectroscopy data has demonstrated that Munc18-1 also regulates the open and closed configuration by binding and shifting the conformational equilibrium of H3 towards an increasingly ordered, folded state. It also demonstrates allosteric control at position 192 by inducing folding and expanding contact with H3/Habc, despite its distance from Munc18-1 (Dawidowski and Cafiso, 2013).

The predictions made for VAMP-2 are mostly in agreement with the literature, Braiman *et al.* for example, have shown that insulin-dependent serine phosphorylation occurs in VAMP-2 located on endocrine cells as a result of PKC (Braiman *et al.* 2001), and Nielander *et al.* have acknowledged the sequences GASQFE and QKLSELD as recognition motifs for CKII, and acknowledge the similarity of sequence RLQQTQ to a consensus motif RxxS\*x targeted by CaMKII (Nielander *et al.* 1995). It is possible that like syntaxin-1a, phosphorylation at these residues may influence docking and fusion. SNAP-25 has a sizeable number of phosphorylation sites, those with scores above 0.7 include: Ser28 located in ESLESTRRM and targeted by PKC, Ser97 in NKLKSSDAY also targeted by PKC, Ser98 in KLKSSDAYK also targeted by PKC, Tyr101 in SSDAYKKAW with no kinase specified, Thr138 located in IRRVTNDAR also unspecified kinase and finally Ser187 found within EKADSNKTR with no kinase specified again. In the literature, Shimazaki *et al.* confirms Ser187 to be the site of phosphorylation by PKC and noted that the residue was situated in proximity to both the botulinum type A and E neurotoxin cleavage sites (Shimazaki *et al.* 1996). Additionally, Thr138 was also recognised as a PKC-target in neuroendocrine cells (Hepp *et al.* 2002), and a PKA-target in synaptic plasma membranes (Risinger and Bennett, 1999).

None of the predicted O-glcNAcylation sites appear in the literature as experimentally determined targets, however there is a strong section of research devoted to determining the significance of O-GlcNAcylation in SNARE mediators such as synaptotagmin I (Syt I) and synapsin I (Syn I). In the case of Syt I, this process appears to be dependent on the coexpression of VAMP-2 in COS-7 cells, with Fukuda, the author of this particular study, discerning that the N-terminal of Syt I interacts with VAMP-2 alone and not when it is part of the SNARE complex (Fukuda, 2002). Whilst in the case of Syn I it was speculated that O-GlcNAcylation of its Thr87 residue might have a hand in regulating

both synaptic plasticity and localisation of Syn I at the synapses (Skorobogatko *et al.* 2014). These studies may prove of interest in the future due to their relevance to membrane fusion.

A recent report identified the Lys204 residue in syntaxin-1a as a potential SUMO substrate through the means of a bioinformatics tool and sought to validate this experimentally (Craig *et al.* 2015). Using site-directed mutagenesis they found that despite mutating Lys204 to an arginine, which cannot undergo sumoylation, syntaxin-1a still underwent sumoylation. Systematic mutation of the neighbouring lysines resulted in the discovery of at least three other lysine sumoylation targets located proximally to the transmembrane C-terminal domain of syntaxin-1a: Lys252, L253 and Lys256. When all three of these sites were mutated into arginine residues in a 3KR mutation, there was a marked increase in synaptic endocytosis (Schorova and Martin, 2016). Results from the binding assays used to determine the possible effect sumoylation might have on syntaxin-1a's protein interactions, revealed a significant decrease in sumoylated syntaxin-1a binding to SNAP-25 and VAMP-2 but no effect on its binding to Munc18-1 (Schorova and Martin, 2016). This would imply that firstly, sumoylation hinders SNARE assembly and secondly, because of Munc18-1's sustained association it promotes the syntaxin-1a's closed configuration.

## 5. SNARE database and systematic analysis of structural features which affect SNARE complex stability

### 5.1 Results

#### 5.1.1 SNARE database and selection of complexes for analysis – three complexes chosen due to their diverse melting temperatures ( $T_m$ )

A database of 63 SNARE complexes was built. It comprised of entries from a range of different organisms, with some PDB-backed and others mined from literature. One of the objectives was to discover what molecular interactions give rise to stability, and specificity, of SNARE complexes. To achieve this, we sought to focus on three complexes, of the 63 complexes collected, which presented diverse melting temperatures ( $T_m$ ) and hence, stabilities. To this end, we aimed to analyse them and discover what differences in the secondary structure of their SNARE motif gives rise to such diverse stabilities, and which common features unite them in their equally extraordinary specificity. The three complexes chosen were 1N7S (*Rattus norvegicus*), whose micro-SNARE truncated structure is said to have a  $T_m$  of 89 °C under native conditions, and under denaturing conditions this drops to 37 °C (Ernst and Brunger, 2003). 1L4A (*Loligo pealeii*) has a  $T_m$  of 73 °C under native conditions (Bracher *et al.* 2002).. Finally, 3B5N (*Saccharomyces cerevisiae*), which has a  $T_m$  of 55 °C under native conditions, and is non-SDS resistant (Strop *et al.* 2008). **Figure 4.1** shows the sequences of all three complexes and **section 1.6** outlines the background literature of each complex.

#### 5.1.2 Hydrophobic Interactions at positions *a* and *d* – segment -2 is uncharacteristically polar

The hydrophilicity of each position *a* and *d*, averaged over all four helices hence “average hydrophilicity”, for all three complexes can be seen in **Figure 5.1**. It is plotted against the segment, which denotes the position of the heptad repeat in the sequences. 1N7S is a complex that represents the standard mammalian neuronal SNARE, and as such, it acts as the baseline complex against which we compare the other complexes. If we look at this complex in isolation, as expected the ionic layer 0 is immediately seen to be highly hydrophilic among the much more hydrophobic pattern of heptad repeats.

The pre-SNARE section -10 to -8 are hydrophilic or at least weakly hydrophobic and indicate that 1N7S's SNARE motif begins at segment -7 and ends at 8, where hydrophobicity is consistent along the motif. Within the motif, the general trend appears to be that the magnitude of hydrophobicity increases on either end towards the ionic layer, such that the segments flanking layer 0 appear to have the highest hydrophobicity, and this decreases on either side towards the ends. The segments -1 and 1, immediately flanking the ionic layer 0 both show relatively high hydrophobicity of -4.18 to -4.15 respectively, indicating the potential for strong hydrophobic interactions nearby the otherwise seemingly disruptive ionic layer.

Segment -2 is the exception to this trend, it shows no relative hydrophobicity, with a value of 0.1, in 1N7S, as in 1L4A, however it is noticeably hydrophilic in 3B5N with a value of 0.75. This is deemed to be a result of the presence of Thr32 and Asn32 in SNAP-25 N-terminal, and VAMP respectively, whilst in 3B5N the nonpolar, large Met32 in SNAP-25 C-terminal has been replaced with a further small sized, polar Thr32 to make the heptad show overall hydrophilicity (please see **Figure 4.1** to view the amino acids in the sequences). Another key difference is the presence of an additional gap with relatively no hydrophobicity observed in 3B5N at segment 6, or position 60, which is not seen in the other two complexes. Upon inspection, it appears that at this position both 1N7S and 1L4A are occupied with Ala60 in syntaxin, SNAP-25 N- and C-termini, and Phe60 in VAMP, whilst in 3B5N, Sso1 is occupied with Gly60 and Sec9 H2 now contains Asn60 (**Figure 4.1** and **Figure 5.1**).

The most dramatic drop in hydrophobicity between the different complexes occurs at segment -5, where 1N7S is highly hydrophobic (-4.35), then 1L4A (-3.4), which is slightly less hydrophobic and finally 3B5N has the lowest value of -1.85. The reduction in hydrophobicity in 1N7S and 1L4A is due to the substitution of extremely hydrophobic Val22 to the slightly hydrophobic Cys22. Whilst in the case of 3B5N, it is due to the substitution of hydrophobic Ile22 (syntaxin) and Val22 (SNAP-25 C-terminal) in 1N7S, to less hydrophobic Met22 (Sso1) and polar Ser22 (Sec9) (**Figure 4.1** and **Figure 5.1**).

Towards the C-terminus, segments 4, 5 and 7 (positions 53, 57 and 64) also present differences in hydrophilicity in 3B5N compared to 1N7S. Both 1N7S and 1L4A have identical residues in segment 4, and their average hydrophobicity is slightly lower at -1.65 compared to 3B5N at -2.83. This has been attributed to the substitution of Asn53 in both 1N7S and 1L4A to the more hydrophobic nonpolar Leu53 in 3B5N. It is worth noting that the effect of this substitution has been slightly offset by the substitution of highly hydrophobic Ile53 in 1N7S and 1L4A for the less hydrophobic Met53 in 3B5N (**Figure 4.1** and **Figure 5.1**). The overall result however averages to indicate that 3B5N is much more strongly hydrophobic in segment 4 than the other two complexes. Segment 5 (position 57) in 3B5N substitutes Asn57 of SNAP-25 N-terminal in 1N7S, for Met57 in the corresponding

Sec9 H1 domain. This time the asparagine substitute contributes to the reduction in hydrophobicity of 3B5N. Finally, in the case of segment 7 (position 64), in 3B5N there is a net loss of an alanine in place of a valine (albeit across different helices) compared to 1N7S, which results in the increased hydrophobicity of position *d* in 3B5N (**Figure 4.1** and **Figure 5.1**).

### **5.1.3 Residue volumes – syntaxin and SNAP-25 N-terminal show the most complementarity of all the *t*-SNARE combinations**

The average residue volumes of positions *a* and *d* in all three complexes, as well as the individual residue volumes of positions *a* and *d* in all four helices of 1N7S alone are presented in **Figure 5.2a** and **Figure 5.2b** respectively. The average residue volume does not vary drastically, and instead maintains a relatively consistent value. All three complexes peak between segments -1 and 2, and on either side of this peak the segments -3, -2, and 3 to 6 all show relatively lower volumes in comparison. In most cases the *d* positions have larger residue volumes than *a*, segments -3, 3 and 7 are exceptions since here all three complexes *d* positions are lower than *a* positions. General comparison between the three complexes shows that 1N7S and 1L4A are the most similar, whilst 3B5N differs the most from both. The most important observation is that in most cases there is a difference in residue volumes between the corresponding *a* and *d* positions, supporting the hypothesis that their “knobs-into-holes”-style complementary interlocking is one contributing factor to the specificity observed with SNAREs. Complementarity here, can be defined as a type of “inverse” relationship between two chains, where when one chain experiences a drop, at the same position another might experience a rise, we choose to describe this as the two chains being complementary at the position of interest. They are complementary because their residue volumes appear to accommodate one another at the same area, allowing the two to interlock.

Let us consider the standard SNARE complex 1N7S, **Figure 5.2b** focuses on the individual chains, and is particularly helpful in visualising the presence or absence of complementarity between them. It appears that at the N-terminal, all four helices have distinctly different residue volumes that allow us to evaluate their relative complementarity. This excludes the C-terminals extending from segment 3 onwards, where the graph traces become noisy and more difficult to interpret. The section comprising of segments -1 to 2 in **Figure 5.2a** shows all four helices with very similar large residue volumes with no evidence of complementarity, suggesting that this could be a point of weakness in the complex. Pre-SNARE segment -8 shows the following pairs having almost identical residue volumes: syntaxin with 25C, and 25N with VAMP. These pairs are complementary to one another since the former have very large volumes and the latter have much smaller volumes.

Similarly at segment -3, syntaxin and 25N show the substantial amount of complementarity, with syntaxin's residue volume approaching  $\sim 190 \text{ \AA}^3$ , and 25N more than half that at  $\sim 60 \text{ \AA}^3$ .

There are three different scenarios to explore in establishing the hierarchy of complex formation, these are based on the literature's inclination towards an initial t-SNARE complex, and these are: syntaxin binds to 25N first, 25N and 25C bind first, or syntaxin and 25C bind first. **Figures 5.2b(i)-(iii)** depicts these three scenarios using isolated t-SNARE traces. It becomes clearer that in terms of residue volumes complementarity, syntaxin and 25N share more complementarity, especially at the N-terminal where they are predicted to begin their association. Specifically, in **Figure 5.2b(i)** there is an extended section starting from pre-SNARE segment -9, reaching towards the more centrally located segment -2. From -2 onwards, the complementarity between the corresponding segments is not as well defined. The other two scenarios however are less convincing, though 25N and 25C shows the most promise of the two scenarios, of binding together first. **Figure 5.2b(iii)** depicts the residue volume traces for 25N and 25C, and a similar section of N-terminally located complementarity can be observed between segments -8 and -6. The last scenario, syntaxin and 25C seen in **Figure 5.2b(ii)**, does not contain an extended section, however it does have two separate small sections of complementarity in it's N-terminal, the first is at segment -5, and the second is between segments -3 and -2.

#### **5.1.4 Buried polar residues at positions *a* and *d* – presence of buried polar residues in hydrophobic hotspots may influence specificity of complex assembly**

There are a number of buried polar residues present in the *a* and *d* layers of the SNARE motif in all three SNARE proteins. These were identified in the 1N7S complex and can be seen highlighted in red typeface in **Figure 5.3**. All centrally located buried polar residues appear in the *d* positions, whilst the flanking buried polar residues at layers -7 and 7 are situated in *a* positions. All buried polar residues were visualised using PyMOL in order to ascertain distances, and subsequently attempt to establish which ones have the potential to form polar contacts. Four such residues presented some potential for polar contact with a neighbouring polar residue, these were Thr29 in 25N, Gln226 in Syn, Gln53 in 25N, Gln174 in 25C, Asn188 in 25C and Thr251 in Syn. All, with the exception of Asn188 and one contact made by Gln174, have contact distances that fall within the traditionally accepted cut-off distance for hydrogen bonds of  $2.5 \text{ \AA}$  (Buck and Karplus, 2001).

#### **5.1.5 Long-range ionic attractions and interhelical salt bridges at positions *bc* and *efg* – evidence supporting hypothesis of syntaxin-25N initial association in rat SNARE complex**

Since *bc* and *efg* are traditionally polar, and often charged especially in the case of *e* and *g*, it follows that theoretical pI, and therefore the charge of those segments, are the most fundamental properties to investigate. SNARE complex formation is initiated at the N-termini of the proteins, so one of the interests of this review is to get an indication as to which helices participate in long-distance attractive forces, thus indicating the hierarchy of binding. Furthermore, the study of these properties in each complex will allow us to gain an understanding of the number and potentially even the strength of interhelical salt bridges along the SNARE motif.

#### *5.1.5.1 Basic N-terminal segments -11 and -7 indicate the high likelihood of syntaxin and 25N participating in long-distance ionic attractions*

The theoretical pI of each *bc* and *efg* segment along the SNARE motif in each helix was calculated using ProtParam (ExPASy) and the values were plotted against the heptad layer in **Figure 5.4**. It appears that the majority of the polar segments in the different helices of each complex have a baseline theoretical pI of ~4, and at no point do any of the segments decrease below ~3.5. It is also possible to predict the basic participants of the salt bridges by looking for the few, very high pI segments. In the *bc* segments of 1N7S, we would expect segments -11, -9, -3, and -7 to contribute basic residues for potential salt bridges, most of which are predicted to come from the SNAP-25 N-terminal. Of the *efg* segments, heptads -8, -4, 0, 4, 6 and 8 all contain very basic pI residues, which can all potentially form salt bridges as well. Predicting the acidic counterpart to these basic residues is a more difficult matter since as aforementioned, most residues remain at a baseline pI of ~4. This means there are too many potential partners, which makes accurate interpretation impossibility without also taking distance between the residues into account.

At the N-terminal (pre-SNARE segments included), where it has been established that assembly is initiated, syntaxin and 25N, and VAMP to a lesser extent, at segments -11 and -7 are considerably basic. Our hypothesis states that syntaxin and 25N initially associate as a result of long-distance ionic attraction, however this data neither fully supports nor contradicts the hypothesis since we cannot pin-point interactions with certainty. Nevertheless, it is an indication of the likelihood of long-distance attractions forming at these positions with syntaxin and 25N being one half of the ionic pair.

Comparing the basic pI residues in 1N7S with the other complexes, the most (approximate) conservation can be seen in 1L4A where *bc* segments -7, -3 and 7 all remain highly basic, and *efg* segments -8, -4, 0, 6 and 8 also retain their heights. The latter of these, segment 8, shows a reversal in pI between 25N and 25C from complex 1N7S to 1L4A. Specifically, at this position in 1N7S, 25N is slightly positive (pI = 8.22), whilst 25C is slightly negative (pI = 5.52), whereas in



1L4A, they are 5.99 and 8.75 respectively. If there were intrahelical interaction within 1N7S's 25N and 25C chains between segments 7 and 8, then in 1L4A, the one in 25C would be converted to an interhelical interaction between it and 25N, and the one in 25N would no longer exist since both segments 25N pIs are negative and would repel. 3B5N echoes 1N7S in that the intrahelical salt bridge in 25C at these positions is maintained, but equally, like 1L4A, the one in 25N is voided because both are negative and would experience repulsion.

3B5N presents the most differences to 1N7S and 1L4A, including that of theoretical pI of polar segment. Of the basic segments in 1N7S, only *bc* segment -7 retains its higher-than-average pI, though still with some differences such as a reduction in pI of Sec9 H1 from 12 in 1N7S to 10 in 3B5N. Shifting perspective towards the *efg* segment, there appears to be a few more basic pI segments than in 1N7S and 1L4A, and among these there is more variety of helices compared to the other structures where the majority of basic pIs come from the SNAP-25 C-terminal helix. In 3B5N, almost every single segment contains a highly basic position from one of the four chains.

#### 5.1.5.2 N-terminal of rat neuronal SNARE complex shows a majority in syntaxin-25N salt bridges

Salt bridge predictions using the software VMD and PyMOL were carried out with an oxygen-nitrogen cut-off distance of 4.0 Å, to complement the data from our tool. **Figure 5.5** shows all of the potential interhelical salt bridges that can be formed between the charged residues of the individual helices of each of the SNARE complexes, 1N7S, 1L4A and 3B5N. This figure can be used to validate or disprove any of the assumptions made based on **Figures 5.4**. 1N7S has potentially 13 interhelical salt bridges along the motif, 1L4A has 10, and 3B5N has 14. Starting from the N-terminal towards the ionic layer 1N7S has approximately 6 interhelical salt bridges, of which 4 are comprised of t-SNAREs alone, and 3 are comprised of syntaxin and SNAP-25 N-terminal. This is convincing evidence supporting the scenario that syntaxin initially associates with the N-terminal of SNAP-25 before SNAP-25 C-terminal. It may however, be unique to the rat SNARE, as a similar phenomenon is not observed in either the squid or yeast SNAREs.

In the case of 1L4A, there are 8 potential interhelical salt bridges pre-ionic layer, and of these 5 take place between t-SNAREs partners alone. There is a bridge between syntaxin and SNAP-25 C-terminal at pre-SNARE positions 11 and 8 respectively, and within the N-terminal of the complex at positions 17-19 there is a bridge between syntaxin and SNAP-25 N-terminal. Likewise, in 3B5N, there are 9 potential interhelical salt bridges pre-ionic layer, and of these 5 are comprised of t-SNAREs alone, and yet of these, each one could support or contradict any of the three scenarios

laid out since three support the two termini initially associating, one pre-SNARE bridge supports syntaxin and 25C, and one closer to the ionic layer supports syntaxin and 25N scenario.

A large majority of the interhelical salt bridges examined contained arginine as the positively charged participant. 1N7S shows the most variety in positively charged salt bridge participants (**Figure 5.5a**), with 4 lysines compared to 8 arginines and even 1 histidine residue appearing to contribute a salt bridge (though this is strongly dependent on the pKa of the solvent). 1L4A and 3B5N, meanwhile, show a stronger bias for arginine, with 1L4A salt bridges containing 8 arginines compared to only one lysine (**Figure 5.5c**), and 3B5N containing 9 arginines compared to 5 lysines (**Figure 5.5e**). It is worth repeating that the guanidinium of arginine can form bidentate side-on or end-on interactions with carboxylates, and the resulting 6-membered ring of atoms is predicted to be in the lowest energy state. Looking at the tables of salt bridges in each complex (**Figure 5.5**), it is clear that of the 8 arginines participating in salt bridges in 1N7S, 7 of these form bidentate interactions. Likewise, 3B5N also leans towards bidentate interactions, with 8 of the 9 arginine salt bridge participants forming side-on or end-on interactions. On the other hand, 1L4A shows a strong bias towards monodentate interactions since of the 8 arginines participating in salt bridges, 6 assuredly form backside interactions.

There are a handful of conserved salt bridges that appear in at least one other structure. Only two salt bridges are conserved between all three structures, the first occurs between 25C Glu145 and 25N Arg30 in 1N7S, 25C Asp152 and 25N Arg33 in 1L4A, and 25C Glu593 and 25N Arg445 in 3B5N, the second occurs between Syn Glu211 and VAMP Arg47 in 1N7S, Syn Glu214 and VAMP Arg56 in 1L4A, and Syn Glu209 and VAMP Arg44 in 3B5N. Due to the substitution of glutamate for an aspartate in the first conserved salt bridge in 1L4A, it takes on a backside conformation, rather than the bidentate side-on interaction observed in 1N7S as seen in **Figure 5.6a**.

In the context of the second conserved salt bridge, in 1N7S, it is a backside interaction at the upper bounds of salt bridge interaction distance, with a value of 3.8 Å (**Figure 5.6c**). In 1L4A, the interaction also takes on a backside conformation, following what is shaping up to be a trend in 1L4A whose arginines appear to preferentially form backside interactions. The corresponding salt bridge in 3B5N presents two possibilities, both monodentate in nature, the first is a 2.6 Å backside interaction to arginine's terminal amino group, and the second scenario is a 2.9 Å salt bridge with nitrogen within the carbon backbone of arginine. The latter requires the arginine be in its protonated tautomer form (i.e.  $sp^2$  R-C=**NH**<sup>+</sup>-(NH<sub>2</sub>)<sub>2</sub>), which is likely to exist as a small population in equilibrium with the majority canonical structure. A similar situation has been observed in 1N7S, where the salt bridge between 25N Glu75 and 25C Arg198 appears to occur between the protonated tautomer form of arginine to allow the nitrogen with its carbon backbone to bond to glutamate's carboxylate

group. The distance between these two groups is 2.8 Å, and there appears to be reasonably good atom overlap that would facilitate salt bridge formation, whereas the distance between the carboxylate and arginine's terminal amino group is at the upper bounds of salt bridge interaction with a value of 3.9 Å (**Figure 5.6h**).

Between the complexes 1N7S and 1L4A, there are two other salt bridges excluding that described above. These are found in the following locations: 25N Arg31 and Syn Glu206 in 1N7S, and its correspondent Syn Glu209 and 25N Arg34 in 1L4A, and Syn Arg232 and VAMP Asp64 in 1N7S, and its correspondent VAMP Asp73 and Syn Arg235 in 1L4A. Despite the fact that these residues are well conserved (i.e. no substitutions have taken place), and they are in relatively the same positions with the same spacing, there are some subtle differences between them. Take the latter salt bridge between syntaxin and VAMP, in 1N7S Arg232 forms a side-on bidentate interaction with aspartate (**Figure 5.6e**), whereas in 1L4A, Arg235 forms a backside monodentate interaction, which is likely to be less stable due to the lack of chelate effect. The former salt bridge, between syntaxin and SNAP-25 N-terminal, is straightforward in the case of 1N7S where it is clearly observed to be a side-on bidentate interaction between Glu206 and Arg31 (**Figure 5.6b**), whereas for 1L4A there two possibilities, it could either form a 2.9 Å backside interaction, or a 3.1/3.2 Å side-on interaction (**Figure 5.6i**). It is presumed that the favourable energetics of the chelation in the side-on interaction will effectively “win” out of the two. On the other hand, it could very well be that the two interactions do not compete but instead co-operate in stabilising each other. The only other salt bridge conserved between 1N7S and 3B5N can be found between 25C Asp620 and VAMP Lys49 near the ionic layer. In 1N7S, there are two possible distances that can be used to form this salt bridge, these are 2.9 Å and 3.0 Å. 1L4A has a similar salt bridge interaction between aspartate and lysine within the same region, however it occurs between SNAP-25 N-terminal and VAMP instead.

There appears to be a high density of salt bridges between layers 0 and 2, corresponding to positions 42-49 on our scale, in the complex 1N7S. Of particular interest are what appear to be two basic residues competing for the same glutamate to form a salt bridge between the two termini of SNAP-25: 25C Arg180 competes with 25C Lys184 for Glu61 (**Figure 5.6g**). It is likely that due to the energetic favourability of the bidentate side-on interaction, arginine preferentially forms the salt bridge, and lysine merely forms a hydrogen bond with the carboxylate, and thus they would reinforce one another rather than compete.

## 5.2 Discussion

Comparing rat, squid and yeast SNAREs, we expected similarities in the hydrophilicity of the *a* and *d* positions along the SNARE motif since the hydrophobic repeat is a central defining feature they should all have in common. It has previously been established that the tightest packing in the SNARE complex occurs at the N-terminus (Margittai *et al.* 2001), and as expected, the N-terminal regions were more complementary in volume than the rest of the chain.

Segment -2 displayed hydrophilicity counter to the hydrophobic heptad repeat, which defines the SNARE motif. Particular attention was paid to 3B5N, which displayed uncharacteristically strong hydrophilicity due to the presence of the small, polar Thr32 in the Sec9 H2 domain. The effect of this size difference between Thr32 and its adjacent residues is clear from the analysis of residue volumes data for 3B5N. The latter is noticeably lower compared to 1N7S or 1L4A. The gap left by smaller side-chain of Thr32 is an access point for water, thus creating a water-filled cavity that is subsequently able to form hydrogen-bonds with the two Thr32 residues in the different H1 and H2 domains of Sec9 (Strop *et al.* 2008). This, coupled with its close proximity to the ionic layer, is expected, and proposed by the original authors (Strop *et al.* 2008), to have a large destabilising effect on the complex. We believe it to be one of the chief reasons for the lower thermal stability of 3B5N compared to 1N7S and 1L4A. It thus appears that segment -2 has a minimal contribution to the stability of the core if at all, and in fact our evidence shows that it may act to destabilise it due to the absence of strong hydrophobic interactions at this segment and between itself and its neighbouring segments within the SNARE complex. It is possible that segment -2 acts to improve specificity of the complex assembly, in a similar capacity to the ionic layer.

The hydrophobicity drops in segments -5 and -4 were caused by alterations that respectively replaced Ile22 and Val25 in 1N7S, with Ser22 and Thr25 in 3B5N. These changes presented not just polarity differences but also disturbances in the packing effect. This is alluded to in the residue volumes data shown in **Figure 5.2a**, where segments -5 and -4 demonstrate a marked reduction in the residue volumes in 3B5N compared to 1N7S and 1L4A. The substitutions of nonpolar residues Ile22 and Val25 to polar residues Ser22 and Thr25 respectively, are assumed to partially contribute to the loss of thermal stability observed in the yeast complex according to the authors of the PDB entry 3B5N (Strop *et al.* 2008). These two residues face each other in the core and are capable of hydrogen-bonding with any water molecules that may potentially come into contact with the core. A similar reduction in hydrophobicity was also observed in 1L4A compared to 1N7S, which was attributed to a Val22 to Cys22 substitution, The effect of this can also be seen in the residue volumes data, where position 22 shows a small reduction in volume in 1L4A compared to 1N7S. It is therefore reasonable to conclude that Asn60 must be the main contribution to the increase in hydrophilicity detected in 3B5N's drop in hydrophobicity. Another change introduced with the substitution of Ala60 to Asn60 in Sec9 H2 domain, is that the longer side-chain presents some

conformational strain. The prospect of the C $\alpha$ -C $\beta$  bond potentially clashing with the neighbouring  $\alpha$ -helix means that the asparagine has a limited number of conformations it can assume, two of which appear to result in loose-packing and conformational variability (Strop *et al.* 2008).

Segment 4 of 3B5N substitutes 1N7S's hydrophobic Leu53 in SNAP-25 C-terminal, for the more polar hydrophilic Asn53 in Sec9 H2 domain. Moreover, Ile53 has been replaced for the larger Met53, whose greater volume compared to asparagine, combined with two bulky isobutyl groups of the two leucines in adjacent chains could potentially result in these residues spacing out to avoid conformational strain, which may lead to weaker packing towards the C-terminus. Indeed, the residue volume of 53d is shown to be considerably larger than the surrounding 4,3-heptad positions in 3B5N.

Analysis of the overall trends in the residue volume of positions *a* and *d*, in all three complexes reveals little difference along the motif. This conservation of volume was to be expected as substantial differences in volume would likely introduce disorder and gaps into what should otherwise be a very regular and well-packed hydrophobic core. Like the hydrophobicity pattern, in 1N7S and 1L4A starting from position 15a moving towards the ionic layer 39d, most *a* positions have slightly larger residue volumes than their counterpart position *d*. One of the exceptions to this in all three complexes is position 29a whose residue volume noticeably drops due to the presence of Gly29a. Though surrounded by the adjacent bulkier side-chains of Phe29a, and Met29a, there is still a sizeable gap in the core.

Based on these estimates, it's clear that the strongest of these buried hydrogen bonds are present in the ionic layer, whose polar contact distances are all <2.0 Å with the exception of one contact made by Gln174. The two polar contacts at the proximal ends of the SNARE motif featuring buried polar residues Thr29 in 25N and Thr251 in Syn (highlighted in blue and green respectively) are also predicted to be exceptionally strong with distances of ~2.0/2.1 Å. The weakest polar interaction, and therefore expected to have the least influence on the specificity of coiled coil "zippering". Thus, we have identified sites in the rat SNARE complex that potentially play an important role in modulating the specificity of SNARE assembly, and are worth investigating further with mutagenesis studies.

Since it is understood that association of the SNARE proteins begins at their N-termini, an examination of the salt bridges occurring at the pre-SNARE, and N-terminal periphery (start of SNARE motif leading up to heptad 0) would reveal a preference towards one of the three t-SNARE binding scenarios hypothesised. This is because it is expected that the ionic interactions would be the initial long-distance attraction that would provoke complex assembly. What is clear from the

results, is that there is no conclusive answer to this hypothesis, and in fact there is likely not a single universal mechanism of assembly for all complexes across species either based on the diversity of salt bridges observed in the rat, squid and yeast complexes investigated here. 1N7S appears to conform to the hypothesis in that the majority of salt bridges in the pre-SNARE/N-terminal region are between syntaxin and 25N, whereas 1L4A shows conflict between the two scenarios of syntaxin and 25N initially associating versus the two SNAP-25 termini associating. 3B5N supports the latter, with 3 of 5 salt bridges between t-SNAREs being between the two termini of SNAP-25.

There was a strong preference for bidentate interactions in the arginine-containing salt bridges of both 1N7S and 3B5N, but notably this was not so for 1L4A. It is odd that the geometries of all the arginine-containing ionic residue pairs in 1L4A did not support bidentate conformation, however no answer has been reached that can explain such a behavioural pattern. All three complexes contain bifurcated salt bridges, though to different extents. This conformation has been marked out as having a distinct topology and geometry suited to protein surfaces and interfaces. Elegantly described as “molecular clips”, they feature at large surface contours, facilitating the interaction of such protein interfaces (Basu and Mukharjee, 2017). As with bidentate interactions, bifurcate interactions benefit from additional stabilisation due to delocalisation of the hydrogen’s partial positive charge onto the carboxyl’s oxygen atoms (Torshin *et al.* 2002). The yeast SNARE, 3B5N, definitively contains 2 such bifurcated salt bridges, whereas 1L4A and 1N7S both contain one and two bifurcated salt bridges respectively, of which at least one is questionable in nature due to the possibility of other competing conformations that may take priority. It is clear from the lack of bifurcated salt bridge conformations observed, that it is not a contributing factor to the stability, or the ability of SNARE proteins to recognise one another.

Turning our attention to the spacings in these interhelical salt bridges, if we consider the standard 1N7S, it appears that pre- and post-SNARE motif appear to host bridges with larger spacings of  $i$  to  $i+5$  and the more common  $i$  to  $i+6$ , however, the SNARE motif itself contains a majority of  $i$  to  $i+2$  spacings. This is to be expected, as it has been previously established that  $i$  to  $i+2$  spacings are the most frequently observed, and therefore the most important interaction in parallel tetramers (Meier *et al.* 2010). Squid and yeast SNAREs 1L4A and 3B5N contrastingly host a range of different sizes of spacings not just in the pre- and post-motif sections, but in the motif itself too, and moreover it appears that this irregularity of spacing is proportional to the instability of the complex with the most unstable complex 3B5N accommodating 5 such large-spaced salt bridges in its’ motif alone, compared to 1L4A which only contains 1, and 1N7S which contains none. This statement must not be misconstrued as a cause-and-effect assumption that the larger the spacing, the weaker the salt bridge. As the distances can attest, the “size” of a spacing has little bearing on the distance between the two residues due to the nature of helical turn.

## 6. Rational design of thermosensitive SNARE-based peptides

**Note:** where abbreviations of peptides and complexes are seen for e.g. “B04” a helpful tool for reference would be **Table 4**, which outlines peptide abbreviations, sequences and the complexes they take part in. An additional reference tool is the Index of Abbreviations at the start of the thesis. Search for the abbreviation to find a description of the complex and the mutant peptides it contains.

### 6.1 Results

**6.1.1 SNARE stability studies** – SNARE complex motif N-terminal up to position 39 has greatest conservation of volume, and truncating VAMP results in lower thermal stability according to SRCD thermal melt studies

**Figure 6.1** depicts the Synchrotron Radiation Circular Dichroism (SRCD) of a range of neuronal SNARE complexes with varying lengths of VAMP (all other SNARE proteins are full length). It can be seen that VAMP34 and 45 show no difference in melting temperature (72°C). Contrastingly, VAMP25 and 27 have melting temperatures closer to physiological range, between 49-57°C, and there is a marked difference between the two. Therefore, within the range of VAMP lengths measured here, VAMP27 can be nominated the threshold length after which any further increase has negligible effect on the melting temperature. For improvement, VAMP27 is the most ideal length, and so we decided to use it as the template to which, we would make modifications that we expect to improve the thermal stability.

In order to understand the concept behind our rational design methodology for the residue volume study, some terminology must first be clarified here. Total residue volume of (hydrophobic) segments (TRV), is used to describe the total volume of residues within each segment. A segment defines a “layer” of a SNARE complex, and will contain four amino acids – one each of the SNARE protein components (syntaxin, SNAP-25 N-terminal, SNAP-25 C-terminal and VAMP). An illustration of how TRV is calculated can be seen in **Figure 6.2e-f**. Using the SNARE protein structure compactness analysis tool, the TRV of each segment in a rat neuronal SNARE complex (PDB: 1N7S) was calculated. An average ( $\mu$  – red central line in **Figure 6.2a-c**), and 1x and 2x standard deviations ( $\sigma$  – solid green/purple lines), were calculated across all TRVs from segment 15 to 70.

The standard deviation of TRV values, based on these 16 TRV values corresponding to specific hydrophobic segments of the assembled SNARE complex, represent how much individual TRV values differ from the mean value for the group. In terms of SNARE structure, it allows the user to

gauge how uneven the lateral dimension of the existing assembled SNARE coiled-coil is *in vivo*. However, the same value should in theory be predicted based on the known deviations of the volumes of individual amino acid side chains, which contribute to the assembled segments. Therefore a predicted deviation ( $\Delta\sigma$  – dashed green/purple lines) was calculated to represent a combination of deviations in each variable (i.e. each chain in the complex).

In order to achieve this, the four contributing polypeptide helices have to be considered as four independent populations of amino acids, where these amino acids are the relevant 16 residues of syntaxin, SNAP-25 N- and C-terminal, and VAMP. The mean predicted TRV is mathematically the same average calculated using four individual standard deviations for each individual chain (group of 16 amino acids). These four standard deviation values are then combined in **equation (1)**.

$$\Delta\sigma \text{ TRV} = \sqrt{(\sigma \text{ TRV syn})^2 + (\sigma \text{ TRV 25N})^2 + (\sigma \text{ TRV 25C})^2 + (\sigma \text{ TRV brev})^2} \quad (1)$$

Two outcomes might be expected. If the distribution of amino acids along the 16 positions of any given helix was truly random, then this “predicted” standard deviation for predicted TRVs would be identical to that calculated earlier from the known amino acid combinations in native SNAREs ( $\sigma$  – solid green/purple lines in **Figure 6.2a-c**).

Interestingly, the predicted standard deviation calculated using Eq. 1 yielded values larger than the standard deviation of the existing hydrophobic layers from existing native SNARE structures (**Figure 6.2a**). This means that if the hydrophobic residues in each of the 16 positions of the four helices (syntaxin, SNAP-25 N- and C-terminals and VAMP) were distributed randomly within the relevant four helices, the resulting coiled coil lateral dimensions would vary more than they do in native SNAREs. This means that the existing order of hydrophobic residues in each of the 16 positions of the four helices is not random, but optimised to reduce the variability of the lateral dimension of the assembled SNARE complex. This is presumably to improve complex stability. Specifically, we have hypothesised earlier that the regularity in volume of the coiled coil, and specifically the tightness of fit in the hydrophobic segments, is one of the driving factors conferring thermal stability to the SNARE complex. Our investigation clearer shows that deviations from the average TRV along the length of the complex are lower than what would be expected if the existing contributing amino acids were reshuffled within the relevant helices. The latter would support our hypothesis that lower variability of TRV volumes correlates with tighter assembly.

To further experimentally provide this conclusion we have found such areas of TRV deviation, and attempted to reduce the deviations in mean TRV by substituting amino acids, returning a profile



closer to the overall calculated average. Moreover, another approach we have taken is to introduce deviation in one component chain, and then “compensate” for it by mutating residues in the corresponding positions in another component chain.

#### *6.1.1.1 Stability Improvement study – rational design of peptides Brev2-12\_27ST, Brev2-32\_27ST, and Brev2-14\_27ST*

In the context of this experiment, “improvement” means we intend to make modifications that increase the thermal stability of the complex by improving the SNARE coiled coil packing. SNARE proteins are highly conserved structurally and functionally between animals, fungi and plants where their ability to self-assemble into highly stable complexes drive membrane fusion. Improving stability of the complex perfected by evolution over hundreds of millions of years is a challenging task. Nevertheless, if successful even to a limited degree, it should prove our hypothesis of TRV conservation as a major contributor to SNARE stability. To be able to detect any such improvement experimentally we first had to decide what length of SNARE complex would be appropriate to use, and specifically, had a low enough melting temperature that our improvements can be conclusively observed. The SNARE protein structure compactness analysis tool was used to conduct an initial analysis of a native SNARE complex (based on PDB 1N7S), and this can be seen in **Figure 6.3a**. We used the average and standard deviation as indicators of “ideal” volumes. For example, anything within the first standard deviation would be considered ideal since it constitutes 68% of the population and falls in line with the average, whereas anything within the second deviation, which represents 95% of the population, would not be ideal as it is further away from the average.

Based on the results for the native sequence, three positions (22, 29, and 36) in the TRV (designated “complex”, with a blue line in **Figure 6.3**) stand out as potential sites for improvement. Starting with position 29, this datum point sits on the lower second deviation ( $\mu-2\sigma$ ), which upon inspection is most likely due to the large discrepancy in residue volumes of phenylalanine ( $189.9 \text{ \AA}^3$ ) in syntaxin, and glycine ( $60.1 \text{ \AA}^3$ ) and alanine ( $88.6 \text{ \AA}^3$ ) in SNAP-25N and SNAP-25C respectively. At  $162.9 \text{ \AA}^3$ , the methionine in VAMP is comparably larger than the amino acids in SNAP-25, however according to the residue volume profile, it is not large enough to bridge the gap with phenylalanine. A suitable substitution for the methionine would be a second phenylalanine, which would increase the overall TRV of the segment and raise it closer to the lower first deviation (**Figure 6.3b**). The mutated VAMP peptide engineered for this purpose is Brev2-13\_27ST. Another two positions 22 and 36 are at the limit of the upper first deviation, and their segments share a very similar composition of leucines, isoleucines, and valines. In both positions, a valine is featured in the VAMP chain. In order to reduce the TRV at these positions and make it more similar to the average

TRV, valines may be substituted by alanines (**Figure 6.3c**). The mutant VAMP peptide for this purpose is Brev2-12\_27ST. Finally, the last complex to be explored is a combination of all three mutations (**Figure 6.3d**), referred to as Brev2-14\_27ST, where it is clear to see that the overall TRV is much more regular and closer to the average than the native sequence.

#### *6.1.1.2 Stability Compensation study – rational design of peptides Brev2-15\_34ST, and Synt1-03\_34ST*

The aim of this challenge is to investigate whether it is possible to intentionally destabilise the complex by mutating key sites in VAMP, then recover stability by mutating the corresponding positions in syntaxin with residues that compensate for the change in TRV residue volume. The task of rescuing stability of the modified complex is as challenging as that of improving stability of the native complex. If successful, this experiment should prove unequivocally the TRV volume conservation strategy. The experimental approach to rescuing stability aims to rescue TRV volumes to near the original values, and the expectation is that the modified complex will also return to approximately the same original stability. Based on the SNARE complex melting data in the CD analyses of SNAREs with different truncated VAMP polypeptides, Brev2-04\_34 (B04) VAMP peptide emerged as the most suitable (see **Table 4**). The complex, C04, formed using this version of VAMP would be within the measurable range of  $T_m$ , and would allow us to observe a very large drop in melting temperature, and potentially  $T_m$  recovery, making it a good candidate peptide length.

Five hydrophobic positions were identified in B04 containing amino acid residues with substantially different sizes to the corresponding residues in syntaxin. These were Thr18, Val22, Val25, Met29, and Asn32. They were mutated, in the VAMP construct, to match the same corresponding residues in syntaxin Leu18, Ile22, Leu25, Phe29, and Met32 respectively. Although the number of possible substitutions is huge, the choice of syntaxin amino acids guarantees the most drastic change to the size complementarity principle. The presence of two identical larger volume residues facing each other in opposite chains in each of the five segments is expected to prevent efficient assembly by introducing steric hindrance, ultimately destabilising the complex. The presence of two identical smaller volume residues facing each other in opposite chains in each of the five segments is expected to further destabilise any assembled complexes. This mutated VAMP is referred to as Brev2-15\_34ST. The expected effect of using Brev2-15\_34ST instead of the native sequence is a substantial drop in  $T_m$ . The difference made to Brev2-04\_34 is illustrated in **Figure 6.4**. To rescue stability of the destabilised complex, the syntaxin protein should be modified. To achieve precise recovery of the changed TRV volumes, and therefore regaining the same stability, changes to syntaxin at the corresponding positions should mirror those carried out in VAMP. The best set of

amino acids would therefore be the amino acids that originally occupied the five relevant positions in Brev2-04\_34. The mutations are: Leu18 to Thr, Ile22 to Val, Phe29 to Met, Met32 to Asn (**Figure 6.4**). The predicted TRV of the mutated syntaxin/mutated VAMP complex should match that of the native proteins (**Figure 6.4f**). If the mutated syntaxin, Synt1-03\_34ST, does indeed compensate for the steric hindrance introduced by the mutated VAMP, it would provide decisive evidence that it is not the “sequence” but TRVs which affect assembly, and stability of the SNARE complex. That would also provide means to modify thermal stability of SNARE protein assemblies.

### **6.1.2 Ionic Interactions: Selection of SNARE constituent, sequence length and modifications for peptide candidates**

#### *6.2.1.1 pH-sensitivity study challenge – rational design of peptides Synt1-02\_34PH, Brev2-06\_34PH, and Brev2-07\_27PH*

The aim of this study is to explore the possibility of introducing pH-sensitivity to the SNARE complex by mutating key positively charged residues, which have been predicted based on 3D structure to participate in salt bridges (**Figure 38a-b**). Histidine amino acids have  $pI \sim 6$  and therefore would display substantial pH dependence. Therefore, histidine is a convenient pH-sensitive building block to use in this study. As with the residue volume study, VAMP was chosen as the SNARE constituent to be modified due to the fact that it binds last in the hierarchy of assembly, and results in the formation of the stable coiled coil helices, easily detectable for example with CD. Four different positively charged residues in VAMP were selected, R31, R47, K52 and K59 (numbering is based on Uniprot/PDB entry P63045/1N7S, **Figure 4.1**). The latter three residues are predicted to participate in salt bridges in 1N7S as indicated in **Figure 5.5a-b**, the former R31 is immediately outside the SNARE motif and participates in a salt bridge in 3B5N as indicated in **Figure 5.5e-f**, though not in 1N7S due to an O-N distance cut-off greater than 3.2 Å (O-N distance in the interaction R31-E151  $\sim 4.4$  Å). **Figure 6.5a-d** contains 3D space-fill images of the VAMP residues of interest, and their proximity to oppositely charged residues in neighbouring chains (i.e. salt bridge partners).

Since the amino acid histidine's imidazole side chain has a  $pK_a$  of 6.0, at physiological pH, small shifts in pH will change the overall average charge. Therefore, it is expected that mutating the selected positively charged residues to histidines will impart pH-sensitivity to the SNARE complexes at pH values above pH 6 but not below. In essence, modulating the pH of the complex solution is predicted to help induce complex assembly and disassembly. Lowering the pH is expected to help induce complex assembly by protonating histidine's imidazole group, which can then participate in

the existing salt bridges, whilst raising the pH will cause the histidines to become unprotonated, breaking the salt bridges and causing disassembly.

#### 6.2.1.2 Salt bridge study – rational design of peptides Brev2-08\_34ST, Brev2-09\_34ST, Brev2-10\_34ST and Brev2-11\_34ST

The aim of this study is to explore importance of a number of predicted salt bridges on the stability of the complex (**Figure 5.5a-b**). Ionic repulsion will be introduced through the mutation of at least one residue in a salt bridge pair. This should weaken or break the salt bridge, thus destabilising the complex. For consistency and all the reasons given previously, the N-terminal of VAMP is the SNARE constituent that will be subject to the modifications envisioned for this study. A length of 34 amino acids will be used rather than 27, as this length will allow us to observe a more substantial drop in melting temperature, which is the main indication of complex stability. Two predicted salt bridges were targeted in the rational design process. These were: K59 in VAMP, which interacts with D179 in SNAP-25C (**Figure 6.5g**), and K52, which interacts with D172 in SNAP-25C (**Figure 6.5f**).

We have engineered peptides with these predicted salt bridges in mind, the first is Brev2-08\_34ST, in which K59 is mutated to glutamate (K59E), breaking the salt bridge with D179 (in 25C), and introducing ionic repulsion to further destabilise the complex. A secondary mutation, D57K, in the same peptide will be used to maintain the pKa of this segment and of the peptide. In this case, D57 was chosen because it is not predicted to participate in any salt bridges, and therefore it is not expected to have an effect on stability. The second peptide is Brev2-09\_34ST, in which K52 is mutated to glutamate (K52E), breaking the predicted salt bridge with D172 (in 25C). Destabilisation is compounded by the introduction of ionic repulsion in the region. As before a secondary mutation, D51K, will be carried out to maintain the pKa of the segment, and of the peptide. This second mutation site is selected such that no ionic bonds should be affected. Finally, the third target is Val43 in VAMP, which of course is not a member of any salt bridge, but happens to be located in the vicinity of a salt bridge member E211 in syntaxin (**Figure 6.5e**). The peptide designed with this in mind is Brev2-10\_34ST, and contains a mutation of V43 to glutamate (V43E). This is envisaged to cause repulsion with E211, effectively weakening its salt bridge with R47 in VAMP, and overall diminishing complex assembly. A secondary mutation, D44A, will maintain the pKa of this segment, and of the peptide. The last peptide, Brev2-11\_34ST, contains all three mutated targets. It is likely that Brev2-11\_34ST would form the weakest, and most pH-sensitive complex of all.

## 6.2 Discussion

Two of the most significant findings were first the relationship between VAMP length and the thermal stability of the SNARE complex, and second, our bioinformatics analyses suggests that residue volumes at the N-terminal of the SNARE complex are highly consistent. This is in line with one of our hypotheses (that general volumes of individual heptad slices are consistently similar from start to end of the motif - see **section 2.3**).

When the total residue volume (TRV) across the SNARE motif of a full-length SNARE complex (PDB: 1N7S) was calculated in the SNARE protein structure compactness analysis tool, it revealed that the N-terminal up to position 39 (ionic layer) had the tightest, most consistent volume compared to the C-terminal (**Figure 6.2**). This conclusion is based on the fact that within the N-terminal up to position 39 there are fewer instances where the TRV (blue line – “Native Full Length”) diverges from the mean, and enters into the region demarcated by the 2x standard deviation lines (purple lines) as seen in **Figure 6.2a**. This has been interpreted to mean that within this region, the volumes of hydrophobic residues have a narrower distribution, and thus there is more consistency. This is clearly evident in **Figures 2.2b and 2.2d**, where the average, 1x and 2x standard deviations, and predicted deviations have been recalculated, tabulated in **Figure 6.2d**, according to the complex N-terminal (segments 15-39) in **Figure 6.2b**, and the C-terminal (segments 43-67) in **Figure 6.2c**. The mean TRV for the N-terminal is greater than the C-terminal, however the standard deviation is two-fold less, showing that the volume of hydrophobic residues in this region are extremely similar. The predicted deviation is slightly less than the standard deviation in the C-terminal indicating that the distribution in this region is more random than the N-terminal, where predicted deviation is instead greater than the standard deviation.

According to the literature, the hierarchy of assembly is that syntaxin initially forms a binary complex with SNAP-25, though no consensus reached as to whether it is N- or C-terminal first, and VAMP binds last in the receptor site formed by the binary complex. With this in mind, we have chosen to focus our efforts on modifying VAMP, as it is the final step in complex assembly. Moreover, we also chose to focus on the N-terminal of the complex, where it has been previously suggested to most likely be where assembly is initiated, and which is shown by our tool to have the tightest assembly. We hypothesise that this region has the most influence on the thermal stability of the assembled complex.

It had been predicted that stability should decrease as the number of hydrophobic repeats in the coiled coil decreases, however the thermal melts in **Figure 6.1** did not show this pattern of

behaviour. Instead, there was a very narrow range in melting temperatures between full-length, 45 and 34 VAMP-complex constructs, and a large, sharp dip in thermal stability ( $\Delta T_m = \sim 19^\circ\text{C}$ ) once the length was reduced to 27. This suggests that the contribution from the hydrophobic repeat segments to the overall stability of the complex is not equal, and some hydrophobic segments are more essential than others. Specifically, it would appear that the segments corresponding to positions 43 and 46 are central to complex integrity since these are the missing between constructs 34 and 27.

Another important fact to consider is that this “missing” area between positions 41 and 57, which disappears in construct 27, is also rich in charged residues, and as a result, is home to the highest density of salt bridges in the entire 1N7S complex (**Figure 5.5b**). There are approximately five salt bridges predicted within this region, an unprecedented amount when compared to surrounding regions, and compared to SNARE complexes 1L4A (squid) and 3B5N (yeast), also shown in **Figure 5.5**. In fact, there are only two predicted salt bridges in the region encompassing the distance between 49 and 68, which corresponds to the distance from truncated VAMP 34 and full length VAMP (54). These two salt bridges are lost in the truncated complex containing VAMP 45, and yet the difference in thermal stability is approximately  $5^\circ\text{C}$ .

VAMP is a direct participant in two of the five predicted salt bridges in the region between positions 41-57, K59 which is one subject of the proposed Salt Bridge study, and forms a salt bridge with D179 in SNAP-25 C-terminal, and D64, which forms a salt bridge with R232 in syntaxin. This supports our hypothesis that long-range ionic interactions are partially responsible for sustaining the stability of the complexes, and furthermore, it indicates that the two salt bridges contributed by VAMP are of critical importance, and constitute an important site that can be mutated with the intent of reducing or increasing SNARE complex melting temperature. The results from this study has informed our next steps in terms of rational design of peptides, and has shown that the SNARE-based constructs are viable candidates for pharmaceutical applications since their stability can easily be attenuated by truncation.

Results from bioinformatics analysis (**section 5.1.3**) suggest that residue volumes at the N-terminal are highly consistent and regular which we believe facilitates “tight” assembly and contributes to the thermal stability to some extent. This constitutes an imperative feature that is partially responsible for maintaining the fidelity of the complex’s characteristic sequence-specific assembly. **Figure 6.2b** and **c** demonstrate the vast difference in the distribution of residue volume from the mean in the N-terminal and C-terminal of the complex. The standard deviation for the C-terminal was twice that of the N-terminal, meanwhile analysis of the predicted deviation revealed that the C-terminal has a greater standard deviation than it’s predicted deviation, indicating greater variance in the volumes of

the population of residues in this region, and thus a greater degree of randomness in assembly here.

## 7. Investigating assembly of truncated SNARE-based peptide complexes

*Note: where abbreviations of peptides and complexes are seen for e.g. “C04” a helpful tool for reference would be **Table 4**, which outlines peptide abbreviations, sequences and the complexes they take part in. An additional reference tool is the Index of Abbreviations at the start of the thesis. Search for the abbreviation to find a description of the complex and the mutant peptides it contains.*

The most significant findings in relation to our aim (rational engineering of thermosensitive protein complexes), was that there was positive correlation between truncating VAMP length and a decrease in the thermal stability of the subsequent SNARE complex formed. Moreover, residue volume was confirmed to play a role in assembly and potentially the thermal stability of the SNARE complex. Bioinformatics analyses also indicated that there was potential to influence thermal stability or introduce pH-sensitivity by targeting ionic interactions.

Mutations have been made to truncated SNARE-based peptides based on the principles outlined in each of these studies, and this chapter focuses on the initial concern of whether they are capable of successful assembly in light of the residue mutations that they have undergone.

### 7.1 Results

#### 7.1.1 CD Spectroscopy: control Protein A – CD spectra of control Protein A are consistent with an $\alpha$ -helical structure

Circular dichroism (CD) is a method of characterising, and confirming complex assembly. A fully assembled SNARE complex is a coiled coil, and as such, it is expected to exhibit  $\alpha$ -helical structure. Partially assembled or disassembled individual SNARE proteins do not possess stable secondary structure. Therefore, the emergence or disappearance of the  $\alpha$ -helical CD spectrum indicates formation or disassembly of the SNARE complex. To establish a positive control, a CD spectrum of Protein A was measured on each CD instrument used. This was then be used as a comparison for the SNARE complexes. **Figure 7.1a** shows the results for the Protein A spectrum conducted on the synchrotron radiation CD beamline and demonstrates  $\alpha$ -helical troughs at 208 and 222 nm as expected for an  $\alpha$ -helical protein (Greenfield, 2007). **Figure 7.4a** shows the results for the Protein A spectrum conducted on the PiStar-180 CD stopped-flow spectrometer, and shows the two  $\alpha$ -helical troughs slightly shifted at ~212 and ~225 nm.



### **7.1.2 CD Spectroscopy: full-length SNARE complex and associated controls** – *CD spectrum of control full-length native SNARE complex confirms $\alpha$ -helical structure indicating successful assembly into coiled coil*

CD spectra of the full-length SNARE complex and the separate individual protein components (full-length syntaxin, VAMP55, and SNAP-25) were obtained, and these can be seen in **Figure 7.1b**. The individual protein components are negative controls, and as expected, they display no measurable  $\alpha$ -helical structure. When all the individual components of the full-length SNARE come together, they assemble into a coiled-coil complex displaying strong  $\alpha$ -helical structure with troughs at 208 and 222 nm. This graph is evidence that the  $\alpha$ -helical structure observed when the combination of SNARE components is tested is due to complex assembly only, and cannot be mistaken for any potential  $\alpha$ -helical content in the separate components.

### **7.1.3 Synchrotron Radiation CD Spectroscopy: control truncated SNARE complexes** – *CD spectra of truncated SNAREs indicate successful assembly and folding into $\alpha$ -helices*

It was necessary to obtain CD spectra of the fully truncated native control SNARE complexes in order to confirm for the first time that they are capable of assembly. A CD experiment using synchrotron radiation was conducted on the following samples: C05 comprising of full-length SNAP-25 (FL S25), Synt1-01\_34 (S01), and Brev2-05\_27 (B05), C04 comprising of SNAP-25, S01, and Brev2-04\_34 (B04), full length complex (referred to as “FL/FL/FL” or “CFL”) containing all full-length SNAP-25, syntaxin, and VAMP, FL SNAP-25 alone, and distilled water as a background signal. See **Table 4** for an outline of the peptide abbreviations, sequences, and the complexes they take part in. The results of this experiment can be seen in **Figure 7.2**. The full-length complex demonstrates two broad troughs, at 215 nm and 230 nm, indicative of an  $\alpha$ -helical structure as expected. SNAP-25 also shows some  $\alpha$ -helical structure, though the troughs are weak and ill defined compared to those in the full-length complex. A look at the control spectrum for SNAP-25 conducted using synchrotron radiation CD, a far superior method, in **Figure 7.1** shows that compared to a full-length complex the  $\alpha$ -helical content of SNAP-25 is minimal to none. Although the first  $\alpha$ -helix trough is not as well-defined as in the full-length complex or SNAP-25, assembly in C05 and C04 can be confirmed, as both still exhibit an  $\alpha$ -helical structure that is sufficiently different from free SNAP-25 to indicate that the signal is not solely from that particular component. The results from this experiment validated the selection of self-assembling peptides used.

#### **7.1.4 Testing full-length and truncated SNARE complexes for SDS-stability – full-length reassembled SNARE complexes are stable in SDS, whereas truncated SNAREs are not stable in SDS**

Polyacrylamide gel electrophoresis (PAGE) can be used to not only confirm assembly, but also measure the extent of assembly with the use of band quantification, and with some modifications, test for SDS-stability. The full-length complex containing syntaxin, SNAP-25 and VAMP (VAMP54 – VAMP of length 54) remains fully assembled in SDS (lane “CFL” in **Figure 7.3a** and **7.3b**), where the band corresponding to unfolded SNAP-25 (25 kDa) has disappeared almost completely, and the majority of the protein migrated as band towards a higher molecular of between 25 and 37 kDa. The fully assembled coiled coil SNARE may show a molecular weight that is different from the arithmetic sum of its molecular weight components due to the tight packing of the four helices in the complex, which remain unfolded under SDS conditions. Due to very high hydrophobic content of part of the SNARE’s portions, a small degree of dimerisation is not unexpected, which can be seen in **Figure 7.3a** at ~75 kDa. Heating to 70°C for 10 min in an SDS-containing loading buffer denatures the complex fully (lane “CFL D” in **Figure 7.3a** and **7.3b**).

CD spectroscopy samples from **Figure 7.2** were subsequently subjected to an SDS-PAGE in order to determine whether they also retain SDS-stability. Untreated (i.e. native, non-denatured), and heat-treated (denatured by heating to 90°C for 5 min) samples included C05 (referred to as FL/S01/B05 in the gel), C04 (referred to as FL/S01/B04), and full-length complex (referred to as FL/FL/FL). Only the full-length complex (FL/FL/FL) showed a band corresponding to the molecular weight of the complex (36 kDa), all others did not, indicating that they are unstable in SDS. This can be seen in **Figure 7.3b**.

#### **7.1.5 CD Spectroscopy: control truncated SNARE complexes – CD spectra of truncated control complexes show successful assembly with progressively decreasing intensity of $\alpha$ -helical structure**

CD spectra were obtained for the full-length SNARE complex (FL/FL/FL), and partially truncated SNARE complexes FL/FL/34 (containing full-length SNAP-25 and syntaxin, and truncated VAMP Brev2-04\_34), and FL/34/34 (containing full-length SNAP-25, and truncated syntaxin Synt1-01\_34 and VAMP Brev2-04\_34), and these are shown alongside the background HEPES buffer in **Figure 7.4**. This is essentially a repeat of the measurements obtained in **section 7.1.3**, however it was conducted on a conventional CD spectrometer rather than with synchrotron radiation CD spectroscopy. Unfortunately, dimethyl sulfoxide (DMSO) was obscuring the  $\alpha$ -helical region, which may be why the signal for complexes C04 and C05 (**Figure 7.2**) did not display a strongly

convincing  $\alpha$ -helical pattern. The complexes were subject to buffer exchange in order to remove the majority of DMSO, and the subsequent signals achieved in **Figure 7.4** display a convincing  $\alpha$ -helical pattern that is consistent with complex assembly, although the two troughs are not well defined and have merged into one at ~215-230 nm. The full-length complex FL/FL/FL yields the most intense  $\alpha$ -helical spectrum, indicating highest  $\alpha$ -helical content. The truncated complexes FL/FL/34 and FL/34/34, do assemble, but yield lower  $\alpha$ -helical content as expected, since the length of the “completed” coiled-coil i.e. the coiled-coil comprising of all three SNARE protein components, decreases with each truncation, and therefore the  $\alpha$ -helical content of the complexes also. The spectrum for FL/34/34 – otherwise referred to as “C04” – also acts as further evidence that truncated syntaxin and VAMP polypeptides are capable of successful assembly.

### **7.1.6 Using native PAGE gels to study the assembly of IR-labelled SNARE proteins**

**complexes and rationally designed peptides** – *SNAP-25 was labelled with an infrared (IR) dye, and successful assembly of complexes was confirmed on native gel by incorporation of this labelled component when visualised at wavelength 800 nm*

#### *7.1.6.1 Labelling SNAP-25 with CF790 succinimidyl ester IR-label*

Having proven the complex assembly with CD spectroscopy (**section 7.1.3** and **section 7.1.5**), and having later confirmed it using pull-down assay experiments (**section 8.1.3**), it was deemed necessary to test complex assembly directly using IR-labelled SNARE proteins, and in particular SNAP-25. SNAP-25 was therefore labelled with an infrared (IR) label “CF790 succinimidyl ester”. The complex assembly was conducted with the resulting IR-SNAP25 as the limiting reagent and all other proteins in excess, and then tested on native PAGE gels which were to be visualised in the 800 nm channel to ensure only IR-labelled samples would be observed. Note that with native PAGE, separation is no longer based on the molecular weight of the proteins, but also on the protein charge under the pH conditions of the electrophoresis. Protein charge depends on the protein pI (see **section 2.2** for more information). Therefore, whilst molecular weight ladders have been used in the gels, they are used to indicate positions rather than identify the molecular weight of bands.

The labelling reaction was successful, as indicated by the band at ~25 kDa corresponding to IR-SNAP25 in the “10 P” lane of **Figure 7.5a**. Purification was necessary to remove the significant amount of excess label, which can be seen below the IR-SNAP25 band. The MW of the dye was ~3267 Da, so it was decided that filter sizes 10 and 30 kDa should be tested to see which is most

effective at removing the excess label impurity. **Figure 7.5a** shows the SDS-PAGE result from the purification, and it is immediately clear that the 30 kDa sized filter “30 P” is the most effective, removing all the unincorporated dye.

Since the native gels were to be observed in the 800 nm channel, it was necessary to optimise IR-labelled SNAP-25 concentration and buffer conditions to ensure that the bands would be visible from gel to gel. Full-length SNARE complexes containing IR-SNAP25 of concentrations 3.2, 0.8 and 0.2 µg/mL, in buffer containing 16 mM HEPES, 80 mM NaCl, 0.1% OG, and different BSA concentrations 1, 0.1 and 0.01 mg/mL (Buffer A, B, and C respectively). The results from this native gel can be seen in **Figure 7.5b**. Note that the dyes in the Precision Plus Dual Colour Standard molecular weight ladder intrinsically appear to be visible in the 700 nm and 800 nm channels, as the scans were conducted without any tags or staining immediately following PAGE. Optimal IR-SNAP25 concentration was determined to be 0.8 µg/mL, since this is the lowest concentration tested that gives a reasonable signal with clear differentiation between the complex and SNAP-25 bands. Buffer B containing BSA at concentration 0.1 mg/mL was determined to be the optimal buffer conditions. This is because it is the best compromise between the positive blocking effect of BSA to facilitate the use of a very low concentration IR-SNAP25, and the negative effect a large concentration of BSA may have on the kinetics of SNARE assembly.

#### *7.1.6.2 Residue Volume study*

All complexes were prepared with syntaxin and VAMP in large excess over IR-SNAP25. This was to ensure that only one band should appear, and this would be indicative of complex assembly or IR-SNAP25 i.e. unsuccessful assembly. **Figure 7.6** shows the results of the native gel testing for assembly among the Residue Volume study complexes. The band for IR-SNAP25 appears in **Figure 7.6a** and **7.6b**, and so can be identified in all gels as the band at MW ladder position 2. A denatured control complex (the complexes with a “D” suffix) was also run alongside each complex to act as yet another method of confirming or disproving assembly.

Returning to the Improvement study complexes, complex C05 shows a reduced density band corresponding to IR-SNAP25 indicating partial assembly in one gel (**Figure 7.6a**, lane 5 “C05”, position 3), as indicated by the depletion of the band corresponding to IR-SNAP25 here. Its denatured counterpart C05 D contains unassembled IR-SNAP25 (**Figure 7.6a**, lane 6 “C05 D”, between position 2-3). This is clear enough proof that C05 assembles successfully. The shift in IR-labelled band for C12 (**Figure 7.6a**, lane 5 “C12”, position 3) compared to the denatured counterpart C12 D (**Figure 7.6a**, lane 6 “C12 D”, position 2-3) supports the conclusion that C12 does assemble.

C13 and C13 D show intense bands corresponding to IR-SNAP25 (**Figure 7.6a**) indicating that it does not assemble at all. Assembly is unclear for C14 in **Figure 7.6a** as lane C14 is devoid of any band.

The results for the Compensation study complexes can be seen in **Figure 7.6b**. The control C04 shows efficient assembly as indicated by a prominent shift of the IR-labelled band (**Figure 7.6b**, lane 3 “C04”, position 3). C15 likewise is shown to assemble efficiently as indicated by the high density of the complex band (**Figure 7.6b**, lane 5 “C15”, position 3), and is validated by the depletion of the IR-SNAP25 band, which instead emerges in the denatured control C15 D (**Figure 7.6b**, lane 6 “C15 D”, position 2). On the other hand, it is confirmed that under these conditions, C0315 does not assemble, as both native and denatured lanes for C0315 are near identical. Assembly of a separate control C0304 could not be confirmed, although there is a difference in intensity in the bands for both the native and denatured lanes, the bands could not be resolved to determine their identity.

The final conclusions reached regarding which complexes form of those in the Improvement study are C05, C12, and potentially C14, and of those in the Compensation study, they are C04, C15, and potentially C0304. This is summarised in the table in **Figure 7.6c**.

#### *7.1.6.3 Ionic Interactions Study*

**Figure 7.7** contains the results of the native gels confirming or disproving the assembly of the complexes pertaining to the Ionic Interactions study. The gel containing the Salt Bridge study complexes can be seen in **Figure 7.7a**. The band corresponding to IR-SNAP25 in the “IR-SNAP25” control lane is not clearly evident here, however it is clearly evident in all the denatured control lanes at MW ladder position 2. All complexes in the Salt Bridge study, C08, C09, C10, and C11, are shown to assemble as indicated by the depletion or absence of the IR-SNAP25 band in the native lanes, and the emergence of strong IR signal corresponding to the assembled complex. An example of this phenomenon can be seen in the native complex “C08” lane 3, which shows IR-labelled complex band at position 3 and fully depleted IR-SNAP25, and its denatured counterpart “C08 D” lane 4, which shows the emergence of the IR-SNAP25 band at position 2, and a partially depleted complex band at position 3.

The gel displaying the complexes in the pH-Sensitivity study can be seen in **Figure 7.7b**, and partially in **Figure 8.6**. Of the six complexes, C06, C0204 and C0205 very clearly assemble with IR-SNAP25 bands present in all denatured lanes, and absent in all native lanes. Complex C0206

appears to also assemble, with IR-SNAP25 absent in the native lane, however the complex band lacks intensity. Similarly, C0207 complex band in the native lane lacks intensity, and there appears to be a shadow of IR-SNAP25. The latter point applies to C07, which also contains a shadow of IR-SNAP25 in the native lane. Ultimately the conclusion reached for these complexes is that all complexes assemble, confirming that these rationally designed substitutions allow assembly under native pH conditions, as expected. In conclusion, all tested complexes were able to self-assemble, summarised in **Figure 7.7c**.

#### **7.1.7 CD Spectroscopy: full-length SNARE complex assembly on nanoparticles – CD spectra demonstrate evidence that full-length SNARE complex assembles on both magnetic, and gold nanoparticles**

One of the concerns for developing a drug delivery device using the SNARE-based peptide complexes conjugated to nanoparticles, is the possibility that the complexes will not assemble correctly, or at all, once attached to the nanoparticles. This was investigated with magnetic nanoparticles (MNPs), using circular dichroism (CD) spectroscopy.

Commercial magnetic Iron(II,III) oxide nanoparticles, with a diameter of 5 nm, and amino-reactive surface-modification (NHS – N-hydroxysuccinimide ester) were used in this study. In order to facilitate complex assembly on the MNP surface, it was decided a linker would be most appropriate to create distance between the complex and the MNP, preventing potential steric hindrance between them as the proteins come into contact with one another. As SNAP-25 is a recombinantly expressed GST-fusion protein (GST – glutathione S-transferase), it made sense to employ GST as the desired linker. Also, immobilisation of GST fusion proteins on nanoparticles has been characterised in detail in the literature (Ma *et al.* 2018). Circular dichroism spectra (**Figure 7.8a**) were acquired for the following set of samples: MNP conjugated to GST (MNP-GST), required as a baseline to characterise GST's  $\alpha$ -helical contribution to the final assembled complex-on-MNP product, MNP-GST-SNAP25, MNP-GST-SYNT/VAMP, which is syntaxin and VAMP (synaptobrevin) together with the MNP-GST-SNAP25 construct, and finally, MNP-GST-SNAP25/SYNT/VAMP, which is the complex-on-MNP product. The intensity of the troughs at 205 and 225 nm in the complex-on-MNP sample indicate that it has substantially more  $\alpha$ -helical content than any of the other control samples (MNP-GST, and the samples containing SNAP-25 or SYNT/VAMP). This is a positive confirmation that the protein successfully assembles on the MNP surface.

The gold nanoparticles (GNPs) used were slightly larger with a diameter of 20 nm. The CD spectra containing the samples from this GNP study can be seen in **Figure 7.8b**. GST is capable of near-

covalent binding to the Au surface through chemisorption. It functions as a linker attaching one component of the complex to the nanoparticle, whilst also maintaining enough distance to allow the components to approach the anchored SNARE component without any danger of steric hindrance preventing successful assembly. The GNP-GST sample demonstrates some  $\alpha$ -helical structure as expected of GST, and there is little difference when syntaxin is added (GNP-GST-SYNT), also expected since syntaxin alone should exhibit disorder. GNPs incubated with SNAP-25 and VAMP55 show little structure, again expected as in the absence of even one SNARE component, the SNARE proteins remain disordered. GNP-GST-SYNT with SNAP25/VAMP55 should form the complex-on-GNP construct, and this sample does indeed contain the greatest amount of  $\alpha$ -helical structure, verifying that SNARE assembly is also successful on the GNP surface.

## 7.2 Discussion

There is a clear difference between the CD spectrum obtained for the full-length complex and those obtained for the individual protein components, which exhibit disorder since they are unstructured (**Figure 7.1**). It is on the basis of this disparity, compounded by the lack of structure in the control full-length SNAP-25 conducted in the same study, that the conclusion was reached that **Figure 7.2** containing spectra of the truncated SNARE complexes C04 and C05 provided evidence of their assembly. The  $\alpha$ -helical troughs demonstrated relatively low intensity, and do lack definition, however this is to be expected since the number of hydrophobic segments contributing to the coiled-coil has been significantly diminished when comparing the full-length SNARE complex to the truncated peptide complexes. This conclusion was further supported on repetition of the CD spectrum of C04 in **Figure 7.4**, which showed an improved definition of the  $\alpha$ -helical trough at 222 nm.

Independent evidence for the assembly of C04 was conceived in the form of IR-labelled native PAGE. In this method, IR labelling of the component SNAP-25, and subsequently keeping syntaxin and VAMP in vast excess over IR-SNAP25, was decided upon as secondary strategy to confirm complex assembly. Using this method, we were able to analyse assembly of complexes in the Residue Volume study (**section 6.1.1**): C04, C05, C12 and C15, which were shown to assemble, and C13 and C0315, which did not assemble (**Figure 7.6**). C13 very clearly was incapable of assembly indicating that the M29F mutation destabilises the  $\alpha$ -helical structure of the complex. The rationale behind the M29F mutation was that the substantially larger phenylalanine residue would be a better fit in this hydrophobic layer co-located next to a glycine and alanine, both of which have the smallest residue volumes of all the residues. Instead, it is more likely that the introduction of this phenylalanine mutant introduced a significant amount of steric hindrance against the other

phenylalanine, also situated in the same hydrophobic layer in the syntaxin chain. Since the complex C14 also contains the M29F mutation, confirmation of its capability to assemble or not would assist in determining the extent of destabilisation this mutation may cause.

We predicted that C15 would be unstable as it contains mutations of key residues in VAMP to the same residues observed in syntaxin, in the same layers. Steric hindrance was expected as a result of these mutations as in each case, the presence of two identical “large” volume residues facing each other in opposite chains in five separate hydrophobic segments should reduce size and volume complementarity between the SNARE chains, and hence it was predicted that this would prevent assembly. Instead, however, C15 containing the five mutations was observed to consistently assemble successfully. Of significant interest, Brev2-15\_34ST also contains the M29F mutation, and it is evident that in this case it does not sufficiently destabilise the complex to cause outright disassembly. Our interpretation as to why it is capable of assembly lies in the hydrophobicity of the mutant residues. Specifically the T18L and N32M mutations, where the native threonine and asparagine in VAMP have hydrophilicity (according to the Kyte and Doolittle scale) of 0.7 and 3.5 compared to the mutants leucine and methionine at -3.8 and -1.9 respectively. It is apparent in this case, that the shift towards increasing the hydrophobic character of the VAMP chain at these positions overcomes the negative design resulting from the M29F mutation, and stabilises assembly thereafter. It is not yet understood at this stage whether these mutations result in a more thermally stable complex compared to the control C04.

Contrary to expectations, C0315 also was incapable of successful assembly. In this complex, the same five positions mutated in VAMP were instead mutated in syntaxin (Synt1-03\_34ST), this time to the original residues that inhabited those positions in the native VAMP. This means that the positive effect of the T18L and N32M mutations in VAMP were rendered obsolete as the threonine and asparagine have been restored but this time in syntaxin as L18T and M32N mutations. Here, we assert that without the essential stability afforded by the additional hydrophobicity at these two positions, the negative effect on complex stability caused by the M29F mutation in VAMP is unsuppressed and results in C0315 being incapable of successful assembly.

It is yet unclear at this stage whether C0304 is capable of assembly. Whilst this complex is not part of the compensation study, it is a reasonable control to determine whether the mutations in Synt1-03\_34ST are destabilising when in complex with native VAMP (Brev2-04\_34). In this case, there is no phenylalanine in position 29, so it is possible that this complex avoids the instability caused by previous iterations of VAMP containing the M29F mutation. This complex does however suffer from a more substantial reduction in hydrophobicity in positions 18 and 32, layers that now contain a threonine and an asparagine residue respectively.



All complexes of the Salt Bridge study, C08, C09, C10, C11, and the pH-sensitivity study, C06, C07, C0204, C0205, C0206, C0207, were confirmed to assemble. Whilst it is not yet understood at this stage whether, and how, the ionic interaction mutations might have affected the stability of the resulting complex, it is clear that they have not hindered the ability of the complex to assemble successfully indicating that in general, the *bc*, and *efg* layers are less essential to assembly than the hydrophobic layers *a* and *d* whose influence on assembly post-mutation was observed above.

This chapter focused on addressing the hypotheses around residue volume and ionic interactions. Specifically these hypotheses were that: 1. The specificity of complex is not governed by the presence of the ionic layer alone, but also by complementary residue volumes that permit a single arrangement of helices, with residue volumes of each segment interlocking “knobs-into-holes” style and 2. The helices come into close proximity due to long-range ionic attraction (i.e. salt bridges) at the N-terminal region. In light of the results for C13, C15, C0315, and the complexes involved in the salt bridge and pH-sensitivity studies, whose outcomes are inconsistent with our predictions, we must also consider the possibility that the hypotheses underlying the predictions are wrong.

Validation of the potential application of these SNARE-based peptide complexes has commenced in parallel with the rational design of peptides aspect of the project. The primary application identified for the SNARE-based peptide complexes is that they may act as a linker between an energy receiver (i.e. a metal nanoparticle), and a payload, in the context of a payload (drug) delivery device. Briefly, the purpose of having an energy receiver, or antenna, is that they will receive energy in the form of either near infrared or electromagnetic radiation, and locally heat the area of interest containing the drug delivery device. The linker, composed of the SNARE-based peptide complex should disassemble as they have been engineered to, and the payload is effectively delivered. There was a distinct possibility the complex would not assemble on any surface, for example, if the surface was “sticky”, the proteins may instead bind in a highly random and disordered state along the surface, and there was also the likelihood of protein aggregation, or their recognition properties may be impaired by nonspecific binding. With these eventualities in mind, the results from the CD spectra for both nanoparticle studies showed that the full-length SNARE complex successfully assembles on both magnetic, and gold nanoparticles. Both of these developments validate the use of magnetic and gold nanoparticles as the antennas for the device.

## 8. Investigating the stability of truncated SNARE-based peptide complexes

### 8.1 Results

#### 8.1.1 Thermostability of control complexes – *pull-down thermal assay results for the truncated complexes C04, C05, and partially truncated CFL04, and CFL05*

Pull-down assay was used to evaluate the thermostability of the complexes prior to CD analyses. Briefly the method involved assembly of the complexes on glutathione agarose beads linked to GST-SNAP25 fusion protein, then incubating aliquots at 4, 26, 45, 55, 65, 75 and 85°C for 20 min. Any disassembled complexes are expected to be released from the beads following the heating. Therefore, the supernatants were collected and tested on the SDS-PAGE to estimate the quantity of the released peptide (disassembled complex) using densitometry analysis on a set of identifiable peptide bands. An example of a typical SDS-PAGE output for the “supernatant” is in **Figure 8.1**, and “beads” products from this methodology can be seen in **Figure 8.8**. The density of the peptide bands was subsequently plotted in graphs, and the red line on these graphs indicates the halfway point between the highest and lowest peptide density and therefore the point at which effectively half the complex is unfolded. This is equivalent to the melting temperature ( $T_m$ ) for this particular method, and gives an indication about the relative thermostability of the complex. Whilst protein interactions in this experiment may be affected by other factors in addition to the SNARE interactions, pull-downs were useful in selecting constructs for SRCD studies, where instrument access was limited. It is also likely that the  $T_m$  recorded using pull-downs may be different from CD experiments as the experimental system is entirely different, and the thermal unfolding regime was also different due to system limitations.

The results of the pull-down thermal assays, all of which were from the “beads” product, for the control complexes C04, C05, CFL04, and CFL05 can be seen in **Figure 8.2**. The expected trend for a typical “beads” product of the pull-down thermal assay is sigmoidal in the sense that there should be the greatest peptide density at the low temperatures, and this should steadily decrease with increasing temperature as the complex unfolds, and finally there should be the lowest peptide density at the highest temperature at which the complex is expected to denature. All the control complexes show the general trend of high peptide density at low temperature, low peptide density at high temperature, however the all with the exception of C04, lack the defined sigmoidal shape.

Partially truncated complex CFL04 showed consistent thermostability until 55°C, at which point peptide density drops sharply and remains stable until 75°C. No peptide was detected at 85°C indicating that at this temperature, the entire complex had disassembled and no peptide was left bound to the beads. The  $T_m$  was recorded as ~60°C. It's counterpart C04, wherein both syntaxin and VAMP have been truncated to length 34 aa, showed a more sigmoidal trend with a steady decrease in peptide density from 45-75°C, and  $T_m$  of 58°C.

The other partially truncated complex CFL05 lacks the initial and ending plateaus, showing a steady decrease in peptide density from 26-75°C. No peptide was detected at 85°C. The  $T_m$  was recorded as ~59°C, extremely close to CFL04. It's counterpart C05, wherein syntaxin has been truncated to 34 aa and VAMP has been truncated to length 27 aa, showed an extremely similar pattern to CFL05, however the gradient of the slope is less steep. The  $T_m$  was recorded as 67-68°C, which is much higher than expected, especially when compared to the relative stability of CFL04 and C04, which should exhibit greater stability due to an extra heptad.

In conclusion, changes in the  $T_m$  were detected, but not entirely consistent with our expectations. CD would provide a more accurate method of detecting true complex unfolding temperature, compared to pull-downs. These are, of course, two very different experimental setups. There are two key differences. Melting on the surface of porous (otherwise solid) beads in a typical pull-down is different from protein unfolding in solution (CD). One other principle difference is pull-down experiments measure protein interaction and physical retention, whilst CD experiments are detecting protein folding and unfolding. The latter is more directly related to protein complex stability and stimuli sensitivity.

### **8.1.2 Thermostability of complexes from the Residue Volume study – mixed results from the pull-down thermal assay, however success shown with the Compensation study complexes in SRCD**

#### *8.1.2.1 pull-down thermal assay*

The results for the pull-down thermal assay of complexes pertaining to the Residue Volume study can be seen in **Figure 8.3**. Of the three complexes in the Improvement study, only C12 and C14 were tested as these were confirmed or suspected of successfully assembling in the native gels in **Figure 7.6**. The results from the supernatant products for both these complexes showed the expected sigmoidal-like behaviour, whereas the beads products did not show a definitive pattern. Beginning with C12, the results from the beads pull-down (**Figure 8.3a**) shows an initial plateau

between 4-26°C, that is followed by a sharp unexpected increase in peptide at 45°C, and a subsequent sharp decrease to 55°C, with a reasonably stable plateau from this point until 75°C. The  $T_m$  was recorded as 51-52°C. The supernatant product (**Figure 8.3b**) showed a low plateau between 4-26°C, then a steady increase up to 75°C. The recorded  $T_m$  was slightly higher at ~54°C.

The results for the beads pull-down of C14 (**Figure 8.3c**) shows a reversal in the expected trend. The low temperatures, which should have the highest peptide density, instead show the lowest peptide density and vice versa for the high temperatures. This behaviour is more characteristic of the supernatant products, and indicates that the data is wholly unreliable. The  $T_m$  was measured at 45°C. The results from the supernatant product (**Figure 8.3d**) were more reliable, exhibiting the trend consistent with this type of data. There was an initial low plateau between 4-45°C, followed by a steady increase to 75°C, then a plateau to 85°C. The  $T_m$  was measured at ~53°C, and is more reliable than the  $T_m$  obtained from the bead pull-down.

The only complex that assembled successfully in the Compensation study was C15. **Figure 7.6** showed that C0315 did not assemble and there was uncertainty about C0304. In regards to C0304, when it was subjected to a pull-down there was no measurable peptide bands under the conditions tested for either the beads or supernatant products, leading to the conclusion that C0304 does not successfully assemble under these conditions. The results from the bead product (**Figure 8.3e**) shows a sharp decrease from 4-45°C, indicating very low thermostability. The  $T_m$  was recorded at ~22-23°C. The results from the supernatant (**Figure 8.3f**) did not show a sigmoidal pattern, instead there was a steady increase from 4-85°C, with no initial or final plateau to indicate the temperatures at which the complex was fully assembled and fully disassembled. The  $T_m$  was recorded as ~63-64°C, which contradicts the results from the beads product.

In conclusion, the expected changes in the  $T_m$  were detected with most of the engineered constructs. There is a clear need to corroborate these independently with CD measurements, which are more direct and less prone to artefacts.

#### *8.1.2.2 SRCD spectroscopy: thermal melts of Compensation complexes*

Following pull-down thermal assays, SRCD was carried out on complexes pertaining to the Compensation study. **Figure 8.4a** shows the melting curves obtained using CD spectroscopy for native control C04, destabilised complex C15, and rescued complex C0315. The curves are % unfolding, which was calculated by measuring the CD signal at 222 nm and recalculating it as 100% change from the start to end of the melt. A four-parametric sigmoidal curve was fitted to each trace

using non-linear least squares method (Kemmer and Keller, 2010). **Figure 8.4b** shows a summary table of the melting temperatures calculated from the curves, along with the confidence intervals and the  $R^2$ .

The results showed that complex C15, which was the destabilised peptide complex containing VAMP (Brev2-15\_34ST) with selected mutations that were expected to introduce steric hindrance with syntaxin, showed a drop in melting temperature of 6°C. Although the rescued complex C0315 did not appear to assemble in the native gel conditions, it was observed to successfully assemble in SRCD. Furthermore, it showed a substantial increase in stability ( $T_m = 86^\circ\text{C}$ ) compared to the destabilised (C15), and native control (C04) complex. This is consistent with our expectations, and supports the TRV volume conservation strategy laid out in **section 6.1.1.2**.

### **8.1.3 Thermostability of complexes from the Salt Bridge study – mixed results from the pull-down thermal assay, however success shown with SRCD**

#### *8.1.3.1 pull-down thermal assay*

The results for the pull-down thermal assay of complexes pertaining to the Salt Bridge study can be seen in **Figure 8.5**. Of the four complexes that were confirmed to successfully assemble in the native gels in **Figure 7.7**, only three gave measurable peptide bands in the pull-down assay gels, these were C08, C09, and C10. C09 was the only complex to give measurable peptide bands in both the beads and supernatant pull-down products. The beads product (**Figure 8.5a**) does not show an initial plateau, instead the peptide band density sharply drops from 4-55°C, and the  $T_m$  was recorded as ~25-26°C. The supernatant counterpart (**Figure 8.5c**) also does not show the expected sigmoidal behaviour, there was no initial or closing plateau to indicate the temperatures at which the complex was stable in a assembled and disassembled state, instead it appeared that the extremes in temperature showed almost similar peptide band densities, The  $T_m$  from this product was recorded as ~55°C, which is substantially greater than the beads.

The pull-down assay for C08 only yielded measurable peptide bands for the beads product, and the result can be seen in **Figure 8.5b**. The peptide band density remains relatively stable until ~65°C, and drops from this point to 85°C. The  $T_m$  was recorded as ~69°C, and the lack of measurable peptide bands in the supernatant has been interpreted as a result of the high thermostability observed in this complex, meaning little peptide was liberated from the beads.

On the other hand, the complex C10 only yielded measurable peptide bands for the supernatant product, consistent with other such similar measurements, and the result can be seen in **Figure 8.5d**. The peptide band density steadily increases from 4-55°C, after which there is a relatively stable plateau, with the exception of an outlier at 65°C. The  $T_m$  was recorded as ~26°C, and again, the lack of measurable peptide bands in the beads product has been interpreted as a result of the low thermostability observed, meaning most of the peptide had been liberated from the beads into the supernatant.

#### 8.1.3.2 SRCD spectroscopy on selected Salt Bridge complexes

Following pull-down thermal assays, SRCD was carried out on the Salt Bridge complexes (C08, C09, C10, C11), and the two native control complexes (C04, C05).

**Figure 8.6** shows the melting curves obtained using CD spectroscopy. The curves are shown as % unfolding, which has been calculated in the same manner as outlined in **section 8.1.2.2**. The Salt Bridge study complexes were engineered to break or weaken “existing” (predicted) salt bridges by introducing ionic repulsion (see **section 6.2.1.2**). In the case of C08, we intended to break or weaken a predicted salt bridge between VAMP and SNAP-25 through a K59E mutation. The melting temperature as determined by SRCD was 51°C, which is a drop of 7°C compared to the native control C04 (58°C). Small, insignificant reductions in temperature (~1-2°C) were observed in the case of both C09 and C10, indicating that although both would have had one predicted salt bridge disruption, it did not affect their stability. C11 was too unstable to conduct a pull-down thermal assay, and the SRCD results confirm this as the  $T_m$  was recorded as 34°C. This complex contained all 3 of the mutations introduced in C08, C09, and C10, and so the substantial reduction in melting temperature is in line with our expectations.

These results show that our approach towards exploring the importance of predicted salt bridges on the stability of the complex is a viable one. It also demonstrates that mutating predicted salt bridges is an adequate method of engineering protein stability.

**8.1.4 CD Spectroscopy: thermal melts of control truncated SNARE complexes compared to full-length SNARE complex** – *thermal melt of full-length complex and partially truncated complex were consistent with expectations*

Circular dichroism was measured as a function of temperature to yield thermal melts of full-length (FL/FL/FL), and partially truncated (FL/FL/34 – containing Brev2-04\_34) SNARE complexes. The results can be seen in **Figure 8.7**. The melting temperature ( $T_m$ ) was recorded as  $\sim 79^\circ\text{C}$  for the full-length complex FL/FL/FL, and  $\sim 71\text{-}72^\circ\text{C}$  for the partially truncated complex FL/FL/34. Thermal melts of these two complexes match that recorded earlier in this study using SRCD (**section 6, Figure 6.1**). This current measurement (**Figure 8.7**) was obtained using a PiStar-180 CD stopped-flow spectrometer. The PiStar-180 CD had to be used because of the very limited access to the SRCD instrument.  $T_m$  values generated on both instruments were consistent. The melting temperatures recorded for the same complexes in **Figure 6.1** is very similar ( $T_m \sim 72^\circ\text{C}$  for 34 aa VAMP, and  $\sim 77^\circ\text{C}$  for full-length complex), and therefore the results generated during this study on two different CD platforms can be compared directly.

#### **8.1.5 pH-sensitivity of complexes from the pH-sensitivity study – *the built-in pH-sensitivity effect was confirmed experimentally in all engineered complexes***

To gain further insight into pH sensitivity and thermostability of engineered complexes, pull-down assays were utilised. Whilst protein interaction may be affected by other factors, in addition to the SNARE interaction, pull-downs remain useful in selecting constructs for SRCD. In the case of the pH-Sensitivity study, the pull-down method involved assembly of the “pH-sensitive” complexes on glutathione agarose beads linked to GST-SNAP25 fusion protein, followed by exposure of aliquots of the resin to buffer with different pH values adjusted to 6, 7, and 8. To analyse complex stability, any remaining protein complexes were eluted from the resin with SDS-PAGE loading buffer containing 2-mercaptoethanol under elevated temperatures in order to liberate the peptides from the beads. The samples were subject to an SDS-PAGE gel, and densitometry analysis was conducted on a set of easily identifiable peptide bands (in this case, it was syntaxin peptides) to quantify the relative proportion of complex that remains bound after incubation at the pH of interest. An example of a typical SDS-PAGE output from this methodology can be seen in **Figure 8.8**. The peptide band density (syntaxin peptide) indicates that complexes were most likely stable, and likely had slightly different pH stabilities. A greater density indicating that more peptide remained bound to the beads and therefore a more stable complex had initially formed. This test indicated that the complexes should be further investigated with SRCD, which is capable of providing undisputable structural evidence of the complex formation and disassembly.

To finalise comparison between all values recorded with pull-downs, peptide band density for each complex were normalised against the value obtained at pH 7, and following this, since the native control complexes C04 and C05 exhibit an inherent baseline stability profile as a function of pH, the

values were subsequently normalised against the equivalent set of values obtained for the appropriate control. The values for complexes C06, C0206, and C0204 were normalised relative to the control C04, and complexes C07, C0207, and C0205 were normalised relative to the control C05. The results of the pH pull-down assay for all complexes pertaining to the pH-sensitivity study can be seen in **Figure 8.9**. The peptides in the pH-sensitivity study have had histidine mutations at key positively charge sites, and it was expected that these mutations would impart pH-sensitivity onto the complexes. Therefore the expected trend in pH-sensitivity was that the complexes should have the greatest stability, and hence the greatest density of peptide at pH 6 (the pKa of histidine is 6, so at this pH the histidine side chains should remain protonated and the original salt bridges should be maintained). At higher pH values, the salt bridges may not be maintained, and the stability of the complexes should decrease. That in turn would reduce the quantity of the peptides retained on beads, and lower density of bands on the gel.

It was observed that the pull-down gels (**Figure 8.8** shows an example) contained the presence of several unspecified bands in the GST-SNAP25 lane, which may have caused non-specific retention of syntaxin or VAMP. It is unlikely that these peptides would be bound stronger to any non-specific proteins than they would to SNAP-25, which they strongly complex with. It is possible that the existence of any non-specific interaction would have interfered with the results of the pull-down. The outcomes shown in **Figure 8.9** were inconclusive, likely because of this, and it was difficult to interpret the results due to the complexity of multicomponent system used.

It appeared that the complexes exhibited the predicted trend, showing a negative correlation between normalised peptide band density, which is indicative of assembly and therefore stability, and increasing pH. With that being said, the differences in normalised peptide density across the pH range were near negligible and this is the reason why there is no definitive conclusion from this particular study. It was clear from the outcome of this study that further work needed to be carried out using a more precise method such as synchrotron radiation CD spectroscopy.

#### **8.1.6. CD Spectroscopy: pH-sensitivity of complexes from the pH-sensitivity study – *the engineered pH-sensitivity was confirmed experimentally using SRCD***

Due to the difficulty in interpreting the results from the pull-downs in **Figure 8.9**, we used the insights learnt in that study, specifically around experimental conditions, and applied them to SRCD. SRCD addresses shortcomings in the pull-down experimental method because it is carried out in solution rather than being confined to the weaknesses of immobilised proteins. There is no GST tag



to interfere or promote nonspecific interactions, and the detection is based on the change in secondary structure rather than protein-protein interaction.

A number of pH sensitive constructs have been tested with SRCD in solution. **Figure 8.10** shows three typical responses to pH by the C04 and C0206 (reengineered) SNARE complexes. Both protein complexes remain stable at pH 6 and 7. However, at pH 8.5 there are substantial differences. Complex C04 remains stable and structurally unchanged, but the reengineered complex C0206 has acquired pH sensitivity. C0206 unfolds almost entirely, and the structure changes to random coil (**Figure 8.10**). This successful test justified further detailed SRCD analysis. **Figure 8.11** shows a summary of pH response curves measured for three typical complexes: C04, C06 and C0206. All protein complexes remain stable at pH values below and including pH 7. However, at pH above 7, there are significant differences. C06 is substantially unfolded at pH 9 and C0206 starts unfolding at pH 8, and is almost fully unfolded at pH 9. These results validate our hypotheses, which led to the engineering of our pH sensitive protein complexes. Unfortunately, studying stability of all the engineered complexes under a range of conditions was not possible due to beamline time limitations. Nevertheless, we were able to prove that our approach to engineering protein stability was correct and working.

## 8.2 Discussion

The aim of the pH-sensitivity study was to explore the possibility of introducing pH-sensitivity to the SNARE complex by mutating key positively charged salt bridge participants to histidine residues. The expectation was that at a pH greater than histidine's pKa (6.0) the complexes would be less stable as the histidine residues would be unprotonated and the salt bridges would not form, whereas at a pH less than or equal to histidine's pKa, the histidines would be protonated and the salt bridges would remain intact and therefore similar stability to the control native complex (C04 or C05 depending on the length of VAMP). The results from the pull-downs revealed that all of the complexes tested followed this expected trend of stability decreasing, typified as normalised peptide band density decreasing, as pH increases. In the case of complexes C06 and C0206, this finding was corroborated by SRCD experiments, which showed differential pH sensitivity between pH 7.0 – 9.0.

Complexes C06 and C07 displayed the most dramatic decline in stability because of increasing pH in the pull-down assays. Similar results were observed for C06 in SRCD, where results were compared to C04 (control), and showed that C06 begins unfolding at ~ pH 8.5. These complexes contain the mutated VAMP peptides Brev2-06\_34PH and Brev2-07\_27PH, and native syntaxin

peptide Synt1-01\_34. The common salt bridges targeted by the histidine mutations in C06 and C07 are VAMP Arg47 with syntaxin Glu211, where the mutation was R47H, and VAMP Lys52 with SNAP-25 C-terminal Asp172, where the mutation was K52H. Due to the truncation in length to 27aa, C07 is missing the salt bridge between VAMP Lys59 and syntaxin Asp179, which is targeted by the K59H mutation in C06. This missing salt bridge may be slightly more stabilising for C06, which shows a greater value for assembly at pH 6 than C07, but thereafter it appears to have little effect on the stability past pH 7. This is suggested by the fact that amount of complex assembled at pH 8 is the same in both complexes.

SRCD was carried out on the pH-sensitivity complexes C06, C0206 with C04 acting as the control. Both C06 and C0206 contain a mutated Brev2-06\_34PH, so the comparison between the two complexes would be drawn by the mutated Synt1-02\_34PH that is present in C0206 and absent in C06. C06 shows greater stability than its counterpart C0206, whose unfolding begins at pH ~7.5-8.0 and then dramatically loses structure past pH 8.0. The difference in their stability could be explained by the R232H mutation in Synt1-02\_34PH, which targets a predicted salt bridge between Arg232 in syntaxin, and Asp64 in VAMP. C06 does not contain this mutation, and therefore the predicted salt bridge remains undisrupted, which may be the reason for its slightly superior stability compared to C0206.

Complexes C0206 and C0207 have a mutated syntaxin peptide Synt1-02\_34PH in commonality with one another. The trends displayed in the pull-down assay differs slightly in that C0206 still displays a somewhat stepwise decline with pH, whereas C0207 shows relatively constant stability until pH 7, and a sizeable drop in assembly at pH 8. One of the histidine mutations in Synt1-02\_34PH targets a salt bridge, which happens to be Arg232 in syntaxin (R232H mutation) with Asp64 in VAMP. Complex C0207 would not contain this salt bridge since Brev2-07\_27PH peptide length stops short of Asp232. This difference does not, however, explain why the pH-sensitivity pattern of C0207 differs from C07. Specifically, in C0207, the level of assembly at pH 6 is almost the same as at pH 7, indicating that assembly and pH-stability has been hindered even at pH 6. There are two other histidine mutations (R204H and R210H) in Synt1-02\_34PH, which are not engineered to target any salt bridges, but appear to have had a negative effect on complex assembly. It is not yet understood why, but it is speculated that it could be due to a gaps forming in these particular regions because of histidine's smaller residue volume ( $153.2 \text{ \AA}^3$ ) compared to arginine ( $173.4 \text{ \AA}^3$ ). The gaps could potentially destabilise complex assembly through the complementarity principle described in our hypothesis (**section 2.3**), and elaborated on in **section 5.1.3**, or by increasing the distance, and thereby decreasing the strength of any ionic interactions that may exist but were not predicted in the salt bridge analysis (**section 5.1.5** and **Figure 5.5**).

This argument is supported by the similar results achieved with complexes C0204 and C0205. These complexes exhibit near-identical trends and stability values (indicated by normalised peptide band density) to their mutated VAMP counterparts C0206 and C0207 respectively. Once again the key difference between the two is the absence of the R232H mutation in C0205, and this is expected to be the difference between the step-wise pH-sensitivity trend observed in the slightly longer 34aa length complex of C0204, and the constant stability until pH 8 observed in the truncated 27aa length complex C0205.

There is good agreement between the melting temperatures of full-length (FL/FL/FL) and partially truncated (FL/FL/34) SNARE complexes obtained using the PiStar-180 CD stopped-flow spectrometer and the synchrotron radiation CD (SRCD) beamline. The truncated SNARE complex FL/34/34 (otherwise referred to as C04) was prepared for thermal melt using the PiStar-180 CD instrument in the same manner as the full-length and partially truncated SNARE complexes, however it proved too unstable, and no structure could be detected. The preparation of samples entailed removal of DMSO, which the peptides were dissolved in, using desalting columns, which was perhaps too mechanically intensive, or the buffer exchange itself may have destabilised the complex causing it to disassemble. This was compounded by a relatively low concentration ( $\sim 3 \mu\text{M}$ ) after desalting. The PiStar-180 is a conventional CD spectrometer and does not have the benefits of the high flux synchrotron radiation, which has a superior signal-to-noise ratio allowing detection at low concentration even in the presence of DMSO, which was observed to absorb in the region of interest. It is desirable that any future CD spectroscopy involving the truncated complexes should be conducted using SRCD.

The trend expected from the thermostability pull-downs is best exemplified by the sigmoidal pattern of the graph generated for C04 (**Figure 8.2c**). Here, the initial plateau indicates assembly at low temperatures, then a decrease as the protein unfolds, and a final plateau at the end to indicate full disassembly. CFL04 showed an extreme version of this trend, with clear consistent initial and final plateaus but a sharp drop to indicate unfolding that contained no data points which reduces the reliability of the data.

This sigmoidal trend was even less well defined in complexes CFL05 and C05, which both lacked an initial and final plateau to indicate full assembly and disassembly. This gave rise to melting temperatures that were higher (in the case of C05 especially) than expected. Discrepancies in the melting temperatures measured using this method compared to CD spectroscopy were expected due to the difference in the heating regimes, and specifically the rate of heating. Therefore, these are interesting results that show the difference between the phenomena measured using CD and pull-down assay. Whilst CD spectra indicates protein folding and the existence of  $\alpha$ -helical structure

typical of fully assembled SNARE complexes, the pull-down does not quantify folding *per se*, but shows the quantity of protein still physically attached to SNAP-25. The latter is not necessarily properly folded at higher temperatures, which is evident from **Figure 8.2d**.

Consider that the complex in the pull-down assay has been exposed to isothermal for 20 min, with no temperature ramp up to the temperature of interest or down to room temperature at the end of the incubation time, whereas the CD samples were exposed to a much gentler, gradual increase in temperature at a rate of 1-2°C/min over a much longer period of time. The heating regime will definitely effect the melting temperature recorded for the protein so differences were expected, however, this cannot account for the overestimation of the melting temperature of C05 relative to CFL05 or even C04, which benefits from an additional heptad repeat. The data obtained for CFL05 and C05 are therefore unreliable, and perhaps would be improved by recording more temperature points to achieve a sigmoidal pattern and therefore permit a more accurate prediction of the 50% unfolded point.

Of the Improvement complexes, C14 was proven capable of successful assembly, which was previously unclear from the results of the native gels in **section 7.1.6.2**. The only pull-down graphs from this “set” with reliable melting trends belonged to the supernatants of complexes C12 and C14. They both similar melting temperatures around ~53-54°C, which is a considerably lower melting temperature than that recorded for the control C05 (~67°C). The expectation for the Improvement study was that the stability of these complexes should increase because of the mutations, however it is evident that there was no improvement in stability, only a decrease in stability was observed. What is also clear is that the M29F mutation in C14 does not cause disassembly, or radically decrease the stability when it is in combination with the other two mutations V22A and V36A. It is unclear why C13 is not capable of assembly with a single M29F mutation, and yet C14 does when in combination with the other mutations. It begs the question, do the other two mutations act to stabilise the negative effect of the M29F mutation? No conclusion has been reached to explain this discrepancy.

To explain the reduction in stability in C12 and C14 compared to the native C05 complex, consider the difference in hydrophobicity between alanine (-1.8) and valine (-4.2). Our interest here was to find out whether improving the regularity and consistency of the total residue volume (TRV) across the SNARE complex would improve the thermostability of the complex, and yet the decrease in stability as a result of mutations intended to achieve this purpose only further supports the supposition that hydrophobicity effectively “trumps” residue volume in terms of influencing complex stability. In this case, the gain that might have been achieved from a better residue volume fit is offset by the negative effect of a less hydrophobic residue in these a layers.

Of the Compensation complexes, only C15 was stable enough to be subjected to a pull-down. The graphs obtained from the beads/supernatant pull-down of this complex were contradictory, and did not follow a sigmoidal pattern. They are therefore unreliable, and cannot be interpreted in any meaningful way. SRCD was carried out on the Compensation complexes to address this weakness, and it was found that both the disrupted peptide complex C15, and the rescued counterpart C0315, was capable of assembly. Results were consistent with our expectations, as the disrupted complex C15 showed a drop in stability compared to the control complex C04. Moreover, the compensated C0315 showed a rise in stability corresponding to an increase in  $T_m$  of 28°C. This experiment provided evidence supporting our TRV volume conservation strategy (**section 6.1.1.2**).

Despite demonstrating successful assembly in the native gels (**section 7.1.6.2**), C11 proved to be too unstable for pull-down assay, as neither the beads nor supernatant products of the assay demonstrated any appreciable peptide bands. This complex contained all the mutations in complexes C08, C09, and C10, which were intended to destabilise the SNARE complex through a combination of breaking existing salt bridges and the simultaneous introduction of ionic repulsion, so this outcome fits the original hypothesis. Moreover, the pull-down itself is quite a mechanically intensive process involving multiple wash and transfer steps, and it's possible that while C11 was stable enough to remain assembled for a relatively straight-forward native gel, it simply wasn't sufficiently stable enough to remain at least partially intact at the end of it at any of the temperatures tested. No repeats were taken so it is also likely that perhaps the conditions on this particular attempt did not support facile complex assembly. SRCD thermal melt was carried out on C11 instead, and as we expected it showed very poor thermal stability with a  $T_m$  of 34°C. This was 24°C less than the control complex C04. This outcome supports our hypothesis and expectations outlined in **section 6.2.1.2**.

None of the other Salt Bridge study complexes showed a fully sigmoidal pattern in the pull-down assays. However, with the exception of some outliers, the trends were observed to have at least some partial sigmoidal character, and so unlike C15 they can be interpreted with some extent of reliability. Weaknesses have been identified in the pull-down assay results, and so in all cases we defer to the results from the SRCD experiment carried out on the Salt Bridge complexes, as this is an unequivocally superior method. C08 showed very strong stability, with a  $T_m$  of ~69°C, substantially higher than the C04 control, but this figure is likely to be overestimated due to the lack of a final plateau to indicate full disassembly. SRCD thermal melt data for C08 showed a  $T_m$  of 51°C, which is 7°C lower than the control complex C04. This complex contains the K59E mutation that was expected to heavily influence the assembly and stability of the complex since it occurs in the highly ionic, salt bridge-rich region between VAMP length 27 and 34 (positions 41-47 on "our"

scale). Moreover, K59 is also a participant of two scissile bonds that are targeted by the cleavage activity of clostridial neurotoxins BoNT D and F. This segment was observed to have a disproportionate effect on the stability of the complex, corresponding to a difference in melting temperature of  $\sim 19$  °C. The interpretation of this result is that the salt bridge between K59 and D179 (in SNAP-25 C-terminal) broken by the K59E mutation does not play an instrumental role in assembly nor acts to support the stability of the complex.

Contradictory results were obtained from the beads ( $T_m \sim 25^\circ\text{C}$ ) and supernatant ( $T_m \sim 55^\circ\text{C}$ ) products of the C09 pull-down, making it difficult to draw any meaningful conclusions about effect of the K52E mutation. Both graphs lacked a sigmoidal pattern, however the supernatant has been deemed less reliable than the beads as the “50% Unfolded” line intersects the graph of peptide band density twice. SRCD thermal melt data for C09 showed a  $T_m$  of  $56^\circ\text{C}$ , which is  $2^\circ\text{C}$  lower than the control complex C04. The mutation of interest was K52E, which was expected to break the salt bridge between K52 and D172 (in SNAP-25 C-terminal). This salt bridge occurs outside the salt bridge rich region between VAMP length 27 and 34, and yet appears to have a massively destabilising effect on the complex compared to the native C04 control. The bifurcated geometry of this particular salt bridge is worth considering when evaluating its apparent significance to the overall stability of the complex. Bifurcated interactions have the added advantage of delocalisation to further stabilise the salt bridge, and it could well be that this difference compared to the single interaction in the K59-D179 salt bridge of C08, contributes towards the greater influence of this mutation on complex stability if the beads results were found to be accurate.

The results for the supernatant product of the C10 pull-down also demonstrate low stability with a  $T_m$  of  $\sim 26^\circ\text{C}$ , and it is worth noting that the gel for the beads product did not reveal any peptide bands for any of the temperatures tested. SRCD thermal melt data for C10 showed a  $T_m$  of  $57^\circ\text{C}$ , indicating that the difference in stability between it and the control complex C04 is negligible. Unlike complexes C08 and C09, this mutation did not target any particular salt bridge, and instead aimed to introduce ionic repulsion between the mutant E43 and the proximally positioned E211 in syntaxin. E211 has been identified as a participant in a long-range salt bridge (with a distance at the upper bounds of interaction at  $3.8 \text{ \AA}$ ) with R47 in VAMP. The results here show that the attempt to introduce ionic repulsion, rather than targeting a specific predicted salt bridge, was not successful in bringing about a change in the stability of the complex.

As indicated in the Objectives (**section 2.2**) and the Methodology (**section 1.5.3**), fluorescence-based methods, FRET-HRM and thermofluor assay, were attempted in order to observe protein-protein interaction, and hence quantify complex assembly, and measure thermostability. In the case of the thermofluor assay (also known as “thermal shift assay”), using SYPRO Orange, despite the

positive control lysozyme showing a strong thermal response as predicted, the supramolecular SNARE complexes (CFL, C04, and C05) did not yield the traditional melting curves expected. This is not surprising since the observed effect is the disassembly of a tertiary protein complex, rather than the melting of a single subunit (as in lysozyme). The raw data for this can be seen in the **Appendix 14.1**. Similarly, no protein-protein interaction could be detected using the FRET-HRM methodology. In this case, it may be that the method itself requires optimisation since the positive control (binding pair Protein A and IgG) also remained undetected using this method. The match between the donor (fluorescein) and acceptor dyes (DABCYL) was not ideal. For the FRET to occur the absorption spectrum of the quencher and the emission, fluorescence spectrum of the donor should overlap. The relative efficiency of FRET depends on the size of the spectral overlap integral and the concentration of both donor and acceptor. The initial FRET experiments were conducted to evaluate experimental system for the detection of protein -protein interactions but the method was not used for the follow up experiments. The raw data obtained from the experiments for this study can be seen in the **Appendix 14.2** and **14.3**.

## 9. General Discussion and Future Research Developments

Bioinformatics analyses showed that hydrophobicity appeared to be greatest at the heptad segment flanking the ionic layer, and decreased towards either terminal. This may be to strengthen the immediate regions surrounding the otherwise disruptive ionic layer. On the subject of disruptive regions, segments -3 *bc* (positions 30-31) and -2 *efg* (positions 33-35) presented notable deviations from the trends in hydrophilicity and residue volumes. The ionic layer is insulated from this stretch by the -1 layer, however their close proximity would make it seem as though they act to destabilise the SNARE complex. This is decidedly unlikely however, since it occurs it is observed even in the standard complex 1N7S, which we know to be highly stable. These deviations must therefore have another purpose, for example, we speculate that the uncharacteristically hydrophobic -2 layer may form a groove that serves to bind other proteins such as the chaperone proteins.

Complementarity observed in the residue volumes between syntaxin and SNAP-25 N-terminal in the neuronal rat SNARE is in line with our hypothesis that these two helices initially bind in priority to SNAP-25 C-terminal. Moreover, this complementarity is greatest at the N-terminal of both chains, which adds further credence to the hypothesis since it is expected that the initial association begins at their N-termini. The residue volumes for the other two t-SNARE scenarios, syntaxin and SNAP-25 C-terminal, and the two SNAP-25 termini on the other hand, showed comparatively lower complementarity. Generally speaking, there was some consistency in the residue volumes of the segments throughout the SNARE motif, however it was not to the standard expected. Ultimately it is difficult to judge the regularity, consistency, or tightness of packing using residue volumes without having a control to compare the SNAREs with. A non-SNARE coiled coil would do well as a control, however as of writing this review, there are no known heterotetrameric parallel coiled coils that are not SNARE complexes.

Evidence was uncovered from a combination of bioinformatics and statistical analysis of hydrophobic residue volumes that supported the hypothesis that residue volumes at the N-terminal are highly consistent and regular in order to facilitate “tight” assembly and stability (**section 6.1.1**). There was a very clear distinction in the distribution of hydrophobic residue volumes between the N- and C-terminal regions of the SNARE complex motif. The N-terminal showed a much narrower distribution, with a standard deviation of 40, which was two-fold less than the C-terminal whose standard deviation was 80. The predicted deviation for the C-terminal was less than its standard deviation indicating greater variance in the population of residue volumes, and thus a greater degree of random distribution than the N-terminal whose predicted deviation was greater than the standard deviation.



Thermal melts SNARE complexes containing truncated VAMP proteins showed a non-linear relationship between the length of VAMP and the thermal stability of the SNARE complex it assembles in. The most significant finding was that the region between positions 41 and 47, encompassing the distance between VAMP of length 34 and 27, had a disproportionate effect on the stability of the complex, appearing to be responsible for a difference in melting temperature of ~19 °C. This region was investigated further, and it was revealed that it is rich in charged residues, with five salt bridges predicted to occur here, of which VAMP contributes two participants. These are D64 and K59, the latter was one of the subjects of the ionic interactions study outlined in **section 6.2.1.2**. It was anticipated that this study would yield results that would shed light on the precise role of this particular salt bridge on the stability of the complex, and whether it could be used as a “switch”, to initiate assembly and disassembly of a truncated peptide complex. In fact, complex C08 containing the mutant K59E, which was engineered to disrupt this salt bridge showed an improvement in thermal stability, negating this supposition and instead suggesting that this salt bridge has little to no impact on complex assembly and stability.

Assembly of complexes C04 and C05 was confirmed by CD spectroscopy, and was corroborated by evidence from native PAGE, and pull-down assay. This alone is a breakthrough in the project, because whilst SNARE complexes containing truncated syntaxin, or truncated VAMP have been reported in numerous publications, the simultaneous, and sizeable truncation of both VAMP and syntaxin to this extent, in a SNARE-based complex has not yet been reported. This is an important advance in terms of applying these SNARE-based complexes as linkers in delivery devices. Shorter linkers are more desirable, especially during the nanoparticle-conjugation process, where longer protein chains are expected to present more interaction sites and therefore a greater propensity for agglomeration or aggregation, which would hinder the payload delivery process.

Successful assembly of full-length SNARE complexes on both magnetic and gold nanoparticles was established by CD spectroscopy. This acts as early validation of the application of SNARE-based complexes as linkers in a delivery device. Next steps would include confirming that disassembly of complex-on-NP is possible by heat-induction, and verifying that truncated peptide complexes are also compatible with this system, and similarly assemble and disassemble on nanoparticles.

Of the Improvement study, mutations made to two of the complexes still supported facile assembly however there was no improvement on the stability of these complexes compared to the control C05. This does not support the hypothesis behind the complementarity principle we outlined initially in **section 2.3**, and elaborated on in **section 5.1.3**. This principle proposes that it is complementarity between the residue volumes inhabiting the same heptad layer that leads to tighter

packing and therefore supports assembly and results in greater stability. The lack of improvement in stability observed in these complexes has been deduced as a result of the reduction in hydrophobicity (i.e. valine to alanine). Thus, hydrophobicity has a greater influence on complex stability than maintaining complementarity and consistency in the total residue volume across the complex.

Of the Compensation study, the complex engineered to have poor stability, C15, was the only complex to show successful assembly in a native gel. Success was observed in the SRCO thermal melt experiment that followed this. The disrupted complex C15 was shown to have slightly lower stability than the control complex, and the rescued complex C0315, was shown to have enhanced stability as a result of the mutations that restored the original TRV. These findings act as supporting evidence that our unique TRV volume conservation strategy works, and is a viable method of peptide design and modification.

The pH-sensitivity study succeeded in its aim of introducing pH-sensitivity into the complexes by mutating key ionic residues to histidines. Different mutated SNARE peptides exhibited slight variations in the expected pH-sensitivity trend. The key characteristics that appear to influence these variations are the type of SNARE peptide that is mutated, and the length of the complex. To elaborate, in the first scenario, a stronger and more dramatic decline from pH 8 was observed when complexes contained a mutated syntaxin (in combination with mutated or native VAMP). In the second scenario, truncated complexes of length 27aa containing the mutated syntaxin peptide exhibited acute pH-sensitivity, in the sense that assembly appeared to be unaffected by pH between 6-7, but a sharp drop was observed at pH 8.

These findings could be exploited as design principles for stimuli sensitive SNARE-based linkers, and indeed, they constitute a significant advancement in the field of rational protein design and engineering. The non-linear trend of the truncated complexes containing the mutated syntaxin peptide could be exploited where acute sensitivity is required, for example, where the complex is required to remain fully intact at physiological pH until a certain time, at which point a simple change in pH will disassemble the complex. If this linker were applied in the context of a delivery device, this type of sensitivity would result in instantaneous release of a payload as a result of a small shift in pH. In the same vein of thought, the step-wise trend of the longer complexes containing mutated VAMP peptides could be utilised where a slow-release of payload is desired. In this case, a payload could be slowly released as a consequence of complex disassembly, in proportion to an increase in pH.

The complexes in the Salt Bridge study were engineered to have lower stability compared to the control, and this was anticipated to be the result of ionic repulsion introduced by the mutations of interest. This hypothesis was validated in the case of complex C11, which contained all three mutations present in the other three Salt Bridge study complexes (C08, C09, C10). This complex showed a remarkable drop in stability compared to the control complex, and shows that targeting predicted salt bridges is a viable option for modifying peptide complex stability. It also shows that targeting multiple predicted salt bridges will have a greater impact on peptide stability. Complexes that contained mutations targeting a single predicted salt bridge showed negligible differences in thermal stability compared to the control complex C04. This is especially apparent in complex C08, which defied expectations that it would have the lowest stability owing to the K59E mutation occurring in a salt bridge rich region that was predicted to be highly influential for complex assembly and stability. Instead it showed a melting temperature only 7°C less than the control C04, refuting this prediction and indicating that the salt bridge involving K59 is inessential for stability unless in combination with other mutations.

The overarching conclusion of both the Residue Volume and Ionic Interactions studies is that hydrophobicity is the most influential characteristic on the ability of a complex to assemble or disassemble. It has the greatest impact on complex stability, and thus the melting temperature, but has not been shown to adversely affect assembly unlike modifying residue volume. Targeting salt bridges has had some success in both reducing and increasing complex stability, however the design process is a lot more difficult than hydrophobicity. The outcomes are seemingly arbitrary, and more difficult to predict. Until repeats are made, and supported by a secondary method such as CD thermal melt, no conclusion can be reached regarding the thermostability of any of the other complexes tested in this study.

Finally, in evaluating the methods used for the stability studies, the fundamental weakness of the pull-down assay method was that the sigmoidal trend expected was often only partially observed meaning such results are unreliable and analysis of the melting temperature is likely to be skewed in either direction resulting in over- or underestimation. More data points are required, as well as refinement of the procedure to make it more reproducible and therefore allow repeats to be conducted that would yield results that are statistically significant.

## 10. Conclusion

In this work, we have contributed to the current understanding of the molecular mechanisms underpinning SNARE complex assembly, and its hierarchy, through bioinformatics analyses conducted on our own unique SNARE protein structure compactness analysis tool, and a database we compiled of SNARE proteins whose structures have previously been elucidated. Our findings suggest that the elevated hydrophobic character of the residues flanking the disruptive ionic layer may be responsible for stabilising this region, and the complementarity observed in the residue volumes at the N-termini of syntaxin and SNAP-25, hypothesised to be the site of the initial association of SNARE proteins, facilitates assembly and lends stability to the nascent complex.

Structural, and thermal melt studies of partially truncated SNARE complexes using high-resolution Synchrotron Radiation Circular Dichroism (SRCD) revealed that the region between VAMP length 34 and 27 aa is the most destabilising in proportion to its length, and the shorter VAMP lengths had the strongest impact on the melting temperature ( $T_m$ ) drawing it closer to the physiological range ( $\sim 57^\circ\text{C}$  in the case of VAMP length 27 aa). Ionic interactions in the form of salt bridges existing between the SNARE proteins in the complex were also predicted. These discoveries have informed the rational design process of the SNARE-based stimuli-sensitive peptides.

This study reported for the first time, that SNARE complexes containing simultaneously truncated syntaxin (length 34 aa) and VAMP (lengths 34 and 27 aa) are capable of assembly. The concern was that such a sizeable truncation of two key SNARE proteins would result in the loss of a number of potentially essential heptad repeats, which would hinder recognition between the SNARE proteins, preventing assembly. These results represent a milestone achievement in view of the greater aim of incorporating these responsive SNARE-based complexes into payload-delivery devices, where shorter linkers are more desirable as they present fewer complications in nanoparticle-conjugation, and payload delivery.

Mutations designed to test the residue volume complementarity principle outlined in the hypothesis, or to target ionic interactions in the form of salt bridges succeeded in influencing the thermostability of a number of complexes. A notable success was the Compensation study complexes, whose experimental results were consistent with our hypothesis regarding residue volume complementarity. This provided evidence to support our unique TRV volume conservation strategy, and showed that it is a viable method of engineering peptide stability. However, in a number of cases the results did not fulfil the original design expectations. It was found that in each individual case, it was the change in hydrophobicity rather than residue volume that was responsible for

influencing these mutant complexes' thermostability. This outcome has revealed that the most efficient way of generating a large impact on coiled-coil complex thermostability is by modifying the hydrophobicity of residues in positions *a* and *d*. Radically altering residue volume is more likely to have an adverse effect on assembly rather than thermostability, and targeting ionic interactions can be fruitful however the consequences are more difficult to predict.

Histidine mutations, designed to introduce pH-sensitivity by targeting key ionic residues, were highly effective in achieving this aim. The variations in the pH-sensitivity trend exhibited by the different complexes of this study have been speculated as a potential design principle for controlling the degree of sensitivity (instantaneous versus slow-release) conferred to the payload delivery device.

Initial concerns about the difficulties of conjugating the SNARE-based protein complexes to nanoparticles were allayed by the results from the proof-of-principle trial wherein full-length SNARE complexes were demonstrated by SRCD to successfully immobilise on both gold and magnetic nanoparticle surfaces. This is an exciting development that validates the use of both of these nanoparticle materials in any later potential biotechnological applications of these SNARE-based peptide complexes.

In conclusion, this study has achieved its central aim of generating stimuli-responsive SNARE-based peptide complexes that are capable of self-assembly, and controlled disassembly within a physiological temperature and pH range. Furthermore, it has demonstrated, in proof-of-principle experiments that it is feasible to conjugate SNARE-based proteins to metal nanoparticles (magnetic iron and gold materials were tested), and the complexes have been shown to assemble successfully on the nanoparticle surface. This validates the application of these stimuli-sensitive peptide complexes as linkers in the context of a nanoparticle-linked delivery device.

## 11. References

- Abadeer, N.S. Murphy, C.J. 2016. Recent Progress in Cancer Thermal Therapy Using Gold Nanoparticles. *J. Phys. Chem. C* 120, 4691–4716. <https://doi.org/10.1021/acs.jpcc.5b11232>
- Akbarzadeh, A. Samiei, M. Davaran, S. 2012. Magnetic nanoparticles: preparation, physical properties, and applications in biomedicine. *Nanoscale Res. Lett.* 7, 144. <https://doi.org/10.1186/1556-276X-7-144>
- Akey, D.L. Malashkevich, V.N. Kim, P.S. 2001. Buried Polar Residues in Coiled-Coil Interfaces †,‡. *Biochemistry* 40, 6352–6360. <https://doi.org/10.1021/bi002829w>
- Amendola, V. Pilot, R. Frasconi, M. Maragò, O.M. Iatì, M.A. 2017. Surface plasmon resonance in gold nanoparticles: a review. *J. Phys. Condens. Matter* 29, 203002. <https://doi.org/10.1088/1361-648X/aa60f3>
- Antonucci, F. Corradini, I. Fossati, G. Tomasoni, R. Menna, E. Matteoli, M. 2016. SNAP-25, a Known presynaptic protein with emerging postsynaptic functions. *Front. Synaptic Neurosci.* 8, 1–9. <https://doi.org/10.3389/fnsyn.2016.00007>
- Apland, J.P. Biser, J.A. Adler, M. Ferrer-Montiel, A. V. Montal, M. Filbert, M.G. 1999. Peptides that mimic the carboxy-terminal domain of SNAP-25 block acetylcholine release at an *Aplysia* synapse. *J. Appl. Toxicol.* 19, 23–26. [https://doi.org/10.1002/\(SICI\)1099-1263\(199912\)19:1+<S23::AID-JAT609>3.0.CO;2-X](https://doi.org/10.1002/(SICI)1099-1263(199912)19:1+<S23::AID-JAT609>3.0.CO;2-X)
- Apostolovic, B. Deacon, S.P.E. Duncan, R. Klok, H. 2011. Cell Uptake and Trafficking Behavior of Non-covalent , Coiled-coil Based Polymer – Drug Conjugates a. *Macromol. Rapid Commun.* 32, 11–18. <https://doi.org/10.1002/marc.201000434>
- Apostolovic, B. Klok, H. 2008. pH-Sensitivity of the E3/K3 Heterodimeric Coiled Coil. *Biomacromolecules* 9, 3173–3180.
- Baker, R.W. Hughson, F.M. 2016. Chaperoning SNARE assembly and disassembly. *Nat. Rev. Mol. Cell Biol.* 17, 465–479. <https://doi.org/10.1038/nrm.2016.65>
- Balch, W.E. Dunphy, W.G. Braell, W.A. Rothman, J.E. 1984. Reconstitution of the Transport of Protein between Successive Compartments of the Golgi Measured by the Coupled Incorporation of N-Acetylglucosamine. *Cell* 39, 405–416.
- Basu, S. Mukharjee, D. 2017. Salt-bridge networks within globular and disordered proteins: characterizing trends for designable interactions. *J. Mol. Model.* 23. <https://doi.org/10.1007/s00894-017-3376-y>
- Batista, A.F.R. Martínez, J.C. Hengst, U. 2017. Intra-axonal Synthesis of SNAP25 Is Required for the Formation of Presynaptic Terminals. *Cell Rep.* 20, 3085–3098. <https://doi.org/10.1016/j.celrep.2017.08.097>
- Baumann, G. Frommel, C. Sander, C. 1989. Polarity as a criterion in protein design. *Protein Eng.*

Des. Sel. 2, 329–334. <https://doi.org/10.1093/protein/2.5.329>

- Bennett, M.K. Calakos, N. Scheller, R.H. 1992. Syntaxin: a synaptic protein implicated in docking of synaptic vesicles at presynaptic active zones. *Science* (80-. ). 257, 255–259.
- Berman, H.M, Westbrook, J. Feng, Z. Gilliland, G. Bhat, T.N. Weissig, H. Shindyalov, I.N. Bourne, P.E. 2000. The Protein Data Bank. *Nucleic Acids Res.* 28, 235–242.
- Binz, T. Blasi, J. Yamasaki, S. Baumeister, A. Link, E. Sudhof, T.C. Jahn, R. Niemann, H. 1994. Proteolysis of SNAP-25 by types E and A botulinum neurotoxins. *J. Biol. Chem.* 269, 1617–1620.
- Blanes-Mira, C. Merino, J.M. Valera, E. Fernández-Ballester, G. Gutiérrez, L.M. Viniegra, S. Pérez-Payá, E. Ferrer-Montiel, A. 2004. Small peptides patterned after the N-terminus domain of SNAP25 inhibit SNARE complex assembly and regulated exocytosis. *J. Neurochem.* 88, 124–135. <https://doi.org/2133> [pii]
- Blasi, J. Chapman, E.R. Yamasaki, S. Binz, T. Niemann, H. Jahn, R. 1993. Botulinum neurotoxin C1 blocks neurotransmitter release by means of cleaving HPC-1/syntaxin. *EMBO J.* 12, 4821–8.
- Blom, N. Gammeltoft, S. Burnak, S. 1999. Sequence and structure-based prediction of eukaryotic protein phosphorylation sites. *J. Mol. Biol.* 294, 1351–1362.
- Bombardier, J.P. Munson, M. 2015. Three steps forward, two steps back: Mechanistic insights into the assembly and disassembly of the SNARE complex. *Curr. Opin. Chem. Biol.* 29, 66–71. <https://doi.org/10.1002/aur.1474>. Replication
- Bowen, M.E. Weninger, K. Brunger, A.T. Chu, S. 2004. Single Molecule Observation of Liposome-Bilayer Fusion Thermally Induced by Soluble N-Ethyl Maleimide Sensitive-Factor Attachment Protein Receptors (SNAREs). *Biophys. J.* 87, 3569–3584. <https://doi.org/10.1529/biophysj.104.048637>
- Bracher, A. Kadlec, J. Betz, H. Weissenhorn, W. 2002. X-ray structure of a neuronal complexin-SNARE complex from squid. *J. Biol. Chem.* 277, 26517–26523. <https://doi.org/10.1074/jbc.M203460200>
- Braiman, L. Alt, A. Kuroki, T. Ohba, M. Tennenbaum, T. Sampson, S.R. 2001. Activation of Protein Kinase C  $\zeta$  Induces Serine Phosphorylation of VAMP2 in the GLUT4 Compartment and Increases Glucose Transport in Skeletal Muscle Activation of Protein Kinase C Induces Serine Phosphorylation of VAMP2 in the GLUT4 Compartment and Incr. *Mol. Cell. Biol.* 21, 7852–7861. <https://doi.org/10.1128/MCB.21.22.7852>
- Brunger, A.T. 2006. Structure and function of SNARE and SNARE-interacting proteins. *Q. Rev. Biophys.* 38, 1. <https://doi.org/10.1017/S0033583505004051>
- Brunger, A.T. Weninger, K. Bowen, M. Chu, S. 2009. Single molecule studies of the neuronal SNARE fusion machinery. *Annu. Rev. Biochem.* 78, 903–928. <https://doi.org/10.1146/annurev.biochem.77.070306.103621>. Single

- Buck, M. Karplus, M. 2001. Hydrogen bond energetics: A simulation and statistical analysis of N-methyl acetamide (NMA), water, and human lysozyme. *J. Phys. Chem. B* 105, 11000–11015. <https://doi.org/10.1021/jp011042s>
- Burkhard, P. Ivaninskii, S. Lustig, A. 2002. Improving coiled-coil stability by optimizing ionic interactions. *J. Mol. Biol.* 318, 901–910. [https://doi.org/10.1016/S0022-2836\(02\)00114-6](https://doi.org/10.1016/S0022-2836(02)00114-6)
- Burkhard, P. Meier, M. Lustig, a, 2000. Design of a minimal protein oligomerization domain by a structural approach. *Protein Sci.* 9, 2294–301. <https://doi.org/10.1110/ps.9.12.2294>
- Burkhardt, P. Hattendorf, D.A. Weis, W.I. Fasshauer, D. 2008. Munc18a controls SNARE assembly through its interaction with the syntaxin N-peptide. *Embo J* 27, 923–933. <https://doi.org/emboj200837> [pii]r10.1038/emboj.2008.37
- Bykhovskaia, M. Jagota, A. Gonzalez, A. Vasin, A. Littleton, J.T. 2013. Interaction of the complexin accessory helix with the C-terminus of the SNARE complex: Molecular-dynamics model of the fusion clamp. *Biophys. J.* 105, 679–690. <https://doi.org/10.1016/j.bpj.2013.06.018>
- Chao, H. Bautista, D.L. Litowski, J. Irvin, R.T. Hodges, R.S. 1998. Use of a heterodimeric coiled-coil system for biosensor application and affinity purification 715, 307–329.
- Chatterjee, D.K. Diagaradjane, P. Krishnan, S. 2011. Nanoparticle-mediated hyperthermia in cancer therapy. *Ther. Deliv.* 2, 1001–1014. <https://doi.org/10.4155/tde.11.72>
- Chen, C. Constantinou, A. Deonarain, M. 2011. Modulating antibody pharmacokinetics using hydrophilic polymers. *Expert Opin. Drug Deliv.* 8, 1221–1236.
- Chen, S. Barbieri, J.T. 2006. Unique substrate recognition by botulinum neurotoxins serotypes A and E. *J. Biol. Chem.* 281, 10906–10911. <https://doi.org/10.1074/jbc.M513032200>
- Chen, S. Kim, J.J.P. Barbieri, J.T. 2007. Mechanism of substrate recognition by botulinum neurotoxin serotype A. *J. Biol. Chem.* 282, 9621–9627. <https://doi.org/10.1074/jbc.M611211200>
- Chen, X. Tomchick, D.R. Kovrigin, E. Arac, D. Machius, M. Sudhof, T.C. Rizo, J. 2002. Three-dimensional structure of the complexin/SNARE complex. *Neuron* 33, 397–409. [https://doi.org/10.1016/S0896-6273\(02\)00583-4](https://doi.org/10.1016/S0896-6273(02)00583-4)
- Chen, Y.-H. Tsai, C.-Y. Huang, P.-Y. Chang, M.-Y. Cheng, P.-C. Chou, C.-H. Chen, D.-H. Wang, C.-R. Shiau, A.-L. Wu, C.-L. 2007. Methotrexate Conjugated to Gold Nanoparticles Inhibits Tumor Growth in a Syngeneic Lung Tumor Model. *Mol. Pharm.* 4, 713–722. <https://doi.org/10.1021/mp060132k>
- Clary, D.O. Rothman, J.E. 1990. Purification of Three Related Peripheral Membrane Proteins Needed for Vesicular Transport\*. *J. Biol. Chem.* 265, 10109–10117.
- Clary, O.D. Griff, I.C. Rothman, J.E. 1990. SNAPs, a family of NSF attachment proteins involved in intracellular membrane fusion in animals and yeast. *Cell* 61, 709–721. [https://doi.org/DOI:10.1016/0092-8674\(90\)90482-T](https://doi.org/DOI:10.1016/0092-8674(90)90482-T)
- COILS ExPASy, n.d. COILS [WWW Document]. URL



- [http://www.ch.embnet.org/software/COILS\\_form.html](http://www.ch.embnet.org/software/COILS_form.html) (accessed 12.27.16).
- Colbert, K.N. Hattendorf, D. a, Weiss, T.M. Burkhardt, P. Fasshauer, D. Weis, W.I. 2013. Syntaxin1a variants lacking an N-peptide or bearing the LE mutation bind to Munc18a in a closed conformation. *Proc. Natl. Acad. Sci. U. S. A.* 110, 12637–42. <https://doi.org/10.1073/pnas.1303753110>
- Conserved Domain Database NCBI, n.d. Conserved Domain Database [WWW Document]. URL <https://www.ncbi.nlm.nih.gov/Structure/cdd/wrpsb.cgi> (accessed 12.27.16).
- Consortium, S. n.d. STRING database [WWW Document]. URL <http://string-db.org> (accessed 12.27.16).
- Cornell, R.M. Schwertmann, U. 2006. *The Iron Oxides: Structure, Properties, Reactions, Occurrences and Uses*. Wiley.
- Craig, T.J. Anderson, D. Evans, A.J. Girach, F. Henley, J.M. 2015. SUMOylation of Syntaxin1A regulates presynaptic endocytosis. *Sci. Rep.* 5, 17669. <https://doi.org/10.1038/srep17669>
- Dai, H. Shen, N. Araç, D. Rizo, J. 2007. A Quaternary SNARE-Synaptotagmin-Ca<sup>2+</sup>-Phospholipid Complex in Neurotransmitter Release. *J. Mol. Biol.* 367, 848–863. <https://doi.org/10.1016/j.jmb.2007.01.040>
- Daraee, H. Eatemadi, A. Abbasi, E. Aval, S.F. Kouhi, M. Akbarzadeh, A. 2016. Application of gold nanoparticles in biomedical and drug delivery. *Artif. Cells, Nanomedicine Biotechnol.* 44, 410–422. <https://doi.org/10.3109/21691401.2014.955107>
- Darby, N.J. Creighton, T.E. 1993. *Protein structure: In focus*. Oxford University Press.
- Dawidowski, D. Cafiso, D.S. 2016. Munc18-1 and the Syntaxin-1 N Terminus Regulate Open-Closed States in a t-SNARE Complex. *Structure* 24, 392–400. <https://doi.org/10.1016/j.str.2016.01.005>
- Dawidowski, D. Cafiso, D.S. 2013. Allosteric control of syntaxin 1a by munc18-1: Characterization of the open and closed conformations of syntaxin. *Biophys. J.* 104, 1585–1594. <https://doi.org/10.1016/j.bpj.2013.02.004>
- Deatherage, B.L. Cookson, B.T. 2012. Membrane Vesicle Release in Bacteria , Eukaryotes , and Archaea : a conserved yet underappreciated aspect of microbial life. *Infect. Immun.* 80, 1948–1957. <https://doi.org/10.1128/IAI.06014-11>
- Deatsch, A.E. Evans, B.A. 2014. Heating efficiency in magnetic nanoparticle hyperthermia. *J. Magn. Magn. Mater.* 354, 163–172. <https://doi.org/10.1016/j.jmmm.2013.11.006>
- Donald, J.E. Kulp, D.W. Degrado, W.F. 2012. Salt Bridges: Geometrically Specific, Designable Interactions. *Biochemistry* 79, 898–915. <https://doi.org/10.1002/prot.22927>.Salt
- Dubois, T. Kerai, P. Learmonth, M. Cronshaw, A. Aitken, A. 2002. Identification of syntaxin-1A sites of phosphorylation by casein kinase I and casein kinase II. *Eur. J. Biochem.* 269, 909–914. <https://doi.org/10.1046/j.0014-2956.2001.02725.x>
- Ernst, J.A. Brunger, A.T. 2003. High resolution structure, stability, and synaptotagmin binding of a

truncated neuronal SNARE complex. *J. Biol. Chem.* 278, 8630–8636.

<https://doi.org/10.1074/jbc.M211889200>

ExPASy, S. n.d. ScanProsite [WWW Document]. URL <http://prosite.expasy.org/scanprosite/> (accessed 12.27.16).

Falagan-Lotsch, P. Grzincic, E.M. Murphy, C.J. 2016. One low-dose exposure of gold nanoparticles induces long-term changes in human cells. *Proc. Natl. Acad. Sci. U. S. A.* 113, 13318–13323. <https://doi.org/10.1073/pnas.1616400113>

Fasshauer, D. 2003a. Structural insights into the SNARE mechanism. *Biochim. Biophys. Acta - Mol. Cell Res.* 1641, 87–97. [https://doi.org/10.1016/S0167-4889\(03\)00090-9](https://doi.org/10.1016/S0167-4889(03)00090-9)

Fasshauer, D. 2003b. Structural insights into the SNARE mechanism 1641, 87–97. [https://doi.org/10.1016/S0167-4889\(03\)00090-9](https://doi.org/10.1016/S0167-4889(03)00090-9)

Fasshauer, D. Sutton, R.B. Brunger, A.T. Jahn, R. 1998. Conserved structural features of the synaptic fusion complex: SNARE proteins reclassified as Q- and R-SNAREs. *Proc. Natl. Acad. Sci. U. S. A.* 95, 15781–6. <https://doi.org/10.1073/pnas.95.26.15781>

Fernandez, I. Ubach, J. Dulubova, I. Zhang, X.Y. Sudhof, T.C. Rizo, J. 1998. Three-dimensional structure of an evolutionarily conserved N-terminal domain of syntaxin 1A. *Cell* 94, 841–849. [https://doi.org/10.1016/S0092-8674\(00\)81742-0](https://doi.org/10.1016/S0092-8674(00)81742-0)

Ferrari, E. Soloviev, M. Niranjana, D. Arsenault, J. Chunjing, G. Vallis, Y. O'Brien, J. Davletov, B. 2012. Assembly of Protein Building Blocks Using a Short Synthetic Peptide. *Bioconjug. Chem.* 23, 479–484. <https://doi.org/10.1021/bc2005208>

Foran, P. Shone, C.C. Dolly, J.O. 1994. Differences in the Protease Activities of Tetanus and Botulinum B Toxins Revealed by the Cleavage of Vesicle-Associated Membrane Protein and Various Sized Fragments. *Biochemistry* 33, 15365–15374. <https://doi.org/10.1021/bi00255a017>

Fries, E. Rothman, J.E. 1980. Transport of vesicular stomatitis virus glycoprotein in a cell-free extract. *Proc. Natl. Acad. Sci. U. S. A.* 77, 3870–4. <https://doi.org/10.1073/pnas.77.7.3870>

Fukuda, M. 2002. Vesicle-associated Membrane Protein-2/Synaptobrevin Binding to Synaptotagmin I promotes O-glycosylation of Synaptotagmin I. *J. Biol. Chem.* 277, 30351–30358. <https://doi.org/10.1074/jbc.M204056200>

Gasteiger, E. Hoogland, C. Gattiker, A. Duvaud, S. Wilkins, M.R. Appel, R.D. Bairoch, A. 2005. Protein Identification and Analysis Tools on the ExPASy Server. *Proteomics Protoc. Handb.* 571–607. <https://doi.org/10.1385/1592598900>

Glick, B.S. Rothman, J.E. 1987. Possible role for fatty acyl-coenzyme A in intracellular protein transport. *Nature* 326, 309–12. <https://doi.org/10.1038/326309a0>

GlobPlot EMBL, n.d. GlobPlot [WWW Document]. URL <http://globplot.embl.de> (accessed 12.27.16).

Gonzalez-Fernandez, M.A. Torres, T.E. Andrés-Vergés, M. Costo, R. de la Presa, P. Serna, C.J. Morales, M.P. Marquina, C. Ibarra, M.R. Goya, G.F. 2009. Magnetic nanoparticles for power

- absorption: Optimizing size, shape and magnetic properties. *J. Solid State Chem.* 182, 2779–2784. <https://doi.org/10.1016/j.jssc.2009.07.047>
- Gonzalez, L. Woolfson, D.N. Alber, T. 1996. Buried polar residues and structural specificity in the GCN4 leucine zipper. *Nature* 3, 1011–1018.
- Greenfield, N.J. 2007. Using circular dichroism spectra to estimate protein secondary structure. *Nat. Protoc.* 1, 2876–2890. <https://doi.org/10.1038/nprot.2006.202>
- Griff, I.C. Schekman, R. Rothman, J.E. Kaiser, C.A. 1992. The Yeast Sec17 Gene-Product Is Functionally Equivalent to Mammalian Alpha-Snap Protein. *J. Biol. Chem.* 267, 12106–12115.
- Guex, N. Peitsch, M.C. 1997. SWISS-MODEL and the Swiss-PdbViewer: An environment for comparative protein modelling. *Electrophoresis* 18, 2714–2723.
- Guo, J. Chen, S. 2013. Unique substrate recognition mechanism of the botulinum neurotoxin D light chain. *J. Biol. Chem.* 288, 27881–27887. <https://doi.org/10.1074/jbc.M113.491134>
- Gupta, R. and S.B. 2002. Prediction of glycosylation across the human proteome and the correlation to protein function. in: *Pacific Symposium on Biocomputing*. pp. 7:310-322.
- Gutiérrez, L.M. Cánaves, J.M. Ferrer-Montiel, A. V. Reig, J.A. Montal, M. Viniegra, S. 1995. A peptide that mimics the carboxy-terminal domain of SNAP-25 blocks Ca<sup>2+</sup>-dependent exocytosis in chromaffin cells. *FEBS Lett.* 372, 39–43. [https://doi.org/10.1016/0014-5793\(95\)00944-5](https://doi.org/10.1016/0014-5793(95)00944-5)
- Han, J. Pluhackova, K. Böckmann, R.A. 2017. The multifaceted role of SNARE proteins in membrane fusion. *Front. Physiol.* 8. <https://doi.org/10.3389/fphys.2017.00005>
- Hayashi, T. McMahon, H. Yamasaki, S. Binz, T. Hata, Y. Südhof, T.C. Niemann, H. 1994. Synaptic vesicle membrane fusion complex: action of clostridial neurotoxins on assembly. *EMBO J.* 13, 5051–61.
- He, R. Zhang, J. Yu, Y. Jizi, L. Wang, W. Li, M. 2018. New Insights Into Interactions of Presynaptic Calcium Channel Subtypes and SNARE Proteins in Neurotransmitter Release. *Front. Mol. Neurosci.* 11, 1–11. <https://doi.org/10.3389/fnmol.2018.00213>
- Hepp, R. Cabaniols, J. Roche, P. 2002. Differential phosphorylation of SNAP-25 in vivo by protein kinase C and protein kinase A. *FEBS Lett.* 532, 52–56. [https://doi.org/10.1016/S0014-5793\(02\)03629-3](https://doi.org/10.1016/S0014-5793(02)03629-3)
- Hess, D.T. Slater, T.M. Wilson, C. Skene, J.H.P. 1992. The 25 kDa Synaptosomal-associated Protein SNAP-25 Is the Major Methionine-Rich Polypeptide in Rapid Axonal Transport and a Major Substrate for Palmitoylation in Adult CNS. *J. Neurosci.* 12, 4634–4641.
- Hodges, R.S. 1996. De novo design of  $\alpha$ -helical proteins: basic research to medical applications. *Biochem. Cell Biol.* 74, 133–154. <https://doi.org/10.1139/o96-015>
- Hong, W.J. Lev, S. 2014. Tethering the assembly of SNARE complexes. *Trends Cell Biol.* 24, 35–43. <https://doi.org/10.1016/j.tcb.2013.09.006>
- Hughson, F.M. 2013. Chaperones that SNARE neurotransmitter release. *Science* (80-. ). 339, 406–

407. <https://doi.org/10.1126/science.1233801>

- Humphrey, W. Dalke, A. Schulten, K. 1996. VMD - Visual Molecular Dynamics. *J. Molec. Graph.* 14, 33–38.
- Huyghues-despointes, B.M.P. Scholtz, J.M. Baldwin, R.L. 1993. Helical peptides with three pairs of Asp-Arg and Glu-Arg residues in different orientations and spacings. *Protein Sci.* 2, 80–85.
- Jahn, R. Scheller, R.H. 2006. SNAREs — engines for membrane fusion. *Nat. Rev. Mol. Cell Biol.* 7, 631–643. <https://doi.org/10.1038/nrm2002>
- Jeffrey, G.A. 1997. An introduction to hydrogen bonding. Oxford University Press, Oxford.
- Johansen, M.B. Kiemer, L. Brunak, S. 2006. Analysis and prediction of mammalian protein glycation. *Glycobiology* 16, 844–853. <https://doi.org/10.1093/glycob/cwl009>
- Kaiser, C.A. Schekman, R. 1990. Distinct sets of SEC genes govern transport vesicle formation and fusion early in the secretory pathway. *Cell* 61, 723–733.
- Kakakhel, M. Tebbe, L. Makia, M.S. Conley, S.M. Sherry, D.M. Al-Ubaidi, M.R. Naash, M.I. 2020. Syntaxin 3 is essential for photoreceptor outer segment protein trafficking and survival. *Proc. Natl. Acad. Sci. U. S. A.* 117, 20615–20624. <https://doi.org/10.1073/pnas.2010751117>
- Kaksonen, M. Roux, A. 2018. Mechanisms of clathrin-mediated endocytosis. *Nat. Rev. Mol. Cell Biol.* 19, 313–326. <https://doi.org/10.1038/nrm.2017.132>
- Kavanagh, D.M. Smyth, A.M. Martin, K.J. Dun, A. Brown, E.R. Gordon, S. Smillie, K.J. Chamberlain, L.H. Wilson, R.S. Yang, L. Lu, W. Cousin, M.A. Rickman, C. Duncan, R.R. 2014. A molecular toggle after exocytosis sequesters the presynaptic syntaxin1a molecules involved in prior vesicle fusion. *Nat. Commun.* 5, 5774. <https://doi.org/10.1038/ncomms6774>
- Kee, Y. Lin, R.C. Hsu, S.C. Scheller, R.H. 1995. Distinct domains of syntaxin are required for synaptic vesicle fusion complex formation and dissociation. *Neuron* 14, 991–998.
- Kemmer, G. Keller, S. 2010. Nonlinear least-squares data fitting in Excel spreadsheets. *Nat. Protoc.* 5, 267–281. <https://doi.org/10.1038/nprot.2009.182>
- Kenworthy, A.K. 2001. Imaging protein-protein interactions using fluorescence resonance energy transfer microscopy. *Methods* 24, 289–296. <https://doi.org/10.1006/meth.2001.1189>
- Koike, S. Jahn, R. 2019. SNAREs define targeting specificity of trafficking vesicles by combinatorial interaction with tethering factors. *Nat. Commun.* 10. <https://doi.org/10.1038/s41467-019-09617-9>
- Krogh, a, Larsson, B. von Heijne, G. Sonnhammer, E. 2001. Predicting transmembrane protein topology with a hidden Markov model: application to complete genomes. *J. Mol. Biol.* 305, 567–580. <https://doi.org/10.1006/jmbi.2000.4315>
- Kümmel, D. Krishnakumar, S. Radoff, D. Li, F. Giraudo, C. Pincet, F. Rothman, J. Reinisch, K. 2012. Complexin cross-links pre-fusion SNAREs into a zig-zag array: a structure-based model for complexin clamping. *Nat struct* 18, 927–933. <https://doi.org/10.1038/nsmb.2101>.Complexin
- Kuo, W. Herrick, D.Z. Ellena, J.F. Cafiso, D.S. 2009. The Calcium-Dependent and Calcium-

- Independent Membrane Binding of Synaptotagmin 1: Two Modes of C2B Binding. *J. Mol. Biol.* 387, 284–294. <https://doi.org/10.1016/j.jmb.2009.01.064>
- Kyte, J. Doolittle, R.F. 1982. A simple method for displaying the hydropathic character of a protein. *J. Mol. Biol.* 157, 105–132.
- Laage, R. Rohde, J. Brosig, B. Langosch, D. 2000. A conserved membrane-spanning amino acid motif drives homomeric and supports heteromeric assembly of presynaptic SNARE proteins. *J. Biol. Chem.* 275, 17481–17487. <https://doi.org/10.1074/jbc.M910092199>
- Landis, D.M. Hall, A.K. Weinstein, L.A. Reese, T.S. 1988. The organization of cytoplasm at the presynaptic active zone of a central nervous system synapse. *Neuron* 1, 201–209.
- Landschulz, W.H. Johnson, P.F. McKnight, S.L. 1988. The Leucine Zipper: A Hypothetical Structure Common to a New Class of DNA Binding Proteins. *Science* (80- ). 240, 1759–1764.
- Langosch, D. Crane, J.M. Brosig, B. Hellwig, a, Tamm, L.K. Reed, J. 2001. Peptide mimics of SNARE transmembrane segments drive membrane fusion depending on their conformational plasticity. *J. Mol. Biol.* 311, 709–721. <https://doi.org/10.1006/jmbi.2001.4889>
- Lau, S.Y. Taneja, a K. Hodges, R.S. 1984. Synthesis of a model protein of defined secondary and quaternary structure. Effect of chain length on the stabilization and formation of two-stranded alpha-helical coiled-coils. *J. Biol. Chem.* 259, 13253–13261.
- Li, C. Wang, J. Wang, Yiguang, Gao, H. Wei, G. Huang, Y. Yu, H. Gan, Y. Wang, Yongjun, Mei, L. Chen, H. Hu, H. Zhang, Z. Jin, Y. 2019. Recent progress in drug delivery. *Acta Pharm. Sin. B* 9, 1145–1162. <https://doi.org/10.1016/j.apsb.2019.08.003>
- Linding, R. Russell, R.B. Neduva, V. Gibson, T.J. 2003. GlobPlot: Exploring protein sequences for globularity and disorder. *Nucleic Acids Res.* 31, 3701–3708. <https://doi.org/10.1093/nar/gkg519>
- Lorentz, A. Baumann, A. Vitte, J. Blank, U. 2012. The SNARE machinery in mast cell secretion. *Front. Immunol.* 3, 1–17. <https://doi.org/10.3389/fimmu.2012.00143>
- Lou, X. Shin, Y.-K. 2016. SNARE zippering. *Biosci. Rep.* 36, e00327–e00327. <https://doi.org/10.1042/BSR20160004>
- Lumb, K.J. Kim, P.S. 1995. A buried polar interaction imparts structural uniqueness in a designed heterodimeric coiled coil. *Biochemistry* 34, 8642–8.
- Lupas, A. van Dyke, M. Stock, J. 1991. Predicting coiled coils from protein sequences. *Science* (80- ). 252, 1162–1164.
- Lyubimov, A.Y. Uervirojnangkoorn, M. Zeldin, O.B. Zhou, Q. Zhao, M. Brewster, A.S. Michels-Clark, T. Holton, J.M. Sauter, N.K. Weis, W.I. Brunger, A.T. 2016. Advances in X-ray free electron laser (XFEL) diffraction data processing applied to the crystal structure of the synaptotagmin-1 / SNARE complex. *Elife* 5, 1–18. <https://doi.org/10.7554/eLife.18740>
- Ma, C. Su, L. Seven, A.B. Xu, Y. Rizo, J. 2013. Reconstitution of the Vital Functions of Munc18 and Munc13 in Neurotransmitter Release. *Science* (80- ). 339, 421–425.

<https://doi.org/10.1126/science.1230473>.Reconstitution

- Ma, L. Kang, Y. Jiao, J. Rebane, A.A. Cha, H.K. Xi, Z. Qu, H. Zhang, Y. 2016.  $\alpha$ -SNAP Enhances SNARE Zippering by Stabilizing the SNARE Four-Helix Bundle. *Cell Rep.* 15, 531–539. <https://doi.org/10.1016/j.celrep.2016.03.050>
- Ma, W. Saccardo, A. Roccatano, D. Aboagye-Mensah, D. Alkaseem, M. Jewkes, M. Di Nezza, F. Baron, M. Soloviev, M. Ferrari, E. 2018. Modular assembly of proteins on nanoparticles. *Nat. Commun.* 9, 1–9. <https://doi.org/10.1038/s41467-018-03931-4>
- Madrigal, M.P. Portalés, A. SanJuan, M.P. Jurado, S. 2019. Postsynaptic SNARE Proteins: Role in Synaptic Transmission and Plasticity. *Neuroscience* 420, 12–21. <https://doi.org/10.1016/j.neuroscience.2018.11.012>
- Mahan, G.D. Plummer, E.W. 2000. Chapter 14 - Many-body Effects in Photoemission, in: Horn, K. Scheffler, M.B.T.-H. of S.S. (Eds.), *Electronic Structure*. North-Holland, pp. 953–987. [https://doi.org/https://doi.org/10.1016/S1573-4331\(00\)80018-9](https://doi.org/https://doi.org/10.1016/S1573-4331(00)80018-9)
- Malenka, R.C. Madison, D. V, Nicoll, R. a, 1986. Potentiation of synaptic transmission in the hippocampus by phorbol esters. *Nature* 321, 175–177. <https://doi.org/10.1038/321175a0>
- Malhotra, V. Orci, L. Glick, B.S. Block, M.R. Rothman, J.E. 1988. Role of an N-ethylmaleimide-sensitive transport component in promoting fusion of transport vesicles with cisternae of the Golgi stack. *Cell* 54, 221–227.
- Margittai, M. Fasshauer, D. Jahn, R. Langen, R. 2003. The Habc domain and the SNARE core complex are connected by a highly flexible linker. *Biochemistry* 42, 4009–4014. <https://doi.org/10.1021/bi027437z>
- Margittai, M. Fasshauer, D. Pabst, S. Jahn, R. Langen, R. 2001. Homo- and Heterooligomeric SNARE Complexes Studied by Site-directed Spin Labeling. *J. Biol. Chem.* 276, 13169–13177. <https://doi.org/10.1074/jbc.M010653200>
- Marz, K.E. Lauer, J.M. Hanson, P.I. 2003. Defining the SNARE complex binding surface of alpha-SNAP. Implications for SNARE complex disassembly. *J. Biol. Chem.* 278, 27000–27008. <https://doi.org/10.1074/jbc.M302003200>
- Matos, M.F. Mukherjee, K. Chen, X. Rizo, J. Su, T.C. 2003. Evidence for SNARE zippering during  $Ca^{2+}$ -triggered exocytosis in PC12 cells. *Neuropharmacology* 45, 777–786. [https://doi.org/10.1016/S0028-3908\(03\)00318-6](https://doi.org/10.1016/S0028-3908(03)00318-6)
- Maximov, A. Tang, J. Yang, X. Pang, Z.P. Sudhof, T.C. 2009. Complexes to Membranes in Fusion Complexin Controls the Force. *Science* (80-. ). 516, 516–521.
- McMahon, H.T. Missler, M. Li, C. Südhof, T.C. 1995. Complexins: Cytosolic proteins that regulate SNAP receptor function. *Cell* 83, 111–119. [https://doi.org/10.1016/0092-8674\(95\)90239-2](https://doi.org/10.1016/0092-8674(95)90239-2)
- Meier, M. Stetefeld, J. Burkhard, P. 2010. The many types of interhelical ionic interactions in coiled coils - An overview. *J. Struct. Biol.* 170, 192–201. <https://doi.org/10.1016/j.jsb.2010.03.003>

- Mima, J. 2018. Reconstitution of membrane tethering mediated by Rab-family small GTPases. *Biophys. Rev.* 10, 543–549. <https://doi.org/10.1007/s12551-017-0358-3>
- Min, D. Kim, K. Hyeon, C. Hoon Cho, Y. Shin, Y.K. Yoon, T.Y. 2013. Mechanical unzipping and rezipping of a single SNARE complex reveals hysteresis as a force-generating mechanism. *Nat. Commun.* 4, 1–10. <https://doi.org/10.1038/ncomms2692>
- Mistry, A.C. Mallick, R. Fro, O. Klein, J.D. Rehm, A. Chen, G. Sands, J.M. 2007. The UT-A1 Urea Transporter Interacts with Snapin , a SNARE-associated Protein \*. *J. Biol. Chem.* 282, 30097–30106. <https://doi.org/10.1074/jbc.M705866200>
- Misura, K.M.S. Scheller, R.H. Weis, W.I. 2000. Three-dimensional structure of the neuronal-Sec1-syntaxin 1a complex. *Nature* 404, 355–362.
- Moitra, J. Szilák, L. Krylov, D. Vinson, C. 1997. Leucine is the most stabilizing aliphatic amino acid in the d position of a dimeric leucine zipper coiled coil. *Biochemistry* 36, 12567–12573. <https://doi.org/10.1021/bi971424h>
- NCBI, n.d. NCBI Blast [WWW Document]. URL <https://blast.ncbi.nlm.nih.gov/Blast.cgi> (accessed 2.23.17).
- NetGlycate 1.0 CBS, n.d. NetGlycate 1.0 [WWW Document]. URL <http://www.cbs.dtu.dk/services/NetGlycate/> (accessed 12.27.16).
- NetPhos 3.1 CBS, n.d. NetPhos 3.1 [WWW Document]. URL <http://www.cbs.dtu.dk/services/NetPhos/> (accessed 12.27.16).
- Ngatchou, A.N. Kisler, K. Fang, Q. Walter, A.M. Zhao, Y. Bruns, D. Sørensen, J.B. Lindau, M. 2010. Role of the synaptobrevin C terminus in fusion pore formation. *Proc. Natl. Acad. Sci. U. S. A.* 107, 18463–18468. <https://doi.org/10.1073/pnas.1006727107>
- Nieler, H.B. Onofrio, F. Valtorta, F. Schiavo, G. Montecucco, C. Greengard, P. Benfenati, F. 1995. Phosphorylation of VAMP/Synaptobrevin in Synaptic Vesicles by Endogenous Protein Kinases. *J. Neurochem.* 65, 1712–1720.
- O’Shea, E.K. Klemm, J.D. Kim, P.S. Alber, T.O.M. 1991. X-ray Structure of the GCN4 Leucine Zipper, a Two-Stranded, Parallel Coiled Coil. *Science* (80-. ). 254, 539–544.
- O’Shea, E.K. Lumb, K.J. Kim, P.S. 1993. Peptide ‘Velcro’: Design of a heterodimeric coiled coil. *Curr. Biol.* 3, 658–667.
- Oakley, M.G. Kim, P.S. 1998. A Buried Polar Interaction Can Direct the Relative Orientation of Helices in a Coiled Coil. *Biochemistry* 37, 12603–12610. <https://doi.org/10.1021/bi981269m>
- Ovsepian, S. V. Dolly, J.O. 2011. Dendritic SNAREs add a new twist to the old neuron theory. *Proc. Natl. Acad. Sci. U. S. A.* 108, 19113–19120. <https://doi.org/10.1073/pnas.1017235108>
- Oyler, G.A. Higgins, G.A. Hart, R.A. Battenberg, E. Billingsley, M. Bloom, F.E. Wilson, M.C. 1989. The identification of a novel synaptosomal-associated protein, SNAP-25, differentially expressed by neuronal subpopulations. *J. Cell Biol.* 109, 3039–3052. <https://doi.org/10.1083/jcb.109.6.3039>

- Palade, G.E. 1974. George E. Palade Nobel Lecture: INTRACELLULAR ASPECTS OF THE PROCESS, in: Nobelprize.Org. Nobel Media AB 2014.
- Palade, G.E. 1959. Subcellular particles, in: Hayashi, T. (Ed.), Subcellular Particles. New York, Ronald Press Co, Massachusetts.
- Palfreyman, M.T. Jorgensen, E.M. 2008. Roles of SNARE proteins in synaptic vesicle fusion. *Mol. Mech. Neurotransmitter Release* 35–59. <https://doi.org/10.1007/978-1-59745-481-0>
- Pechar, M. Pola, R. 2013. The coiled coil motif in polymer drug delivery systems. *Biotechnol. Adv.* 31, 90–96. <https://doi.org/10.1016/j.biotechadv.2012.01.003>
- Pevsner, J. Hsu, S.C. Braun, J.E.A. Calakos, N. Ting, A.E. Bennett, M.K. Scheller, R.H. 1994. Specificity and regulation of a synaptic vesicle docking complex. *Neuron* 13, 353–361. [https://doi.org/10.1016/0896-6273\(94\)90352-2](https://doi.org/10.1016/0896-6273(94)90352-2)
- Pobbati, A. V. 2006. N- to C-Terminal SNARE Complex Assembly Promotes Rapid Membrane Fusion. *Science* (80-. ). 313, 673–676. <https://doi.org/10.1126/science.1129486>
- PRALINE IBIVU, n.d. PRALINE [WWW Document]. URL <http://www.ibi.vu.nl/programs/pralinewww/> (accessed 1.28.17).
- Protein Data Bank RCSB, n.d. Protein Data Bank (PDB) [WWW Document]. URL <http://www.rcsb.org/pdb/home/home.do> (accessed 12.27.16).
- ProtParam ExPASy, n.d. ProtParam [WWW Document]. URL <http://web.expasy.org/protparam/> (accessed 12.27.16).
- ProtScale ExPASy, n.d. ProtScale [WWW Document]. URL <http://web.expasy.org/protscale/> (accessed 12.27.16).
- PyMOL, n.d. The PyMOL Molecular Graphics System, Version 2.0 Schrödinger, LLC.
- Qiu, J. Wei, W.D. 2014. Surface plasmon-mediated photothermal chemistry. *J. Phys. Chem. C* 118, 20735–20749. <https://doi.org/10.1021/jp5042553>
- Ramakrishnan, N.A. Drescher, M.J. Drescher, D.G. 2012. The SNARE complex in neuronal and sensory cells. *Mol. Cell. Neurosci.* 50, 58–69. <https://doi.org/10.1016/j.mcn.2012.03.009>
- Rathore, S.S. Liu, Y. Yu, H. Wan, C. Lee, M.S. Yin, Q. Stowell, M.H.B. Shen, J. 2019. Intracellular Vesicle Fusion Requires a Membrane-Destabilizing Peptide Located at the Juxtamembrane Region of the v-SNARE. *Cell Rep.* 29, 4583-4592.e3. <https://doi.org/10.1016/j.celrep.2019.11.107>
- Rehman, A. Archbold, J.K. Hu, S. Norwood, S.J. 2014. Reconciling the regulatory role of Munc18 proteins in SNARE-complex assembly. *IUCrJ* 25, 505–513. <https://doi.org/10.1107/S2052252514020727>
- Richards, F.M. 1977. Areas, volumes, packing, and protein structure. *Annu. Rev. Biophys. Bioeng.* 6, 151–76.
- Rickman, C. Meunier, F.A. Binz, T. Davletov, B. 2004. High Affinity Interaction of Syntaxin and SNAP-25 on the Plasma Membrane Is Abolished by Botulinum Toxin E. *J. Biol. Chem.* 279,



644–651. <https://doi.org/10.1074/jbc.M310879200>

- Risinger, C. Bennett, M.K. 1999. Differential phosphorylation of syntaxin and synaptosome-associated protein of 25 kDa (SNAP-25) isoforms. *J. Neurochem.* 72, 614–624. <https://doi.org/10.1046/j.1471-4159.1999.0720614.x>
- Rizo, J. Chen, X. Araç, D. 2006. Unraveling the mechanisms of synaptotagmin and SNARE function in neurotransmitter release. *Trends Cell Biol.* 16, 339–350. <https://doi.org/10.1016/j.tcb.2006.04.006>
- Rizo, J. Rosenmund, C. 2008. Synaptic vesicle fusion. *Nat. Struct. Mol. Biol.* 15, 665–74. <https://doi.org/10.1038/nsmb.1450>
- Rizo, J. Südhof, T.C. 2012. The Membrane Fusion Enigma: SNAREs, Sec1/Munc18 Proteins, and Their Accomplices—Guilty as Charged?, *Annual Review of Cell and Developmental Biology*. <https://doi.org/10.1146/annurev-cellbio-101011-155818>
- Rose, A. Meier, I. 2004. Scaffolds, levers, rods and springs: diverse cellular functions of long coiled-coil proteins. *Cell. Mol. Life Sci. C.* 61, 1996–2009. <https://doi.org/10.1007/s00018-004-4039-6>
- Ruiter, M. Kádková, A. Scheutzow, A. Malsam, J. Söllner, T.H. Sørensen, J.B. 2019. An Electrostatic Energy Barrier for SNARE-Dependent Spontaneous and Evoked Synaptic Transmission. *Cell Rep.* 26, 2340-2352.e5. <https://doi.org/10.1016/j.celrep.2019.01.103>
- Safeukui, I. Millet, P. Boucher, S. Melinard, L. Fregeville, F. Receveur, M.C. Pistone, T. Fialon, P. Vincendeau, P. Fleury, H. Malvy, D. 2008. Evaluation of FRET real-time PCR assay for rapid detection and differentiation of Plasmodium species in returning travellers and migrants. *Malar. J.* 7, 1–11. <https://doi.org/10.1186/1475-2875-7-70>
- Schiavo, G. Benfenati, F. Poulain, B. Rossetto, O. Poverino de Laureto, P. DasGupta, B.R. Montecucco, C. 1992. Tetanus and botulinum-B neurotoxins block neurotransmitter release by proteolytic cleavage of synaptobrevin. *Nature* 359, 832–835. <https://doi.org/10.1038/359832a0>
- Schiavo, G. Malizio, W.S. Trimblell, W.S. Lauretos, P.P. De, Milant, G. Montecuccoi, C. 1994. Botulinum G Neurotoxin Cleaves VAMP / Synaptobrevin at a Single. *J. Biol. Chem.* 269, 20213–20216.
- Schiavo, G. Rossetto, O. Catsicas, S. De Laureto, P.P. DasGupta, B.R. Benfenati, F. Montecucco, C. 1993a. Identification of the nerve terminal targets of botulinum neurotoxin serotypes A, D, and E. *J. Biol. Chem.* 268, 23784–23787.
- Schiavo, G. Shone, C.C. Rossetto, O. Alexander, F.C.G. Montecucco, C. 1993b. Botulinum neurotoxin serotype F is a zinc endopeptidase specific for VAMP/synaptobrevin. *J. Biol. Chem.* 268, 11516–11519.
- Schorova, L. Martin, S. 2016. Sumoylation in synaptic function and dysfunction. *Front. Synaptic Neurosci.* 8. <https://doi.org/10.3389/fnsyn.2016.00009>
- Seroski, D.T. Hudalla, G.A. 2018. Self-Assembled Peptide and Protein Nanofibers for Biomedical

- Applications. *Biomed. Appl. Funct. Nanomater.* 569–598. <https://doi.org/10.1016/B978-0-323-50878-0.00019-7>
- Shimazaki, Y. Nishiki, T. Omori, A. Sekiguchi, M. Kamata, Y. Kozaki, S. Takahashi, M. 1996. Phosphorylation of 25-kDa Synaptosome-associated Protein. *J. Biol. Chem.* 271, 14548–14553.
- Shin, W. Arpino, G. Thiyagarajan, S. Su, R. Ge, L. McDargh, Z. Guo, X. Wei, L. Shupliakov, O. Jin, A. O’Shaughnessy, B. Wu, L.G. 2020. Vesicle Shrinking and Enlargement Play Opposing Roles in the Release of Exocytotic Contents. *Cell Rep.* 30, 421-431.e7. <https://doi.org/10.1016/j.celrep.2019.12.044>
- SIB, S.-P. n.d. Swiss-PdbViewer [WWW Document]. URL <http://spdbv.vital-it.ch> (accessed 12.27.16).
- Sikorra, S. Henke, T. Galli, T. Binz, T. 2008. Substrate recognition mechanism of VAMP/synaptobrevin-cleaving clostridial neurotoxins. *J. Biol. Chem.* 283, 21145–21152. <https://doi.org/10.1074/jbc.M800610200>
- Skorobogatko, Y. Landicho, A. Chalkley, R.J. Kossenkov, A. V. Gallo, G. Vosseller, K. 2014. O-Linked -N-Acetylglucosamine (O-GlcNAc) Site Thr-87 Regulates Synapsin I Localization to Synapses and Size of the Reserve Pool of Synaptic Vesicles. *J. Biol. Chem.* 289, 3602–3612. <https://doi.org/10.1074/jbc.M113.512814>
- Sollner, T. Bennett, M.K. Whiteheart, S.W. Scheller, R.H. Rothman, J.E. 1993a. A protein assembly-disassembly pathway in vitro that may correspond to sequential steps of synaptic vesicle docking, activation, and fusion. *Cell* 75, 409–418.
- Sollner, T. Whiteheart, S.W. Brunner, M. Bromage, H.E. Geramano, S. Tempst, P. Rothman, J.E. 1993b. SNAP receptors implicated in vesicle targeting and fusion. *Nature* 362, 318–324.
- Strop, P. Kaiser, S.E. Vrljic, M. Brunger, A.T. 2008. The structure of the yeast plasma membrane SNARE complex reveals destabilizing water-filled cavities. *J. Biol. Chem.* 283, 1113–1119. <https://doi.org/10.1074/jbc.M707912200>
- Stuchinskaya, T. Moreno, M. Cook, M.J. Edwards, D.R. Russell, D.A. 2011. Targeted photodynamic therapy of breast cancer cells using antibody–phthalocyanine–gold nanoparticle conjugates. *Photochem. Photobiol. Sci.* 10, 822–831. <https://doi.org/10.1039/C1PP05014A>
- Subramanian, S. Krishna Molecular Sciences and Chemical Engineering, M.C.B.T.-R.M. in C. 2014. In Vivo Electron Paramagnetic Resonance Imaging. Elsevier. <https://doi.org/https://doi.org/10.1016/B978-0-12-409547-2.11029-7>
- Südhof, T.C. 2013. Neurotransmitter release: The last millisecond in the life of a synaptic vesicle. *Neuron* 80, 675–690. <https://doi.org/10.1016/j.neuron.2013.10.022>
- Szklarczyk, D. Franceschini, A. Wyder, S. Forslund, K. Heller, D. Huerta-Cepas, J. Simonovic, M. Roth, A. Santos, A. Tsafou, K.P. Kuhn, M. Bork, P. Jensen, L.J. Von Mering, C. 2015. STRING v10: Protein-protein interaction networks, integrated over the tree of life. *Nucleic Acids*

- Res. 43, D447–D452. <https://doi.org/10.1093/nar/gku1003>
- Tang, J. Maximov, A. Shin, O.H. Dai, H. Rizo, J. Südhof, T.C. 2006. A Complexin/Synaptotagmin 1 Switch Controls Fast Synaptic Vesicle Exocytosis. *Cell* 126, 1175–1187. <https://doi.org/10.1016/j.cell.2006.08.030>
- Tang, Y. Ghirlanda, G. Vaidehi, N. Kua, J. Mainz, D.T. Goddard, W.A. DeGrado, W.F. Tirrell, D.A. 2001. Stabilization of coiled-coil peptide domains by introduction of trifluoroleucine. *Biochemistry* 40, 2790–2796. <https://doi.org/10.1021/bi0022588>
- Tian, J.H. Das, S. Sheng, Z.H. 2003. Ca<sup>2+</sup>-dependent phosphorylation of syntaxin-1A by the death-associated protein (DAP) kinase regulates its interaction with Munc18. *J. Biol. Chem.* 278, 26265–26274. <https://doi.org/10.1074/jbc.M300492200>
- TMHMM v 2.0 CBS, n.d. TMHMM v 2.0 [WWW Document]. URL <http://www.cbs.dtu.dk/services/TMHMM/> (accessed 12.27.16).
- Torshin, I.Y. Weber, I.T. Harrison, R.W. 2002. Geometric criteria of hydrogen bonds in proteins and identification of 'bifurcated' hydrogen bonds. *Protein Eng. Des. Sel.* 15, 359–363. <https://doi.org/10.1093/protein/15.5.359>
- Truebestein, L. Leonard, T.A. 2016. Coiled-coils: The long and short of it. *BioEssays* 38, 903–916. <https://doi.org/10.1002/bies.201600062>
- Tsui, M.M. Banfield, D.K. 2000. Yeast Golgi SNARE interactions are promiscuous. *J. Cell Sci.* 113 ( Pt 1, 145–152.
- Tzamarias, D. Pu, W.T. Struhl, K. 1992. Mutations in the bZIP domain of yeast GCN4 that alter DNA-binding specificity. *Proc. Natl. Acad. Sci. U. S. A.* 89, 2007–2011. <https://doi.org/10.1073/pnas.89.6.2007>
- Ungermann, C. Langosch, D. 2005. Functions of SNAREs in intracellular membrane fusion and lipid bilayer mixing. *J. Cell Sci.* 118, 3819–28. <https://doi.org/10.1242/jcs.02561>
- Uniprot, n.d. Universal Protein Resource [WWW Document]. URL <http://www.uniprot.org> (accessed 12.27.16).
- Urbina, F.L. Gupton, S.L. 2020. SNARE-Mediated Exocytosis in Neuronal Development. *Front. Mol. Neurosci.* 13, 1–17. <https://doi.org/10.3389/fnmol.2020.00133>
- Vaidyanathan, V. V. Yoshino, K. Jahnz, M. Dörries, C. Bade, S. Nauenburg, S. Niemann, H. Binz, T. 2002. Proteolysis of SNAP-25 Isoforms by Botulinum Neurotoxin Types A, C, and E. *J. Neurochem.* 72, 327–337. <https://doi.org/10.1046/j.1471-4159.1999.0720327.x>
- Vennekate, W. Schroder, S. Lin, C.-C. van den Bogaart, G. Grunwald, M. Jahn, R. Walla, P.J. 2012. Cis- and trans-membrane interactions of synaptotagmin-1. *Proc. Natl. Acad. Sci.* 109, 11037–11042. <https://doi.org/10.1073/pnas.1116326109>
- Vivona, S. Cipriano, D.J. O'Leary, S. Li, Y.H. Fenn, T.D. Brunger, A.T. 2013. Disassembly of all snare complexes by N-ethylmaleimide-sensitive factor (NSF) is initiated by a conserved 1:1 interaction between alpha-soluble NSF attachment protein (SNAP) and SNARE complex. *J.*

- Biol. Chem. 288, 24984–24991. <https://doi.org/10.1074/jbc.M113.489807>
- Wagschal, K. Tripet, B. Mant, C. Hodges, R.S. Lavigne, P. 2008. The role of position a in determining the stability and oligomerization state of  $\alpha$ -helical coiled coils: 20 amino acid stability coefficients in the hydrophobic core of proteins. *Protein Sci.* 8, 2312–2329. <https://doi.org/10.1110/ps.8.11.2312>
- Wahajuddin, Arora, S. 2012. Superparamagnetic iron oxide nanoparticles: Magnetic nanoplateforms as drug carriers. *Int. J. Nanomedicine* 7, 3445–3471. <https://doi.org/10.2147/IJN.S30320>
- Walshaw, J. Woolfson, D.N. 2001. Socket: a program for identifying and analysing coiled-coil motifs within protein structures. *J. Mol. Biol.* 307, 1427–1450. <https://doi.org/10.1006/jmbi.2001.4545>
- Wang, D. Xu, Z. Yu, H. Chen, X. Feng, B. Cui, Z. Lin, B. Yin, Q. Zhang, Z. Chen, C. Wang, J. Zhang, W. Li, Y. 2014. Treatment of metastatic breast cancer by combination of chemotherapy and photothermal ablation using doxorubicin-loaded DNA wrapped gold nanorods. *Biomaterials* 35, 8374–8384. <https://doi.org/https://doi.org/10.1016/j.biomaterials.2014.05.094>
- Wang, F. Wang, Y.-C. Dou, S. Xiong, M.-H. Sun, T.-M. Wang, J. 2011. Doxorubicin-Tethered Responsive Gold Nanoparticles Facilitate Intracellular Drug Delivery for Overcoming Multidrug Resistance in Cancer Cells. *ACS Nano* 5, 3679–3692. <https://doi.org/10.1021/nn200007z>
- Wang, Y. Geer, L.Y. Chappay, C. Kans, J.A. Bryant, S.H. 2000. Cn3D: sequence and structure views for Entrez. *Trends Biochem Sci.* 25, 300–2.
- Wang, Y. Tang, B.L. 2006. SNAREs in neurons - Beyond synaptic vesicle exocytosis (review). *Mol. Membr. Biol.* 23, 377–384. <https://doi.org/10.1080/09687860600776734>
- Wang, Y.J. Li, F. Rodriguez, N. Lafosse, X. Gourier, C. Perez, E. Pincet, F. 2016. Snapshot of sequential SNARE assembling states between membranes shows that N-terminal transient assembly initializes fusion. *Proc. Natl. Acad. Sci.* 113, 3533–3538. <https://doi.org/10.1073/pnas.1518935113>
- Wattenberg, B.W. Rothman, E. 1986. Multiple Cytosolic Components Promote Intra-Golgi Protein Transport. *J. Biol. Chem.* 261, 2208–2213.
- Weidman, P.J. Melancon, P. Block, M.R. Rothman, J.E. 1989. Binding of an N-ethylmaleimide-sensitive fusion protein to Golgi membranes requires both a soluble protein(s) and an integral membrane receptor. *J. Cell Biol.* 108, 1589–1596. <https://doi.org/10.1083/jcb.108.5.1589>
- Weimbs, T. Mostov, K. Low, S.H. Hofmann, K. 1998. A model for structural similarity between different SNARE complexes based on sequence relationships. *Trends Cell Biol.* 8, 260–262. [https://doi.org/http://dx.doi.org/10.1016/S0962-8924\(98\)01285-9](https://doi.org/http://dx.doi.org/10.1016/S0962-8924(98)01285-9)
- Wen, X. Saltzgeber, G.W. Thoreson, W.B. 2017. Kiss-and-run is a significant contributor to synaptic exocytosis and endocytosis in photoreceptors. *Front. Cell. Neurosci.* 11, 1–18. <https://doi.org/10.3389/fncel.2017.00286>

- Wilson, D.W. Wilcox, C.A. Flynn, G.C. Chen, E. Kuang, W.J. Henzel, W.J. Block, M.R. Ullrich, A. Rothman, J.E. 1989. A fusion protein required for vesicle-mediated transport in both mammalian cells and yeast. *Nature* 339, 355–359. <https://doi.org/10.1038/340301a0>
- Winter, U. Chen, X. Fasshauer, D. 2009. A Conserved Membrane Attachment Site in alpha-SNAP Facilitates N-Ethylmaleimide-sensitive Factor (NSF)-driven SNARE Complex Disassembly. *J. Biol. Chem.* 284, 31817–31826. <https://doi.org/10.1074/jbc.M109.045286>
- Wittwer, C.T. 2009. High-resolution DNA melting analysis: advancements and limitations. *Hum. Mutat.* 30, 857–859. <https://doi.org/10.1002/humu.20951>
- Wojnacki, J. Nola, S. Bun, P. Cholley, B. Filippini, F. Pressé, M.T. Lipecka, J. Man Lam, S. N'guyen, J. Simon, A. Ouslimani, A. Shui, G. Fader, C.M. Colombo, M.I. Guerrero, I.C. Galli, T. 2020. Role of VAMP7-Dependent Secretion of Reticulon 3 in Neurite Growth. *Cell Rep.* 33. <https://doi.org/10.1016/j.celrep.2020.108536>
- Woolfson, B.D.N. 2005. THE DESIGN OF COILED-COIL STRUCTURES AND ASSEMBLIES. *Adv. Protein Chem.* 70, 79–112. [https://doi.org/10.1016/S0065-3233\(04\)70004-2](https://doi.org/10.1016/S0065-3233(04)70004-2)
- Woolfson, D.N. 2005. THE DESIGN OF COILED-COIL STRUCTURES AND ASSEMBLIES. *Adv. Protein Chem.* 70, 79–112. [https://doi.org/10.1016/S0065-3233\(04\)70004-2](https://doi.org/10.1016/S0065-3233(04)70004-2)
- Wu, K. Yang, J. Liu, J. 2012. Coiled-coil based drug-free macromolecular therapeutics : In vivo efficacy. *J. Control. Release* 157, 126–131. <https://doi.org/10.1016/j.jconrel.2011.08.002>
- Wu, W. He, Q. Jiang, C. 2008. Magnetic iron oxide nanoparticles: Synthesis and surface functionalization strategies. *Nanoscale Res. Lett.* 3, 397–415. <https://doi.org/10.1007/s11671-008-9174-9>
- Xi, Z. Gao, Y. Sirinakis, G. Guo, H. Zhang, Y. 2012. Single-molecule observation of helix staggering, sliding, and coiled coil misfolding. *Proc. Natl. Acad. Sci.* 109, 5711–5716. <https://doi.org/10.1073/pnas.1116784109>
- Xiang, Q. Morais, P.C. 2014. Remote Hyperthermia, Drug Delivery and Thermometry: The Multifunctional Platform Provided by Nanoparticles. *J. Nanomed. Nanotechnol.* 05. <https://doi.org/10.4172/2157-7439.1000209>
- Xu, J. Brewer, K.D. Perez-Castillejos, R. Rizo, J. 2013. Subtle interplay between synaptotagmin and complexin binding to the SNARE complex. *J. Mol. Biol.* 425, 3461–3475. <https://doi.org/10.1016/j.jmb.2013.07.001>
- Xue, M. Reim, K. Chen, X. Chao, H. Deng, H. Rizo, J. Brose, N. Rosenmund, C. 2007. Distinct domains of Complexin I differentially regulate neurotransmitter release. *Nat Struct Mol Biol.* 14, 949–958. <https://doi.org/10.1016/j.ceca.2012.06.001>. Calcium
- Yallapu, M. Othman, S. Curtis, E. Gupta, B. Jaggi, M. Chauhan, S. 2011. Multi-functional Magnetic Nanoparticles for Magnetic Resonance Imaging and Cancer Therapy. *Biomaterials* 32, 1890–1905. <https://doi.org/10.1016/j.biomaterials.2010.11.028>. Multi-functional
- Yang, J. Kopecek, J. 2015. *Journal of Drug Delivery Science and Technology Polymeric*

- biomaterials and nanomedicines. *J. Drug Deliv. Sci. Technol.* 30, 318–330.  
<https://doi.org/10.1016/j.jddst.2015.05.012>
- Yang, B. Gonzalez Jr, L. Prekeris, R. Steegmaier, M. Advani, R.J. Scheller, R.H. 1999. SNARE Interactions Are Not Selective. *Biochemistry* 274, 5649–5653.
- Yang, B. Steegmaier, M. Gonzalez, L.C. Scheller, R.H. 2000. nSec1 binds a closed conformation of syntaxin1A. *J. Cell Biol.* 148, 247–252. <https://doi.org/10.1083/jcb.148.2.247>
- Yang, J. Bahreman, A. Daudey, G. Bussmann, J. Olsthoorn, R.C.L. Kros, A. 2016. Drug Delivery via Cell Membrane Fusion Using Lipopeptide Modified Liposomes. *ACS Cent. Sci.* 2, 621–630. <https://doi.org/10.1021/acscentsci.6b00172>
- YinOYang 1.2 CBS, n.d. YinOYang 1.2 [WWW Document]. URL <http://www.cbs.dtu.dk/services/YinOYang/> (accessed 12.27.16).
- Yoon, T.Y. Munson, M. 2018. SNARE complex assembly and disassembly. *Curr. Biol.* 28, R397–R401. <https://doi.org/10.1016/j.cub.2018.01.005>
- Zamyatnin, A.A. 1984. Amino Acid, Peptide, and Protein Volume in Solution. *Annu. Rev. Biophys. Bioeng.* 13:145-165. <https://doi.org/https://doi.org/10.1146/annurev.bb.13.060184.001045>
- Zhang, F. Chen, Y. Su, Z. Shin, Y.K. 2004. SNARE assembly and membrane fusion, a kinetic analysis. *J. Biol. Chem.* 279, 38668–38672. <https://doi.org/10.1074/jbc.M404904200>
- Zhang, X. Rebane, A.A. Ma, L. Li, F. Jiao, J. Qu, H. Pincet, F. Rothman, J.E. Zhang, Y. Brunger, A.T. 2016. Stability, folding dynamics, and long-range conformational transition of the synaptic t-SNARE complex. *Proc. Natl. Acad. Sci. U. S. A.* 113, E8031–E8040. <https://doi.org/10.1073/pnas.1605748113>
- Zhao, M. Wu, S. Zhou, Q. Vivona, S. Cipriano, D.J. Cheng, Y. Brunger, A.T. 2015. Mechanistic insights into the recycling machine of the SNARE complex. *Nature* 518, 61–67. <https://doi.org/10.1038/nature14148.Mechanistic>
- Zheng, T. Bulacu, M. Daudey, G. Versluis, F. Voskuhl, J. Martelli, G. Raap, J. Sevink, G.J.A. Kros, A. Boyle, A.L. 2016. A non-zipper-like tetrameric coiled coil promotes membrane fusion. *RSC Adv.* 6, 7990–7998. <https://doi.org/10.1039/C5RA26175A>
- Zhou, Q. Lai, Y. Bacaj, T. Zhao, M. Lyubimov, A.Y. Uevirojnangoorn, M. Zeldin, O.B. Brewster, A.S. Sauter, N.K. Cohen, A.E. Soltis, S.M. Alonso-Mori, R. Chollet, M. Lemke, H.T. Pfuetzner, R.A. Choi, U.B. Weis, W.I. Diao, J. Südhof, T.C. Brunger, A.T. 2015. Architecture of the synaptotagmin-SNARE machinery for neuronal exocytosis. *Nature* 525, 62–67. <https://doi.org/10.1038/nature14975>

## 12. Tables

**Table 1: Proposed  $\alpha$ -SNAP binding sites on the SNARE complex according to Marz *et al.* (Marz *et al.* 2003). These acidic residues are arranged in diagonal bands across the SNARE complex bundle in zones that are proximal to the basic diagonal band present on the  $\alpha$ -SNAP concave surface.**

<b>Protein</b>	<b>Site 1</b>	<b>Site 2</b>	<b>Site 3</b>
<b>Syntaxin</b>	Asp214, Asp218	Glu228	Glu238
<b>VAMP</b>	Asp51, Glu55	Asp65	-
<b>SNAP-25 C-terminal</b>	Glu183	-	Asp166
<b>SNAP-25 N-terminal</b>	-	Glu38, Asp41	Asp51, Glu55

**Table 2: Woolfson and Walshaw's amino acid profile for long parallel two-stranded coiled coils** (Walshaw & Woolfson 2001). Shows the normalised\* frequencies of occurrence of each amino acid at each heptad position compiled from a set of non-redundant, long ( $\geq 15$  residues), parallel, two-stranded coiled coils. The number of residues used totalled 252.

\* Normalisation was carried out by dividing the amino acid profile for long parallel two-stranded coiled coils by the relative frequency of each amino acid in swissprot (Walshaw and Woolfson, 2001).

Amino acid	Normalised frequencies of occurrence at each heptad position						
	<i>a</i>	<i>b</i>	<i>c</i>	<i>d</i>	<i>e</i>	<i>f</i>	<i>g</i>
<b>A</b>	1.35	2.71	0.31	0.29	1.94	1.55	0.31
<b>C</b>	0	0	0	0	0	0	0
<b>D</b>	0	1.15	0.58	0	0	1.67	1.15
<b>E</b>	0.4	1.91	2.86	0	4.16	2.77	4.76
<b>F</b>	0	0	0	0	0	0	0
<b>G</b>	0	0	0	0	0	0	0.89
<b>H</b>	0	0	2.71	0	0	0	0
<b>I</b>	1.77	0.52	0	0	0.51	0	0
<b>K</b>	0.86	1.53	0.51	0.37	1.49	1.49	3.57
<b>L</b>	2.18	0.32	0.64	7.61	0.62	0.31	0
<b>M</b>	0	0	3.84	4.59	0	0	0
<b>N</b>	4.04	2.73	0.68	0	0	2.65	0
<b>P</b>	0	0	0.62	0.44	0	0	0
<b>Q</b>	0.65	0.76	4.58	0	2.96	0.74	2.29
<b>R</b>	0.41	1.17	1.17	0.42	2.85	1.71	2.94
<b>S</b>	0.36	1.7	0	0.3	0.41	2.06	0
<b>T</b>	0.45	0.53	2.14	0.38	1.04	1.04	1.07
<b>V</b>	3.12	0.46	1.38	0.33	0.89	0.89	0.46
<b>W</b>	0	0	0	0	0	0	0
<b>Y</b>	0.8	1.81	0	0.68	0	0	0



**Table 3: Percentage compositions, and molecular weight, for each of the synaptic proteins obtained using Protparam computational tool from ExPASy.**

Amino acid	Percentage composition (%)			
	Syntaxin-1a	VAMP2	SNAP-25b (Isoform 1)	SNAP-25a (isoform 2)
<b>Ala</b>	5.6	12.9	7.8	7.8
<b>Arg</b>	7.6	5.2	8.3	8.3
<b>Asn</b>	2.8	3.4	6.8	7.3
<b>Asp</b>	7.6	6.0	9.2	9.2
<b>Cys</b>	1.0	0.9	1.9	1.9
<b>Gln</b>	3.8	6.0	6.3	6.3
<b>Glu</b>	12.2	4.3	11.7	11.2
<b>Gly</b>	3.8	4.3	6.8	6.8
<b>His</b>	1.7	0.0	0.5	1.0
<b>Ile</b>	10.4	8.6	5.3	5.3
<b>Leu</b>	5.6	8.6	7.8	7.8
<b>Lys</b>	8.0	6.0	5.8	5.8
<b>Met</b>	4.2	3.4	6.3	6.3
<b>Phe</b>	2.8	1.7	1.0	1.0
<b>Pro</b>	1.0	6.9	1.0	1.0
<b>Ser</b>	9.0	5.2	4.9	4.9
<b>Thr</b>	5.6	5.2	3.4	2.9
<b>Trp</b>	0.0	1.7	0.5	0.5
<b>Tyr</b>	1.7	1.7	0.5	0.5
<b>Val</b>	5.6	7.8	4.4	4.4
<b>Molecular Weight (Da)</b>	33067.48	12690.78	23315.08	23336.10

**Table 4: SNARE-based peptides tabulated with their sequences.** The central ionic residue is underlined, whilst the coloured font of residues denote mutations. All “Brev”-prefixed peptides (i.e. VAMP peptides) have cysteines (C) at their N-termini to allow labelling to occur through the sulphur (-SH) functional group. All “Synt”-prefixed peptides (i.e. syntaxin peptides) have a glycine (G) at their N-termini to allow labelling to occur at this end. To prevent non-specific labelling occurring at K17, a K17R mutation was performed in all synt-peptides except the “PH-suffixed” peptide, which has a K17H mutation that is specific to the pH-sensitivity study. The rationale behind the mutations specific to each peptide (i.e. the red coloured amino acids) is detailed in **section 6.1**. The column at the end of the table specifies which complexes the peptide can be found in. The yellow highlighted numbers show how you can tell that the peptide is involved in that complex i.e. in complex “C0204”, the central “02” tells you that the syntaxin in this complex is “S02”. All complexes contain a full-length recombinant SNAP-25. The table can be used as a guide to find out which study each peptide is involved in.

Type	Abbreviation	Study	Sequence	Peptide is found in the following complexes (note: all complexes contain full length recombinant SNAP-25)
<b>Native (for reference only)</b>				
Syntaxin	N/A	N/A	SEIIKLENSIRELHDMFMDMAMLVESQ <u>G</u> EMIDRIE	N/A
Brevin (i.e. VAMP)	N/A	N/A	RRLQQTQAQVDEVVDIMRVNVDKVL <u>R</u> DQKLSELD	N/A
<b>Peptide (Name)</b>				
Synt1-01_34	S01	All	GEI <u>R</u> LENSIRELHDMFMDMAMLVESQ <u>G</u> EMIDRIE	C04, C05, C06, C07, C08, C09, C10, C11, C12, C13, C14, C15 (with B04, B05, B06, B07, B08, B09, B10, B11, B12, B13, B14, and B15 respectively).
Synt1-02_34PH	S02	pH-sensitivity	GEI <u>H</u> LENSI <u>H</u> ELHDMFMDMAMLVESQ <u>G</u> EMID <u>H</u> IE	C0204 (with B04), C0205 (with B05), C0206 (with B06), C0207 (with B07)
Synt1-03_34ST	S03	Compensation	GEI <u>R</u> TENS <u>V</u> RE <u>V</u> HDM <u>M</u> MD <u>N</u> AMLVESQ <u>G</u> EMIDRIE	C0304 (with B04), C0315 (with B15)
Brev2-04_34	B04	All	CRLQQTQAQVDEVVDIMRVNVDKVL <u>R</u> DQKLSELD	C04 (with S01)
Brev2-05_27	B05	Improvement	CRLQQTQAQVDEVVDIMRVNVDKVL <u>R</u> D	C05 (with S01)
Brev2-06_34PH	B06	pH-sensitivity	<u>C</u> HLQQTQAQVDEVVDIM <u>H</u> VNVD <u>H</u> VL <u>R</u> DQ <u>H</u> LSELD	C06 (with S01)
Brev2-07_27PH	B07	pH-sensitivity	<u>C</u> HLQQTQAQVDEVVDIM <u>H</u> VNVD <u>H</u> VL <u>R</u> D	C07 (with S01)
Brev2-08_34ST	B08	Salt bridge	CRLQQTQAQVDEVVDIMRVNVDKVL <u>R</u> K <u>Q</u> ELSELD	C08 (with S01)
Brev2-09_34ST	B09	Salt bridge	CRLQQTQAQVDEVVDIMRVN <u>V</u> KEVL <u>R</u> DQKLSELD	C09 (with S01)

Brev2-10_34ST	B10	Salt bridge	CRLQQTQAQVDEV <b>E</b> AIMRVNVDKVL <u>ER</u> DQKLSELD	C <b>10</b> (with S01)
Brev2-11_34ST	B11	Salt bridge	CRLQQTQAQVDEV <b>E</b> AIMRVNV <b>K</b> EVLER <b>K</b> QELSELD	C <b>11</b> (with S01)
Brev2-12_27ST	B12	Improvement	CRLQQTQAQ <b>A</b> DEVVDIMRVNVDK <u>AL</u> ERD	C <b>12</b> (with S01)
Brev2-13_27ST	B13	Improvement	CRLQQTQAQVDEVVD <b>I</b> FRVNVDKVL <u>ER</u> D	C <b>13</b> (with S01)
Brev2-14_27ST	B14	Improvement	CRLQQTQAQ <b>A</b> DEVVD <b>I</b> FRVNVDK <u>AL</u> ERD	C <b>14</b> (with S01)
Brev2-15_34ST	B15	Compensation	CRLQQLQAQ <b>I</b> DELVD <b>I</b> FRV <b>M</b> VDKVL <u>ER</u> DQKLSELD	C <b>15</b> (with S01)

**Table 5: Composition of SNARE complex samples for CD spectroscopy.**

Sample	SNAP-25 (13 $\mu$ M) / $\mu$ L	Syntaxin (35 $\mu$ M) / $\mu$ L	Synt1-01_34 (241 $\mu$ M) / $\mu$ L	Synapto- brevin (114 $\mu$ M) / $\mu$ L	Brev2-04_34 (241 $\mu$ M) / $\mu$ L	100 mM HEPES / $\mu$ L	ddH <sub>2</sub> O / $\mu$ L
FL/FL/FL	36.1	17.1	-	5.3	-	20	121.4
FL/FL/34	36.1	17.1	-	-	2.5	20	124.2
FL/34/34	36.1	-	2.5	-	2.5	20	138.9

**Table 6: Preparation of 5X stock solutions of buffers A-C.**

Sample (5X Stock Solutions)	BSA (10 mg/mL) / $\mu$ L	Buffer (200 mM HEPES/ 1 M NaCl) / $\mu$ L	10% OG / $\mu$ L	ddH <sub>2</sub> O / $\mu$ L
Buffer A (5 mg/mL BSA/ 0.5% OG)	500	400	50	50
Buffer B (0.5 mg/mL BSA/ 0.5% OG)	50	400	50	500
Buffer C (0.05 mg/mL BSA/ 0.5% OG)	5	400	50	545

**Table 7: Assembly of optimisation samples for native gel containing full-length SNARE complex (CFL), BSA 0.01-1 mg/mL and OG at 0.1%, and control IR-SNAP25.**

IR-SNAP25 conc	Sample of CFL (full-length complex)	Buffer	Buffer vol / $\mu$ L	CFL / IRS25 STOCK	Full length Complex vol / $\mu$ L	ddH <sub>2</sub> O / $\mu$ L	4X-LB vol / $\mu$ L
3.2 $\mu$ g/mL IR-SNAP25	1	A	3	A	8.3	-	3.7
	2	B	3	A	8.3	-	3.7
	3	C	3	A	8.3	-	3.7
0.8 $\mu$ g/mL IR-SNAP25	4	A	3	B	8.3	-	3.7
	5	B	3	B	8.3	-	3.7
	6	C	3	B	8.3	-	3.7
0.2 $\mu$ g/mL IR-SNAP25	7	A	3	C	8.3	-	3.7
	8	B	3	C	8.3	-	3.7
	9	C	3	C	8.3	-	3.7
3.2 $\mu$ g/mL IR-SNAP25	10 - 3.2 $\mu$ g/mL IR-SNAP25 alone	A	3	-	2.8	5.5	3.7
3.2 $\mu$ g/mL IR-SNAP25	11 - 0.2 $\mu$ g/mL IR-SNAP25 alone	C	3	D	3.8	4.5	3.7

**Table 8: Composition of MNP-SNAREs samples for CD spectroscopy.**

Sample	MNP-GST (32 $\mu$ M protein) / $\mu$ L	MNP-GST-SNAP25 (18 $\mu$ M protein) / $\mu$ L	Synt/vamp master mix (12.5 $\mu$ M) / $\mu$ L	Sodium Phosphate buffer (10 mM) / $\mu$ L
MNP-GST	15	-	-	35
MNP-GST-SNAP25	-	12	-	38
MNP-GST/SYNT/VAMP	15	-	20	15
MNP-GST- SNAP25/SYNT/VAMP	-	12	20	18

**Table 9: Composition of GNP-SNAREs samples for CD spectroscopy.**

Sample	GNP / $\mu$ L	GST (0.08 mg/mL) / $\mu$ L	GST-SYNT (0.6 $\mu$ M) / $\mu$ L	SNAP25/VAMP55 master mix / $\mu$ L	Distilled water / $\mu$ L
GNP	100	-	-	-	100
GNP-GST	100	100	-	-	-
GNP-GST-SYNT	50	-	50	-	-
GNP with SNAP25/VAMP55	100	-	-	10	-
GNP-GST with SNAP25/VAMP55	50	50	-	10	-
GNP-GST-SYNT with SNAP25/VAMP55	50	-	50	10	-

**Table 10: Preparation of 100 mM potassium phosphate buffer pH 6-8.**

pH buffer (200 mM potassium phosphate buffer)	1 M $K_2HPO_4$ (dibasic) / $\mu$ L	1 M $KH_2PO_4$ (monobasic) / $\mu$ L	ddH <sub>2</sub> O / $\mu$ L
6	26.4	173.6	800
6.4	55.6	144.4	800
7	123	77	800
7.4	160.4	39.6	800
8	188	12	800

**Table 11: Preparation of complex on beads (GST-complex) and associated controls for pH-sensitivity pull-down SDS-gel.**

\* For GST-SNAP25 sample, excess buffer was removed from beads, and 2X-LB was added to make up a total volume of ~20  $\mu$ L.

Sample	GST-SNAP25 (0.4 mg/mL; 8.19 $\mu$ M) / $\mu$ L	Syntaxin (1 mg/mL) / $\mu$ L	Synaptobrevin (1 mg/mL) / $\mu$ L	10X Buffer (160 mM HEPES, 1 mg/mL BSA, 1% OG) / $\mu$ L	ddH <sub>2</sub> O / $\mu$ L	2X-LB / $\mu$ L
GST-Complex	90	15	15	15	15	-
GST-SNAP25	10	-	-	1	-	*
Synaptobrevin peptide	-	-	1	1	4	4
Syntaxin peptide	-	1	-	1	4	4
BSA	-	-	-	2	4	4

**Table 12: Preparation of complex on beads (GST-complex) and associated controls for thermostability pull-down SDS-gel.**

\* Excess buffer was removed from beads, and 3X-LB was added to make up a total volume of ~20  $\mu$ L.

\*\* Full-length recombinant proteins would have double the volume compared to the synthetic peptides i.e. 30  $\mu$ L as opposed to 15  $\mu$ L. The volume of ddH<sub>2</sub>O was adjusted to keep the total volume at 150  $\mu$ L.

Sample	GST-SNAP25 (0.4 mg/mL; 8.19 $\mu$ M) / $\mu$ L	Syntaxin (1 mg/mL) / $\mu$ L **	Synaptobrevin (1 mg/mL) / $\mu$ L **	10X Buffer (160 mM HEPES, 1 mg/mL BSA, 1% OG) / $\mu$ L	ddH <sub>2</sub> O / $\mu$ L	2X-LB / $\mu$ L
GST-Complex	90	15	15	15	15	-
GST-SNAP25	10	-	-	1	-	*
Synaptobrevin peptide	-	-	1	1	4	4
Syntaxin peptide	-	1	-	1	4	4
BSA with Synt/Brev	-	1	1	2	2	4

**Table 13: Preparation of SNARE complex samples for thermofluor assay.**

Component Volume / $\mu$ L	SYPRO Orange concentration / X
	10X
Complex 8 $\mu$ M master mix	31.2
SYPRO Orange	10
Buffer (180 mM HEPES, 900 mM NaCl, 1% OG)	5.6
ddH <sub>2</sub> O	3.8
Total volume	50

**Table 14: Individual components of each sample for fluorescent emission study, and its quantities.**

Sample	Component	Concentration (mg/mL)	Vol ( $\mu$ L)
IgG-FITC	IgG-FITC	0.01	50
	Buffer		150
IgG-FITC + Labelled Protein A (LPA)	IgG-FITC	0.01	50
	Dab-3	0.05	30
	Buffer		120
IgG-FITC + Unlabelled Protein A (UPA)	IgG-FITC	0.01	50
	Protein A	0.05	30
	Buffer		120
IgG-FITC + 100 XS UPA	IgG-FITC	0.01	50
	Protein A	5	30
	Buffer		120
IgG-FITC + 100 XS UPA + LPA	IgG-FITC	0.01	50
	Dab-3	0.05	30
	Protein A	5	30
	Buffer		90

**Table 15: Preparation of labelled Protein A – IgG complex and associated controls for HRM.**

Sample	Component	Concentration (mg/mL)	Vol ( $\mu$ L)
IgG-FITC	IgG-FITC	0.01	5
	Buffer		15
IgG-FITC + Labelled Protein A (LPA)	IgG-FITC	0.01	5
	Dab-3	0.05	3
	Buffer		12
IgG-FITC + 100 XS UPA	IgG-FITC	0.01	5
	Protein A	5	3
	Buffer		12
IgG-FITC + 100 XS UPA + LPA	IgG-FITC	0.01	5
	Dab-3	0.05	3
	Protein A	5	3
	Buffer		9

**Table 16: Preparation of labelled peptides complex and associated controls for HRM.**

Sample	Distilled water ( $\mu$ L)	100 mM Sodium Bicarbonate ( $\mu$ L)	SNAP-25 ( $\mu$ L)	Syntaxin ( $\mu$ L)	Vamp ( $\mu$ L)
1			3	10	10
2	3	10		10	10
3	3	10			10
4		9	3		10
5			3	1 (FL)	10

## 13. Figures

### 13.1 Figures in Chapter 1

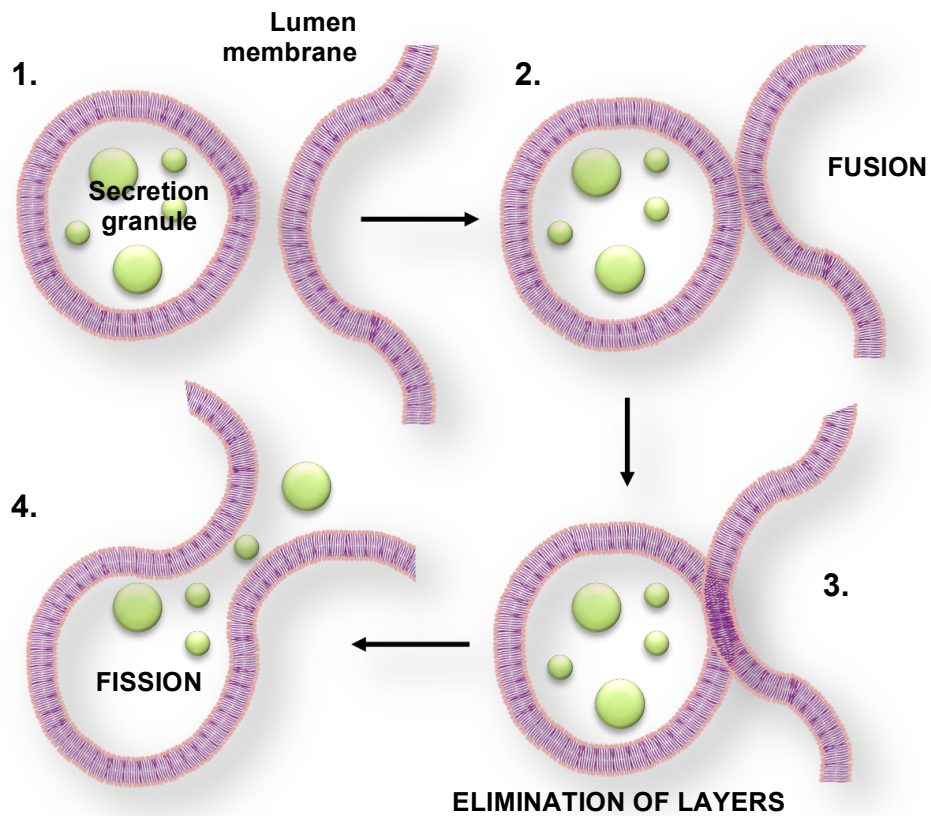
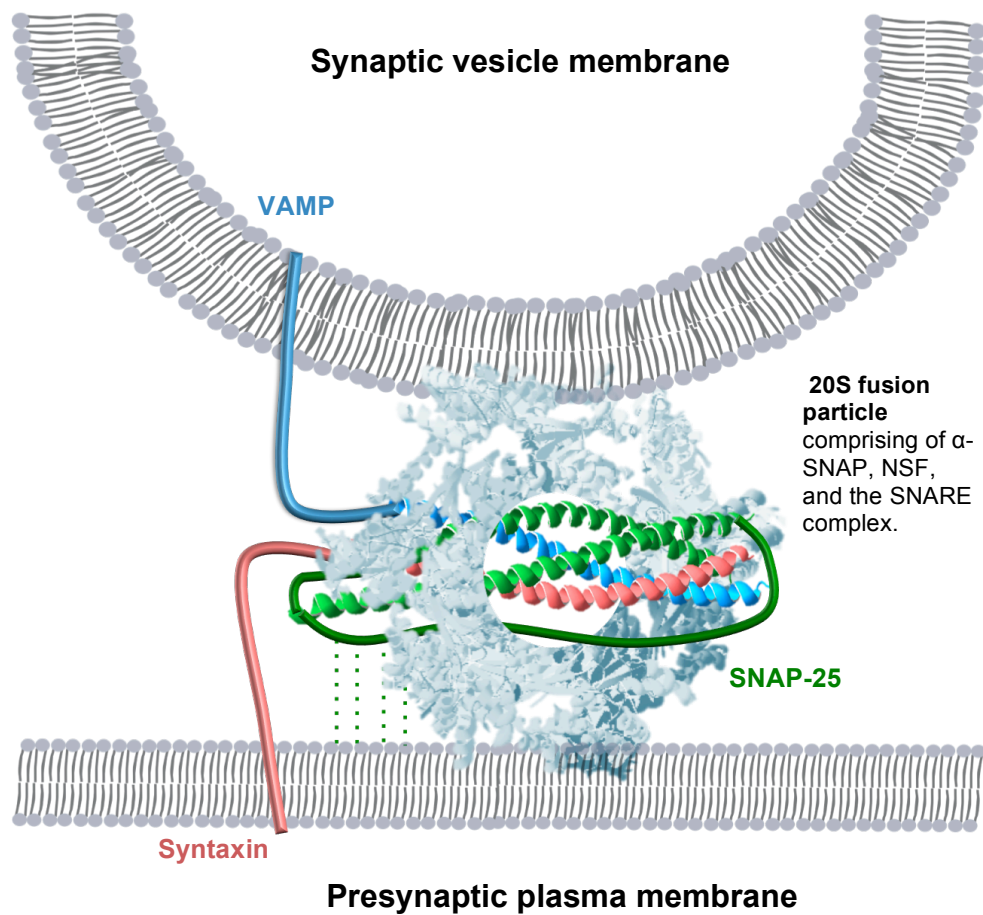


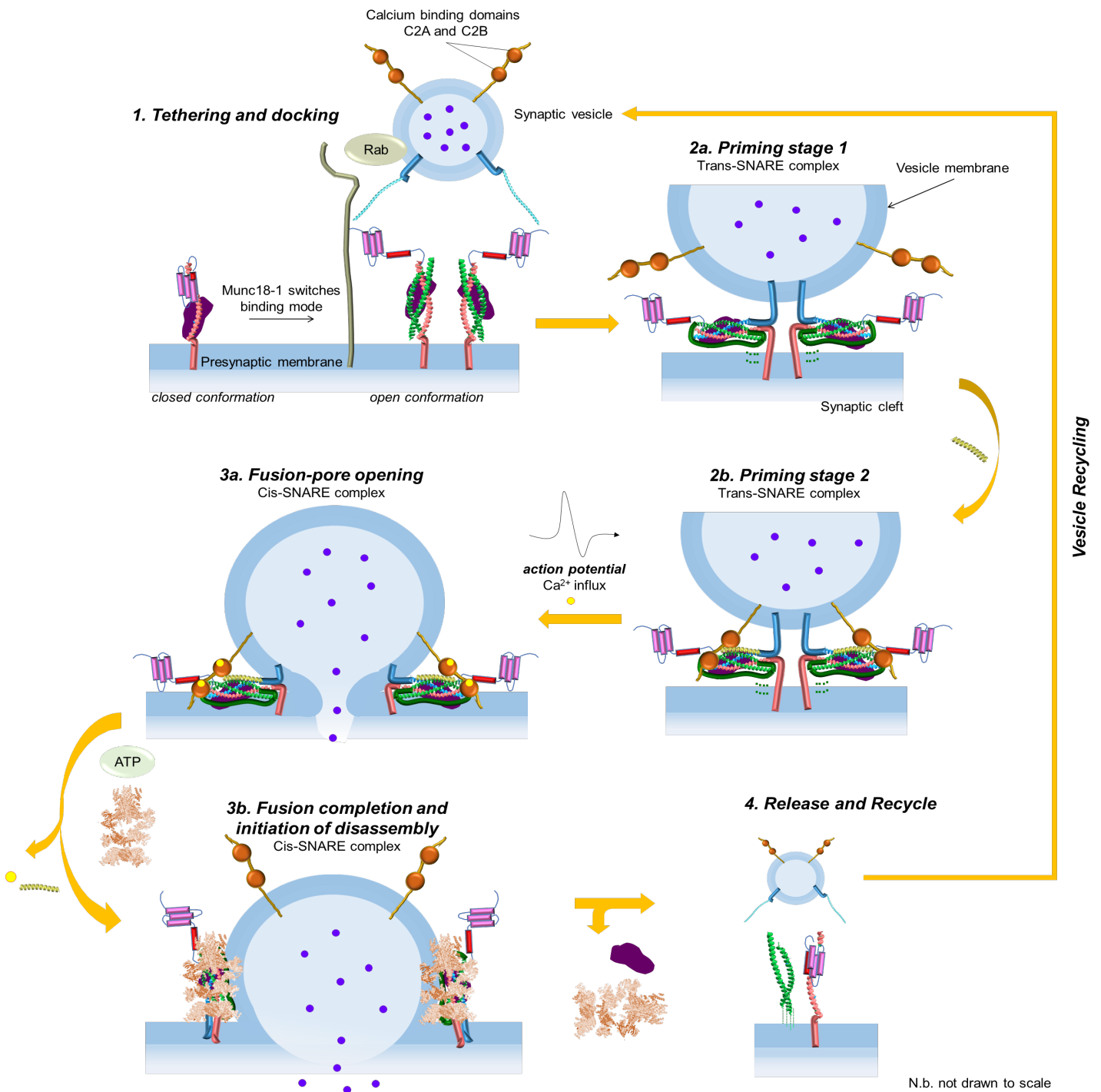
**Figure 1.1: Early understanding of membrane fusion.** A schematic delineating the steps, including membrane fusion, involved in the discharge of secretion granule contents into a plasmalemma lumen according to George E. Palade Adapted from (Palade, G.E., 1979).





*N.b. not drawn to scale.*

**Figure 1.2: SNARE fusion machinery as it was understood in 1993.** A schematic illustrating the understanding of SNARE fusion machinery based on the findings reported by Söllner in 1993. The fusion particle, consisting of an  $\alpha$ -SNAP-NSF complex (light blue) bound to the SNARE coiled coil, was ostensibly referred to by its sedimentation coefficient 20S. Both syntaxin (pink) and VAMP (blue) are membrane-associated proteins and hence, are anchored by their transmembrane domains, whilst the cytosolic SNAP-25 (green) is only tethered to the membrane by its palmitoylated cysteine residues (green dotted lines). *Figure not drawn to scale.* Adapted from (Sollner, 1993).



**Key**

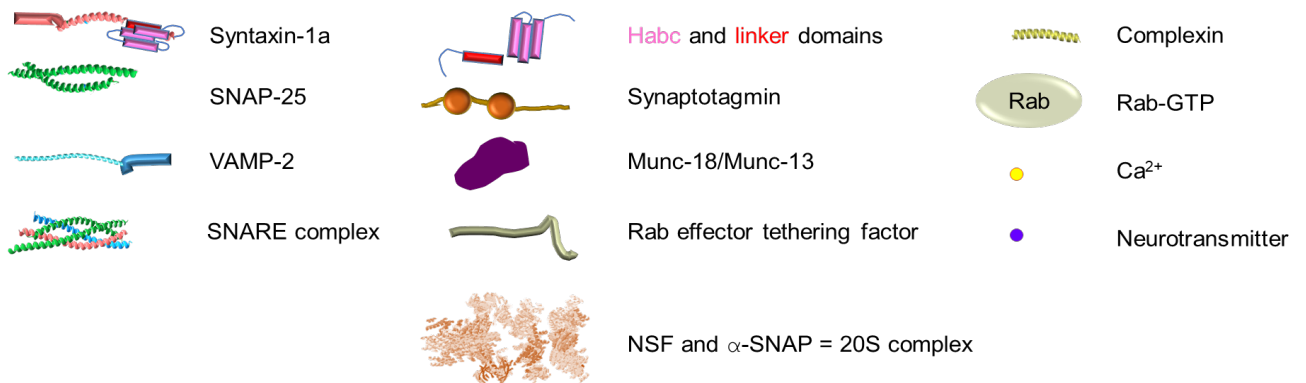


**Figure 1.3: SNARE-mediated exocytosis, showing the fusion machinery and heterotypic membrane fusion, as it is currently understood (2020).** A schematic demonstration of the contemporaneous understanding of SNARE fusion machinery, and heterotypic membrane fusion as adapted from Chen *et al.* (Chen *et al.* 2020), He *et al.* (He *et al.* 2018), Kavanagh *et al.* (Kavanagh *et al.* 2014), and Yoon and Munson (Yoon and Munson 2018). Presented here are the four steps of SNARE mediated exocytosis at the synaptic junction, detailing the key proteins involved and their interactions with the SNARE proteins that helps bring about membrane fusion. The first step is tethering and docking of the vesicle (**panel 1**). Tethering factors in the presynaptic membrane, such as Rab effector, work in tandem with Rab GTPases to tether the vesicle to the target membrane. Syntaxin-1a starts in its closed state with the Habc and H3 domains bound together, stabilised by Munc18-1, but when the docking process begins Munc18-1 switches the binding mode and triggers syntaxin-1a to “open” and create contacts with SNAP-25 to form a pre-complex of t-SNAREs. Priming stage 1 (**panel 2a**) begins when VAMP-2 comes into contact with the t-SNAREs. The SNARE complex is initiated at the N-termini and is characterised by the loosely bound, transient trans-complex. It is called “trans” because the transmembrane SNARE proteins are on opposing membranes. Munc-18 acts as a facilitator in keeping the SNARE bundle together. Priming stage 2 (**panel 2b**) involves an accessory helix called complexin binding to a groove between VAMP-2 and syntaxin-1a. This acts to delay C-terminal assembly and inhibit fusion. Synaptotagmin, which acts as a calcium sensor, binds to VAMP-2 at this stage, and contributes to the suppression of fusion. As the membranes approach one another there is increasing electrostatic repulsion, but when an action potential arrives at the synaptic junction, there is an influx of calcium which binds to synaptotagmin, reducing this electrostatic repulsion. Since the SNAREs are already exerting torque through their zippering, the membranes are sheared and fuse together creating the fusion-pore opening (**panel 3a**). There are a number of different models of exocytosis, at the fusion stage, proposed in the literature. Under the “kiss-and-run” model, the fusion-pore opening is followed by closure and release and recycling. Under the full-vesicle fusion model, the fusion-pore expands and then collapses into the plasma membrane, which is demonstrated in fusion completion (**panel 3b**). Calcium binding to synaptotagmin causes complexin to detach in the process. Following membrane fusion, the bound calcium is released and synaptotagmin is displaced from the resulting cis-SNARE complex. It is called “cis” because the SNARE proteins are on the same now-fused membrane. Disassembly is initiated by the binding of four  $\alpha$ -SNAP proteins, antiparallel to a single SNARE complex, followed by ATPase NSF (**panel 3b**). The final step is the recycling of the vesicle, and the SNARE complex into its constituent monomers (**panel 4**). The fusion particle (20S complex), comprising of  $\alpha$ -SNAP and NSF, bound to the SNARE coiled coil, applies rotational forces to unwind it in a shearing motion. This releases the SNARE monomers, allowing the process to start again. *Figure not drawn to scale.*

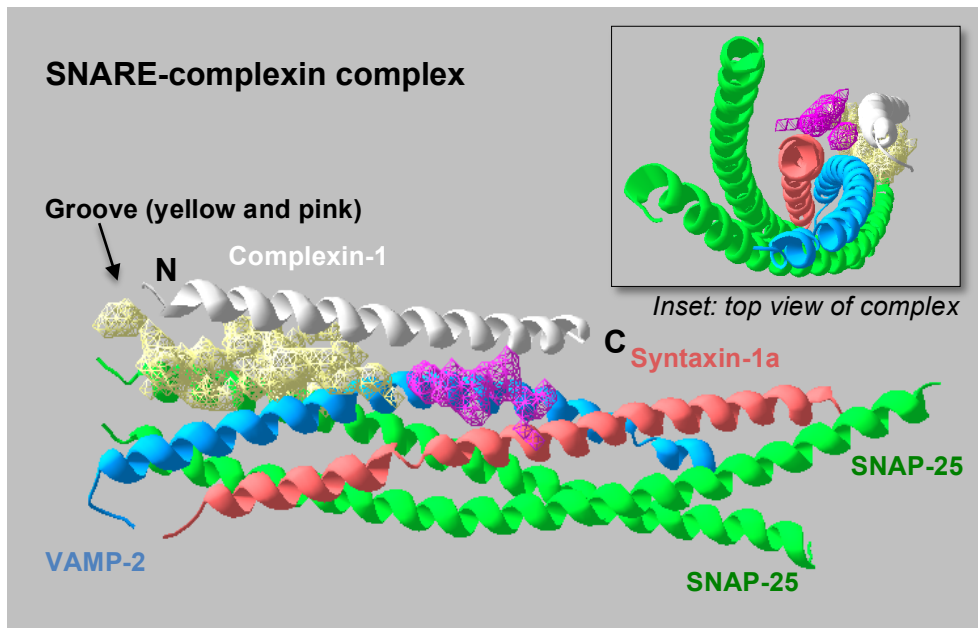


**Figure 1.4: Structure of the SNARE-complexin complex elucidated using a combination of X-ray and TROSY-based NMR (PDB: 1KIL).** It can be seen that complexin-1 (white) binds within the groove (yellow and pink) formed between VAMP-2 (blue helical strand) and syntaxin-1a (pink helical strand). Based on the NMR data, the C-terminal of complexin-1 is believed to bind to the middle of the groove, where it associates with the central polar layer of the SNARE complex; whilst there not to be any points of contact between the N-terminal and the SNARE complex. Protein Data Bank was used to obtain the crystal structure atomic coordinates and structure factors for this complex (see PDB ID quoted above) and Swissprot PDB viewer was used to view and make superficial modifications.

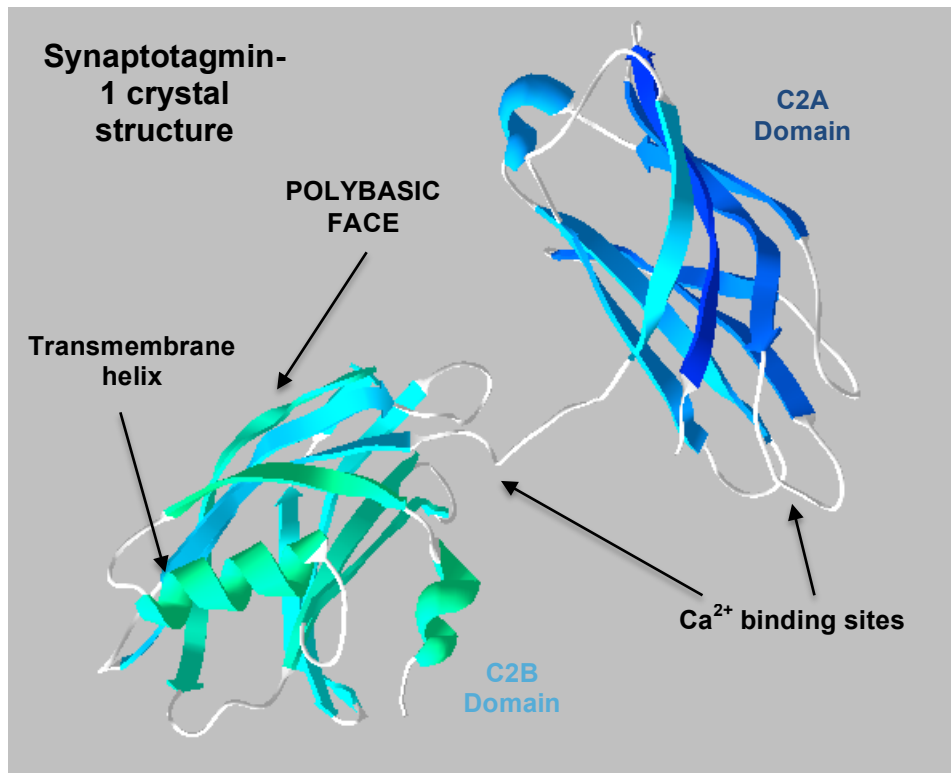


**Figure 1.5: Crystal structure of synaptotagmin-1 (PDB ID: 5KJ7).** The two C2 domains, C2A and C2B, can be seen highlighted in dark blue and turquoise respectively. The transmembrane domain is the helical structure on the C2B domain and acts as a binding site for isolated VAMP-2. The polybasic face, so-called for the significant number of positively charged lysine residues, is the primary contact surface for SNARE complexes and anionic phospholipid membranes; whilst on the opposite side is C2B's  $\text{Ca}^{2+}$ -binding site. C2A also possesses a corresponding  $\text{Ca}^{2+}$ -binding site. Protein Data Bank was used to obtain the crystal structure atomic coordinates and structure factors for this complex (see PDB ID quoted above) and Swissprot PDB viewer was used to view and make superficial modifications.

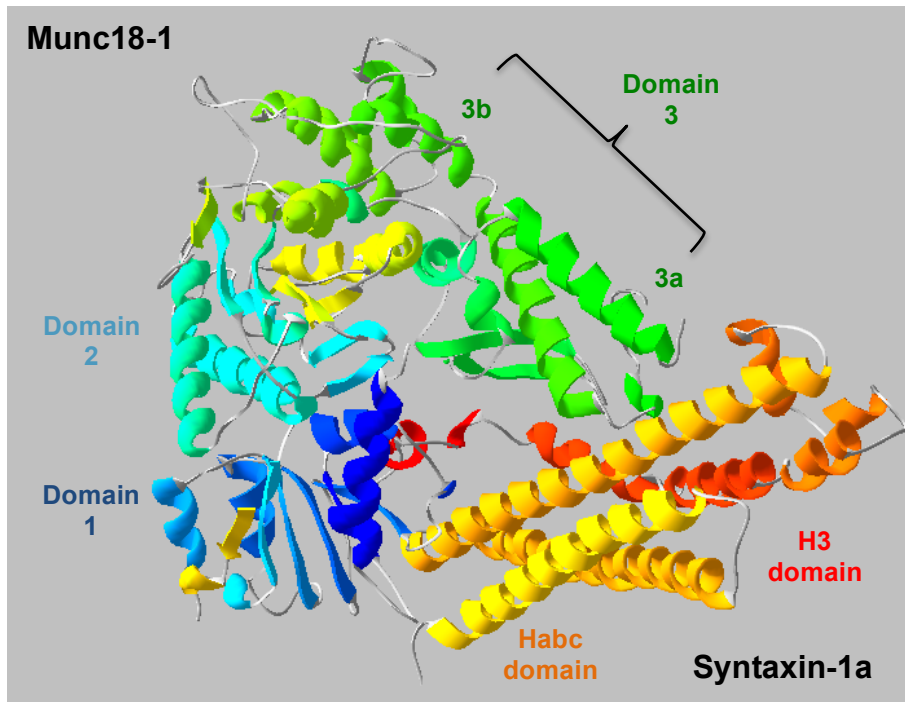


**Figure 1.6: Crystal structure of Munc18-1 complexed with syntaxin-1a in its closed configuration (Munc18a-Syx1a PDB ID: 4JEU) (Colbert *et al.* 2013).** Domains 1 (darker blue) and 3a (green) of Munc18-1 are the primary binding sites, seen here interacting with syntaxin-1a (Habc is the triple-stranded helix in yellow with the N-peptide being the small yellow section interacting with domain 1 of Munc18-1; H3 region is highlighted in red and the flexible linker is orange coloured). Protein Data Bank was used to obtain the crystal structure atomic coordinates and structure factors for this complex (see PDB ID quoted above) and Swissprot PDB viewer was used to view and make superficial modifications.

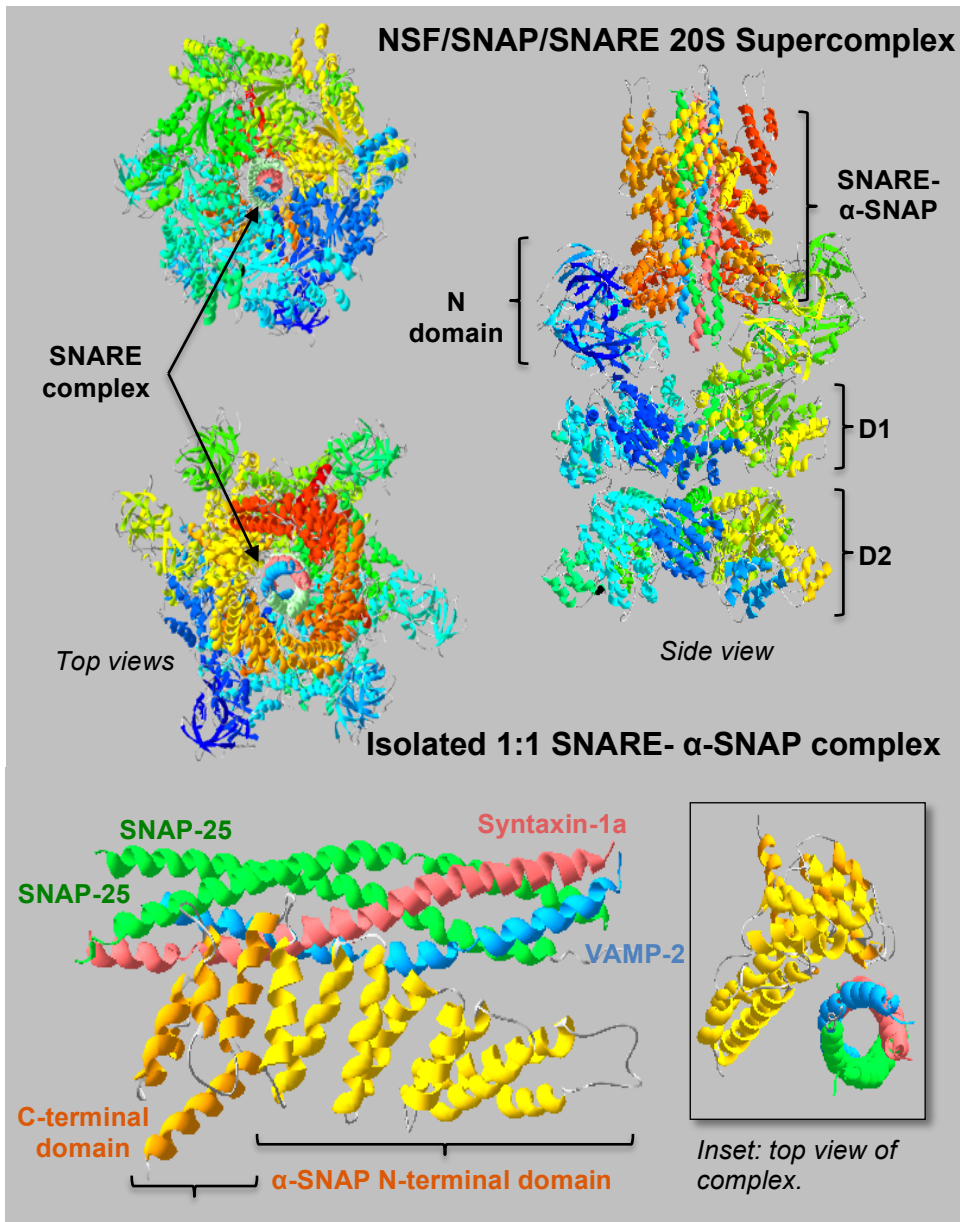
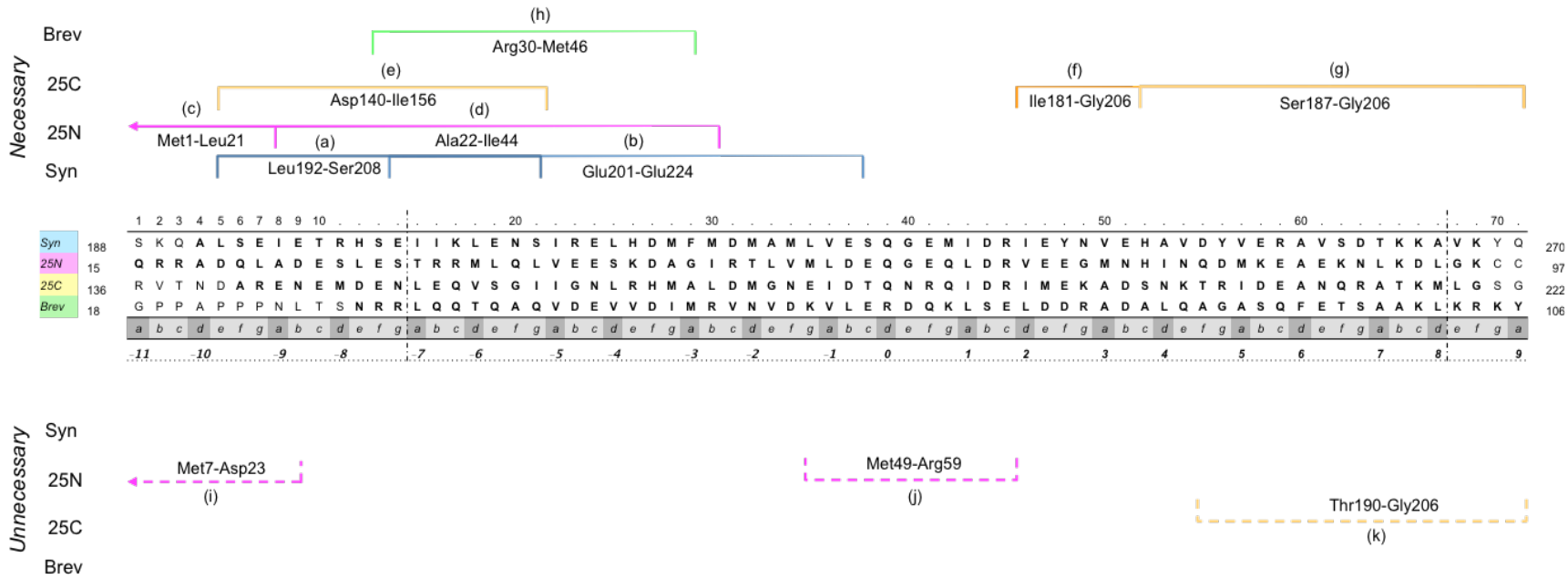


**Figure 1.7: Crystal structure of the NSF/SNAP/SNARE 20S supercomplex elucidated using single particle cryoelectron microscopy (PDB: 3J96).** *Top:* Both ends of the complex are depicted here, with the SNARE complex visible in the centre. Structurally, the hexameric N-ethylmaleimide Sensitive Factor (NSF) is comprised of three layers: two rings designated D2 and D1, themselves comprised of six D2 and six D1 domains respectively; and an N layer consisting of six N-terminal domains in ATP-bound NSF and four when it is ADP-bound. The N layer is the primary site of interaction with the  $\alpha$ -SNAP/SNARE complex according to composition-gradient multi-angle light scattering (CG-MALS) data. *Below:* 1:1 SNARE- $\alpha$ -SNAP complex isolated from the 20S supercomplex showing how they interact. At their interface, the concave surface of  $\alpha$ -SNAP is shown to sheathe the convex SNARE complex (see inset). Protein Data Bank was used to obtain the crystal structure, and Swissprot PDB viewer was used to view and make superficial modifications.



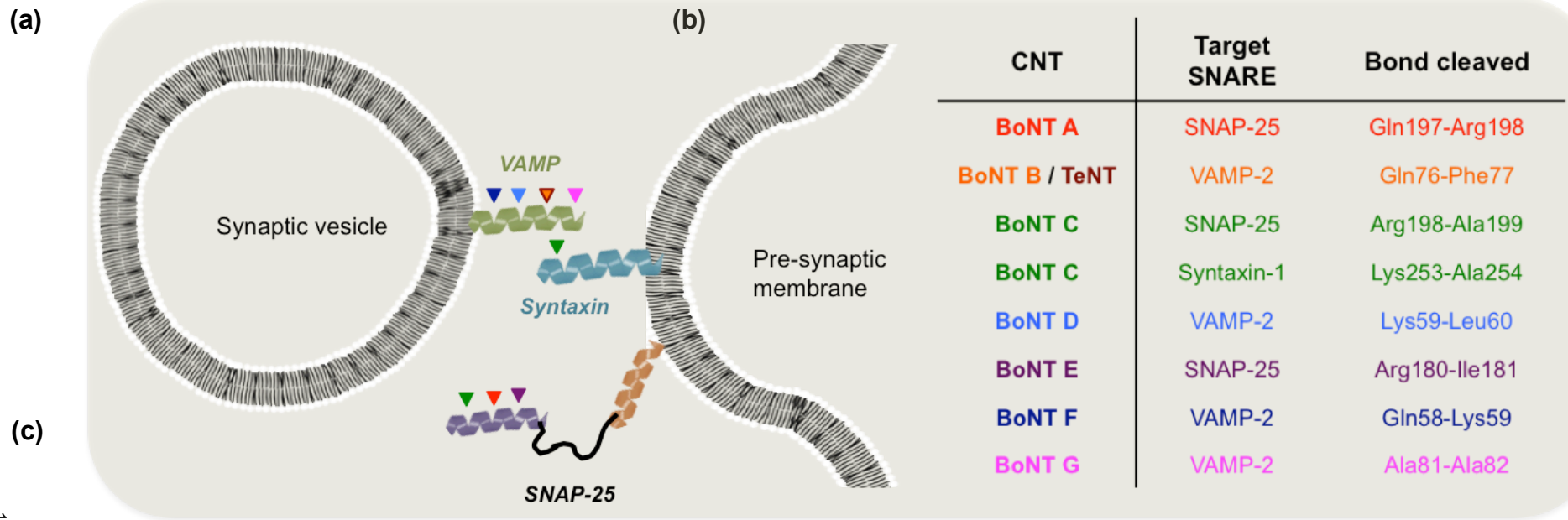
**Neuronal SNARE complex (*Rattus Norvegicus*)**



Section	Chain	Region	Description	Reference
a	syn	Leu192-Ser208	peptide modelled after this decreased membrane fusion by up to ~50% of the control	Jung et al. 2008
b	syn	Glu201-Glu224	minimum length that exhibits best linker binding properties	Ferrari et al. 2012
c	25N	Met1-Leu21	peptide modelled after this inhibited SDS-resistant complex by up to ~25%	Blanes-Mira et al. 2004
d	25N	Ala22-Ile44	peptide modelled after this inhibited SDS-resistant complex by up to ~50%	Blanes-Mira et al. 2004
e	25C	Asp140-Ile56	peptide modelled after this reduced membrane fusion by up to ~80% of the control	Jung et al. 2008
f	25C	Ile181-Gly206	syntaxin binding site: loss of this region by BoNT/E treatment resulted in loss of syn	Rickman et al. 2004
g	25C	Ser187-Gly206	peptide modelled after this inhibited exocytosis by ~65%	Gutiérrez et al. 1995
h	Brev	Arg30-Met46	peptide modelled after this reduced membrane fusion by up to ~55%	Jung et al. 2008
i	25N	Met7-Asp23	peptide modelled after this had no effect on membrane fusion or the amount of SNARE complex formed	Jung et al. 2008
j	25N	Met49-Arg59	peptide modelled after this did not affect secretion	Gutiérrez et al. 1995
k	25C	Thr190-Gly206	peptide modelled after this had no effect on membrane fusion or the amount of SNARE complex formed	Jung et al. 2008

**Figure 1.8: Regions within the SNARE complex that have been identified in the literature as necessary, or unnecessary for binding and assembly.** The top figure illustrates which regions are necessary (above), and unnecessary (below) in any capacity, for SNARE complex assembly. The table at the bottom provides further information about the sections marked out in the figure, as well as the references to the studies that provided them.





187

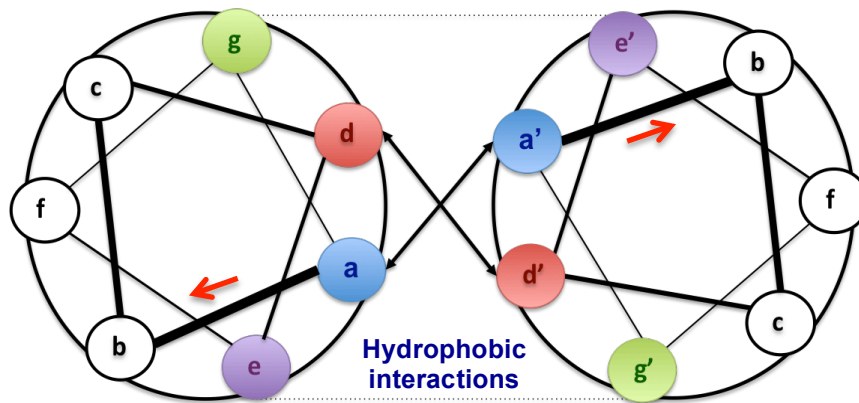
Neuronal SNARE complex (*Rattus Norvegicus*)

Syntaxin-1a	188	S	K	Q	A	L	S	E	I	E	T	R	H	S	E	I	I	K	L	E	N	S	I	R	E	L	H	D	M	F	M	D	M	A	M	L	V	E	S	Q	G	227		
SNAP-25 N-terminal	15	Q	R	R	A	D	Q	L	A	D	E	S	L	E	S	T	R	R	M	L	Q	L	V	E	E	S	K	D	A	G	I	R	T	L	V	M	L	D	E	Q	G	54		
SNAP-25 C-terminal	136	R	V	T	N	D	A	R	E	N	E	M	D	E	N	L	E	Q	V	S	G	I	I	G	N	L	R	H	M	A	L	D	M	G	N	E	I	D	T	Q	N	175		
VAMP-2	18	G	P	P	A	P	P	P	N	L	T	S	N	R	R	L	Q	Q	T	Q	A	Q	V	D	E	V	V	D	I	M	R	V	N	V	D	K	V	L	E	R	D	57		
		a	b	c	d	e	f	g	a	b	c	d	e	f	g	a	b	c	d	e	f	g	a	b	c	d	e	f	g	a	b	c	d	e	f	g	a	b	c	d	e			
		-11			-10				-9			-8			-7			-6			-5			-4			-3			-2			-1			0								
Syntaxin-1a	228	E	M	I	D	R	I	E	Y	N	V	E	H	A	V	D	Y	V	E	R	A	V	S	D	T	K	K	A	V	K	Y	Q	S	K	A	R	R	K	K	I	M	267		
SNAP-25 N-terminal	55	E	Q	L	D	R	V	E	E	G	M	N	H	I	N	Q	D	M	K	E	A	E	K	N	L	K	D	L	G	K	C	C	G	L	F	I	C	P	C	N	K	94		
SNAP-25 C-terminal	176	R	Q	I	D	R	I	M	E	K	A	D	S	N	K	T	R	I	D	E	A	N	Q	R	A	T	K	M	L	G	S	G	X	X	X	X	X	X	X	X	X	215		
VAMP-2	58	Q	K	L	S	E	L	D	D	R	A	D	A	L	Q	A	G	A	S	Q	F	E	T	S	A	A	K	L	K	R	K	Y	W	W	K	N	L	K	M	M	I	97		
		f	g	a	b	c	d	e	f	g	a	b	c	d	e	f	g	a	b	c	d	e	f	g	a	b	c	d	e	f	g	a	b	c	d	e	f	g	a	b	c			
				1			2				3			4				5				6				7				8				9				10				11		

**Figure 1.9: Cleavage sites of various clostridial neurotoxins (CNTs) situated on SNARE proteins.** (a) Schematic of neuronal SNARE proteins on pre-synaptic and synaptic membranes. The coloured triangles represent the CNTs (BoNT – botulinum neurotoxin; TeNT – tetanus neurotoxin) serotypes that target each SNARE protein. (b) Table of CNT serotypes, the SNARE proteins they target and the bonds they cleave. (c) C-terminal sequences of neuronal SNARE complex from *Rattus norvegicus* (based on PDB 1N7S). The coloured-coded triangles indicate the cleavage site of specific CNT serotypes.

## Dimer

### Ionic interactions



## Tetramer

### Ionic interactions

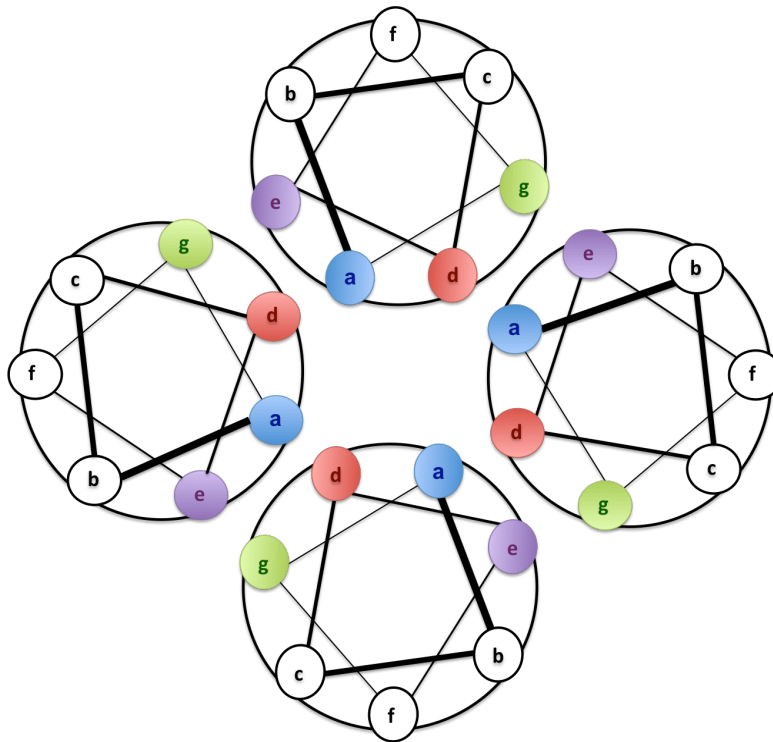
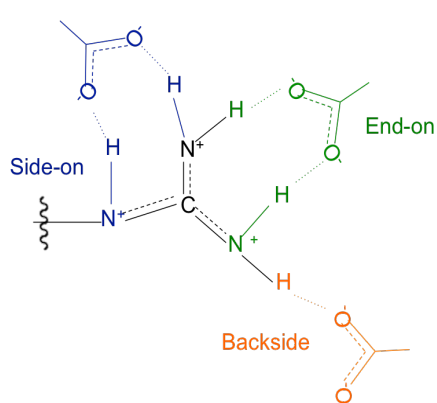
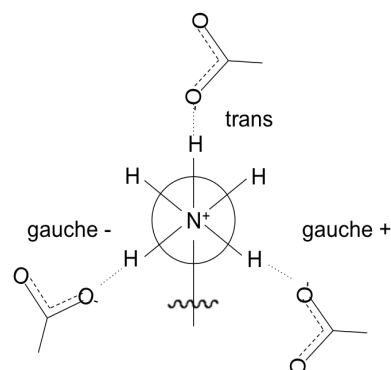


**Figure 1.10: Helical wheel diagrams depicting a birds-eye view of the helix axis from the N-terminus in a dimeric coiled coil (top) and tetrameric coiled coil (below).** There are seven amino acid residue positions along the helix circumference; these have been labelled *a-g*, with *a-d* representing the hydrophobic residues, and *e-g* representing the polar residues. The decreasing thickness of the lines connecting the residues, along with the red arrow, indicates the chirality of the helix. Hydrophobic residues *a* (red) and *d* (blue) interact at the interface, forming the hydrophobic core of the coiled coil; whilst polar residues *e* (purple) and *g* (green) partake in interhelical electrostatic interactions at the periphery of this core.



**(a) Arginine salt bridge conformations**



**(b) Lysine salt bridge conformations**

**Figure 1.11: Potential salt bridge conformations in arginine and lysine.** (a) Positive charge can be delocalised onto any of the three nitrogens in the guanidinium group of arginine. Dashed lines indicate the potential formation of a double bond due to delocalisation, whilst the dotted lines represent the salt bridges. Arginine can form three different conformations, two of which are characterised as six-membered rings forming as a result of bidentate interactions with the acidic residue in their syn conformation; whilst the third, less energetically stable conformation has the acidic residue in its anti conformation. Incidentally, since the side-on and end-on conformations occur with arginine in its tautomeric form. (b) The Newman projection shows lysine in a staggered conformation, where all three acidic residues interact with the amine group in their anti conformations. Trans interactions are generally favoured over gauche interactions, which usually present hindrance to bond rotation.

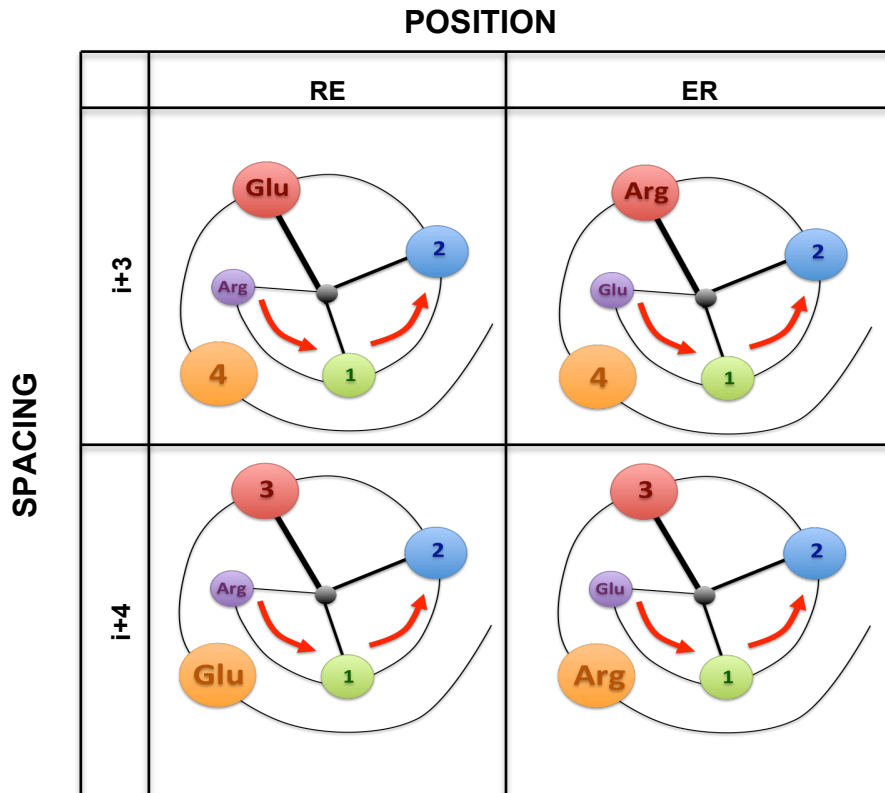
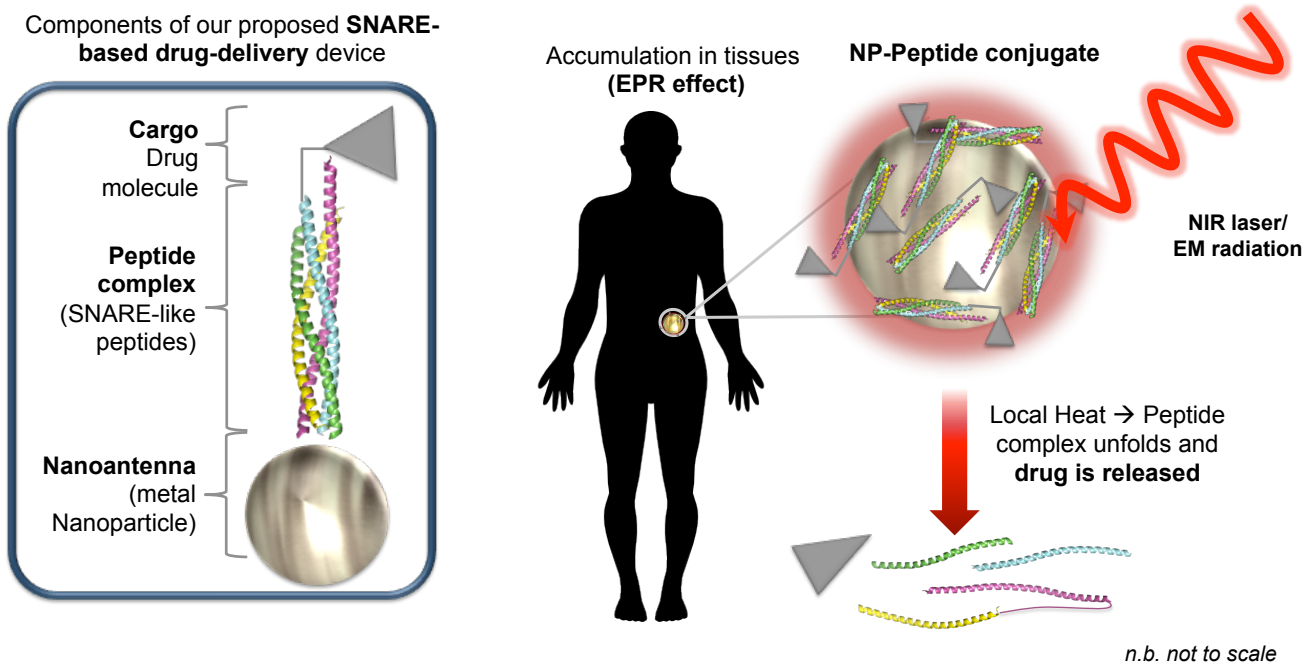


**Figure 1.12: Punnett square depicting helical wheel diagrams for the possible spacing and positioning of arginine and glutamate within a monomeric  $\alpha$ -helix.** Intrahelical ionic interactions are one of the key factors influencing  $\alpha$ -helical stability, with arginine and glutamate amino acids being the main residues contributing to the formation of such salt bridges. They have two possible spacing arrangements,  $i+3$ , and  $i+4$ ; with  $i$  standing for the initial residue within the helix, and 3 and 4 representing the number of residues between  $i$  and the residue of interest. The different arrangements for these residues are referred to as: (from left clockwise)  $3RE$ ,  $3ER$ ,  $4RE$ , and  $4ER$ .

**(a) Our proposed drug-delivery system incorporating SNARE-based peptides**



**(b) Example simplistic drug delivery system from literature**

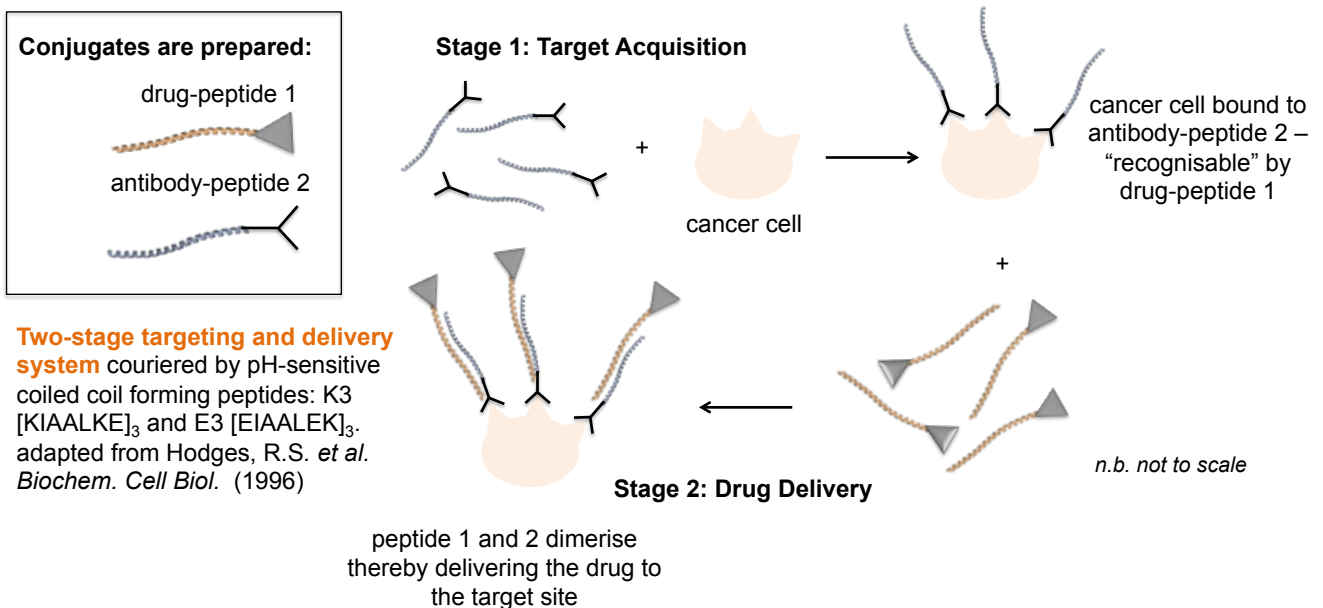
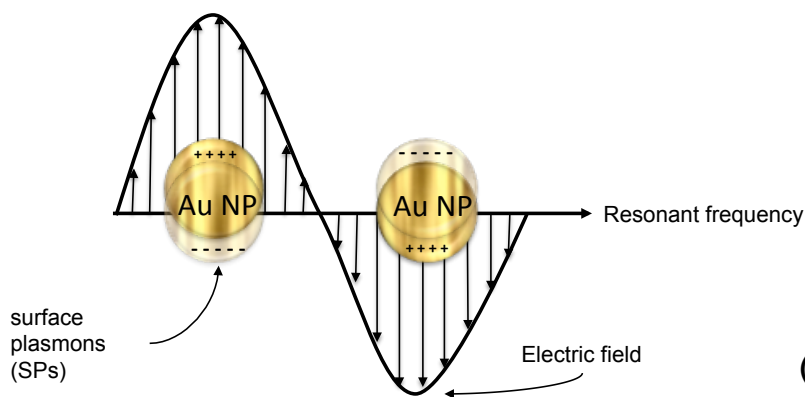
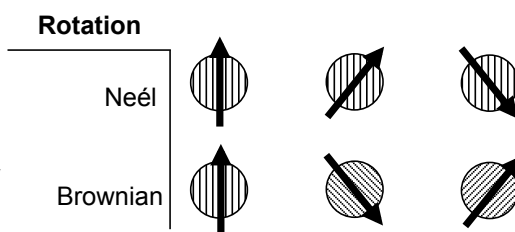


**Figure 1.13: Schematics of our proposed SNARE-based drug-delivery system, and an example of a simplistic drug delivery system from literature.** Our proposed drug delivery system is shown in (a). We envisage that the peptides will act as a thermally (or potentially pH-sensitive) linker between a payload (drug) and its vehicle (e.g. nanoparticle). In this vision, we would expect the construct to accumulate in target tissues through the enhanced permeation retention (EPR) effect, which arises because of leaky vasculature common with tumour tissue. There are other methods of targeted drug-delivery for e.g. attachment of an antibody as shown in the literature example (b), however EPR is a simpler approach. The tissue region of interest could be locally heated through electromagnetic induction or near infrared radiation in order to induce metal nanoparticle hyperthermia and initiate complex disassembly, delivering the payload (drug) in a controlled manner. The example from the literature is adapted from Hodges *et al.* (1996), and shows a simplistic two-stage drug targeting and delivery system. One chain (peptide) of a heterodimeric coiled coil is ligated to a therapeutic drug, and its counterpart is conjugated to a structure with recognition properties, such as a monoclonal antibody. The latter is administered first to seek the target, and the former is delivered some time later; by virtue of the coiled coil specificity qualities, the two chains dimerise, delivering the drug to the target in a controlled and site-specific manner (Hodges 1996).

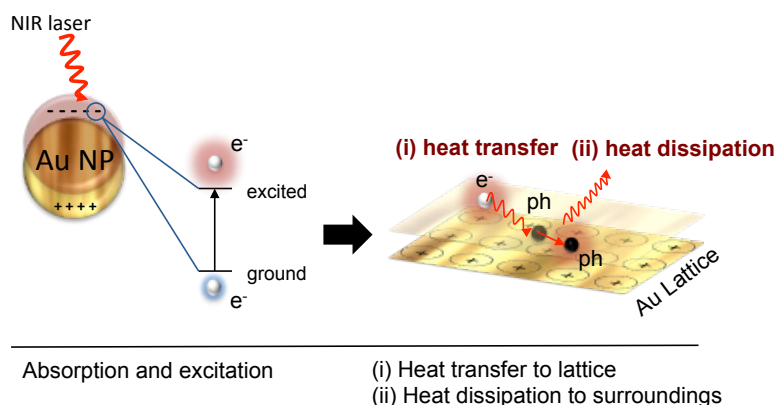
### (a) Surface Plasmon Resonance



### (c) Magnetic rotation



### (b) Au NP Hyperthermia



### (d) Influence of NP size on magnetisation

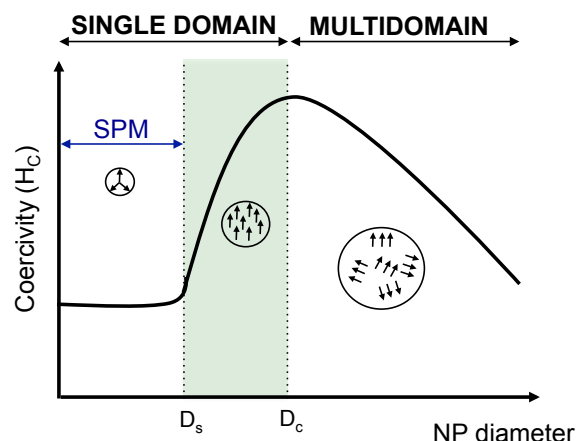


**Figure 1.14: An illustration of the surface plasmon resonance and hyperthermia phenomena in gold nanoparticles (Au NPs), and the different types of magnetic rotation and behaviour in magnetic NPs (MNPs).** (a) Schematic of surface plasmon resonance on gold nanoparticles (Au NPs). The surface plasmons (SPs) undergo oscillation at resonant frequencies when subjected to an alternating electric field. (b) The sequence of events in Au NP hyperthermia: a near infra-red laser is fired at the Au NP exciting the delocalised electrons in the SPs, light is converted to heat which is transferred from the hot electrons to phonons in the Au lattice through electron-phonon coupling, phonons in the lattice then dissipate heat to the surroundings via phonon-phonon interactions causing a localised temperature elevation of a few degrees. (c) Image adapted from Deatsch, 2014. Magnetic NPs are capable of generating heat through magnetic rotation, of which there are two types: Néel rotation, where the particle remains fixed and the magnetic moment rotates with each field oscillation; and Brownian rotation, where the magnetic moment rotates in parallel with the particle orientation with each field oscillation. (d) Image adapted from Akbarzadeh *et al*, 2012.  $D_s$  and  $D_c$  defined the thresholds for superparamagnetism and critical size respectively. Below  $D_s$ , MNPs will exhibit superparamagnetism where they align with an applied magnetic field, but in the absence of the magnetic field, they have no net magnetisation due to rapid reversal of the magnetic moment. Between  $D_s$  and  $D_c$ , nano-sized MNPs are ferromagnetic and maintain a net magnetisation even in absence of the external field. Beyond  $D_c$ , micron-sized MNPs exhibit non-uniform magnetisation that is typically referred to as multidomain behaviour.

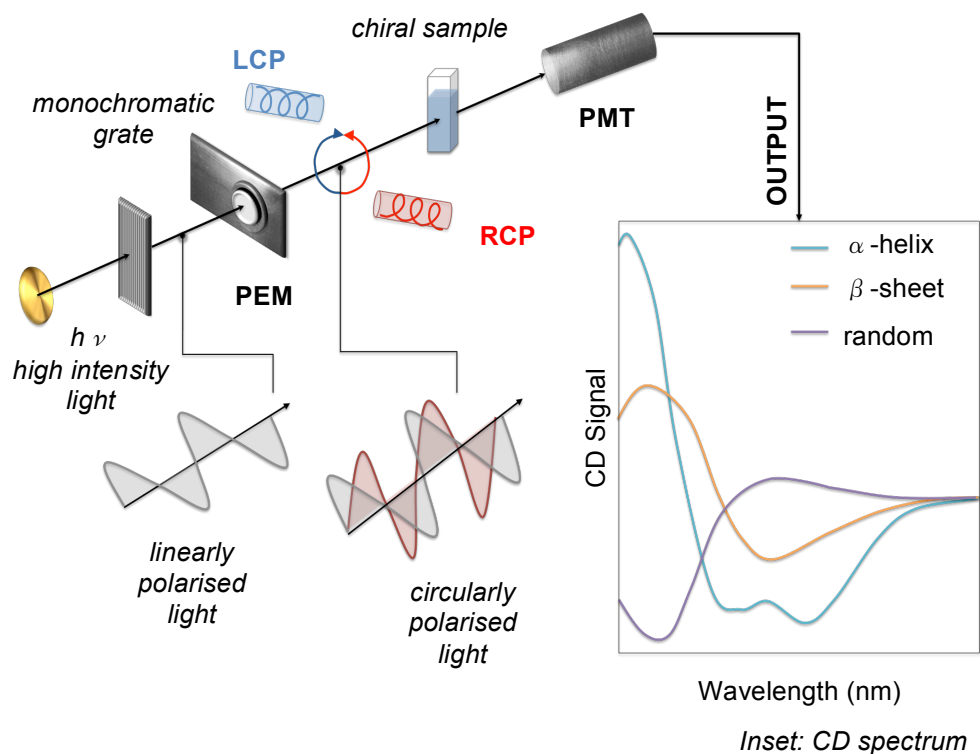


**Figure 1.15: Schematic of a circular dichroism (CD) spectrometer.** High intensity, polychromatic light is passed through a monochromator, which linearly polarises it. This monochromatised light then passed through a photoelastic modulator (PEM), which effectively transforms it into circularly polarised light that alternates between being right-handed (RCP) and left-handed (LCP). RCP and LCP light are absorbed differently by the chiral sample, and is detected by a photomultiplier tube (PMT). The output is a CD spectrum, which shows the differential absorption of circularly polarised light as a function of light wavelength. Key protein secondary structures exhibit signature spectra that are easily identifiable; these can be seen in the inset image labelled 'CD spectrum' (right). Proteins containing any of these secondary structures will deliver an absorption spectrum that can be deconvoluted to reveal their individual contributions to the protein's overall structure.



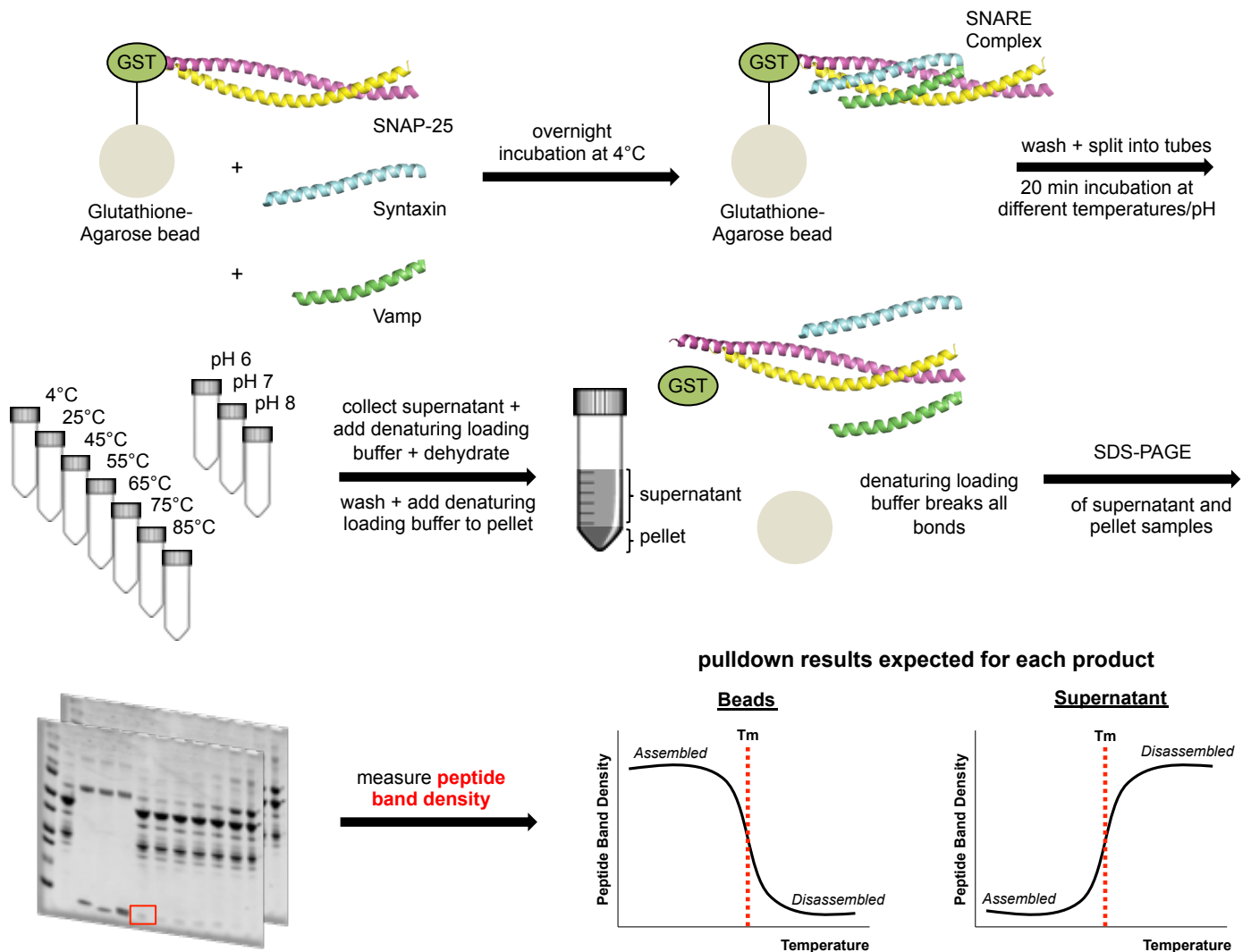


**Figure 1.16: Flow-chart schematic depicting the “pull-down” assay methodology, which is conducted in conjunction with Polyacrylamide Gel Electrophoresis (PAGE) to measure the thermostability or pH-sensitivity of the SNARE-based complexes.** GST-SNAP-25 fusion protein is bound to a solid support in the form of glutathione-agarose beads. This is mixed with an excess of syntaxin and vamp peptides and incubated overnight at 4°C. After washing the excess peptide away, the complex is split into separate tubes for incubation at different temperatures or pH. The supernatant is collected and prepared for SDS-PAGE, and then the pellet is washed and prepared for SDS-PAGE. Following SDS-PAGE, the gel is visualised using Coomassie Brilliant Blue staining, unless it is an IR-labelled gel in which case it’s visualised without any stain in the 700 nm and 800 nm channels. The density of the peptide bands is then measured and plotted as a function of temperature. The melting temperature ( $T_m$ ), or the temperature at which 50% of the complex is unfolded, is calculated by finding the mid-point of the highest and lowest peptide band densities. Different trends are expected for each pull-down product, both should show a sigmoidal pattern, however the beads product should show the greatest peptide band density at lower temperatures where more complex (and therefore peptide) should have remained bound to the solid support, and the lowest peptide band density at higher temperatures where the complex is likely to have denatured and less peptide is bound to the solid support. The converse is expected for the supernatant product, which contains the peptide released from the solid support.



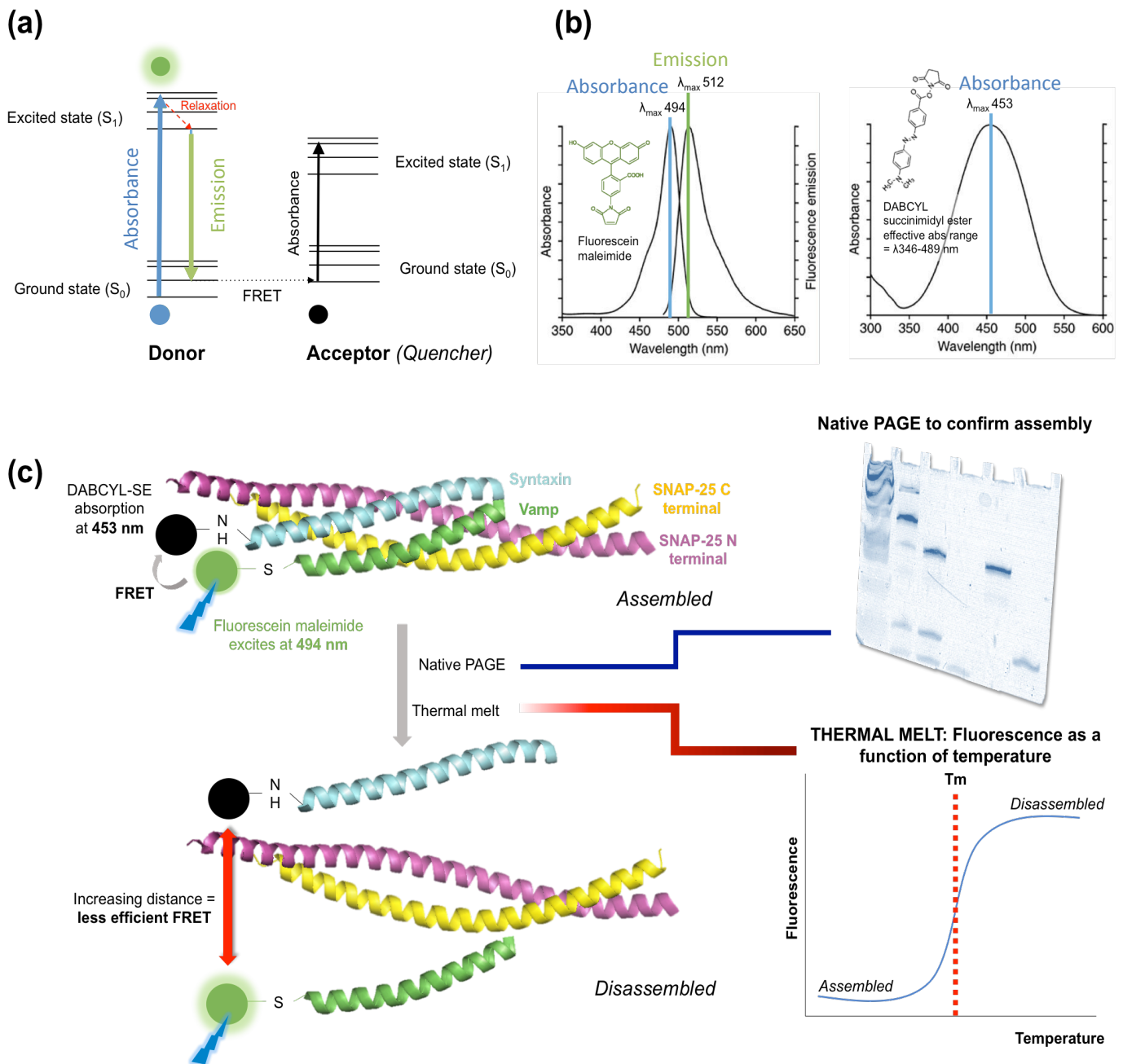


**Figure 1.17: Outline of methodology for observing complex formation, and analysing thermal stability, using a combination of native polyacrylamide gel electrophoresis (PAGE) and real-time HRM (high-resolution melt).** The Jablonski diagram in (a) illustrates the electronic transitions occurring between a donor fluorophore and acceptor quencher as our methodology describes. The donor (fluorescein) is excited by light corresponding to the energy gap between its ground and excited states; there is a small amount of non-radiative relaxation, before it emits fluorescence. Provided the donor and acceptor are located proximally to one another, Förster Resonance Energy Transfer (FRET) occurs, wherein energy is transferred from the emission of the donor to the acceptor through non-radiative dipole-dipole coupling. The acceptor utilised in this study is a quencher, and so fluorescence is ultimately quenched when FRET occurs. High-resolution melt can be used to observe melting in real-time. The fluorescent probe fluorescein maleimide and the quencher DABCYL succinimidyl ester (SE) were selected as the FRET pair that will be used to label the peptides for the high-resolution melt; and the curves in (b) show the wavelengths of their absorbance and emission. Fluorescein maleimide is a cysteine-reactive probe that will be used to label VAMP peptides; it will be excited using the green excitation channel in high-resolution melt (HRM) mode. The amino-reactive quencher DABCYL-SE, which is conjugated to syntaxin, then absorbs the emitted light. The experiment will start with a bound complex and no emission, since the quencher is absorbing all emitted light very efficiently due to the short distance between the two probes; as the temperature in the sample increases the complex unfolds, and distance increases between the two probes reducing the efficiency of energy transfer. Hence quenching decreases and emission from fluorescein will be measured. A schematic of this process, and the melt-curve trace expected is shown in (c). Native PAGE will be used to observe and confirm complex assembly as it is expected to have minimal impact on the complex's integrity. SDS-PAGE is unsuitable as it would disrupt the complex and therefore prevent observation of complex assembly.

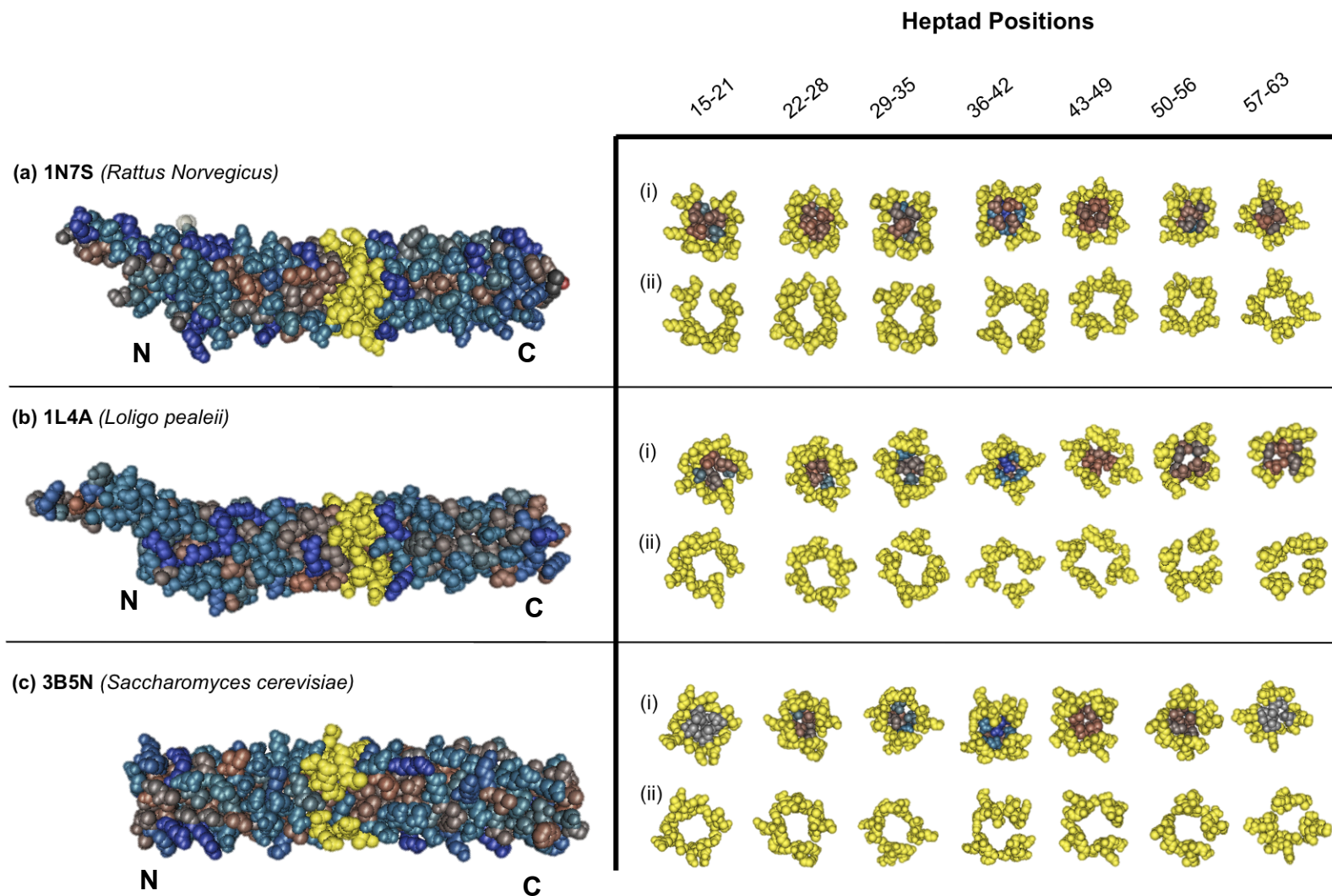


**Figure 1.18: 3D structures of SNARE complexes of interest showing spacefill representations of each heptad in the SNARE motif.** SNARE complexes of interest are shown on the left and include **(a) 1N7S (*Rattus norvegicus*)**, **(b) 1L4A (*Loligo pealeii*)**, and **(c) 3B5N (*Saccharomyces cerevisiae*)**. The ionic layer of each complex has been highlighted in yellow. On the right are the spacefill representations of each heptad slice (positions are in accordance to our scale shown in **Figure 1.24**) where **(i)** shows all residues in the heptad (abcdefg) and **(ii)** shows only the polar residues (bcefg – coloured in yellow). Complex 1L4A has tight packing at the N-terminal, however from position 43-63 the packing becomes less defined and looser. Complex 3B5N has three water-filled cavities found in heptad positions 22-28, 29-35, and 57-63.

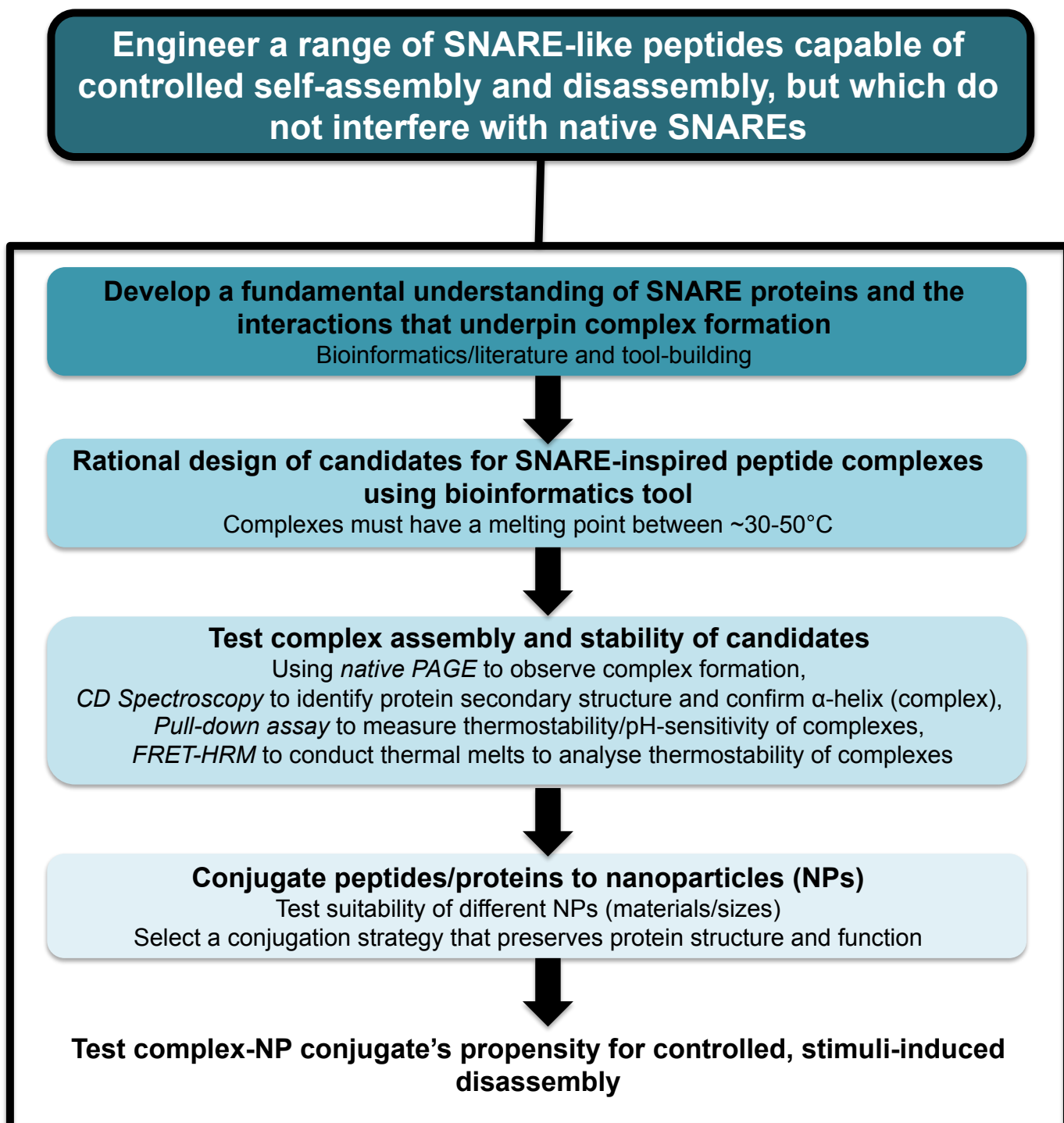


**Figure 2.1: Flow chart summarising the aim and stages defining the project.** The aim of the project is outlined at the very top of the figure, and the five stages that lead up to achieving this aim are shown in sequential order from top to bottom.

### 13.3 Figures in Chapter 3

	A	B	C	D	E	F	G	H	I	J	K	L	M	N	O	P	Q	R	S	AA	AB	AC	AD	AE	AF	AG	AH	AI	AJ	
7												7		100	0															
8		(a)	(b)	(c)	(d)	(e)	(f)	(g)	(h)	(i)	(j)	(k)	(l)	(m)	(n)															
9																				1	2	3	4	5	6	7	8	9	10	
10		Protein	Citation	Notes	Datablock Name	Chain ID	uniprot AC	Organism	FASTA from PDB structures	TOT	USE or DON'T USE	N-terminal extend	"Start"	Length	C-terminal extend	Recalc "Start"	TOT	Display	TOT	a	b	c	d	e	f	g	a	b	c	
11	>	Syntaxin-1A			1KIL	B	P32851	Rattus nor	MKDRTQE	288		7	195	100	0	188	0			0										
12	>	SNAP-25 N-terminal			1KIL	C	P60880.2	Homo sapi	MAEDADM	206		7	22	100	0	15	0			0										
13	>	SNAP-25 C-terminal			1KIL	D	P60880.2	Homo sapi	MAEDADM	206		7	143	100	0	136	0			0										
14	>	VAMP-2			1KIL	A	P63045	Rattus nor	MSATAATV	116		7	25	100	0	18	0			0										
15	>	Syntaxin-1A			1N7S	B	P32851	Rattus nor	MKDRTQE	288	1	7	195	100	0	188	107	SKQALSEI	107	107	S	K	Q	A	L	S	E	I	E	T
16	>	SNAP-25 N-terminal			1N7S	C	P60881.2	Rattus nor	MAEDADM	206	1	7	22	100	0	15	107	QRRADQL	107	107	Q	R	R	A	D	Q	L	A	D	E
17	>	SNAP-25 C-terminal			1N7S	D	P60881.2	Rattus nor	MAEDADM	206	1	7	143	100	0	136	107	RVTNDAR	107	107	R	V	T	N	D	A	R	E	N	E
18	>	VAMP-2			1N7S	A	P63045	Rattus nor	MSATAATV	116	1	7	25	100	0	18	107	GPPAPPP	107	107	G	P	P	A	P	P	P	N	L	T

198

**Figure 3.1: The SNARE complex database.** All cells that are filled in grey contain formulae and cannot be changed. All non-grey cells require input from the user. (a) Protein type “syntaxin”(red fill)/“SNAP-25 N-terminal”(light green fill)/“SNAP-25 C-terminal”(dark green fill)/“VAMP-2” (ilac fill) with proteins in yellow indicating non-traditional SNARE. (b) Citations and comments are especially helpful for SNAREs from literature or speculated additions. (c) Datablock name and chain I.D. for PDB structures. (d) Uniprot accession codes. Those filled with red indicate duplicated accession codes in the database. (e) FASTA obtained from the PDB report and the column adjacent indicates the total amount of characters in the sequence. (f) “USE or DON’T USE” column allows the user to select a sequence for analysis. Inputting any character in the cell will cause it to be included in analysis as can be seen in the rows 15-18. Leaving it empty will result in the subsequent columns remaining empty and the sequence not being included in analysis as can be seen in all the rows other than 15-18. (g) Cell L7 allows the user to select the number of amino acids that will make up the “N-terminal extension” in relation to the start position chosen by the user. (h) “Start” position of the motif, must be input by the user, and will apply to ALL complexes under analysis. The numbers that are currently in the database were retrieved from the protein-protein blast between PDB I.D. and uniprot accession code in the cases of elucidated structures. In the case of literature-based or speculated additions, these positions were obtained by alignment with known structures. (i) Cell N7 allows the user to select the “Length” of sequence, which will apply to ALL complexes selected for analysis. (j) Cell O7 allows the user to select the number of amino acids that make up the “C-terminal extension” in relation to the end of the chosen “length” of the sequence. (k) “Recalculated start” subtracts the “N-terminal extension” column from the “start” column. (l) This column tells the user how many characters are in the sequence. (m) “Display” column displays the sequence that has been selected based on the previous parameters set by the user. (n) This column tells the user how many characters are in the sequence in the display column. (o) Columns AA to DV display single characters of the entire sequence in the “display” column.



(a)	(b)	(c)	(d)	(e)	(f)	(g)	(h)
A	B	C	D	E	F	G	H
<b>SELECTION =&gt;</b>							
Amino Acid	3 LETTER CODE	Hydrophilicity	Approx. CHARGE	Av. MASS	Residue Volume	Av. volume buried	van der Waals volume
A	Ala	-1.8	0	71.0788	88.6	92	67
C	Cys	-0.4	0	103.1388	108.5	106	86
D	Asp	3.5	-1	115.0886	111.1	125	91
E	Glu	3.5	-1	129.1155	138.4	155	109
F	Phe	-2.8	0	147.1766	189.9	203	135
G	Gly	0.4	0	57.0519	60.1	66	48
H	His	3.2	0	137.1411	153.2	167	118
I	Ile	-4.5	0	113.1594	166.7	169	124
K	Lys	3.9	1	128.1741	168.6	171	135
L	Leu	-3.8	0	113.1594	166.7	168	124
M	Met	-1.9	0	131.1926	162.9	171	124
N	Asn	3.5	0	114.1038	114.1	135	96
P	Pro	1.6	0	97.1167	112.7	129	90
Q	Gln	3.5	0	128.1307	143.8	161	114
R	Arg	4.5	1	156.1875	173.4	225	148
S	Ser	0.8	0	87.0782	89	99	73
T	Thr	0.7	0	101.1051	116.1	122	93
V	Val	-4.2	0	99.1326	140	142	105
W	Trp	0.9	0	186.2132	227.8	240	163
Y	Tyr	1.3	0	163.176	193.6	203	141
X	X	N/A	N/A	N/A	N/A	N/A	N/A

**Figure 3.2: “Scales” in the SNARE database.** (a) Amino acid scale that is used to index-match (an excel function that allows a user to lookup a value in a defined array, and returns a value based on it’s position) each amino acid in the selected sequences to a value from any given scale selected in the analysis page. (b) Amino acid 3-letter code has also been integrated for potential use later on in the project. (c) Hydrophilicity scale (Kyte, J., Doolittle 1982). (d) Approximate charge of amino acids at physiological pH. (e) Average mass of amino acids. (f) Residue volumes (Zamyatin 1984). (g) Average volume buried (Richards 1977; Baumann *et al.* 1989). (h) van der Waals volume (Darby & Creighton 1993).

(a)

	B	C	D	F	G	H	I	J	K	L	M	N	U	V	W	X	Y	Z	AA	AB	AC
1																					
2	Select SCALE to use			(c) Vertical line (Y's)		-4.5	4.5	(b)	Max=	4.3	Min=	-4.4						INDIVIDUAL A.A. DATA	1	2	3
3	Enter column letter (CAPITAL)			N-terminal extension boundary		7	7		Max=	4.5	Min=	-4.5						Four-helical complex	2.3	1.5	2.6
4	as in the SCALES worksheet								Max=	4.5	Min=	-4.5						Syntaxin	0.8	3.9	3.5
5	E.g. for hydrophilicity enter C			Vertical line (Y's)		-4.5	4.5		Max=	4.5	Min=	-4.5						SNAP-25 N-terminal	3.5	4.5	4.5
6	c			C-terminal extension boundary		101	101		Max=	4.5	Min=	-4.5						SNAP-25 C-terminal	4.5	-4.2	0.7
7		C		Scaling graphs		MAX=	4.50											Synaptobrevin	0.4	1.6	1.6
8	SCALE heading:	Hydrophilicity				MIN =	-4.50											A.A. RANGES' DATA			
9						Upper =	4.50											Four-helical complex	1.2	1.4	1.3
10	Selected values are shown below					Lower =	-4.50											Syntaxin	1.3	0.5	0.6
11	A	-1.8		Vertical line (Y's)		-4.4	3.0	(d)	Max=	2.1	Min=	-2.0						SNAP-25 N-terminal	2.1	2.8	3.0
12	C	-0.4		N-terminal extension boundary		7	7		Max=	2.8	Min=	-3.7						SNAP-25 C-terminal	0.9	1.6	1.0
13	D	3.5							Max=	3.0	Min=	-2.5						Synaptobrevin	0.4	0.7	0.8
14	E	3.5		Vertical line (Y's)		-4.4	3.0		Max=	2.9	Min=	-1.2									
15	F	-2.8		C-terminal extension boundary		101	101		Max=	2.8	Min=	-4.4									

**Figure 3.3: General overview of “Analysis” section of the SNARE database.** (a) User selects the scale they would like to analyse the sequence against by choosing the column from the “Scales” page of the Excel spreadsheet. The yellow-filled cells also show the chosen scale for reference. (b) returns the maximum and minimum values in each of the four sequences in columns AA onwards (follow the red lines), whilst cell N9 “select window size” allows the user to average the results for the sequences by choosing between a window size of 1,3,5,7 and 9. The results for this are returned in rows 9-13 titled “A.A. RANGES’ DATA”. (c) This module allows the user to scale and visualise vertical lines that represent the start and end of the motif on the results graphs by taking into account the minimum and maximum values from module (b) and the N- and C-terminal extensions set in the database. (d) This feature is still being optimised but will allow the user to shift between sequence data of any particular row in the database allowing comparisons to be made between complexes. The output can be manipulated using the functions outlined in **Figure 3.4**.

**(a) Single amino acid data**

	W	X	Y	Z	AA	AB	AC	AD	AE	
1	INDIVIDUAL A.A. DATA									
2	Four-helical complex					2.3	1.5	2.6	-0.5	1.2
3	Syntaxin					0.8	3.9	3.5	-1.8	-3.8
4	SNAP-25 N-terminal					3.5	4.5	4.5	-1.8	3.5
5	SNAP-25 C-terminal					4.5	-4.2	0.7	3.5	3.5
6	Synaptobrevin					0.4	1.6	1.6	-1.8	1.6
7										
8	A.A. RANGES' DATA									
9	Four-helical complex					1.2	1.4	1.3	1.4	1.1
10	Syntaxin					1.3	0.5	0.6	1.0	0.2
11	SNAP-25 N-terminal					2.1	2.8	3.0	2.0	1.2
12	SNAP-25 C-terminal					0.9	1.6	1.0	1.5	1.4
13	Synaptobrevin					0.4	0.7	0.8	0.9	1.4

	1	2	3	4	5
109					
110					
111					
112					
113					
114					
115	0.8	3.9	3.5	-1.8	-3.8
116	3.5	4.5	4.5	-1.8	3.5
117	4.5	-4.2	0.7	3.5	3.5
118	0.4	1.6	1.6	-1.8	1.6
119					
120					
121					
122					
123					
124					
125					
126					
127					
128					
129					
130					

	1	2
110		
111		
112		
113		
114		
115	0.8	3.9
116	3.5	4.5
117	4.5	-4.2
118	0.4	1.6
119		
120		
121		
122		
123		
124		
125		
126		
127		
128		
129		
130		

**(b) Moving averages using window size**

	L	M	N	V	W	X	Y	Z	AA	AB	AC	AD	AE	AF	AG	AH	AI	AJ	AK	AL	
1	INDIVIDUAL A.A. DATA																				
2	187.7	Min-	86.4		116.6	148.7	136.5	95.0	125.4	108.5	147.8	127.0	132.6	127.3	128.6	136.3					
3	193.6	Min-	60.1		Syntaxin					89.0	168.6	143.8	88.6	166.7	89.0	138.4	166.7	138.4	116.1	173.4	153.2
4	227.8	Min-	60.1		SNAP-25 N-terminal					143.8	173.4	173.4	88.6	111.1	143.8	166.7	88.6	111.1	138.4	89.0	166.7
5	173.4	Min-	60.1		SNAP-25 C-terminal					173.4	140.0	116.1	114.1	111.1	88.6	173.4	138.4	116.1	138.4	162.9	111.1
6	227.8	Min-	60.1		Synaptobrevin					60.1	112.7	112.7	88.6	112.7	112.7	112.7	114.1	166.7	116.1	89.0	114.1
7	A.A. RANGES' DATA																				
8	window size (1,3,5,7,9):			7	Four-helical complex					99.3	124.4	121.8	125.5	127.0	124.7		128.2	129.7	133.5	130.7	134.6
9					Syntaxin					98.0	131.3	124.3	126.3	137.4	133.1		129.1	141.2	139.3	139.3	139.3
10	156.3	Min-	99.3		SNAP-25 N-terminal					115.8	138.1	139.0	143.0	135.1	126.2	121.2	121.2	129.2	128.4	117.3	121.2
11	168.6	Min-	98.0		SNAP-25 C-terminal					108.7	130.9	123.9	131.0	126.0	122.3	125.4	132.4	132.4	139.5	131.1	135.1
12	161.0	Min-	106.2		Synaptobrevin					74.8	97.4	99.9	101.7	109.5	117.2	117.7	117.7	117.9	126.6	135.3	142.8

**Figure 3.4: Analysis of single amino acids, and taking moving averages in the SNARE database.** The scores for all amino acids in the selected sequences based on whichever scale has been selected is returned in rows 111 and below (cells are filled in grey to indicate formulae, empty cells correspond to unselected sequences). **(a)** Relates to single, or “individual” amino acid data. Rows 2-6 return scores for individual amino acids of the selected sequences. Row 2 shows the average score across the entire four-helical complex at any particular position as seen in the lines highlighted in red and labelled (i). The scores returned in rows 3-6 refer to single helices only, for e.g. in the blue lines labelled (ii) the average is taken at this position for all syntaxin helices in selected complexes. **(b) Note:** This is conducted on a different tab hence the duplication of row numbers. Relates to moving averages, which can be controlled by selecting window size. The results are returned in rows 9-13 titled “A.A. RANGES’ DATA”, where the top row refers to an average of the scores for the entire four-helical complex; and rows 10-13 refer to an average of the scores for single helices at the column position indicated. Taking the example of synaptobrevin, the arrow labelled (iii) indicates that the formula in the highlighted cell takes into account the selected window size, 7, which then selects the appropriate number of cells to average from the corresponding row in “INDIVIDUAL A.A. DATA” rows. Please note that the excel conditional formula (a nested IF/OR formula) includes all possibilities of window sizes up to 9 and so 9 cells are highlighted but in this case, only 7 will be averaged.

	U	V	W	X	Y	Z	AA	AB	AC	AD	AE	AF	AG	
<b>Groups analysis</b>														
<b>Number of sets analysed</b>														
(a)	Four-helical complex		a		0.00									
			Number of seq. entries		0									
	Four-helical complex		d							-0.48				
			Number of seq. entries							1				
	Syntaxin		bc		3.90 3.50									
			Number of seq. entries		1 1									
			Averaged values		3.70 3.70									
	Syntaxin		efg							-3.80	0.80	3.50		
			Number of seq. entries							1	1	1		
			Averaged values							0.17	0.17	0.17		
	SNAP-25 N-terminal		bc		4.50 4.50									
			Number of seq. entries		1 1									
			Averaged values		4.50 4.50									
	SNAP-25 N-terminal		efg							3.50	3.50	-3.80		
			Number of seq. entries							1	1	1		
			Averaged values							1.07	1.07	1.07		
(b)	SNAP-25 C-terminal		bc		-4.20 0.70									
			Number of seq. entries		1 1									
			Averaged values		-1.75 -1.75									
	SNAP-25 C-terminal		efg							3.50	-1.80	4.50		
			Number of seq. entries							1	1	1		
			Averaged values							2.07	2.07	2.07		
	Synaptobrevin		bc		1.60 1.60									
			Number of seq. entries		1 1									
			Averaged values		1.60 1.60									
	Synaptobrevin		efg							1.60	1.60	1.60		
			Number of seq. entries							1	1	1		
			Averaged values							1.60	1.60	1.60		
							1	2	3	4	5	6	7	
							0.8	3.9	3.5	-1.8	-3.8	0.8	3.5	
							3.5	4.5	4.5	-1.8	3.5	3.5	-3.8	
							4.5	-4.2	0.7	3.5	3.5	-1.8	4.5	
							0.4	1.6	1.6	-1.8	1.6	1.6	1.6	

**Figure 3.5: “Group analysis” section of the SNARE database.** The following relates to “Group analysis” of nonpolar and polar layers in the complexes. The scores for all amino acids in the selected sequences based on whichever scale has been selected is returned in rows 111 and below (cells are filled in grey to indicate formulae, empty cells correspond to unselected sequences). These are referenced in the formulae for “Group analysis”. (a) Refers to nonpolar layers “a” and “d” of the selected complexes. The blue-filled cell returns an average score for the column it is in, i.e. if it is in a column representing “a” positions like column AA, then it will return an average score for all amino acids in that column as the arrow indicates. The peach-filled cell below that gives an indication of how many complexes have been sampled to give this value. (b) Refers to polar layers “bc” and “efg” of the selected complexes. They follow the same format as (a), but there is an additional row of cells filled in yellow that average the scores in the blue-filled cells and then duplicate (for “bc” layers) or triplicate (for “efg” layers) the result for aesthetic effect in the results bar graphs. Specifically, they give the bars for each layer a thickness of two (for “bc” layers), or three (for “efg” layers) lines to allow the user to differentiate quickly between the two, as can be seen in the example of the graph of synaptobrevin pointed out by the blue arrow.



# 13.4 Figures in Chapter 4

(a) Protein identifiers for each complex

PDB I.D.	Chain	Protein	Abbreviations	Uniprot A.C.
1N7S (Rattus norvegicus)	B	Syntaxin	(Syn, Stx)	P32851
	C	SNAP-25 N-terminal	(25N, SNAP-25N, SNAP-25 H1)	P60881.2
	D	SNAP-25 C-terminal	(25C, SNAP-25C, SNAP-25 H2)	P60881.2
	A	VAMP-2 (otherwise known as synaptobrevin)	(Brev, VAMP)	P63045
1L4A (Loligo pealeii)	B	Syntaxin (a.k.a. S-syntaxin)	(Syn, Stx)	O46345
	C	SNAP-25 N-terminal (a.k.a. Synaptosomal-associated protein)	(25N, SNAP-25N, SNAP-25 H1)	Q8T3S4
	D	SNAP-25 C-terminal (a.k.a. Synaptosomal-associated protein)	(25C, SNAP-25C, SNAP-25 H2)	Q8T3S4
	A	VAMP-2 (otherwise known as synaptobrevin)	(Brev, VAMP)	P47194
3B5N (Saccharomyces cerevisiae)	B	Protein Sso1	(Syn, Stx)	P32867
	C	Sec9 (a.k.a. Sec9p)	(Sec9 H1, 25N, SNAP-25N, SNAP-25 H1)	P40357
	D	Sec9 (a.k.a. Sec9p)	(Sec9 H2, 25C, SNAP-25C, SNAP-25 H2)	P40357
	A	Synaptobrevin	(Brev, VAMP)	P31109

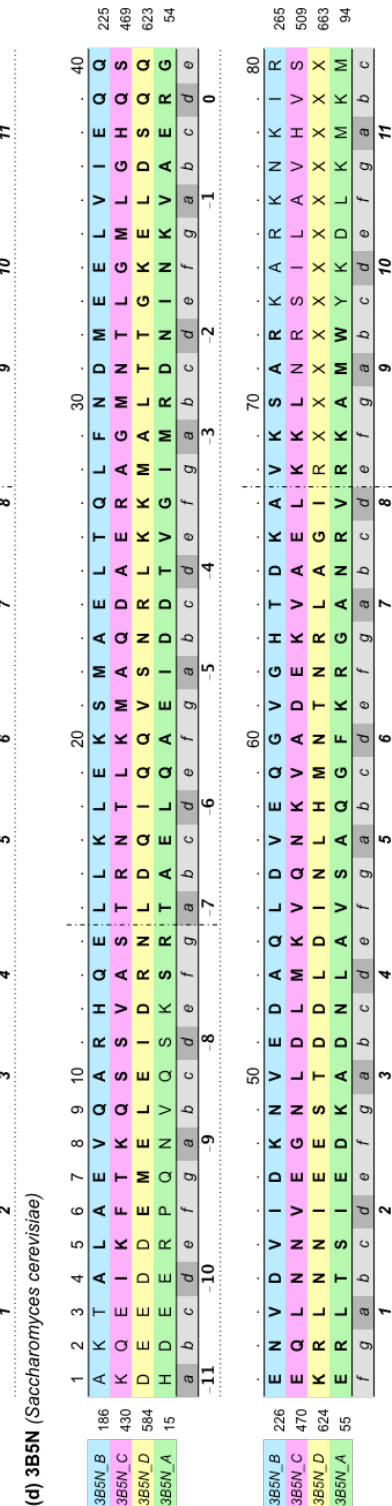
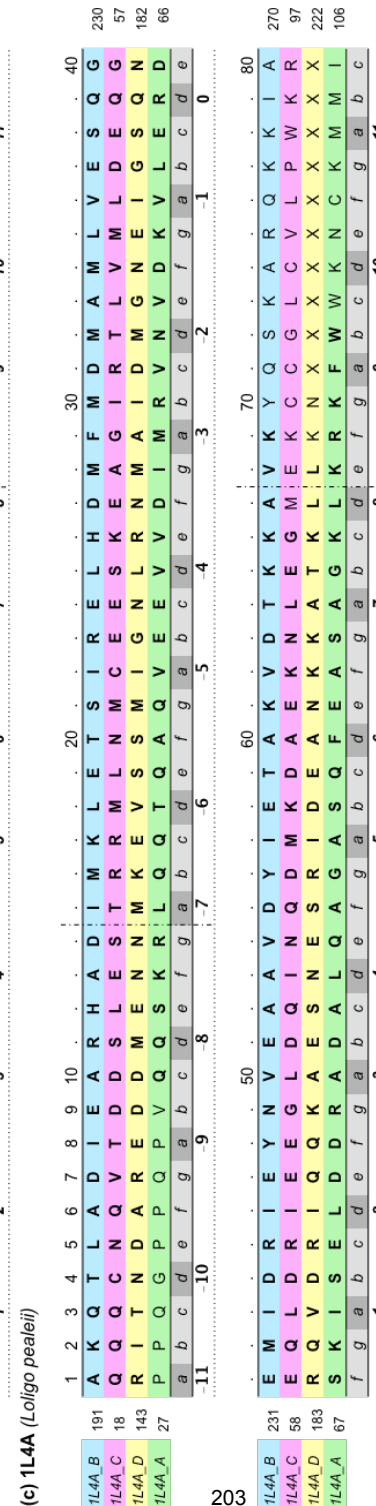
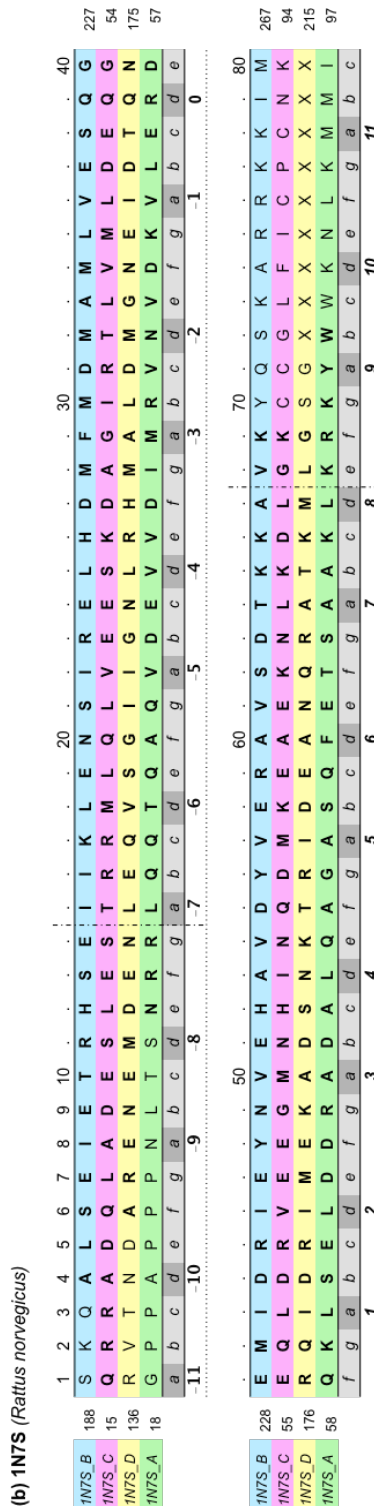


**Figure 4.1: The sequence for each complex alongside start and stop positions in a range of different scales including PDB scale, our positioning, segments and “4,3-layers” scale. (a)** Tabulates the protein identifiers for each complex. Each complex is a parallel heterotetrameric QabcR SNARE and is composed of three t-SNAREs that are, or act in the capacity of, syntaxin, SNAP-25 N-terminal, SNAP-25 C-terminal, and the R-SNARE VAMP-2 (otherwise referred to as synaptobrevin). In subsequent analyses and figures, the proteins may be referred to interchangeably as any of the names or abbreviations defined in this table. The sequences in tables **(b)**, **(c)** and **(d)** were obtained using the uniprot accession codes in the last column of this table (see below). Tables *(b)*, *(c)*, and *(d)* show the sequence alignment of the three complexes 1N7S *(b)*, 1L4A *(c)* and 3B5N *(d)*. The first column specifies the chain according to the PDB file, whilst the second and last columns indicate the start and end positions of the sequence in the protein. Above the sequences is the “Position” scale used in the bioinformatics tool that has been created for the purpose of this project. Directly below the sequences is the “Segment” position which refers to the (abcdefg)<sub>n</sub> heptad repeat, and the “4,3-layers”, which refers to the hydrophobic layers *a* and *d* specifically, can be seen at the bottommost row. Within the sequences themselves, the amino acids in **bold** font are present in the PDB sequences. The broken lines indicate the start and end of the SNARE motif. The start and end positions of the protein sequences were chosen to show an N- and C-terminal extension of at least two heptads (i.e. 2x 4,3-layers). Although these are external to the motif, we expect amino acids in these extensions to form interactions with the motifs for e.g. as seen in the salt bridge study in **Figure 5.5**.

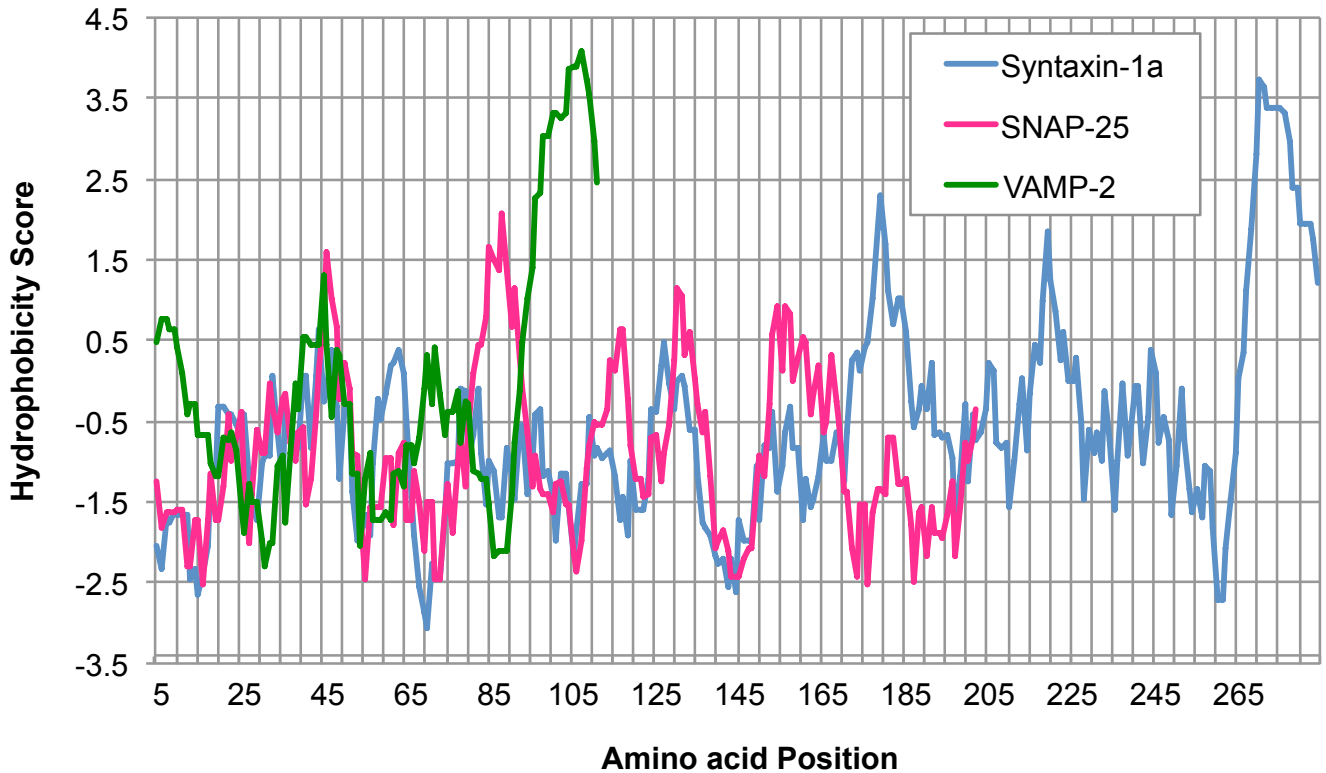
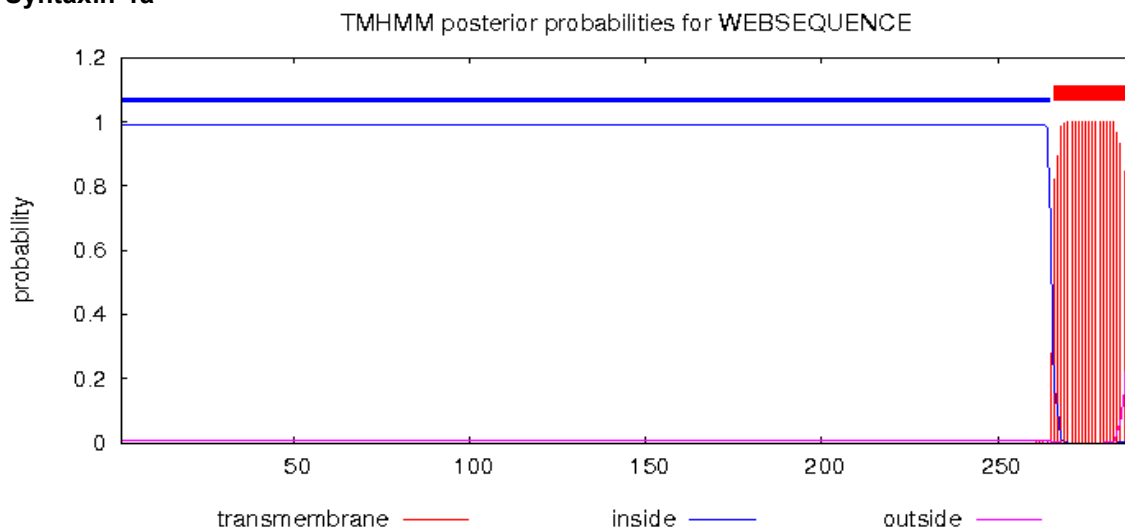
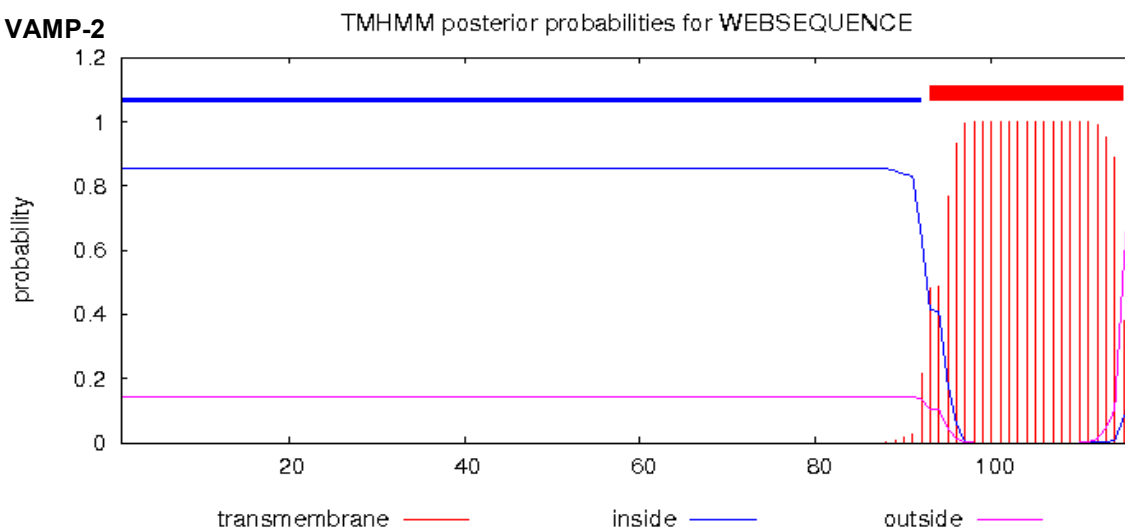


**Figure 4.2: Hydrophobicity profile overlay for each protein sequence calculated using Kyte and Doolittle's amino acid hydrophobicity scale and obtained using Protscale (ExpASy).** The Uniprot accession code input for syntaxin-1a was P32851, SNAP-25 was P60881, and VAMP-2 was P63045. These correspond to the Uniprot accession codes for 1N7S in **Figure 4.1**. Both syntaxin-1a (*blue*) and VAMP-2 (*green*) display a strong rise in hydrophobicity score towards the end of the sequence suggesting the presence of transmembrane domains at their C-terminals. In contrast, SNAP-25 (*pink*) scores consistently low for hydrophobicity throughout the entire sequence.

### Syntaxin-1a



### VAMP-2



### SNAP-25b

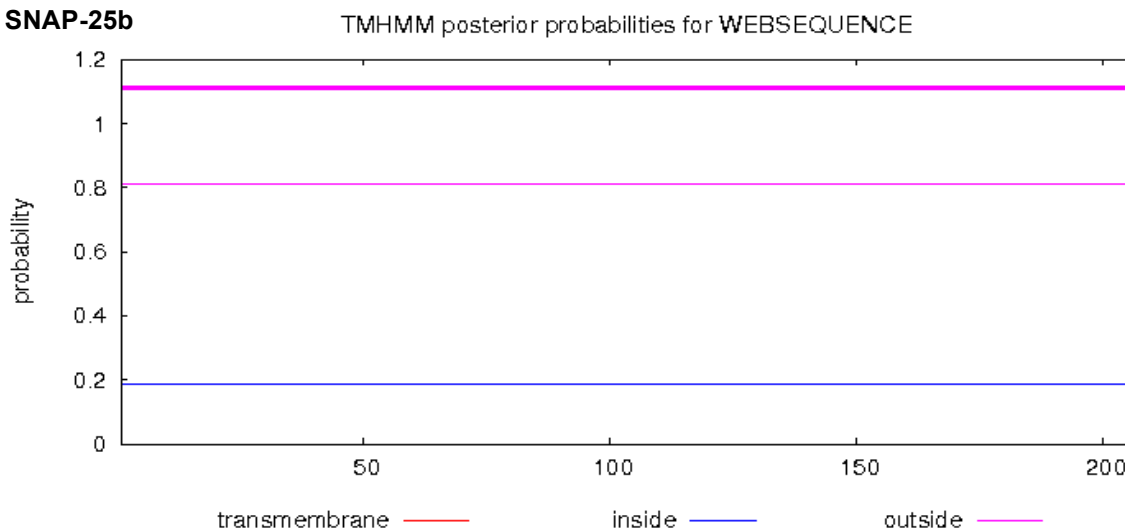
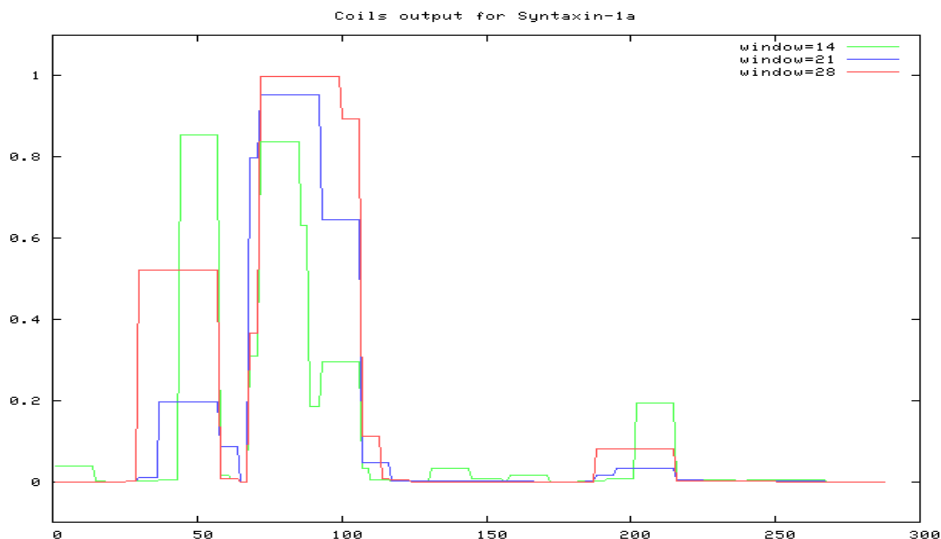
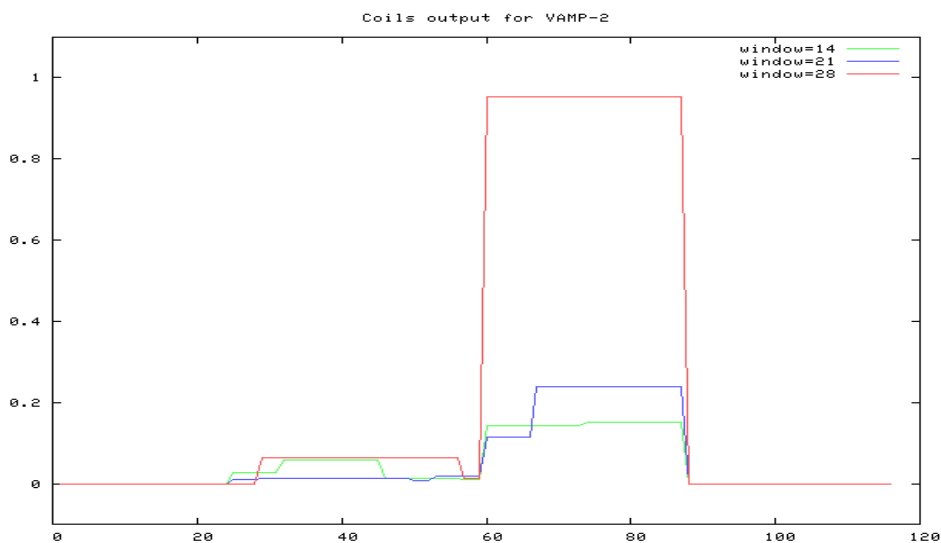


**Figure 4.3: TMHMM (CBS) prediction of transmembrane helices in syntaxin-1a (top); VAMP-2 (middle) and SNAP-25b (bottom).** As expected based on the results of their hydrophobicity profiles, syntaxin-1a and VAMP-2 possess transmembrane C-terminals whilst SNAP-25b bears none at all.

### Syntaxin-1a



### VAMP-2



### SNAP-25

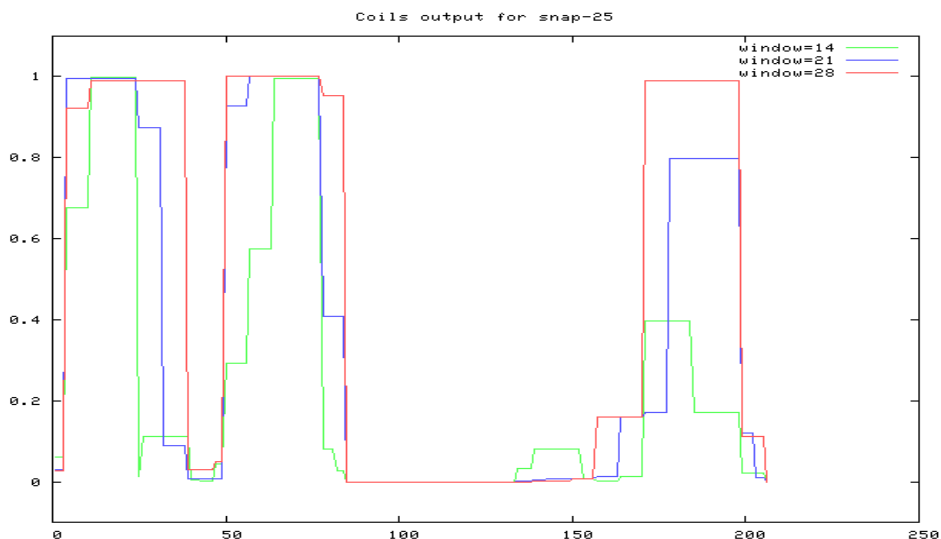


**Figure 4.4: COILS (Expasy) output predicting the presence of coiled-coil topologies in syntaxin-1a (top); VAMP-2 (middle) and SNAP-25 (bottom).** The three data sets in each output represent the coiled-coil forming probability within the scanning window of 14 (green), 21 (blue), and 28 (red) residues. Syntaxin-1a presents two coiled-coil regions with reasonable probability (indicated by the score on the x-axis); VAMP-2 displays one coiled-coil with high probability and SNAP-25 presents three coiled-coil regions, two in close proximity located in the N-terminal and one slightly more remote and found in the C-terminal.

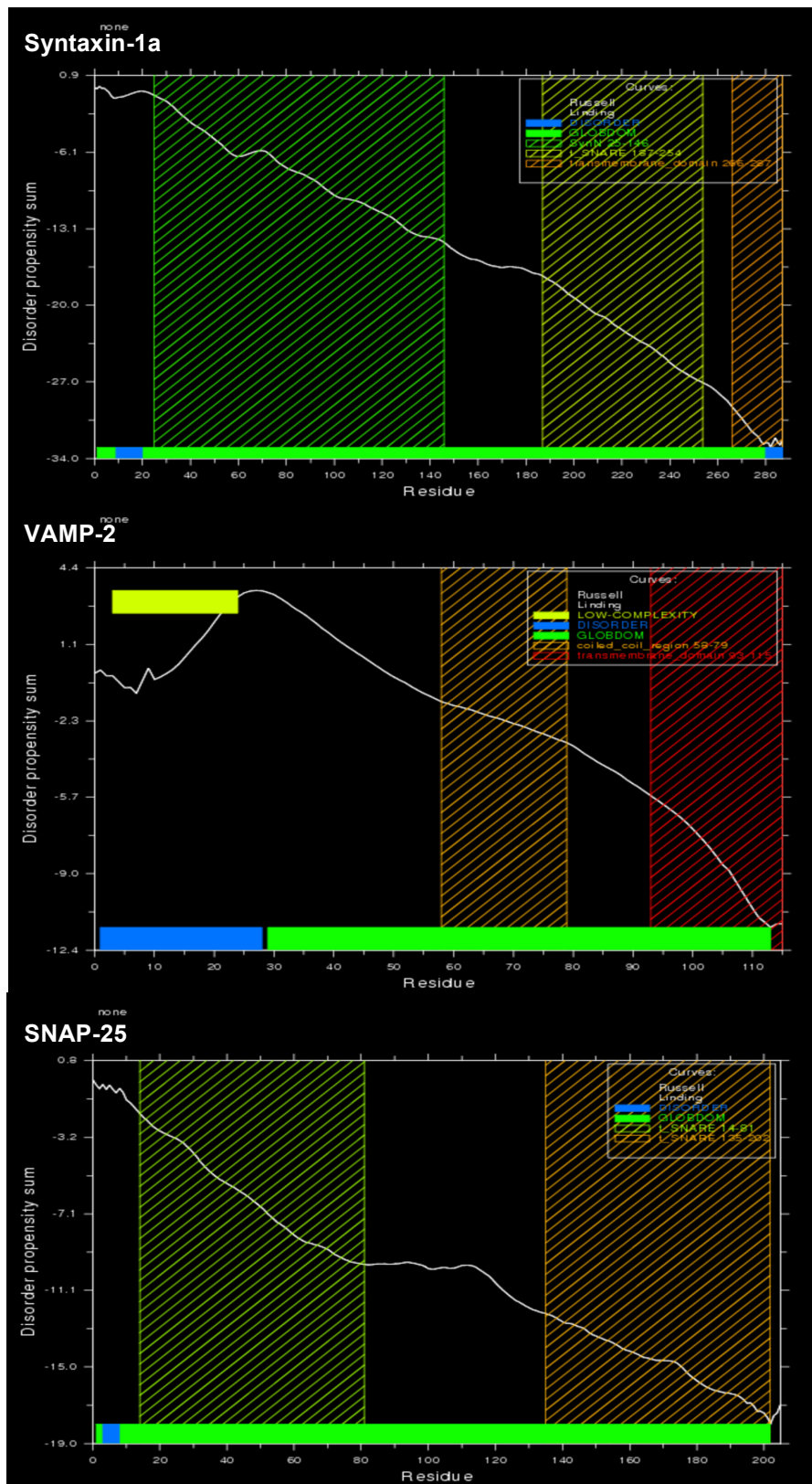


**Figure 4.5: GlobPlot (EMBL) prediction of disorder and globular segments within syntaxin-1a (top); VAMP-2 (middle) and SNAP-25 (bottom).** For all proteins the white line is going down-hill which corresponds to the globular domains (GlobDoms) highlighted at the very bottom of the graph in solid green; and in the specific case of VAMP-2, the initial up-hill region corresponds to protein disorder, which is highlighted in solid blue at the very bottom of the graph. For VAMP-2, since this disordered region is also marked as 'low complexity' indicated by the yellow boxes. Syntaxin-1a also displays the named regions: synN between residues 25-146 (striped green), T\_SNARE 187-254 (striped yellow), and a transmembrane region 266-287 (striped orange). VAMP-2 displays the named regions: coiled-coil 59-79 (striped orange) and transmembrane 93-115 (striped red). Finally, SNAP-25 displays the named regions: t-SNARE 14-81 (striped green) and a second t-SNARE between 135-202 (striped orange).

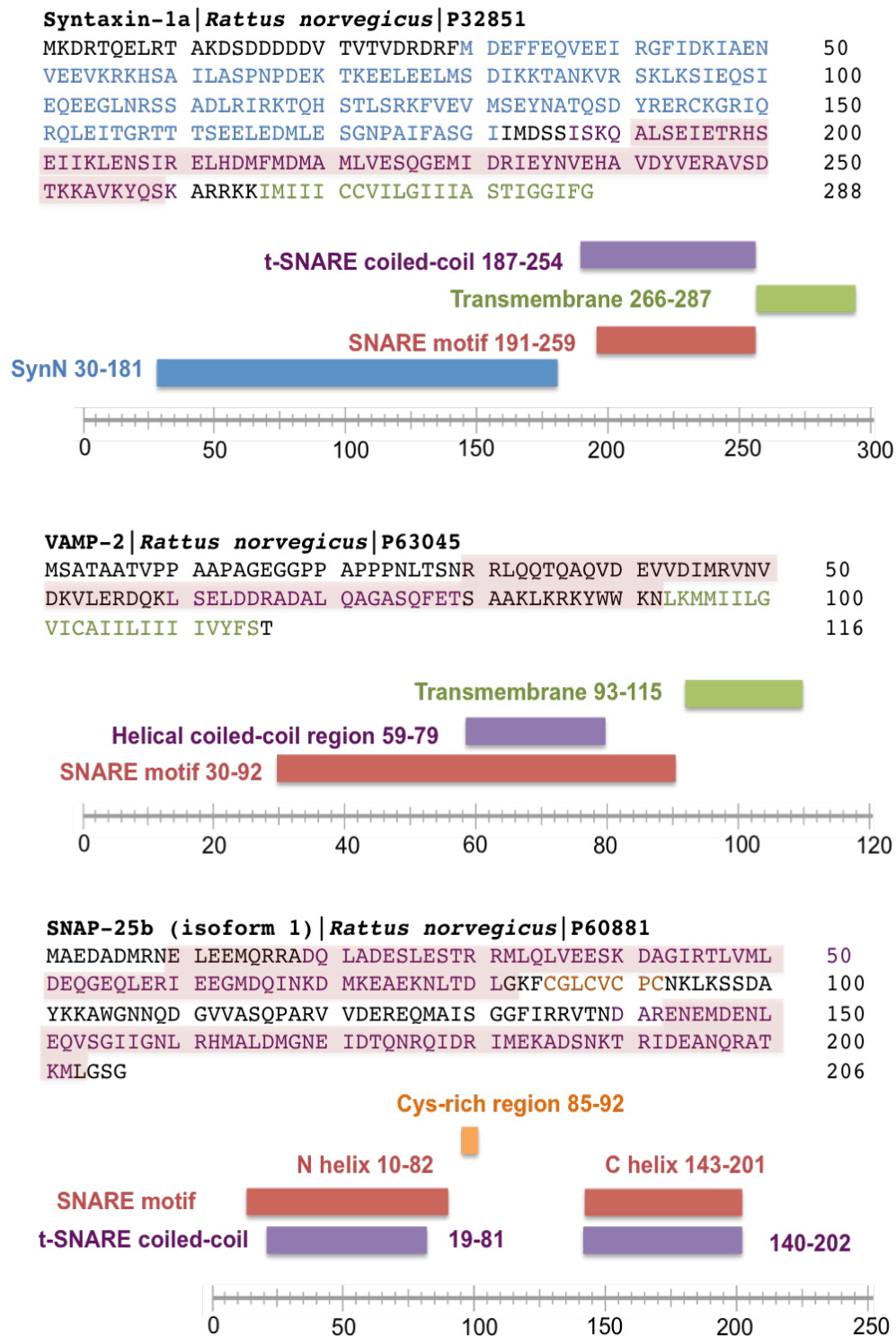


**Figure 4.6: Conserved domains obtained from collated from ProtParam (ExPASy), Conserved Domain Database (NCBI) and Globplot (EMBL) using each protein's swissprot accession number (quoted beside protein name).** Syntaxin-1a possesses a synN protein domain, which includes the conserved N-terminal domain Habc. Target-membrane associated SNAREs Syntaxin-1a and SNAP-25 both possess t-SNARE coiled coil homologies, however SNAP-25 possesses two such domains. The transmembrane domains present in Syntaxin-1a and VAMP-2 are both helical anchors for type IV membranes. SNAP-25 is not a membrane-associated SNARE and is instead tethered via up to four palmitoylated cysteines residing within a cysteine-rich region. All SNARE proteins contain a SNARE motif, a coiled coil approximately 60-70 residues in length and featuring heptad repeats. SNAP-25 features two SNARE motifs at each of its terminals.

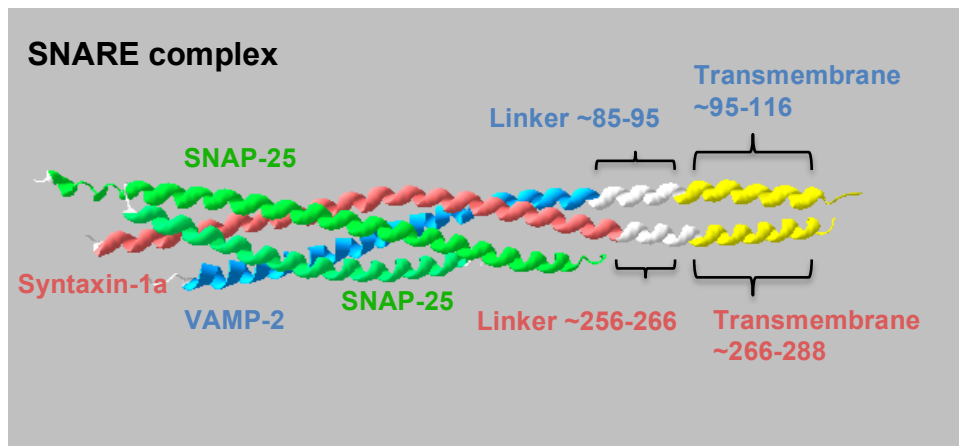


**Figure 4.7: X-ray structure of SNARE complex (*Rattus norvegicus*) displaying transmembrane and linker regions (PDB: 3HD7).** Membrane-associated synaptic SNARE proteins syntaxin-1a (pink) and VAMP-2 (blue) both contain a transmembrane region that is connected to the rest of the helix by a short linker region of approximately 10 residues in length. Circular dichroism data indicates that these regions lend an additional layer of stability to the SNARE complex.



Syntaxin SNARE motif alignment



7..6...5..4...3..2...1..0...1..2...3..4...5..6...7..8

...a...d...a...d...a...d...a...d...a...d...a...d...a...d...a...d

Key

088983 QKI IQEQDAGLDALSSI ISRQKQMGQEIGNELDEQNEI IDDLANLVENTDEKLRTEARRVTLV  
 Q9Z2Q7 QKI IQEQDAGLDALSSI ISRQKQMGQEIGNELDEQNEI IDDLANLVENTDEKLRTEARRVTLV  
 Q9UNK0 QKI IQEQDAGLDALSSI ISRQKQMGQEIGNELDEQNEI IDDLANLVENTDEKLRNETRRVNMV  
 Q3T075 QKI IQEQDAGLDALSSI ISRQKQMGQEIGNELDEQNEI IDDLANLVENTDEKLRTEARRVNLV  
 O60499 QLIMDEQDQOLEMVSGS IQVLKHMSGRVGEELDEQGIMLDAFAQEMDHTQSRMDGVLRKLAQV  
 O43752 QLIVEQODEQLELVSGS IGVLKNMSQRIGGELEEQAVMLEDF SHELESTQSRLDNVMKKLAKV  
 Q5R6Q2 QLIVEQODEQLELVSGS IGVLKNMSQRIGGELEEQAVMLEDF SHELESTQSRLDNVMKKLAKV  
 Q9JJK1 QLIVEQODEQLELVSGS IGVLKNMSQRIGGELEEQAVMLEDF SHELESTQSRLDNVMKKLAKV  
 Q63635 QLIVEQODEQLELVSGS IGVLKNMSQRIGGELEEQAVMLEDF SHELESTQSRLDNVMKKLAKV  
 Q9P2W9 -----DEVROIEGRVVEISRLQEIFTEKVLQOEAEIDS IHQLVVGATENIKEGNEDIAEA  
 Q5REB4 -----DEVROIEGRVVEISRLQEIFTEKVLQOEAEIDS IHQLVVGATENIKEGNEDIAEA  
 Q9Z158 IPRDQNAAESWETLEADLIELSHLVTDMSSLVNSQQEKIDS IADHVNSAAVNVEEGTKNLQKA  
 Q9D0I4 IPQDQNAAESWETLEADLIELSHLVTDMSSLVSSQQEKIDS IADHVNSAAVNVEEGTKNLQKA  
 P56962 IPQDQNAAESWETLEADLIELSQLVTD FSLLVNSQQEKIDS IADHVNSAAVNVEEGTKNLGKA  
 Q5E9Y2 IPRDQNAAESWETLEADLIELSQLVTD FSLLVNSQQEKIDS IEDHVNTAAVNVEEGTKNLGKA  
 O14662 TLMVEEREREIRQIVQS ISDLNEIFRDLGAMIVEQGTVLDRIDYNVEQSCIKTEDGLKQLHKA  
 Q8BVI5 TLMVEEREREIRQIVQS ISDLNEIFRDLGAMIVEQGTVLDRIDYNVEQSCVKTEDGLKQLHKA  
 Q3ZBT5 LRLIHERESSIRQLEADIMDINEIFKDLGMMIHEQGVIDS IEANVENAEVHVQQANQQLSRA  
 O70439 LRLIHERESSIRQLEADIMDINEIFKDLGMMIHEQGVIDS IEANVENAEVHVQQANQQLSRA  
 O15400 LRLIHERESSIRQLEADIMDINEIFKDLGMMIHEQGVIDS IEANVENAEVHVQQANQQLSRA  
 Q5R602 LRLIHERESSIRQLEADIMDINEIFKDLGMMIHEQGVIDS IEANVENAEVHVQQANQQLSRA  
 O70257 LRLIHERESSIRQLEADIMDINEIFKDLGMMIHEQGVIDS IEANVENAEVHVQQANQQLSRA  
 G3V7P1 LELIKERETAIRQLEADILDVNQIFKDLAMMIHQDGLIDS IEANVESSEVHVERASDQLQRA  
 Q86Y82 LELIKERETAIRQLEADILDVNQIFKDLAMMIHQDGLIDS IEANVESSEVHVERATEQLQRA  
 Q5RBW6 LELIKERETAIRQLEADILDVNQIFKDLAMMIHQDGLIDS IEANVESSEVHVERATEQLQRA  
 Q9ER00 LELIKERETAIRQLEADILDVNQIFKDLAMMIHQDGLIDS IEANVESSEVHVERATDQLQRA  
 Q13190 DSYIQSRADTMQNIESTIVELGSIFQOLAHMVKEQEETIQRIDENVLGAQLDVEAAHSEILKY  
 Q08851 DSYIQSRADTMQNIESTIVELGSIFQOLAHMVKEQEETIQRIDENVLGAQLDVEAAHSEILKY  
 Q8K1E0 DSYIQSRADTMQNIESTIVELGSIFQOLAHMVKEQEETIQRIDENVLGAQLDVEAAHSEILKY  
 Q08DB5 DSYIQSRADTMQNIESTIVELGSIFQOLAHMVKEQEETIQRIDENVLGAQLDVEAAHSEILKY  
 Q0VCI2 LSEIEQRHKELVNLENQIKDLRDLFIQISLLVEEQGESVNS IEMIVNGTKEYVNNTKEKFGLA  
 Q8R1Q0 LSEIEQRHKELVNLENQIKDLRDLFIQISLLVEEQGESINS IEVMVNSTKDYVNNTKEKFGLA  
 Q8N4C7 LSEIEQRHKELVNLENQIKDLRDLFIQISLLVEEQGESINNIEMTVNSTKEYVNNTKEKFGLA  
 Q5RAL4 LSEIEQRHKELVNLENQIKDLRDLFIQISLLVEEQGESINNIEMTVNSTKEYVNNTKEKFGLA  
 O75558 LNEIESRHRELLRLESRI RDVHELFLQMAVLVEKQADTLNV IELNVQKTVDYTGQAKAQRKA  
 Q9D3G5 LNEIESRHRELLRLEGRIRDVHELFLQMAVLVEKQEDTLNV IELNVQKTLDYTGQAKAQRKA  
 Q12846 LNEISARHSEIQQLERS IRELHIFTFLATEVEMQGEMINRIEKNILSSADYVERGQEHVKTA  
 Q3SWZ3 LNEISARHSEIQQLERS IRELHIFTFLATEVEMQGEMINRIEKNILSSADYVERGQEHVKVA  
 P70452 LNEISARHSEIQQLERS IRELHIFTFLATEVEMQGEMINRIEKNILSSADYVERGQEHVKIA  
 Q08850 LNEISARHSEIQQLERTIRELHIFTFLATEVEMQGEMINRIEKNILSSADYVERGQEHVKIA  
 Q13277 LSEIEGRHKDIVRLESSIKELHDMFMDIAMLVENQGEMLDNIELNVMHTVDHVEKARDETKKA  
 Q64704 LSEIEGRHKDIVRLESSIKELHDMFMDIAMLVENQGEMLDNIELNVMHTVDHVEKARDETKRA  
 Q08849 LSEIEGRHKDIVRLESSIKELHDMFMDIAMLVENQGEMLDNIELNVMHTVDHVEKARDETKRA  
 P61266 LNEIETRHNIEIKLETSIRELHDMFVDMAMLVESQGEMIDRIEYNVEHSVDYVERAVSDTKKA  
 P61265 LNEIETRHNIEIKLETSIRELHDMFVDMAMLVESQGEMIDRIEYNVEHSVDYVERAVSDTKKA  
 P61264 LNEIETRHNIEIKLETSIRELHDMFVDMAMLVESQGEMIDRIEYNVEHSVDYVERAVSDTKKA  
 P61267 LNEIETRHNIEIKLETSIRELHDMFVDMAMLVESQGEMIDRIEYNVEHSVDYVERAVSDTKKA  
 P61268 LNEIETRHNIEIKLETSIRELHDMFVDMAMLVESQGEMIDRIEYNVEHSVDYVERAVSDTKKA  
 P32850 LSEIETRHSIEIKLENSIRELHDMFMDMAMLVESQGEMIDRIEYNVEHSAVDYVERAVSDTKKA  
 P32851 LSEIETRHSIEIKLENSIRELHDMFMDMAMLVESQGEMIDRIEYNVEHSAVDYVERAVSDTKKA  
 Q16623 LSEIETRHSIEIKLENSIRELHDMFMDMAMLVESQGEMIDRIEYNVEHSAVDYVERAVSDTKKA  
 Q5R4L2 LSEIETRHSIEIKLENSIRELHDMFMDMAMLVESQGEMIDRIEYNVEHSAVDYVERAVSDTKKA  
 O35526 LSEIETRHSIEIKLETSIRELHDMFMDMAMLVESQGEMIDRIEYNVEHSAVDYVERAVSDTKKA  
 P32856 LNEIESRHKDIMKLETSIRELHEMFMDMAMFVETQGEMINNIERNVNMATDYVEHAKKEETKKA  
 P50279 LNEIESRHKDIMKLETSIRELHEMFMDMAMFVETQGEMVNNIERNVVNSVDYVEHAKKEETKKA  
 Q00262 LNEIESRHKDIMKLETSIRELHEMFMDMAMFVETQGEMVNNIERNVVNSVDYVEHAKKEETKKA  
 6448657555745885594675676457645855\*6659758636955744486564556467

- 0
- 1
- 2
- 3
- 4
- 5
- 6
- 7
- 8
- 9
- 10

VAMP SNARE motif alignment



7..6...5..4...3..2...1..0...1..2...3..4...5..6...7..8  
 .a..d...a..d...a..d...a..d...a..d...a..d...a..d

Key

P63044	RLQQTQAQVDEVVDIMRVNVDKVLERDQKLSELDDRADALQAGASQFETSAAKLKRKYWWK	0
P63027	RLQQTQAQVDEVVDIMRVNVDKVLERDQKLSELDDRADALQAGASQFETSAAKLKRKYWWK	1
P63045	RLQQTQAQVDEVVDIMRVNVDKVLERDQKLSELDDRADALQAGASQFETSAAKLKRKYWWK	2
P63026	RLQQTQAQVDEVVDIMRVNVDKVLERDQKLSELDDRADALQAGASQFETSAAKLKRKYWWK	3
Q9N0Y0	RLQQTQAQVDEVVDIMRVNVDKVLERDQKLSELDDRADALQAGASQFETSAAKLKRKYWWK	4
Q15836	RLQQTQNVDEVVDIMRVNVDKVLERDQKLSELDDRADALQAGASQFETSAAKLKRKYWWK	5
P63024	RLQQTQNVDEVVDIMRVNVDKVLERDQKLSELDDRADALQAGASQFETSAAKLKRKYWWK	6
P63025	RLQQTQNVDEVVDIMRVNVDKVLERDQKLSELDDRADALQAGASQFETSAAKLKRKYWWK	7
Q2KJD2	RLQQTQNVDEVVDIMRVNVDKVLERDQKLSELDDRADALQAGASQFETSAAKLKRKYWWK	8
Q4R8T0	RLQQTQNVDEVVDIMRVNVDKVLERDQKLSELDDRADALQAGASQFETSAAKLKRKYWWK	9
Q63666	RLQQTQAQVEEVVDIMRVNVDKVLERDQKLSELDDRADALQAGASVFESSAAKLKRKYWWK	10
P23763	RLQQTQAQVEEVVDIIRVNVDKVLERDQKLSELDDRADALQAGASQFESSAAKLKRKYWWK	
Q62442	RLQQTQAQVEEVVDIMRVNVDKVLERDQKLSELDDRADALQAGASQFESSAAKLKRKYWWK	
Q0V7N0	RLQQTQAQVEEVVDIMRVNVDKVLERDQKLSELDDRADALQAGASQFESSAAKLKRKYWWK	
O95183	ELERCQQQANEVTEIMRNNGKVLERGKLAELQQRSDQLDMSSTFNKTTQNLAQKKCWE	
Q9Z2P8	ELKQCQQQADEVTEIMLNNFDKVLERHGKLAELEQRSDQLDMSSAFSKTTKTLAQQKRWE	
Q9Z2J5	ELERCQRQADQVTEIMLNNFDKVLERDQKLSELQQRSDQLDMSSAFSKTTKTLAQQKRWE	
Q2KHY2	ELERCQRQADEVTEIMLNNFDKVLERDQKLSELQQRSDQLDMSSAFSKTTKTLAQQKRWE	
Q3T0Y8	RVRNLRDEVEGVKNIMTQNVVERILARGENLDHLRNKTEDLEATSEHFKTTSQKVARKFVWK	
O70404	RVRNLQSEVEGVKNIMTQNVVERILSRGENLDHLRNKTEDLEATSEHFKTTSQKVARKFVWK	
Q9BV40	RVRNLQSEVEGVKNIMTQNVVERILARGENLEHLRNKTEDLEATSEHFKTTSQKVARKFVWK	
Q5REQ5	RVRNLQSEVEGVKNIMTQNVVERILARGENLEHLRNKTEDLEATSEHFKTTSQKVARKFVWK	
Q9WUF4	RVRNLQSEVEGVKNIMTQNVVERILARGENLDHLRNKTEDLEATSEHFKTTSQKVARKFVWK	
O75379	KIKHVQNQVDEVIDVMQENITKVIERGERLDELQDKSESLSDNATAFSNRSKQLRRQMWWR	
O70480	KIKHVQNQVDEVIDVMQENITKVIERGERLDELQDKSESLSDNATAFSNRSKQLRRQMWWR	
Q32L97	KIKHVQNQVDEVIDVMQENITKVIERGERLDELQDKSESLSDNATAFSNRSKQLRRQMWWR	
P51809	KVMETQAQVDELKGIMVRNIDLVAQRGERLELLIDKTENLVDSSVTFKTTSRNLARAMCMK	
P70280	KVMETQAQVDELKGIMVRNIDLVAQRGERLELLIDKTENLVDSSVTFKTTSRNLARAMCMK	
Q17QI5	KVMETQAQVDELKGIMVRNIDLVAQRGERLELLIDKTENLVDSSVTFKTTSRNLARAMCMK	
Q5RF94	KVMETQAQVDELKGIMVRNIDLVAQRGERLELLIDKTENLVDSSVTFKTTSRNLARAMCMK	
Q9JHW5	RVTETQAQVDELKGIMVRNIDLVAQRGERLELLIDKTENLVDSSVTFKTTSRNLARAMCVK	
	786669598878569954*877977*667*66*478685*565865*66775686875578	



## SNAP-25 SNARE motif alignment

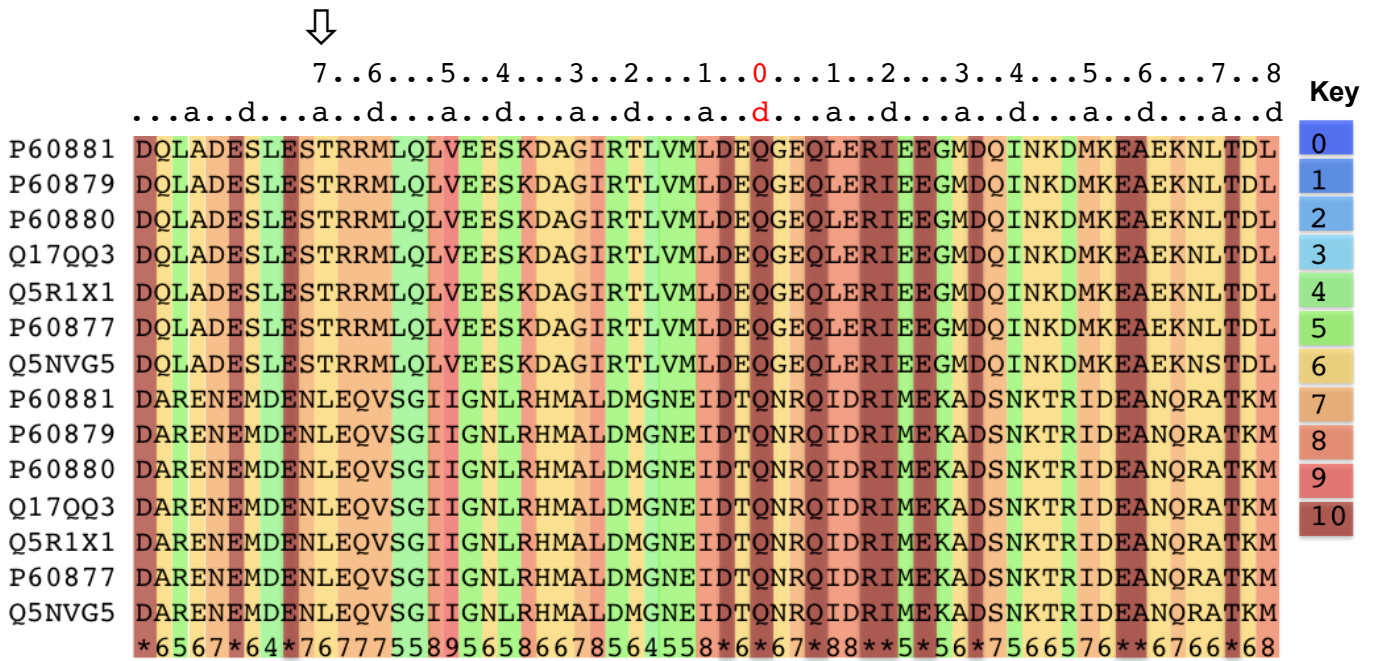


**Figure 4.8: SNARE motif alignment of all the mammalian SNARE proteins collated into the database thus far, showing conservation of residues as predicted by PRALINE.** Conservation is indicated by colour according to the consistency scale set forth in the key, where 0 shows no conservation and 10 indicates highly conserved residues. The scale immediately above the sequences shows the *a* and *d* positions, whilst the scale above that shows the “4,3-layers” (as referenced in **Figure 4.1**). The arrow indicates the start of the motif.

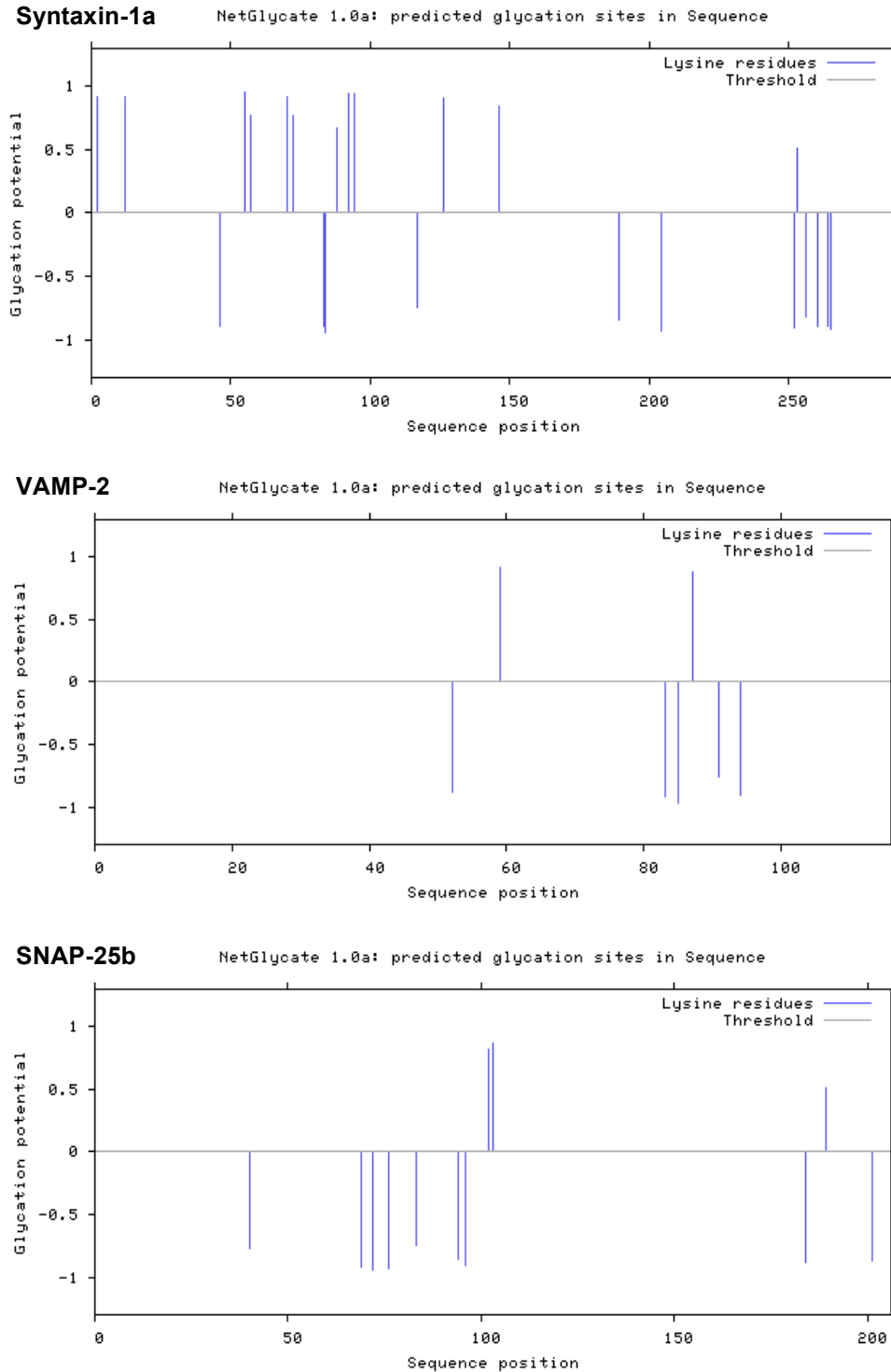


**Figure 4.9: NetGlycate 1.0 (CBS) prediction of lysine  $\epsilon$ -amino acid groups for each of the synaptic proteins: Syntaxin-1a (top), VAMP-2 (middle), and SNAP-25b (bottom).** Syntaxin-1a has the highest percentage composition of lysine (8%) and accordingly, it holds the greatest number of lysines with glycation potential above the threshold, especially concentrated between positions 50-100 where helices are featured. VAMP-2 and SNAP-25 have similar percentages of lysine (6 and 5.8% respectively) and an expectedly lower number of predicted glycation sites.

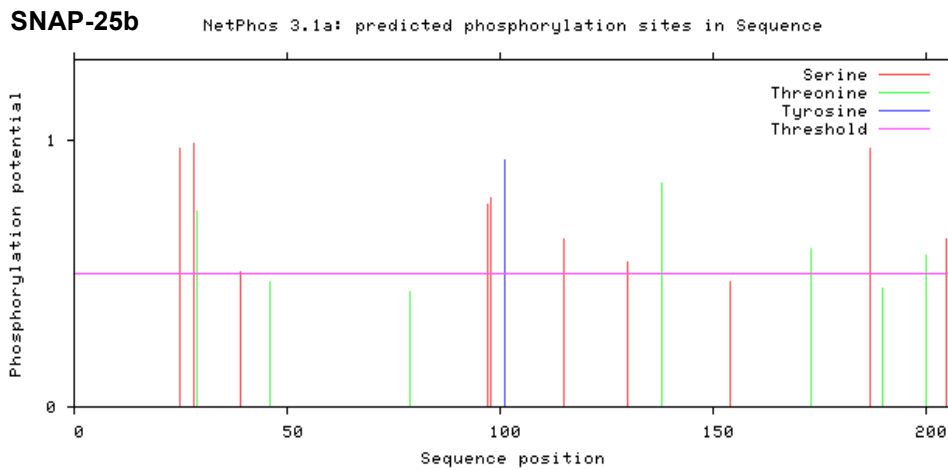
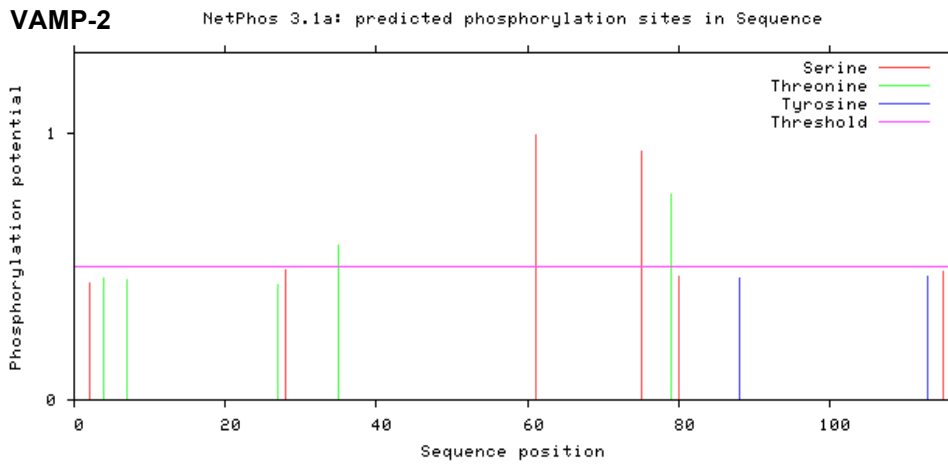
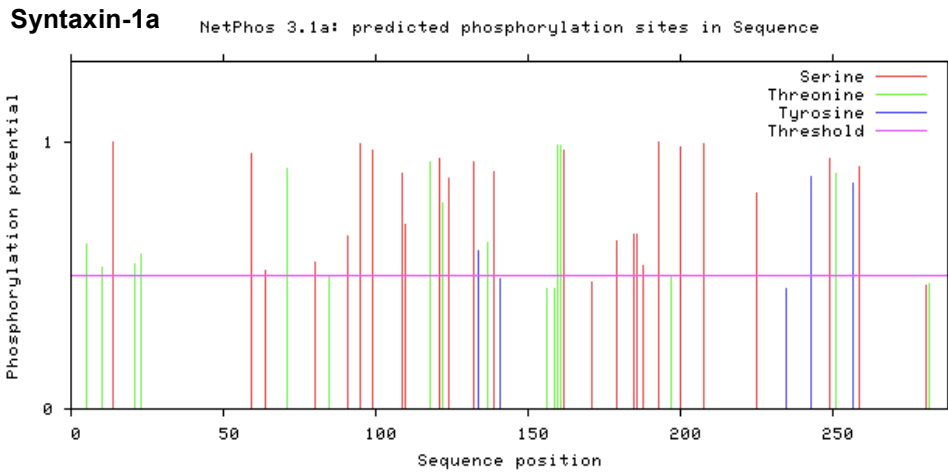


**Figure 4.10: NetPhos 3.1 (CBS) prediction of serine, threonine and tyrosine phosphorylation sites within the three synaptic proteins syntaxin-1a (top), VAMP-2 (middle), and SNAP-25b (bottom).** Syntaxin-1a possesses the largest collective number of serine, threonine, and tyrosine residues and accordingly, the greatest number of viable phosphorylation sites compared to the other proteins.

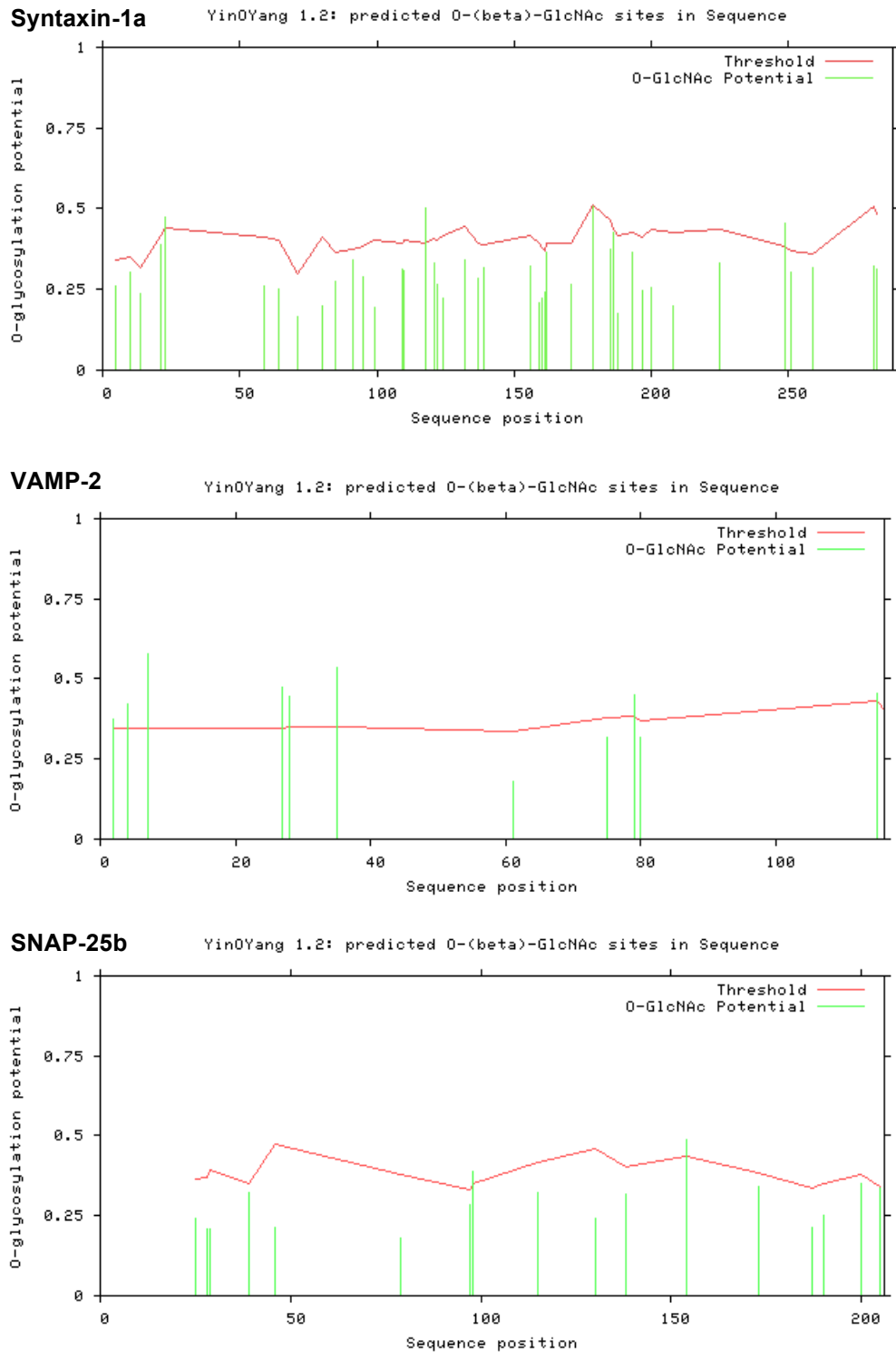


**Figure 4.11: YinOYang 1.2 (CBS) prediction of O-GlcNAcylated serine and threonine residues in syntaxin-1a (top), VAMP-2 (middle) and SNAP-25b (bottom).** According to the server's prediction, syntaxin-1a does not contain any discernable sites to note, however it can be observed that VAMP-2 and SNAP-25b hold a sparing number with varying potential scores that are worth further consideration.

### 13.5 Figures in Chapter 5

217

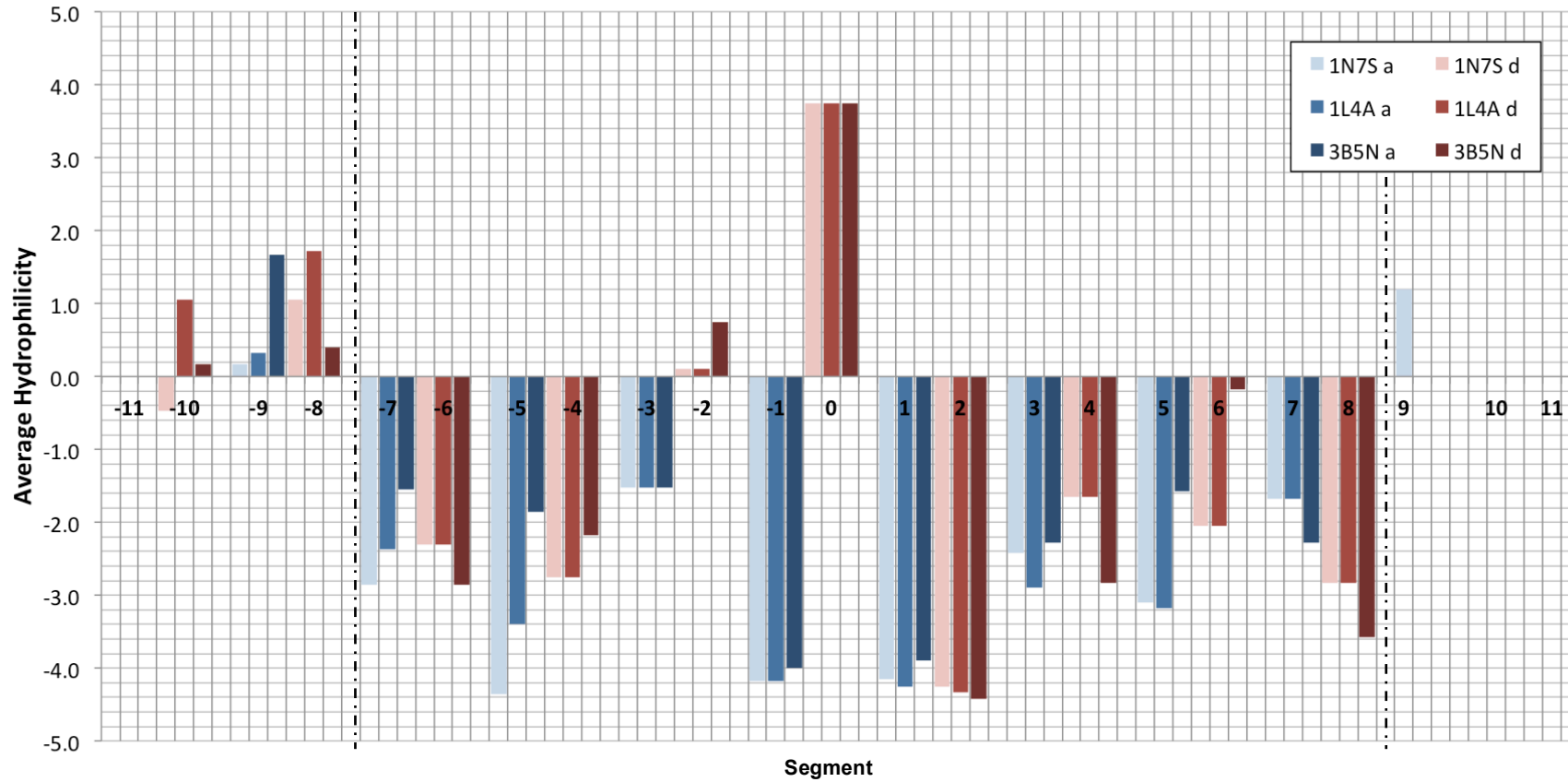
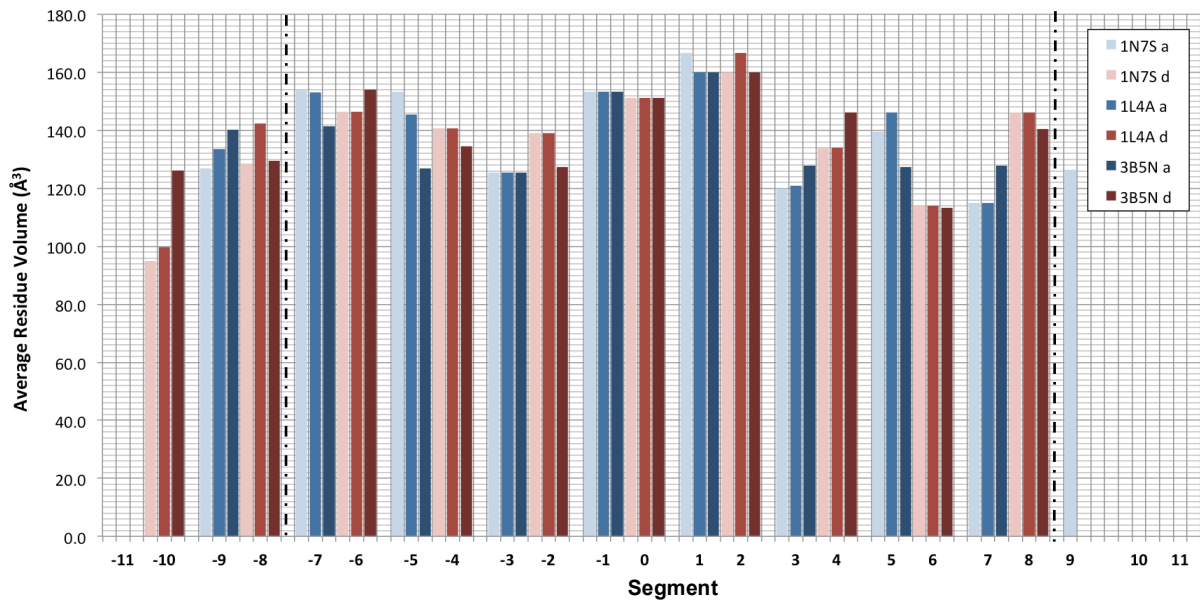
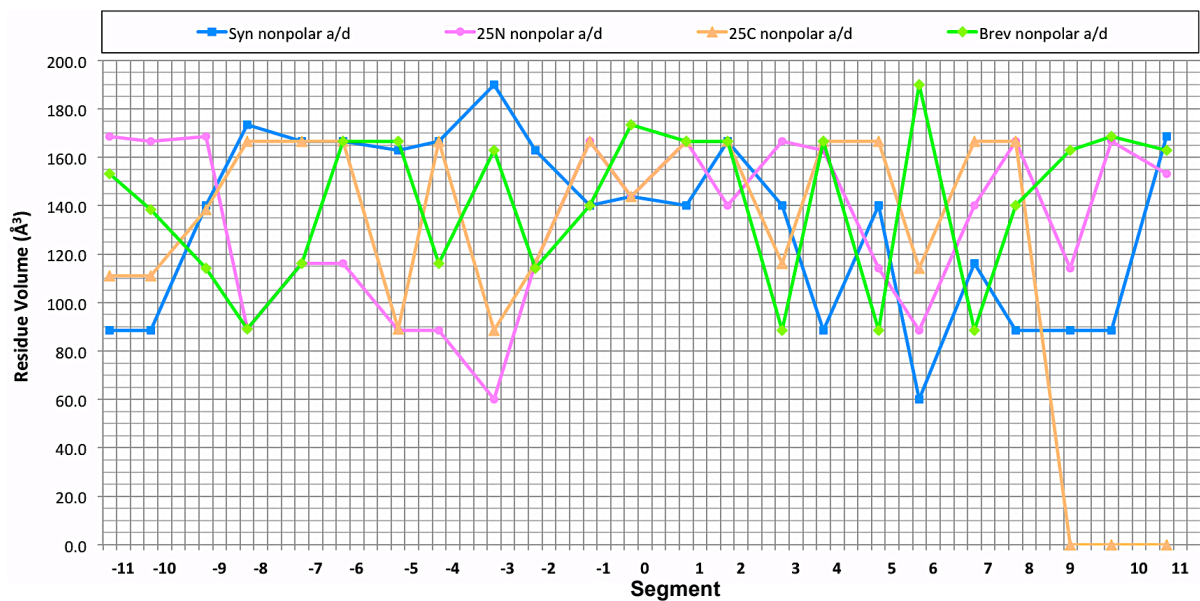


**Figure 5.1: Average hydrophilicity of nonpolar layers of each complex.** Hydrophilicity of positions *a* (blue bars) and *d* (red bars) averaged across all four helices of the SNARE complex, plotted against the heptad layer, for all three complexes: 1N7S (*Rattus norvegicus*), 1L4A (*Loligo pealeii*), and 3B5N (*Saccharomyces cerevisiae*). The broken lines indicate the start and end of the SNARE motif.

(a) Average residue volume of positions *a* and *d* in all three complexes 1N7S, 1L4A and 3B5N



(b) Individual residue volume of positions *a* and *d* in all four helices of 1N7S



(i)

(ii)

(iii)

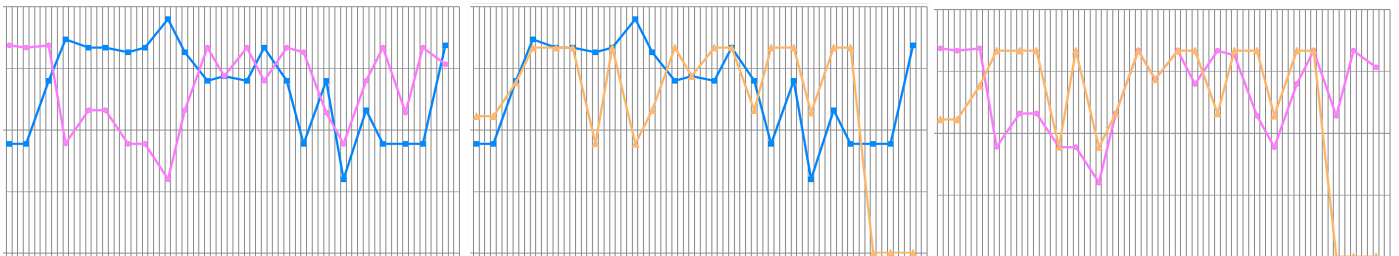


**Figure 5.2: Residue volume of positions *a* and *d* in all three complexes (a), and in all four helices of complex 1N7S (b).** In (a) the residue volumes were averaged at each position *a* (blue bars) and *d* (red bars) across all four helices of each complex 1N7S (*Rattus norvegicus*), 1L4A (*Loligo pealeii*) and 3B5N (*Saccharomyces cerevisiae*) and plotted against segment; whilst in (b) the individual residue volumes at each *a* and *d* position of each helix (syntaxin, SNAP-25 N-terminal, SNAP-25 C-terminal and synaptobrevin) are plotted against segment. The broken lines indicate the start and end of the SNARE motif. The panels (i)-(iii) show the isolated traces of the three combinations of t-SNARE proteins: syntaxin and SNAP-25 N-terminal (i), syntaxin and SNAP-25 C-terminal (ii), and SNAP-25 N- and C-termini (iii).



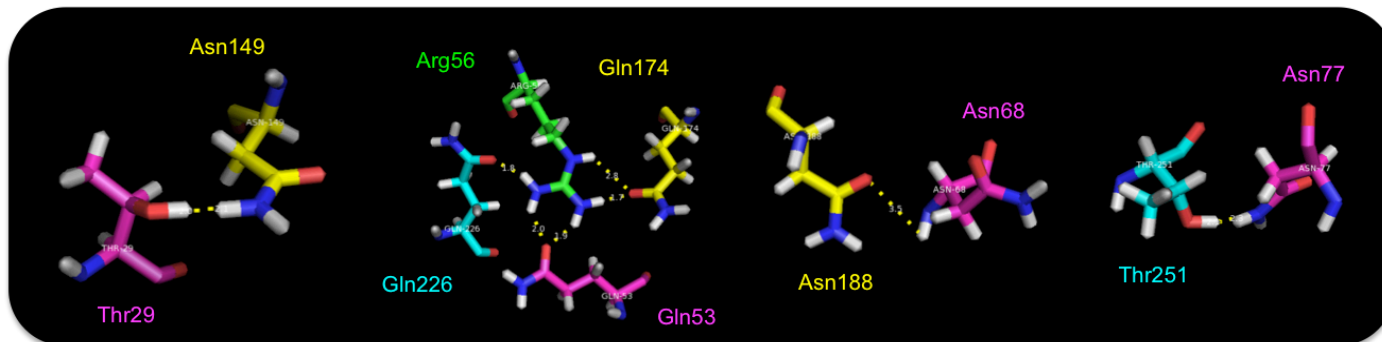
(a) Table of polar contacts with buried polar residues in 1N7S (*Rattus norvegicus*)

Buried Polar Residue	Contact Residue	Contact distance (Å)
25N Thr29	25C Asn149	2.0
Syn Gln226	VAMP Arg56	1.8
25N Gln53	VAMP Arg56	1.9
25C Gln174	VAMP Arg56	1.7/2.8
25C Asn188	25N Asn68	3.5
Syn Thr251	25N Asn77	2.1

(b) Polar contacts with buried polar residues highlighted in 1N7S (*Rattus norvegicus*)

1N7S_B	188	S	K	Q	A	L	S	E	I	E	T	R	H	S	E	I	I	K	L	E	N	S	I	R	E	L	H	D	M	F	M	D	M	A	M	L	V	E	S	Q	G	227			
1N7S_C	15	Q	R	R	A	D	Q	L	A	D	E	S	L	E	S	T	R	R	M	L	Q	L	V	E	E	S	K	D	A	G	I	R	T	L	V	M	L	D	E	Q	G	54			
1N7S_D	136	R	V	T	N	D	A	R	E	N	E	M	D	E	N	L	E	Q	V	S	G	I	I	G	N	L	R	H	M	A	L	D	M	G	N	E	I	D	T	Q	N	175			
1N7S_A	18	G	P	P	A	P	P	P	N	L	T	S	N	R	R	L	Q	Q	T	Q	A	Q	V	D	E	V	V	D	I	M	R	V	N	V	D	K	V	L	E	R	D	57			
		a	b	c	d	e	f	g	a	b	c	d	e	f	g	a	b	c	d	e	f	g	a	b	c	d	e	f	g	a	b	c	d	e	f	g	a	b	c	d	e				
		-11	-10	-9	-8	-7	-6	-5	-4	-3	-2	-1	0																																
1N7S_B	228	E	M	I	D	R	I	E	Y	N	V	E	H	A	V	D	Y	V	E	R	A	V	S	D	T	K	K	A	V	K	Y	Q	S	K	A	R	R	K	K	I	M	267			
1N7S_C	55	E	Q	L	D	R	V	E	E	G	M	N	H	I	N	Q	D	M	K	E	A	E	K	N	L	K	D	L	G	K	C	C	G	L	F	I	C	P	C	N	K	94			
1N7S_D	176	R	Q	I	D	R	I	M	E	K	A	D	S	N	K	T	R	I	D	E	A	N	Q	R	A	T	K	M	L	G	S	G	X	X	X	X	X	X	X	X	X	215			
1N7S_A	58	Q	K	L	S	E	L	D	D	R	A	D	A	L	Q	A	G	A	S	Q	F	E	T	S	A	A	K	L	K	R	K	Y	W	W	K	N	L	K	M	M	I	97			
		f	g	a	b	c	d	e	f	g	a	b	c	d	e	f	g	a	b	c	d	e	f	g	a	b	c	d	e	f	g	a	b	c	d	e	f	g	a	b	c				
				1		2				3				4				5				6				7				8						9				10				11	

(c) 3D representation of buried polar contacts in 1N7S (*Rattus norvegicus*)





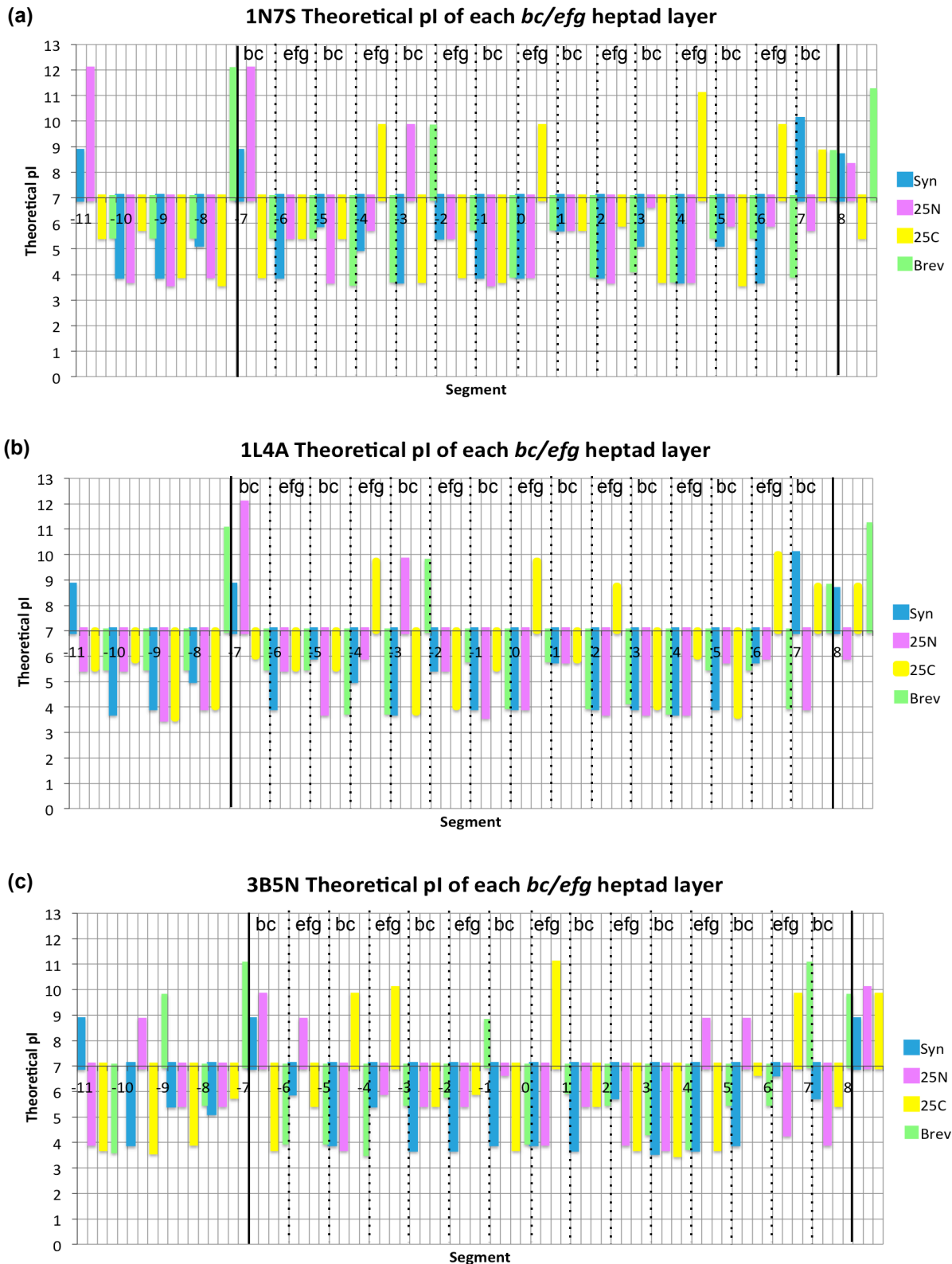











**Figure 5.3: Buried polar contacts in a and d layers of 1N7S.** (a) Table of buried polar contacts in 1N7S, showing the contact distance. (b) Protein sequences in the 1N7S complex (B corresponds to syntaxin; C corresponds to SNAP-25 N-terminal; D corresponds to SNAP-25 C-terminal and A corresponds to VAMP-2 - this terminology is consistent with the protein identifiers outlined in **Figure 4.1**). The a layers have been highlighted in blue and d layers highlighted in red; all buried polar residues are in red typeface; buried polar residues that potentially form polar contacts are outlined in colour-coded boxes that correspond to the colours in the table. The start and end positions of the SNARE motif is indicated by the broken vertical lines. (c) 3D representations of the buried polar contacts outlined in the table and sequences.

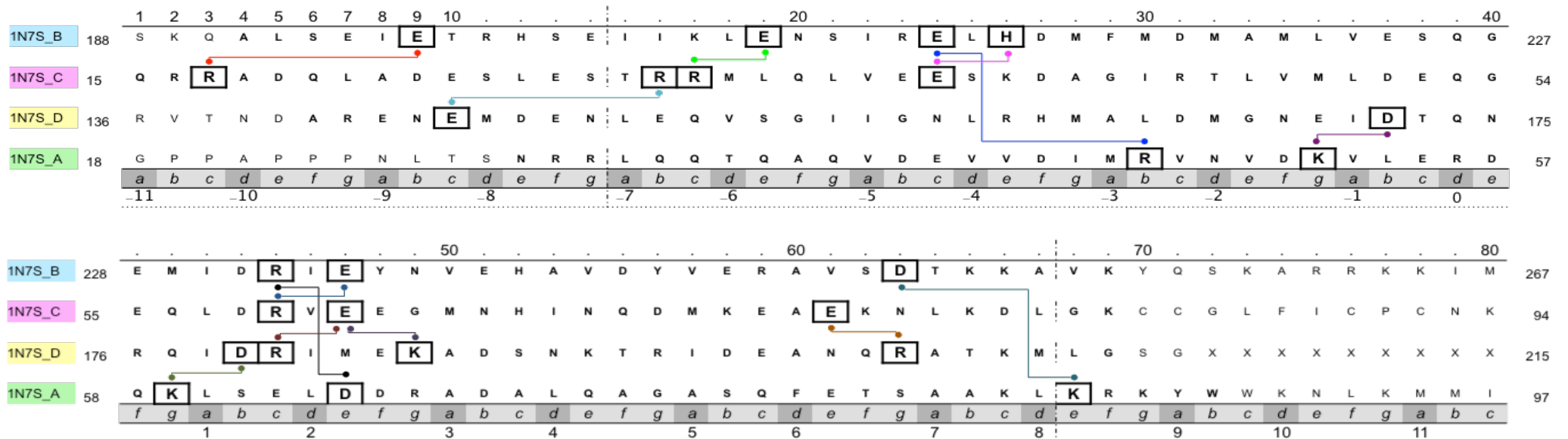


**Figure 5.4: Theoretical pI of polar segments.** The theoretical pI of each polar segment “bc” and “efg” in all four helices acting in the capacity of syntaxin, SNAP-25 N- and C-terminal, and synaptobrevin for the complexes (a) 1N7S, (b) 1L4A, and (c) 3B5N plotted against their 4,3-layer. Theoretical pI was calculated using ProtParam (ExPASy). The solid lines indicate the start and end of the SNARE motif, whilst the dashed lines demarcate the segments.

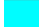









(a) Table of predicted salt bridges in 1N7S (*Rattus norvegicus*)

Salt bridge participants	Spacing	Configuration	Salt bridge distance (Å)
 25N Arg17 and Syn Glu196	i to i+6	cb	<b>3.0/3.9</b> side-on interaction
 25C Glu145 and 25N Arg30	i to i+6	cb	<b>2.9/2.9</b> side-on interaction
 25N Arg31 and Syn Glu206	i to i+2	ce	<b>2.8/2.9</b> side-on interaction
 25N Glu38 and Syn His213	i to i+2	ce	<b>2.6</b>
 Syn Glu211 and VAMP Arg47	i to i+6	cb	<b>3.8</b> backside interaction
 VAMP Lys52 and 25C Asp172	i to i+2	gb	<b>2.7/3.2</b> bifurcated interaction
 Syn Arg232 and VAMP Asp64	i to i+2	ce	<b>2.9/3.1</b> side-on interaction
 25N Arg59 and Syn Glu234	i to i+2	ce	<b>2.7/3.0</b> side-on interaction
 25C Asp179 and VAMP Lys59	i to i+2	gb'	<b>2.9</b>
 25C Arg180 and 25N Glu61	i to i+2	ce	<b>2.8/2.9</b> side-on interaction
 25N Glu61 and 25C Lys184	i to i+2	eg'	<b>2.8</b>
 25N Glu75 and 25C Arg198	i to i+2	eg'	<i>2 possibilities: 2.8/3.9 side-on interaction or 3.7 to N in chain (Arg198 in zwitterionic tautomer form)*</i>
 Syn Asp250 and VAMP Lys85	i to i+5	ge'	<b>3.0</b>

221 (b) Sequence alignment with predicted salt bridges highlighted for 1N7S (*Rattus norvegicus*)

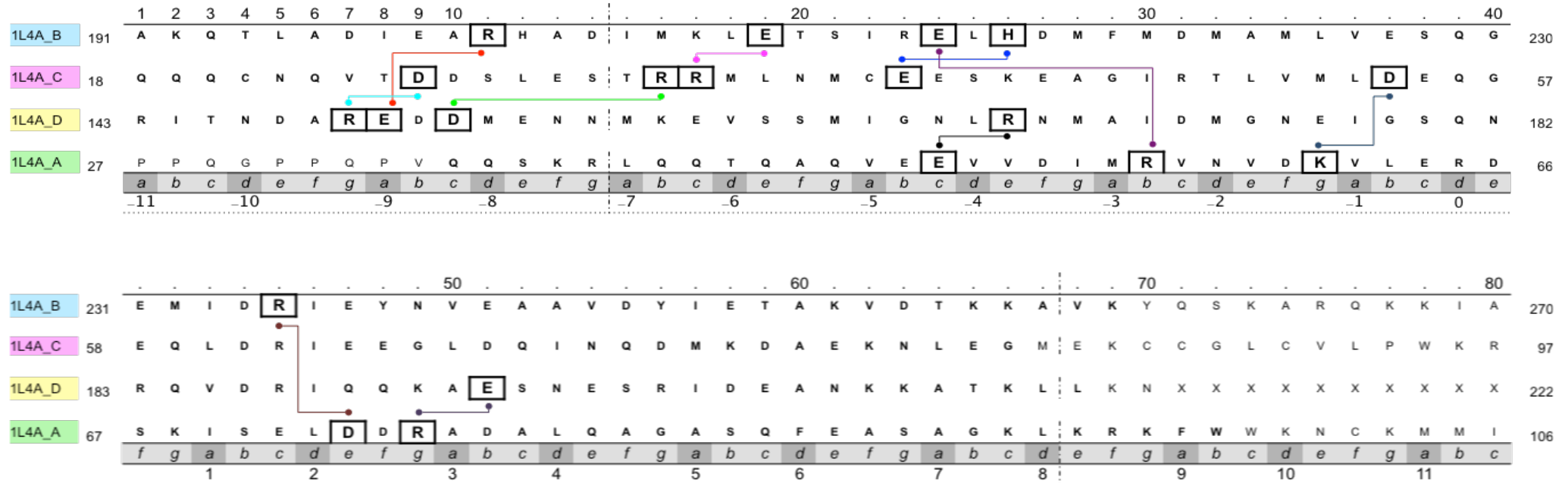


(c) Table of predicted salt bridges in 1L4A (*Loligo pealeii*)

Salt bridge participants	Spacing	Configuration	Salt bridge distance (Å)
 25C Arg149 and 25N Asp26	i to i+2	gb'	<b>3.2</b> <i>backside interaction</i>
 Syn Arg201 and 25C Glu150	i to i+3	ad'	<b>2.7</b> <i>backside interaction</i>
 25C Asp152 and 25N Arg33	i to i+6	cb'	<b>3.2</b> <i>backside interaction</i>
 Syn Glu209 and 25N Arg34	i to i+2	ce'	<b>2.9</b> <i>backside interaction</i> or <b>3.1/3.2</b> <i>side-on interaction**</i>
 VAMP Glu50 and 25C Arg168	i to i+2	ce'	<b>2.8/2.8</b> <i>side-on interaction</i>
 25N Glu41 and Syn His216	i to i+3	be	<b>3.5</b>
 Syn Glu214 and VAMP Arg56	i to i+6	cb'	<b>3.1</b> <i>backside interaction</i>
 25C Asp186 and VAMP Lys68	i to i+2	gb'	<b>3.1</b>
 VAMP Asp73 and Syn Arg235	i to i+2	ce'	<b>3.0</b> <i>backside interaction</i>
 25C Glu193 and VAMP Arg75	i to i+2	gb'	<b>2.7</b> <i>backside interaction</i>

(d) Sequence alignment with predicted salt bridges highlighted for 1L4A (*Loligo pealeii*)

232



(e) Table of predicted salt bridges in 3B5N (*Saccharomyces cerevisiae*)

Salt bridge participants	Spacing	Configuration	Salt bridge distance (Å)
25C Glu591 and 25N Lys437	i to i+2	fa	3.5
25C Glu591 and Syn Arg196	i to i+3	ad'	2.6/2.7 end-on interaction
25C Glu593 and 25N Arg445	i to i+6	cb'	2.7/3.0 side-on interaction
25C Asp599 and VAMP Arg28	i to i+2	gb'	2.9/3.0 bifurcated interaction
VAMP Asp38 and 25C Lys609	i to i+3	be	3.5
Syn Glu209 and VAMP Arg44	i to i+6	cb'	2.6/2.9 side-on interaction
25N Glu455 and 25C Arg607	i to i+2	ce'	2.6/2.9 side-on interaction
Syn Glu218 and 25N Arg456	i to i+6	fe'	2.8/2.9 end-on interaction
25C Asp620 and VAMP Lys49	i to i+2	gb'	2.9
25C Glu630 and VAMP Arg56	i to i+5	ge'	3.0/3.0 bifurcated interaction
25N Glu476 and 25C Arg625	i to i+5	ge'	2.9/3.1 side-on interaction
Syn Asp241 and VAMP Lys75	i to i+5	ge'	3.0
Syn Asp250 and 25N Lys492	i to i+2	gb	2.9/3.0 side-on interaction
25N Glu495 and Syn Arg257	i to i+6	cb'	2.9 /3.0 side-on interaction

(f) Sequence alignment with predicted salt bridges highlighted for 3B5N (*Saccharomyces cerevisiae*)

223

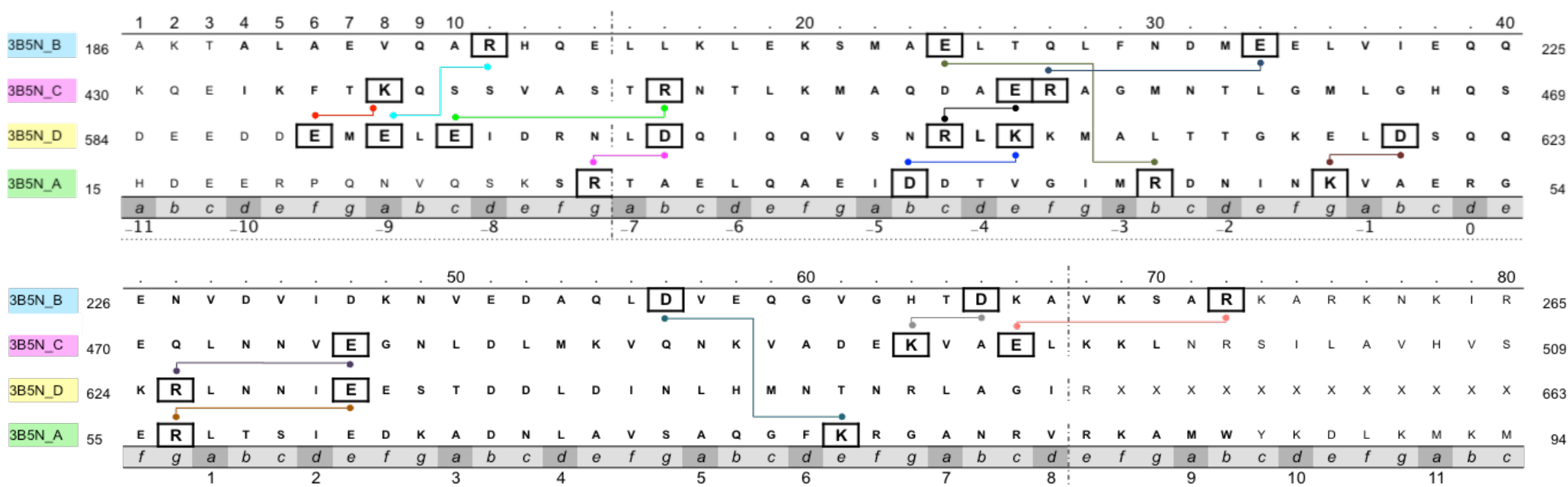


**Figure 5.5: Predicted interhelical salt bridges, with an O-N distance cut off of 4.0 Å, between the proteins in each complex 1N7S, 1L4A and 3B5N calculated using VMD software.** Tables (a), (c), and (e) outline the participants of each salt bridge, colour-coded to match the colour of the salt bridges in the sequence alignments (b), (d) and (f); it also shows the spacing, configuration (where the prime indicates the position on the second chain), and salt bridge distances. Salt bridges with more than one distance specified indicate that more than one salt bridge configuration is possible. Sequence alignments (b), (d) and (f) highlight the participants in each salt bridge, and the broken lines indicate the start and end of the SNARE motif.

\* and \*\*: It is acknowledged that there are more than one possibility of salt bridge arrangement for these pairs of residues, however another option also exists beyond the ones outlined in the tables. They could also be a combination of simultaneous bifurcate and side-on interaction.

**Salt bridges in 1N7S  
conserved in at least one structure**

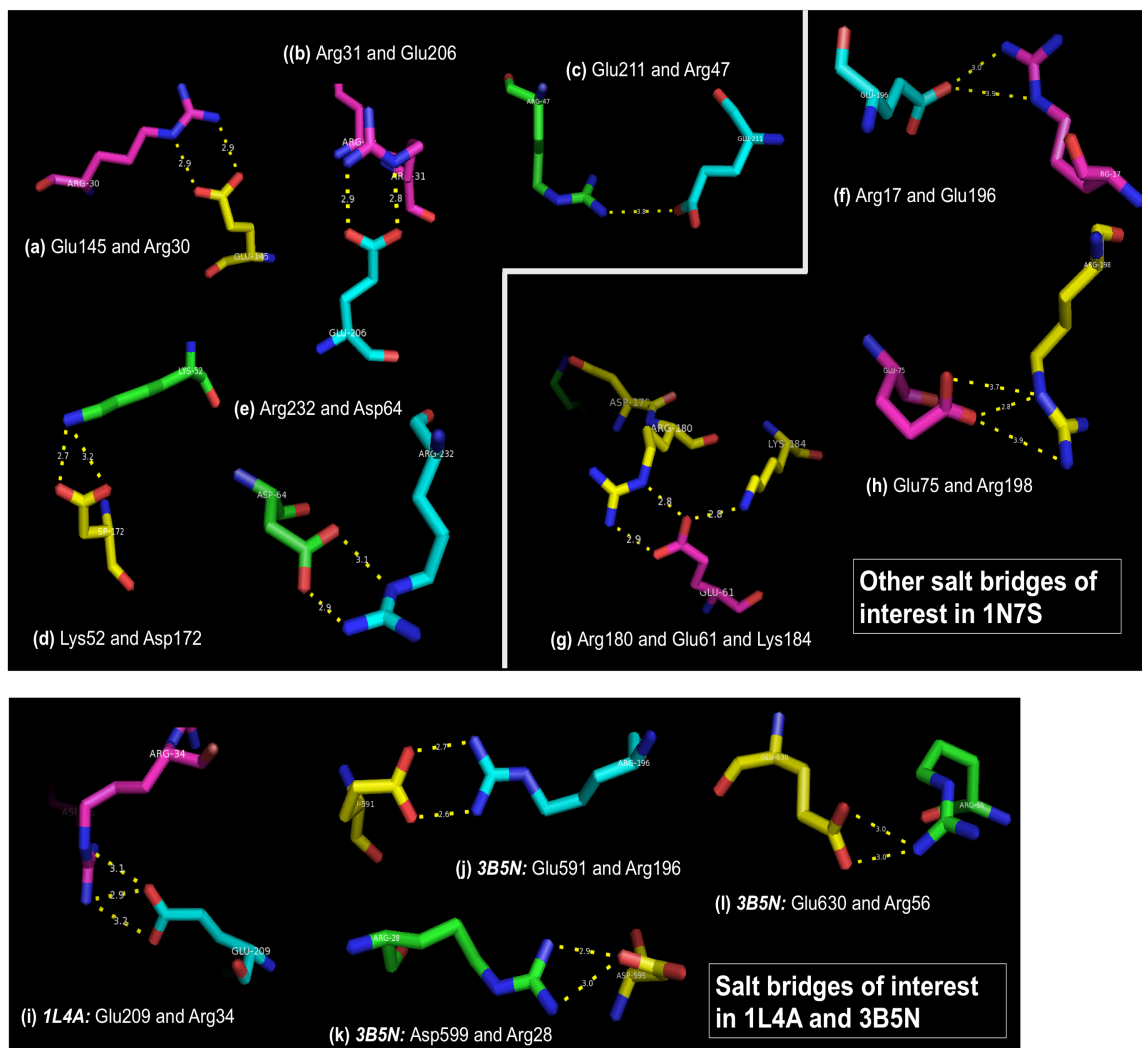
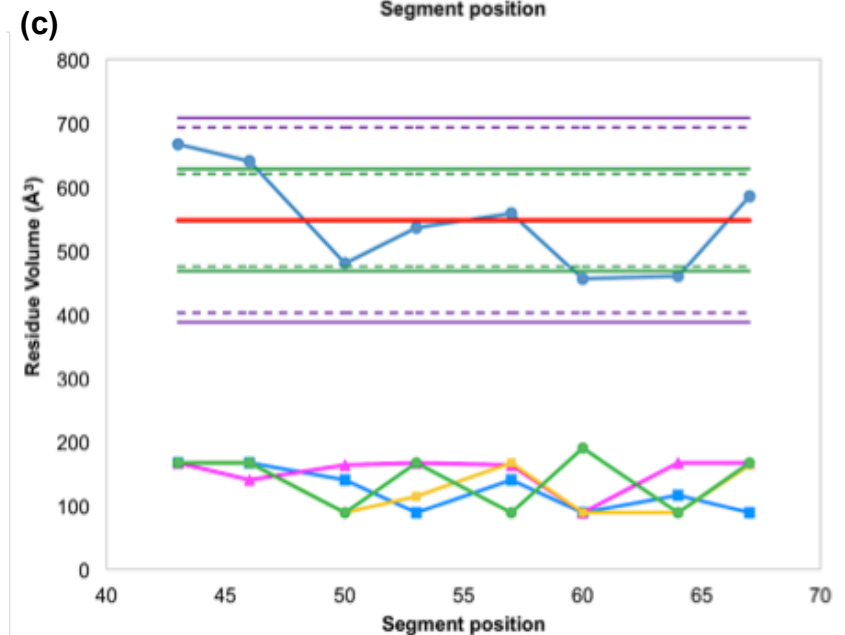
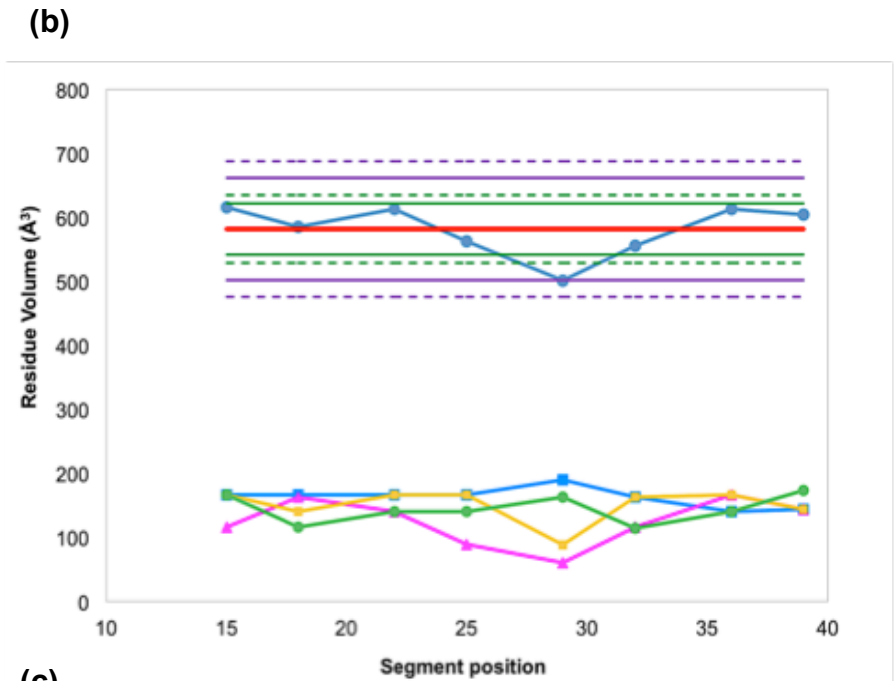
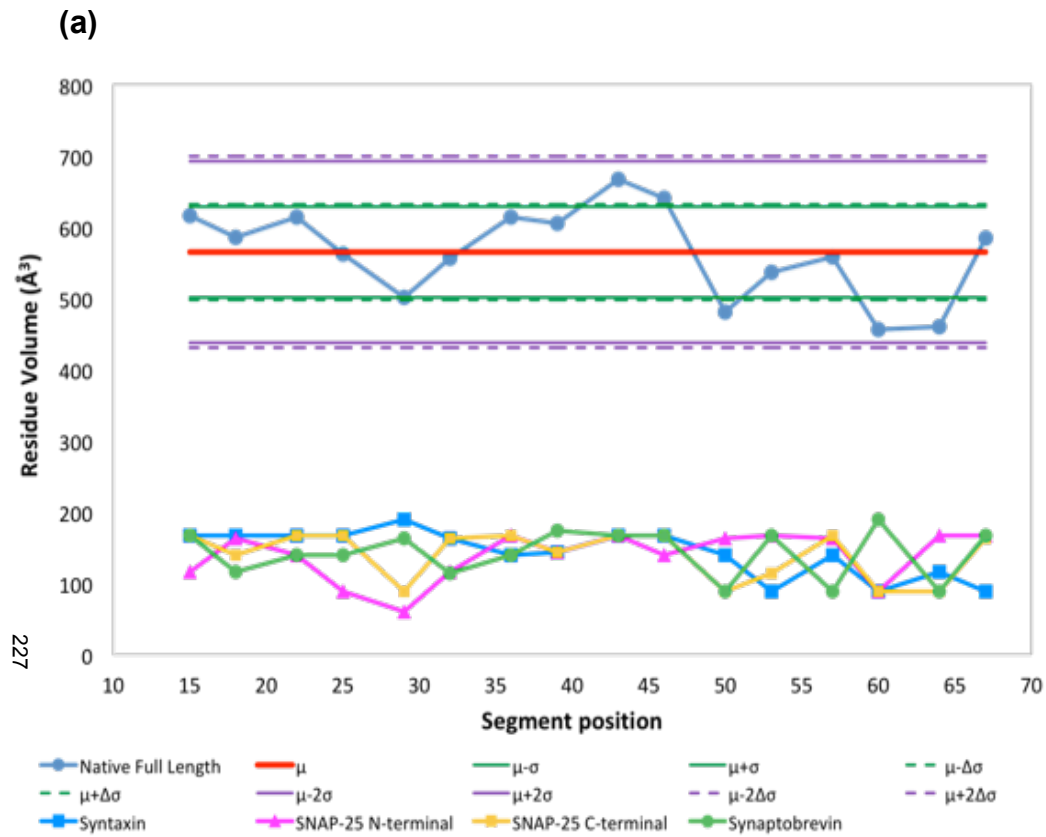


**Figure 5.6: 3D representation of salt bridges of interest created using PyMOL.** Salt bridges of interest in 1N7S (a-h), 1L4A (i), and 3B5N (j-l). Salt bridges that are have been conserved between 1N7S and at least one other complex out of 1L4A and 3B5N are shown in (a-e). All salt bridges were calculated using oxygen-nitrogen cutoff distance of 4.0 Å by the software VMD.

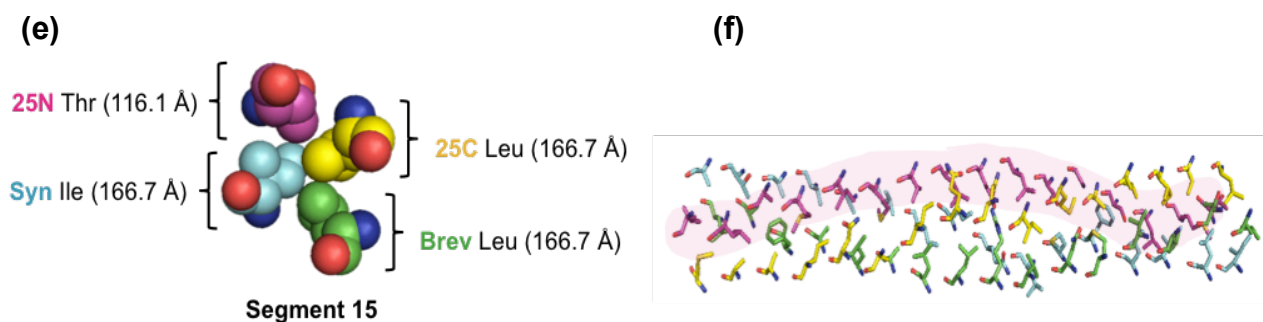






**(d)**

Parameter	N-Terminal	C-Terminal
Mean ( $\mu$ )	582	548
Standard Deviation ( $\sigma$ )	40	80
Predicted Deviation ( $\Delta\sigma$ )	53	73



**TRV of segment 15** ( $\text{\AA}^3$ ) = **Syn** (166.7  $\text{\AA}$ ) + **25N** (116.1  $\text{\AA}$ ) + **25C** (166.7  $\text{\AA}$ ) + **Brev** (166.7  $\text{\AA}$ )

**Average** ( $\mu$ ) = Average of all hydrophobic segment TRVs

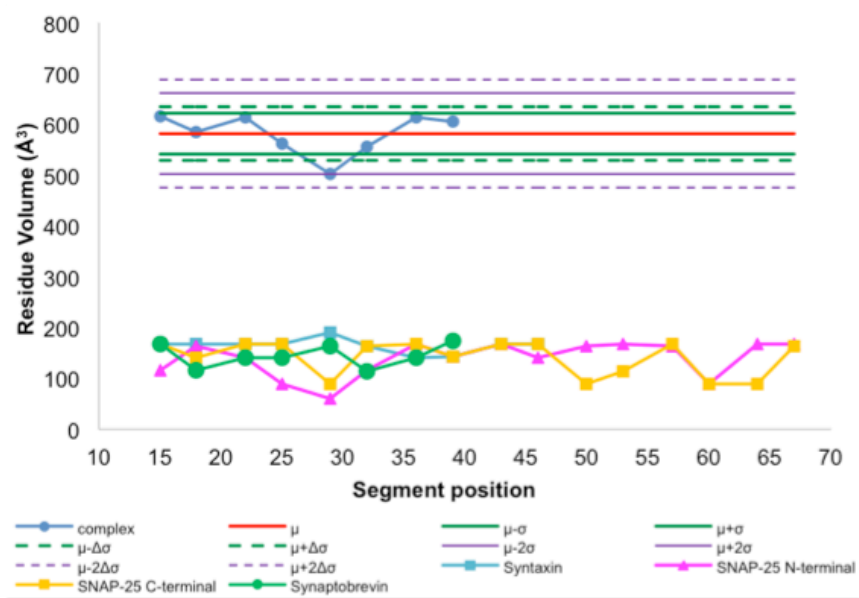
**Standard deviation** ( $\sigma$ ) = Standard deviation of all hydrophobic segment TRVs

**Predicted deviation** ( $\Delta\sigma$ ) = Standard deviation of hydrophobic residue volume across each protein is calculated (for example **25N**: standard deviation is taken for all volumes of hydrophobic residues highlighted in pink) then each standard deviation is substituted into Equation 1.

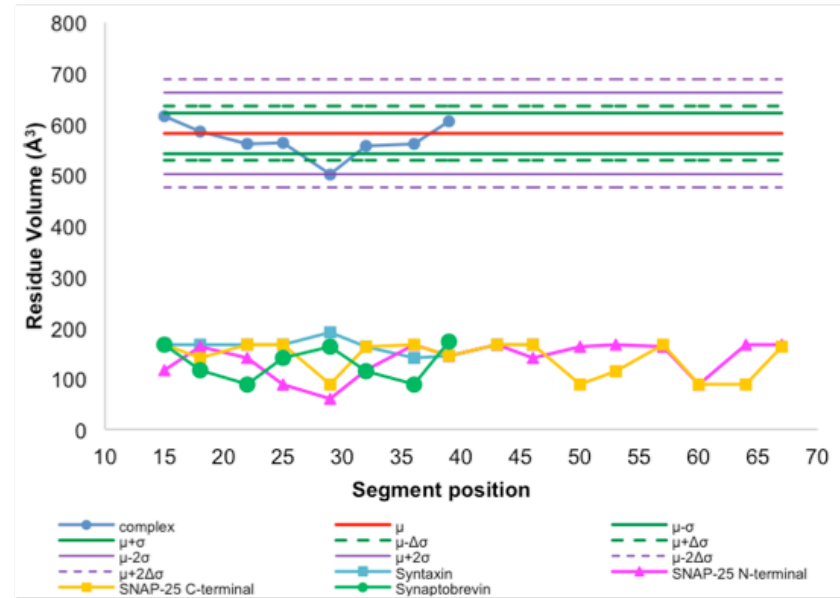
$$\Delta\sigma \text{ TRV} = \sqrt{(\sigma \text{ TRV syn})^2 + (\sigma \text{ TRV 25N})^2 + (\sigma \text{ TRV 25C})^2 + (\sigma \text{ TRV brev})^2} \quad (1)$$

**Figure 6.2: Total residue volume (TRV) of each hydrophobic segment in a native full-length SNARE complex motif (PDB ID: 1N7S), with statistical comparators “average” total residue volume, and the deviations associated with it.** A segment comprises of four residues from each of the four components of the SNARE complex (syntaxin, synaptobrevin, SNAP-25 N- and C-termini), as shown in the example (e). The total residue volume (TRV) of each hydrophobic segment is calculated by totalling all of the residue volumes in the segment. This is carried out across the length of the complex, and is plotted as “Native Full Length” (based on PDB 1N7S) in (a). An average, as well as 1x and 2x standard deviations is plotted as a single value across the complex (red; green and purple solid lines respectively). Finally, a “predicted deviation” is calculated, wherein the standard deviation is calculated separately for each chain (e.g. in (f) the 25N chain has been highlighted to show all the residues whose volumes are incorporated into its standard deviation). These individual standard deviations are substituted into Equation 1, to give a predicted deviation that is calculated as 1x and 2x deviations and plotted as a single value across the complex (green and purple dashed lines respectively). This analysis was applied separately for the N- (b) and C-termini (c) of the complex. Table (d) shows that the standard deviation in the C-terminal is twice that of the N-terminal indicating looser, less consistent assembly. Meanwhile, the predicted deviation of the N-terminal is greater than the actual standard deviation, indicating that the assembly of residues is not random, and rather suggests an element of design.

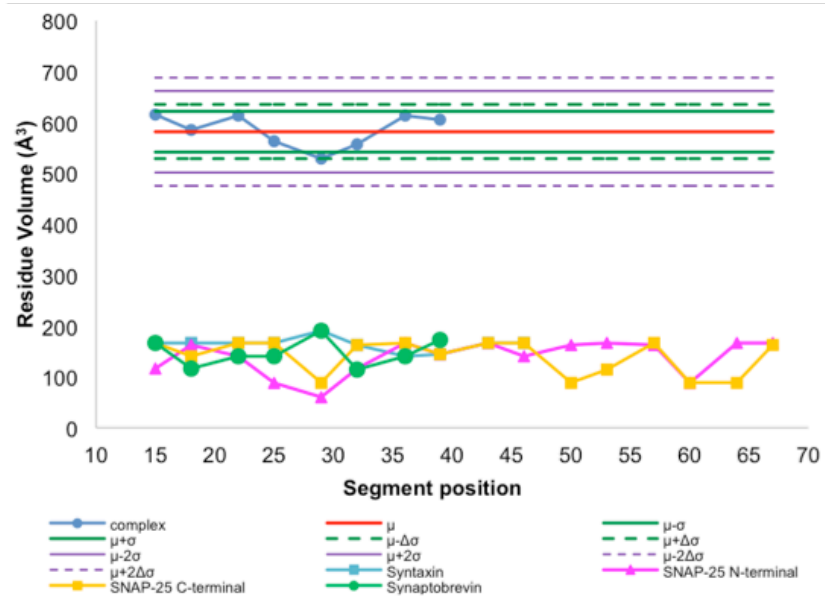
(a) Native complex: Synt1-01\_34 and Brev2-05\_27



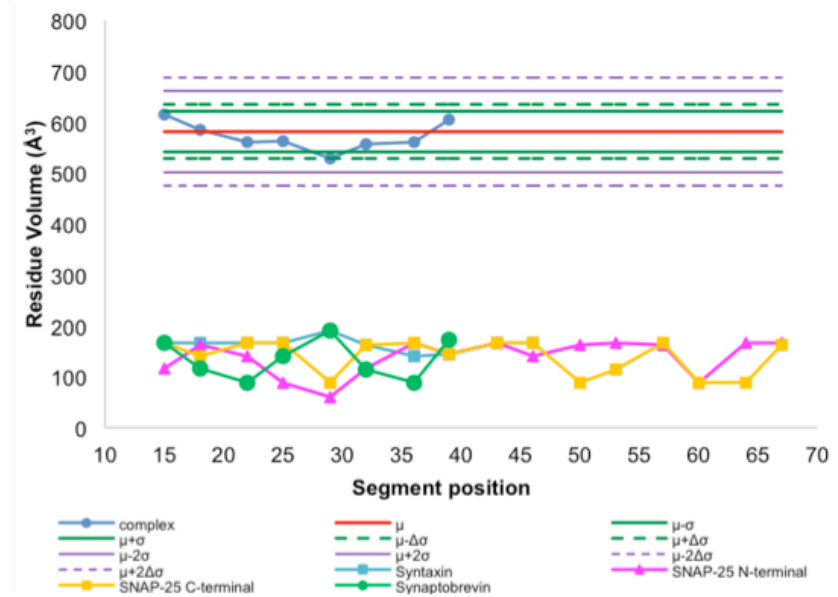
(c) V22A V36A mutations: Synt1-01\_34 and Brev2-12\_27ST



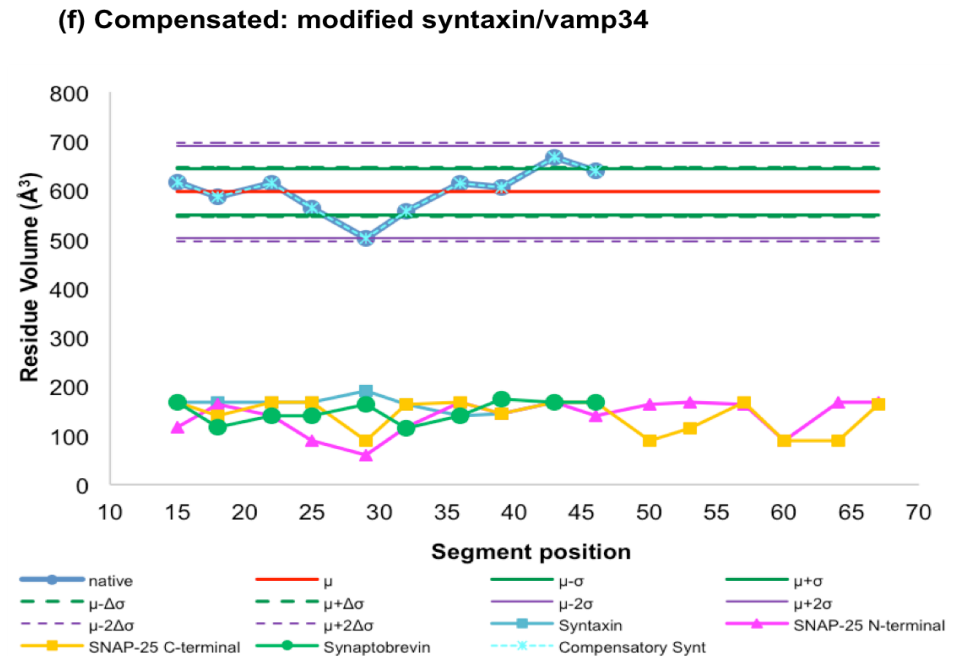
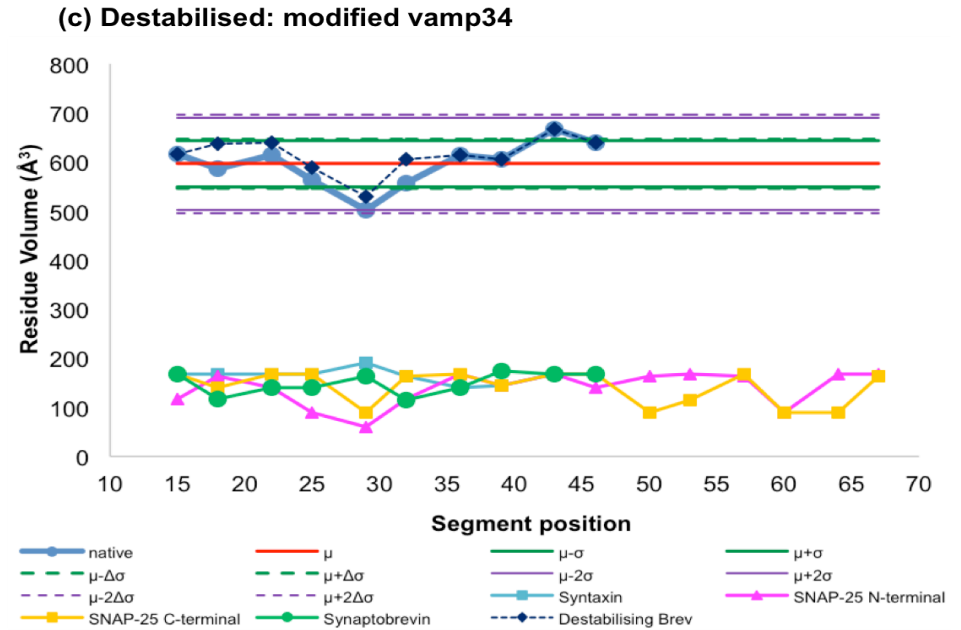
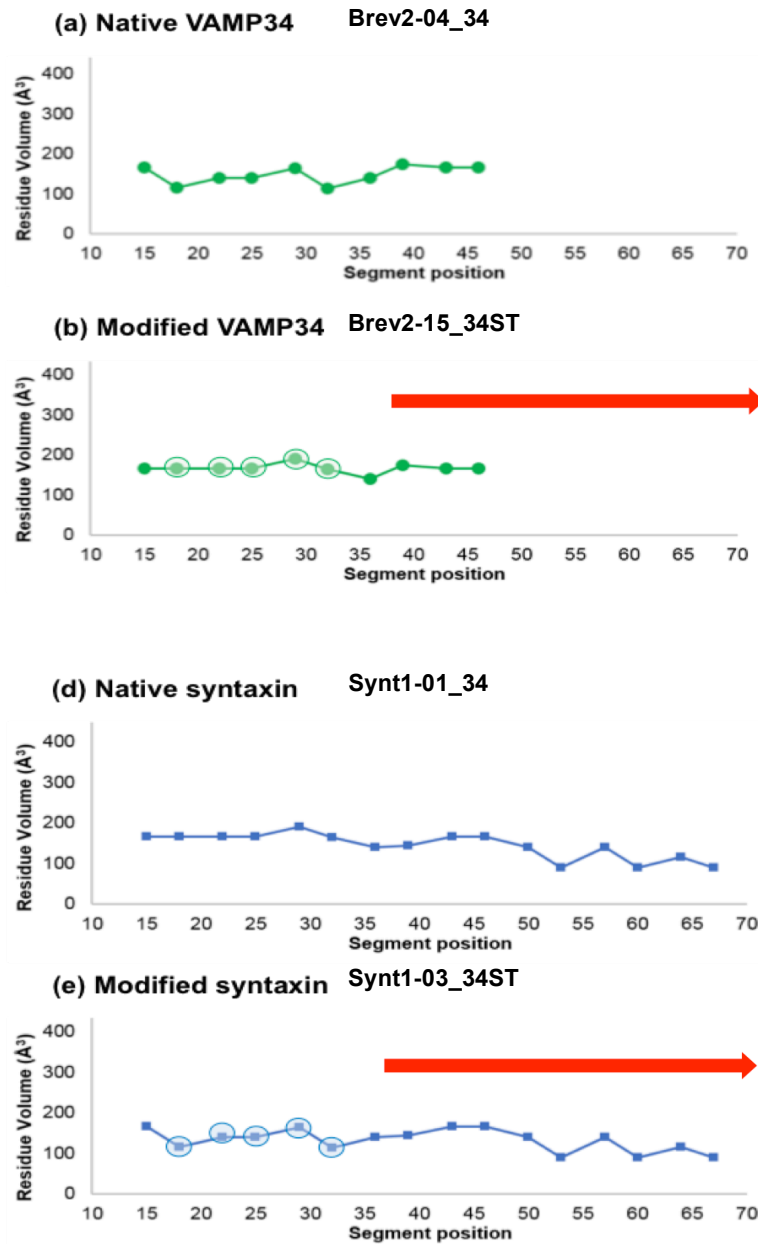
(b) M29F mutation: Synt1-01\_34 and Brev2-13\_27ST



(d) M29F V22A V36A mutations: Synt1-01\_34 and Brev2-14\_27ST

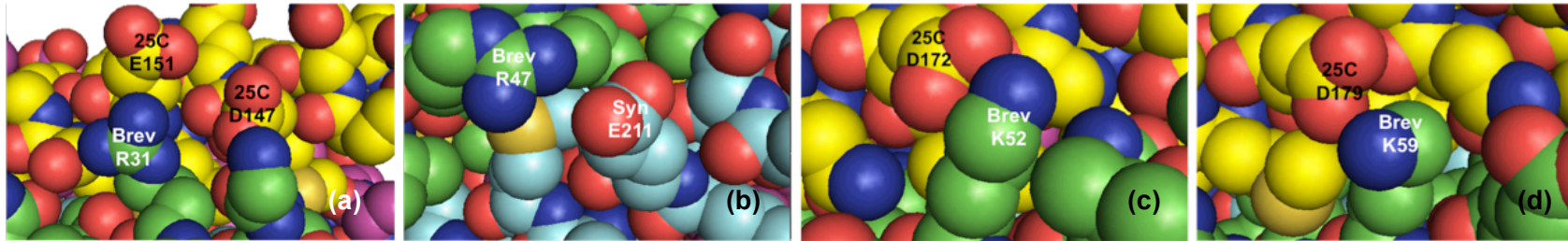




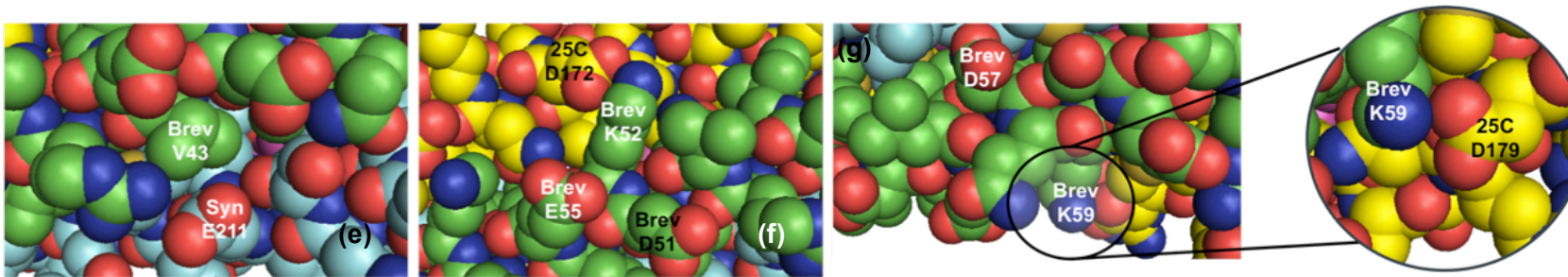








**pH-sensitive sequence mutations:** positively charged residues in vamp (R31, R47, K52 and K59) are mutated to histidine resulting in pH-influenced stability.



**Mutations to destabilise complex:** breaking or weakening existing salt bridges by introducing ionic repulsion.

(h)

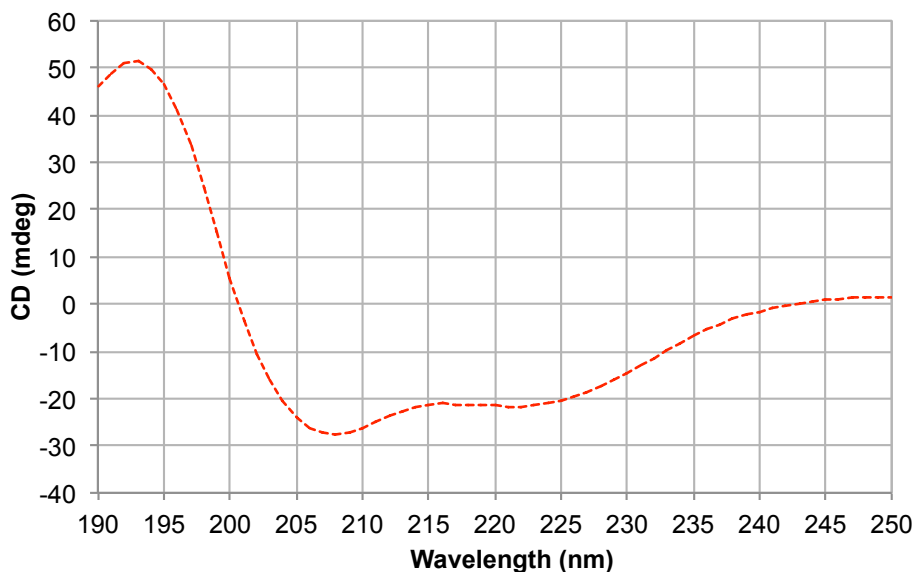
Peptide	Sequence	Mutation Rationale	Figure
Brev2-08_34ST	CRLQQTQAQVDEVDIMRVNV <b>DK</b> VLER <b>KQ</b> ELSELD	<b>K59E</b> : breaking the salt bridge between K59 and D179 in 25C (+ introducing ionic repulsion to further destabilise). <b>D57K</b> : mutation will maintain the pKa of this segment, which changes as a result of K59E.	(g)
Brev2-09_34ST	CRLQQTQAQVDEVDIMRVNV <b>KE</b> VLERD <b>Q</b> KLSELD	<b>K52E</b> : breaking the salt bridge between K52 and D172 in 25C (+ introducing ionic repulsion to further destabilise). <b>D51K</b> : mutation will maintain the pKa of this segment, which changes as a result of K52E.	(f)
Brev2-10_34ST	CRLQQTQAQVDEV <b>EA</b> IMRVNV <b>DK</b> VLERD <b>Q</b> KLSELD	<b>V43E</b> : the position of this residue makes it likely that a mutation to negatively charged glutamate will experience repulsion from E211 in syntaxin. <b>D44A</b> : mutation will maintain the pKa of this segment, which changes as a result of V43E.	(e)
Brev2-11_34ST	CRLQQTQAQVDEV <b>EA</b> IMRVNV <b>KE</b> VLER <b>KQ</b> ELSELD	All mutations above.	





## 13.7 Figures in Chapter 7

(a) Protein A spectrum



(b) SNARE complex (length = 55 amino acid) alongside individual protein chain

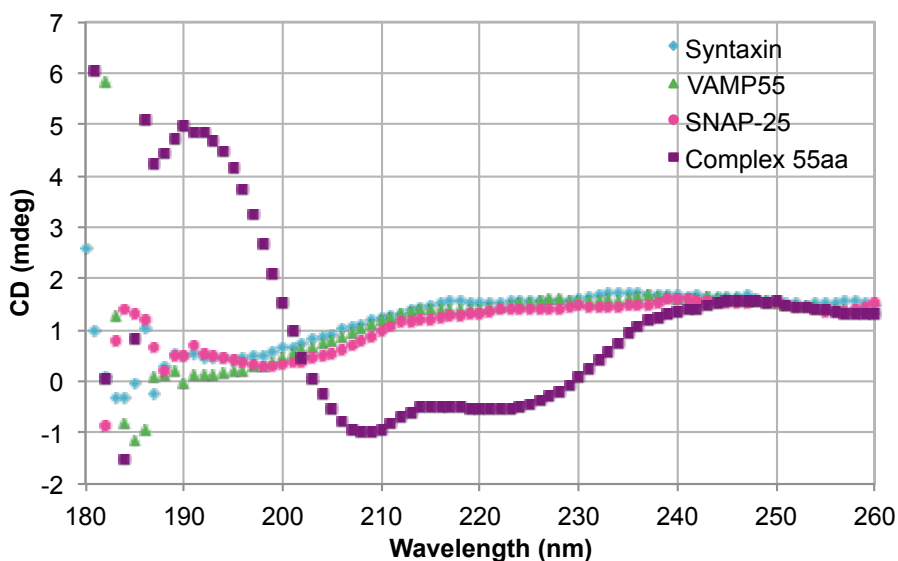


**Figure 7.1: Circular Dichroism (CD) spectra of positive control Protein A, full-length SNARE complex, and the separate protein chain components.** Protein A (a) acts as a good positive control as it has a strongly  $\alpha$ -helical structure, typified by troughs at  $\sim 208$  nm and  $\sim 222$  nm, which is expected of the full-length SNARE complex. Comparison of the Protein A spectrum with the full-length SNARE complex will allow us to confirm and characterise assembly. The spectrum for the full-length SNARE complex is shown in (b). The characteristic  $\alpha$ -helical troughs are present at 208 nm and 222 nm confirming assembly. This conclusion is further supported by the fact that the separate protein chain components (syntaxin, VAMP55, SNAP-25) exhibit disordered structure. Synchrotron Radiation Circular Dichroism (SRCD) was performed using a nitrogen-flushed Module X end-station spectrophotometer at B23 Synchrotron Radiation CD Beamline at the Diamond Light Source, Oxfordshire, UK. Dr. Enrico Ferrari (University of Lincoln) is acknowledged for his contribution towards the experiments, which ultimately produced the data in this figure, including providing the recombinant full-length proteins.

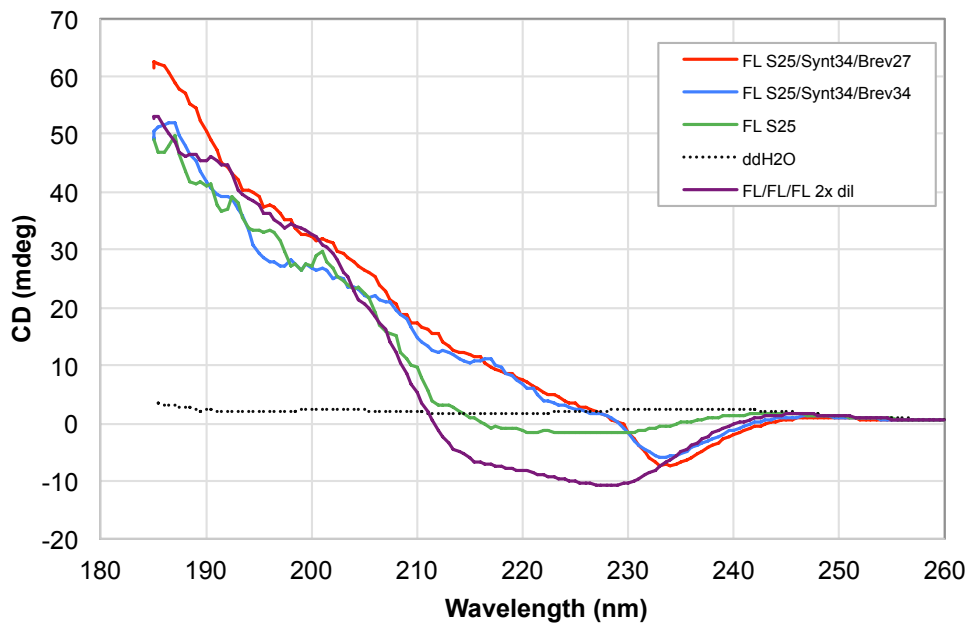
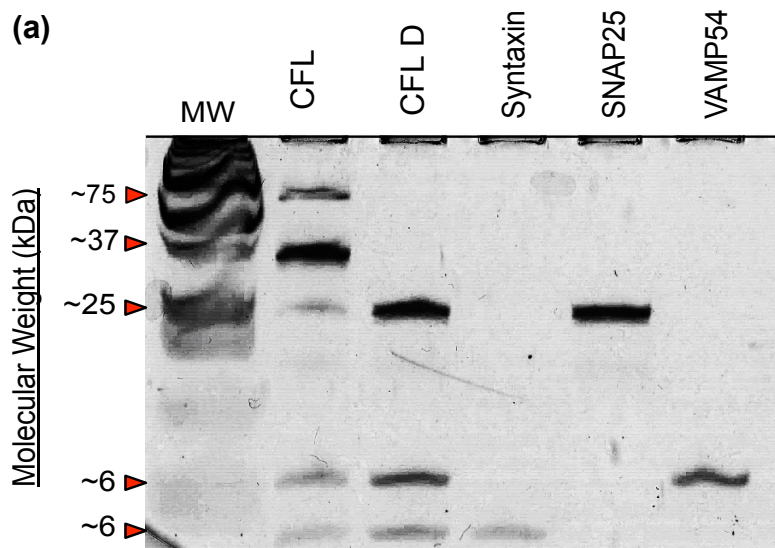
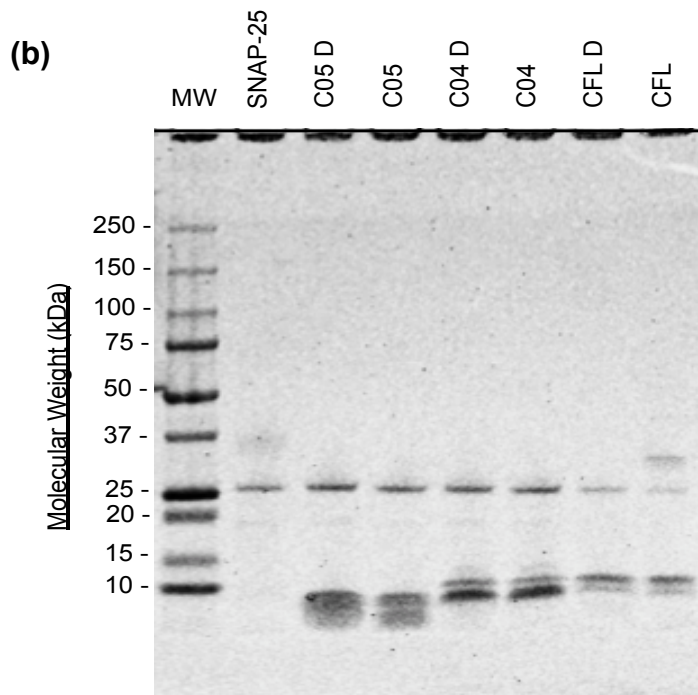


**Figure 7.2: Circular dichroism (CD) spectrum of a full-length SNARE complex, and Synt34 SNARE complexes containing Brev34 (Brev2-04\_34) and Brev27 (Brev2-05\_27).** Samples tested include full-length SNARE complex (FL/FL/FL – purple); SNARE complex containing full length SNAP-25, Synt34 and Brev34 (FL S25/Synt34/Brev34 – blue); SNARE complex containing full length SNAP-25, Synt34 and Brev27 (FL S25/Synt34/Brev27 – red); full-length SNAP-25 control (FL S25 –green); and distilled water as a baseline (ddH<sub>2</sub>O – dotted black). The full-length SNARE complex shows broad troughs at approximately 215 and 230 nm, characteristic of an  $\alpha$ -helical structure. The complexes containing truncated synaptobrevin peptides (Brev34/27) both demonstrate traces consistent with an  $\alpha$ -helical structure, and are sufficiently different from the SNAP-25 trace to indicate complex formation. Circular Dichroism was performed using a nitrogen-flushed PiStar-180 CD stopped-flow spectrometer at University of Lincoln, UK. Elina Dosadina is acknowledged for conducting the experiment and generating the data presented here, and Dr. Enrico Ferrari (University of Lincoln) is acknowledged for arranging access to instrument, contributing towards the experimental design and providing the recombinant full-length proteins.



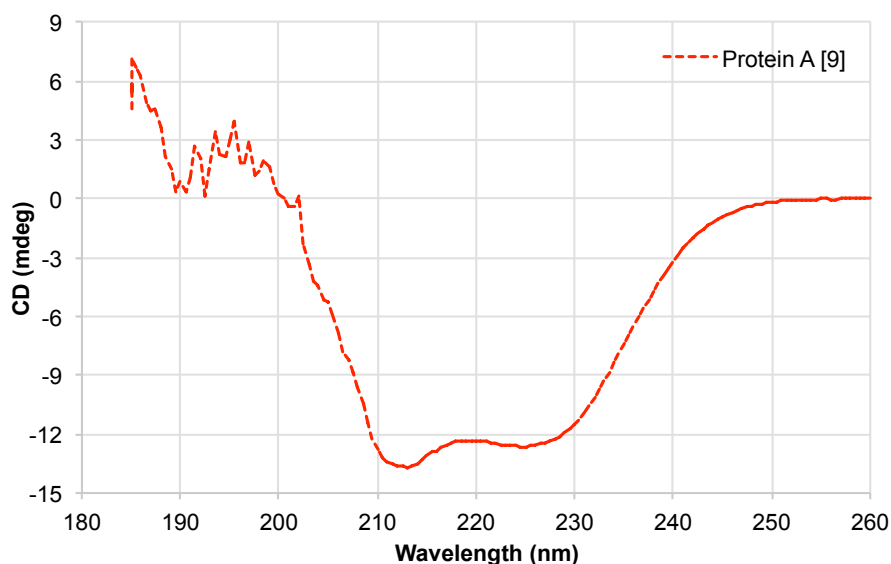
15% SDS-Gel with Precision Plus Protein Dual color standards molecular weight (MW) ladder (Biorad).



4-15% gradient mini-PROTEAN TGX precast SDS-gel with Precision Plus Protein Dual color standards molecular weight (MW) ladder (Biorad).

**Figure 7.3: Testing the truncated SNARE complexes for stability in SDS, and comparing with full-length complex.** The 15% acrylamide gel on the left (a) shows the precision plus protein ladder (M), the full-length complex (CFL) containing syntaxin, SNAP-25 and synaptobrevin (VAMP54, length = 54 aa), denatured complex (CFL D – heated to 70°C for 10 min), and the control complex components syntaxin, SNAP-25, and VAMP54. The full-length complex demonstrates SDS-stability, as evidenced by the band at 36 kDa. There is also a band at ~75 kDa, which is tentatively assumed to be a SNARE complex dimer. Heat-treatment in combination with SDS clearly denatures the complex as verified by the absence of a complex band. The gradient gel (4-15% acrylamide) on the right (b) shows heat-treated and untreated SNARE complexes containing peptides Synt1-01\_34, Brev2-04\_34 and Brev2-05\_27, as well as full-length (FL) syntaxin and synaptobrevin. These SNARE complexes are the same subjects of the circular dichroism experiment (Figure 7.2). Treatment consists of denaturing the complexes by heating to 90°C for 5 min. None of the peptide-containing complexes (C04 and C05) show SDS-stability, demonstrated by the lack of a band corresponding to a complex observed in the full-length complex (CFL) at ~36 kDa. Elina Dosadina is acknowledged for conducting the experiment and generating the data presented in (b).

(a) Protein A control spectrum



(b) Full-length and various truncated SNARE complexes.

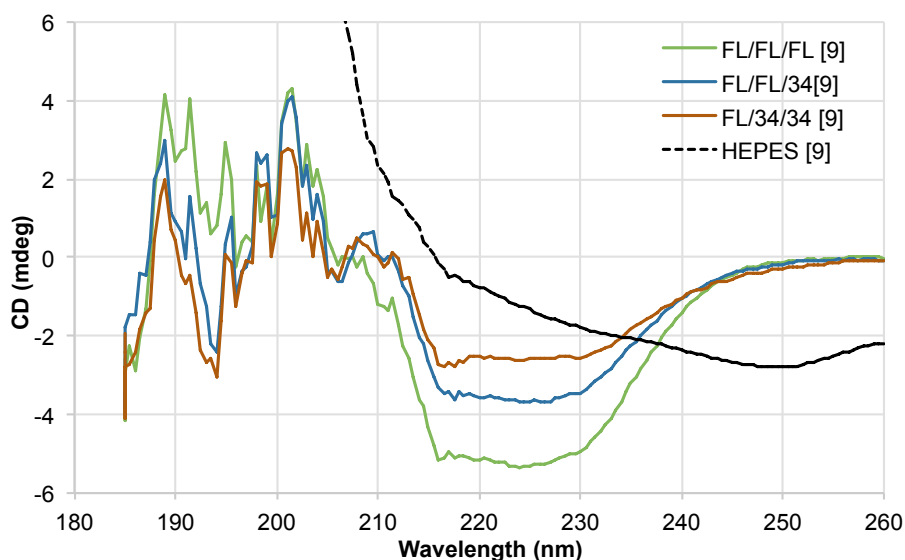
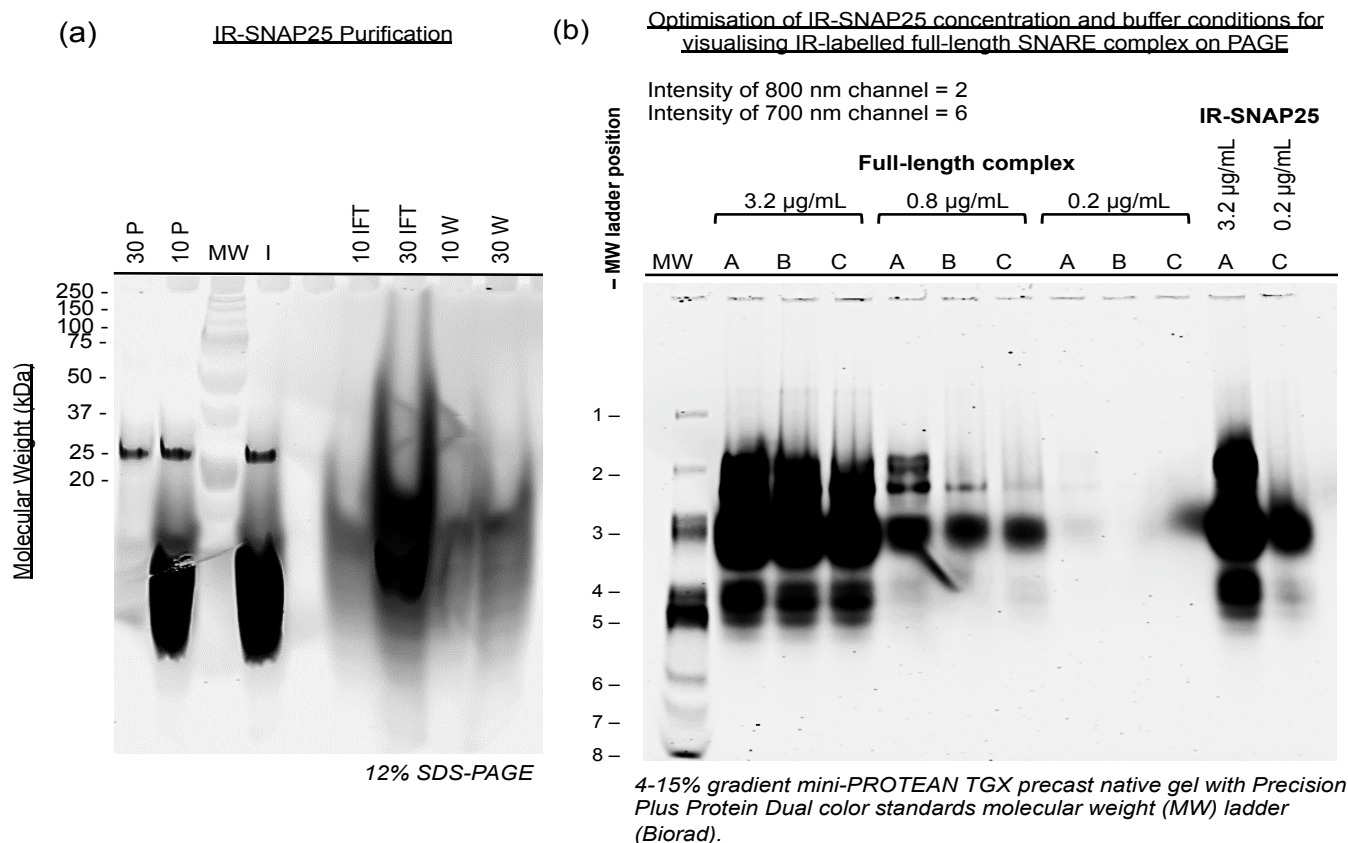


**Figure 7.4: Circular dichroism (CD) spectra of Protein A control, full-length SNARE complex (FL/FL/FL), SNARE complexes with truncated synaptobrevin (FL/FL/34), and both truncated synaptobrevin and syntaxin (FL/34/34), as well as HEPES buffer background.** Protein A control spectrum (a) was repeated as these experiments were performed on a different CD spectrometer. The two  $\alpha$ -helical troughs appear slightly shifted at  $\sim 212$  nm and  $\sim 225$  nm. Spectra were obtained for SNARE complexes (b) including full-length SNARE complex (FL/FL/FL); SNARE complex containing full-length SNAP-25, full-length syntaxin, and truncated synaptobrevin of length 34 aa (FL/FL/34); SNARE complex containing full-length SNAP-25, and both truncated syntaxin and synaptobrevin of length 34 aa (FL/34/34); and 10 mM HEPES buffer background (black dashed line). Unlike the Protein A control, the  $\alpha$ -helical troughs are less defined, and only one at  $\sim 215$ - $230$  nm is clearly visible in all complexes however, the shape is still consistent with an  $\alpha$ -helical structure. The intensity of this trough decreases as the extent of complex truncation increases, as is expected since the quantity of  $\alpha$ -helical structure also decreases. These results confirm that successful assembly can be achieved with both syntaxin and synaptobrevin truncated to a length of 34 aa. All spectra shown here have undergone HEPES background subtraction, and were averaged over five scans, and the resulting data was subsequently averaged over a window length of 9 values to improve the signal-to-noise ratio. Circular Dichroism was performed using a nitrogen-flushed PiStar-180 CD stopped-flow spectrometer at University of Lincoln, UK. Lauren Nelles is acknowledged for preparing and conducting the Protein A control experiment. Elina Dosadina is acknowledged for her guidance in using the instrument, and Dr. Enrico Ferrari (University of Lincoln) is acknowledged for arranging access to instrument, contributing towards the experimental design, and providing the recombinant full-length proteins.



Key

MW – Molecular Weight ladder

30 – 30 kDa filter size

10 – 10 kDa filter size

P – purified

I – impure

IFT – initial flow through

W – wash

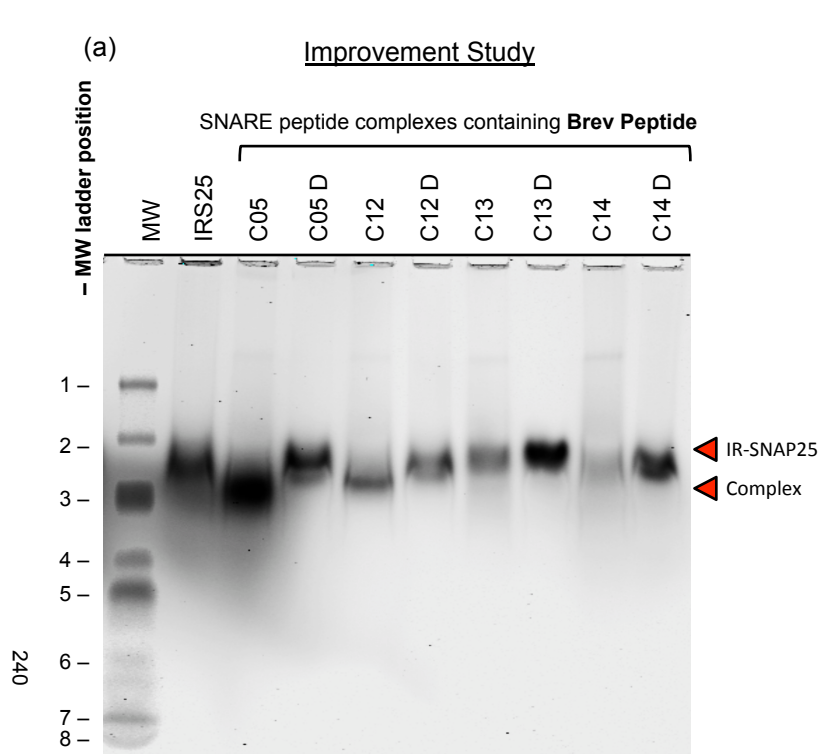
**A – 1 mg/mL BSA / 0.1% OG with HEPES 16 mM and NaCl 80 mM**

**B – 0.1 mg/mL BSA / 0.1% OG with HEPES 16 mM and NaCl 80 mM**

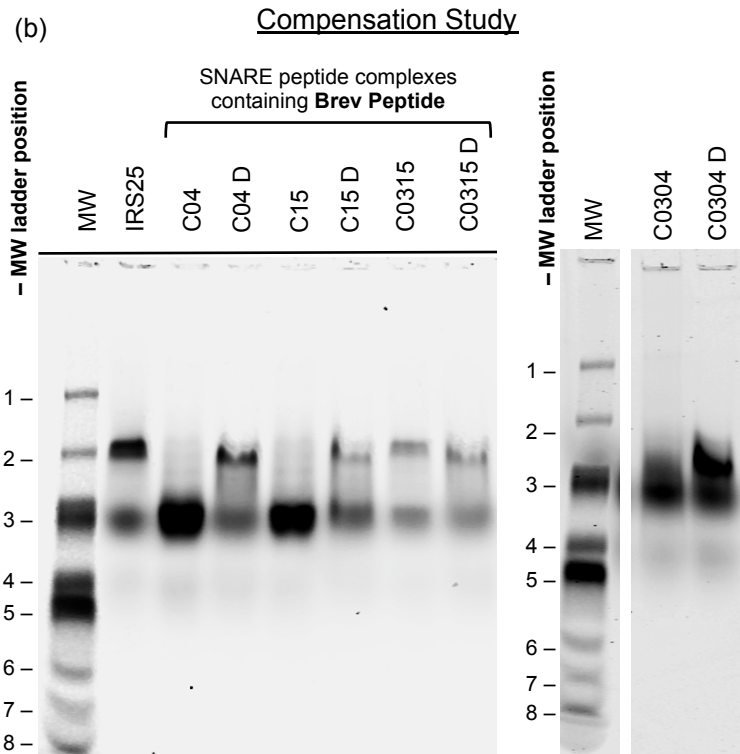
**C – 0.01 mg/mL BSA / 0.1% OG with HEPES 16 mM and NaCl 80 mM**

Full-length complex contains IR-SNAP25, recombinant syntaxin and VAMP54.

**Figure 7.5: Results from preparation and purification of infrared (IR) labelled SNAP-25 (“IR-SNAP25”), and optimisation of IR-SNAP25 concentration and buffer conditions for visualisation on polyacrylamide gel.** Full-length SNAP-25 was successfully labelled with CF790 succinimidyl ester IR label. The unpurified (“impure”) sample showed excess label below 20 kDa, so a 10 and 30 kDa sized filter were used for purification. Purification was achieved with the 30 kDa sized filter, as observed in lane “30 P”, and supported by the majority of impurity appearing in lane “30 IFT”. IR-SNAP25 concentration and buffer optimisation was conducted using a full-length SNARE complex assembled with IR-SNAP25, and visualised on a native gradient gel in the 800 nm channel. Optimal IR-SNAP25 concentration was determined as 0.8 µg/mL, and Buffer B (with 0.1 mg/mL BSA) was determined as the best compromise between the positive blocking effect of BSA to facilitate the use of very low concentration IR-SNAP25, and the negative effect a large concentration of BSA might have on the kinetics of SNARE assembly.



4-15% gradient mini-Protean TGX precast native gel visualised in 700 nm and 800 nm channels. D = denatured. All samples were prepared in Buffer B (16 mM HEPES, 80 mM NaCl, 0.1 mg/mL BSA, 0.1% OG).



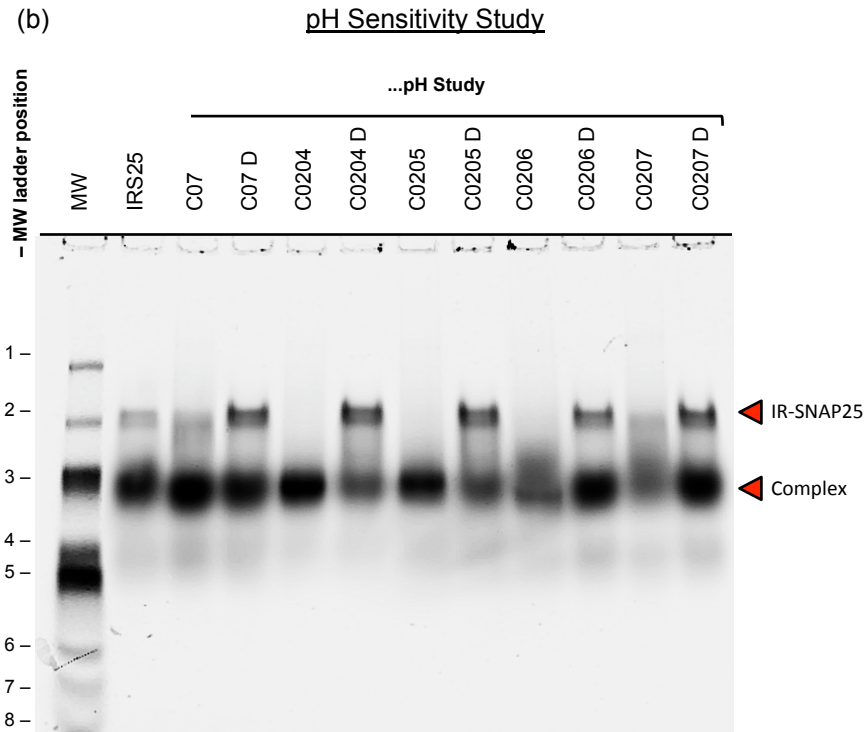
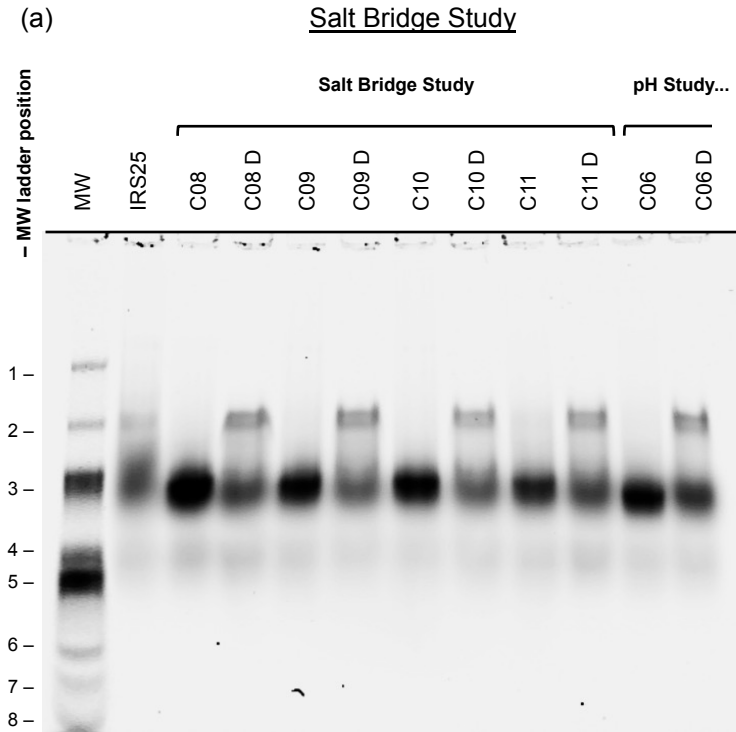
4-15% gradient mini-Protean TGX precast gel visualised in 700 nm and 800 nm channels. D = denatured. Samples C04-C0315 were prepared in Buffer A (16 mM HEPES, 80 mM NaCl, 1 mg/mL BSA, 0.1% OG), whilst sample C0304 was prepared in Buffer B (16 mM HEPES, 80 mM NaCl, 0.1 mg/mL BSA, 0.1% OG).

**Figure 7.6: Assembly of all complexes in the Residue Volume study was investigated on native PAGE gels and the results are shown here.** All samples were prepared with syntaxin and synaptobrevin components in large excess over IR-SNAP25. Presence of an IR-SNAP25 band in a lane would indicate unsuccessful assembly or disassembly (in the case of denatured “D” samples). Gel (a) shows the results of the improvement study. Here the distance between IR-SNAP25 band and complex band is very close, but it can be discerned that C05 and C12 in this case do assemble, whilst C14 is unclear in this gel. C13 does not appear to assemble at all. Gel (b) shows the results of the compensation study. It is very evident that C04, and C15 are the only complexes that assemble successfully. It is unclear whether C0304 also assembles. Table (c) summarises the conclusions reached regarding assembly of Residue Volume study complexes.

(c) Table of complex descriptions and whether they assemble (indicated by Yes (Y) or No (N))

Complex	Description	Assembles Y/N
C04	Synt1-01_34, <b>Brev2-04_34</b> , IR-SNAP25	Y
C05	Synt1-01_34, <b>Brev2-05_27</b> , IR-SNAP25	Y
C12	Synt1-01_34, <b>Brev2-12_27ST</b> , IR-SNAP25	Y
C13	Synt1-01_34, <b>Brev2-13_27ST</b> , IR-SNAP25	N
C14	Synt1-01_34, <b>Brev2-14_27ST</b> , IR-SNAP25	?
C15	Synt1-01_34, <b>Brev2-15_34ST</b> , IR-SNAP25	Y
C0315	<b>Synt1-03_34ST</b> , <b>Brev2-15_34ST</b> , IR-SNAP25	N
C0304	<b>Synt1-03_34ST</b> , <b>Brev2-04_34</b> , IR-SNAP25	?





(c) Table of complex descriptions and whether they assemble (indicated by Yes (Y) or No (N))

Complex	Description	Assembles Y/N
C08	Synt1-01_34, <b>Brev2-08_34ST</b> , IR-SNAP25	Y
C09	Synt1-01_34, <b>Brev2-09_34ST</b> , IR-SNAP25	Y
C10	Synt1-01_34, <b>Brev2-10_34ST</b> , IR-SNAP25	Y
C11	Synt1-01_34, <b>Brev2-11_34ST</b> , IR-SNAP25	Y
C06	Synt1-01_34, <b>Brev2-06_34PH</b> , IR-SNAP25	Y
C07	Synt1-01_34, <b>Brev2-07_34PH</b> , IR-SNAP25	Y
C0204	<b>Synt1-02_34PH</b> , <b>Brev2-04_34</b> , IR-SNAP25	Y
C0205	<b>Synt1-02_34PH</b> , <b>Brev2-05_27</b> , IR-SNAP25	Y
C0206	<b>Synt1-02_34PH</b> , <b>Brev2-06_34PH</b> , IR-SNAP25	Y
C0207	<b>Synt1-02_34PH</b> , <b>Brev2-07_34PH</b> , IR-SNAP25	Y

**Figure 7.7: Assembly of all complexes in the Ionic Interactions study was investigated on native PAGE gels and the results are shown here.** As previously, all samples were prepared with syntaxin and synaptobrevin components in large excess over IR-SNAP25. Presence of an IR-SNAP25 band in a lane would indicate unsuccessful assembly or disassembly (in the case of denatured “D” samples). Gel (a) shows the results for the Salt Bridge study, and it is clearly evident that all complex mixtures assemble successfully, with IR-SNAP25 present in all denatured “D” lanes to support this conclusion. The last two lanes of gel (a) and the all of gel (b) shows the results for the pH Sensitivity study and all complex mixtures appear to assemble. Table (c) summarises the conclusions reached regarding assembly of Ionic Interactions study complexes.

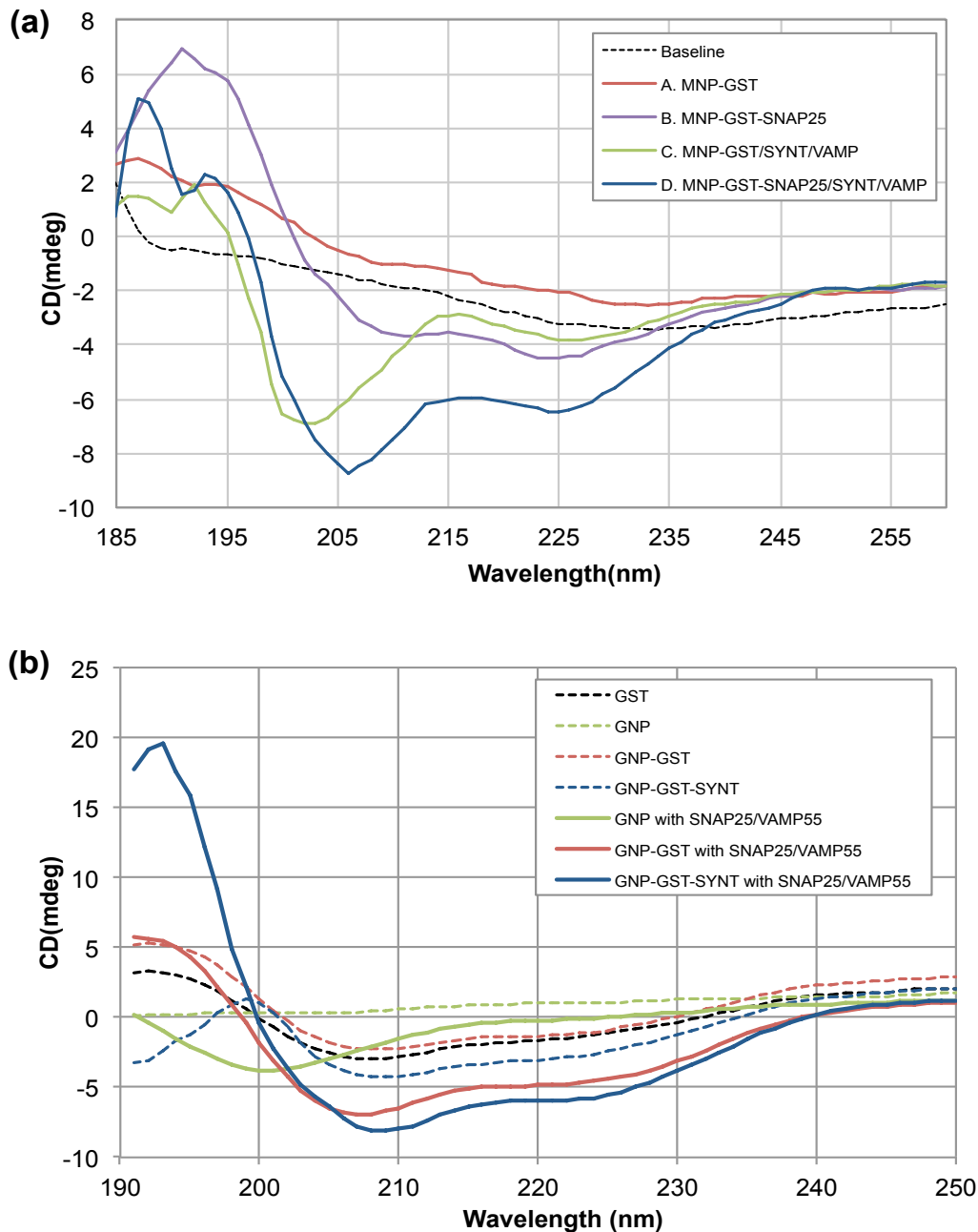


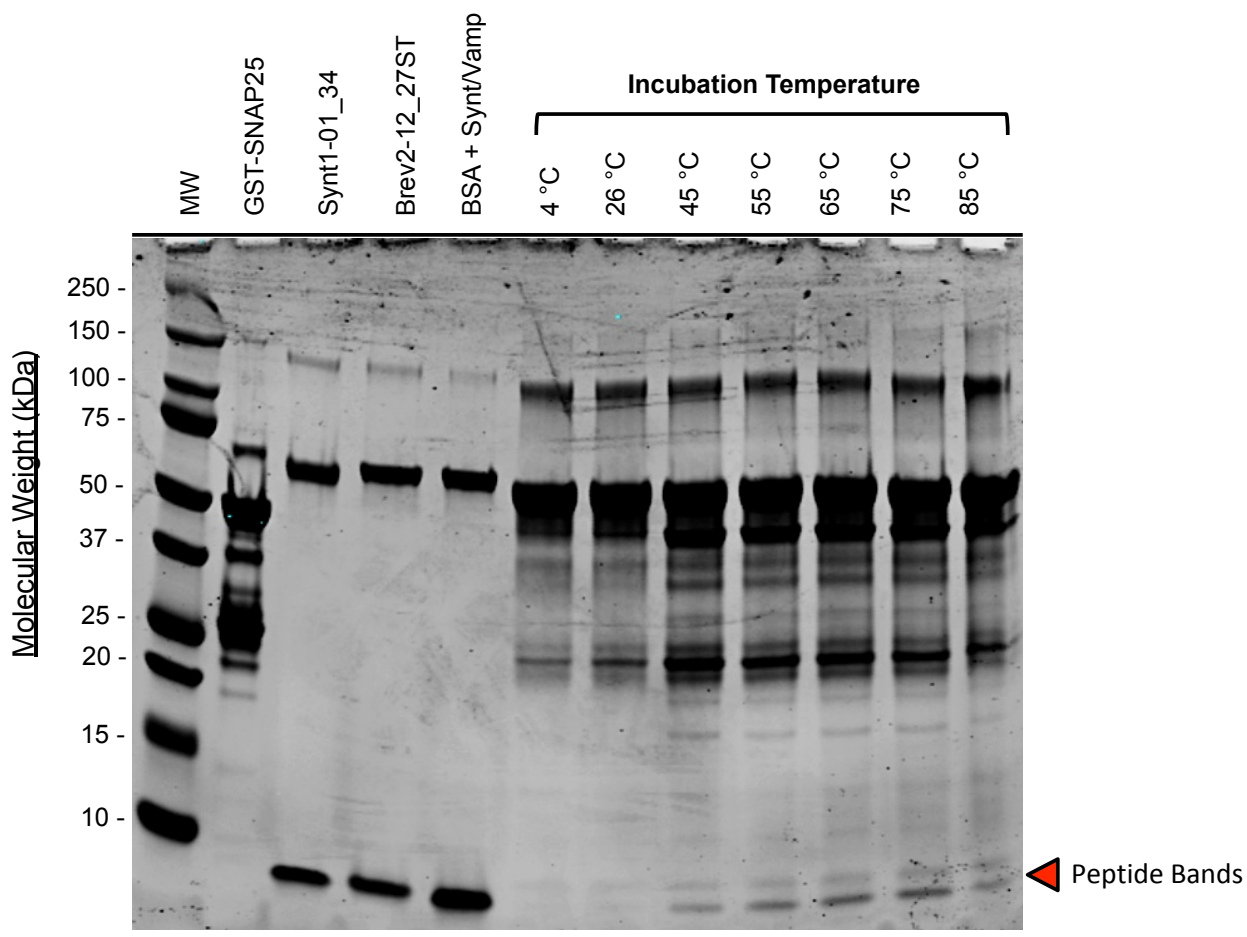
**Figure 7.8: Circular dichroism (CD) spectra of full-length complex conjugated to magnetic iron oxide nanoparticles (MNP), and gold nanoparticles (GNPs) and associated controls.** The graph (a) provides evidence that protein assembly occurs on the MNP surface. The MNPs used for this study were amino-reactive (NHS - N-hydroxysuccinimide ester surface modification) iron(II,III) oxide nanoparticles with a diameter of 5 nm. A linker was desired to create distance between the complex and the MNP, in order to facilitate assembly by preventing potential steric hindrance as the proteins come into contact with one another. Since SNAP-25 was recombinantly expressed as a GST-fusion protein (GST: glutathione S-transferase) protein, GST was maintained as said linker. Since GST contains a substantial amount of  $\alpha$ -helical secondary structure, it was important to characterise the control MNP-GST in order to ascertain its  $\alpha$ -helical contribution to the main sample MNP-GST-SNAP25/SYNT/VAMP (i.e. MNP-GST conjugated to the full-length SNARE complex). It can be seen that the amount of  $\alpha$ -helical content in the complex sample is substantially greater than either MNP-GST, or the samples containing SNAP-25 or SYNT/VAMP. The baseline is MNP solution that has been diluted to give an absorbance of 0.05. The graph (b) provides evidence that protein assembly similarly occurs on the GNP surface too. The GNPs used for this study had a diameter of 20 nm, and were functionalised with GST, which binds through sulphur-cysteine chemistry. GNP-GST-SYNT particles (i.e. GNP functionalised with GST that are bound to syntaxin through amino groups) show some  $\alpha$ -helical structure, with similar intensity to GST alone since this is the main contributor; however, when SNAP-25 and full length synaptobrevin (VAMP55) are added, the amount of  $\alpha$ -helical structure is substantially greater. This clearly indicates that the SNARE complex assembles successfully on the GNP surface.



## 13.8 Figures in Chapter 8

### Example of pull-down Temperature Assay (supernatant):

#### GST-C12 Melting Temperature Assay pull-down **supernatant** SDS-PAGE gel



4-20% gradient TruPage precast SDS-gel (Sigma) with Precision Plus Protein Dual color standards molecular weight (MW) ladder (Biorad).

All samples (except MW) contain Buffer E (10 mM HEPES, 0.1 mg/mL BSA, 0.1% OG).

**Figure 8.1: Example of typical SDS-gels containing the results from the supernatant product of temperature pull-down assay, which tests for thermal stability in the complexes pertaining to the Residue Volume, and Salt Bridge studies.** Complexes were assembled on glutathione agarose beads linked to GST-SNAP25 fusion protein. After thorough washing, the complexes were incubated at temperatures 4, 25, 45, 55, 65, 75, and 85 °C, as specified in the gel lanes under “Incubation Temperature”. The amount of peptide in each supernatant should gradually increase as the complex approaches, and eventually progresses past the melting temperature ( $T_m$ ) and disassembles releasing peptide from the bead. The pellet (or “beads”) is washed, and then heat-denatured and reduced with 2-mercaptoethanol in order to liberate the remaining protein and peptides from the beads, which should gradually decrease with temperature as the complex disassembles. There are many extraneous bands in the complex lanes (under the heating “Incubation Temperature”) because the glutathione-agarose-GST-SNAP25 beads are impure, and contain all the cell lysate products alongside GST-SNAP25 immobilised on the beads. GST-SNAP-25 band was identified at ~ 50 kDa. Densitometry analysis of the coomassie-stained gel was then performed on any set of peptide bands that is most easily identifiable. Gels were scanned, and analysis was conducted on an Odyssey CLx scanner (Li-Cor Biosciences).

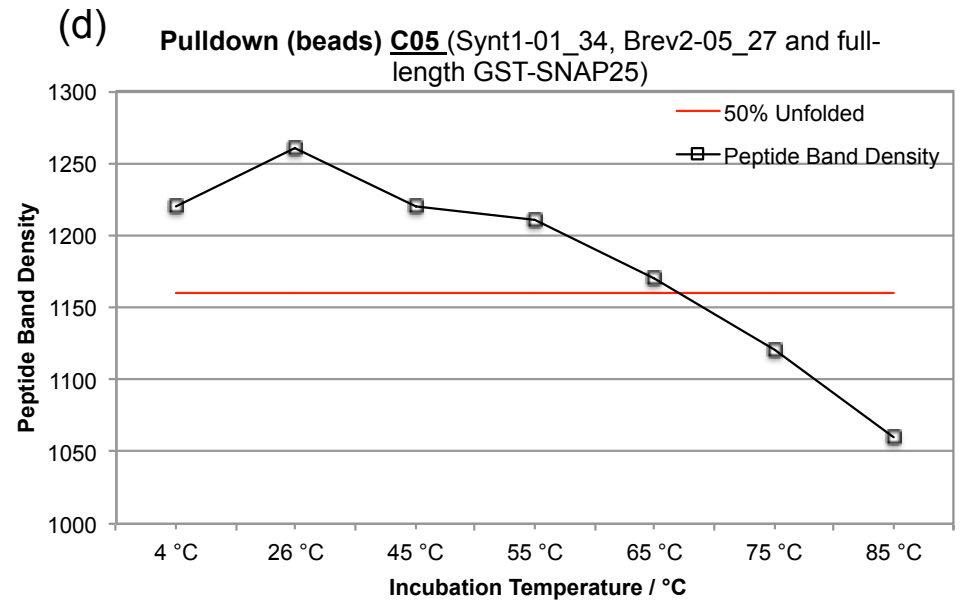
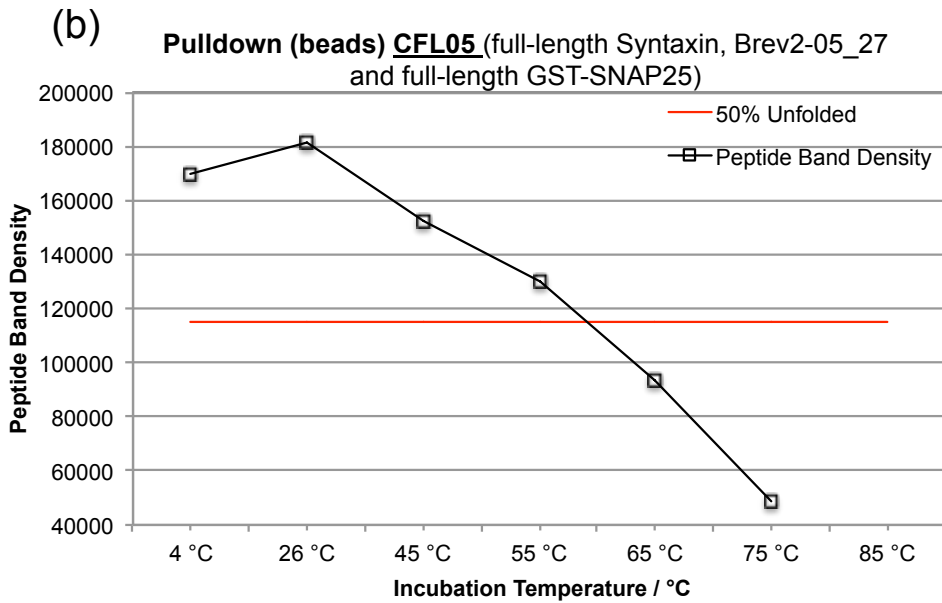
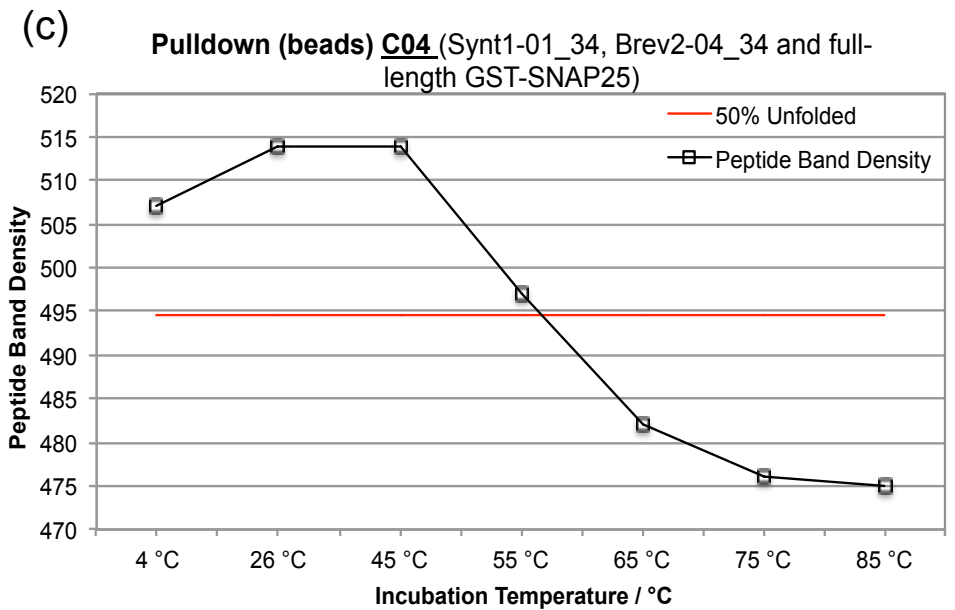
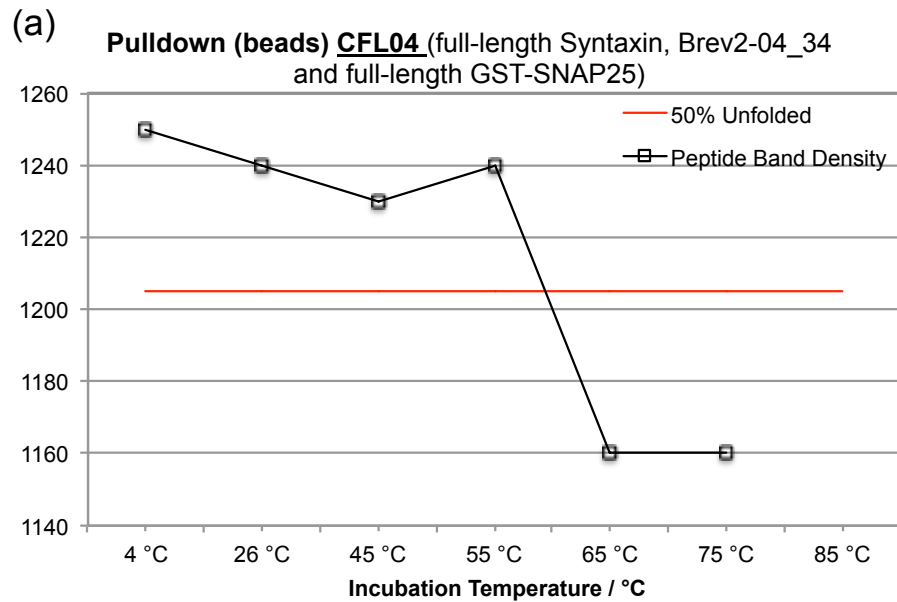


**Figure 8.2: Results from the pull-down “beads” assays testing for relative thermal stability of the control complexes including partially truncated SNARE complexes (i.e. where synaptobrevin alone has been truncated), and SNARE complexes where both syntaxin and synaptobrevin are truncated.** The density of a single set of peptide bands in the SDS-gel was measured, and this was plotted as a function of the incubation temperature. The red line “50% Unfolded” represents the halfway point between the highest and lowest band intensities. The intersection point between the peptide band density and the “50% Unfolded” line is effectively the melting temperature ( $T_m$ ) determined using this methodology. Partially truncated complex CFL04 ((a) with synaptobrevin of length 34) shows a  $T_m$  of  $\sim 60^\circ\text{C}$ , with relatively consistent thermostability until  $55^\circ\text{C}$  and a sharp drop from this point till  $65^\circ\text{C}$ . Partially truncated complex CFL05 ((b) with synaptobrevin of length 27) shows a slightly lower  $T_m$  of  $\sim 59^\circ\text{C}$ , however the drop in thermostability is a steady decrease compared to the sharp drop observed in CFL04. Truncated complex C04 ((c) with both syntaxin and synaptobrevin of length 34) showed a  $T_m$  of  $\sim 58^\circ\text{C}$ , showing a sigmoidal curve characteristic of protein melting, with a steady decrease in thermostability from  $45^\circ\text{C}$  onwards. Truncated complex C05 ((d) with syntaxin at length 34, and synaptobrevin at length 27) showed an unexpectedly higher  $T_m$  of  $68^\circ\text{C}$ . The trend in thermostability is also substantially steadier than C04. Densitometry analysis was performed on an Odyssey CLx scanner (Li-Cor Biosciences).

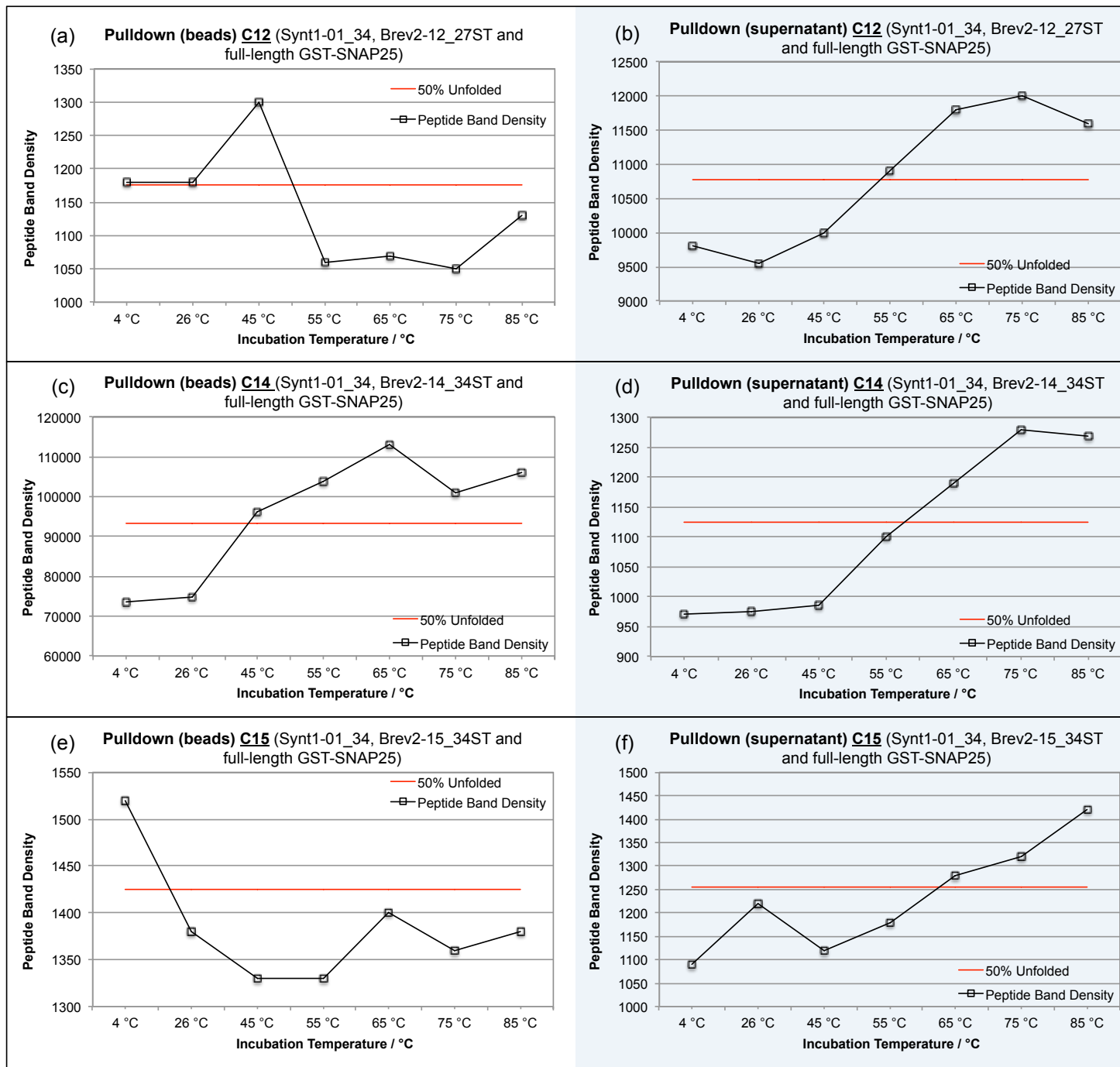
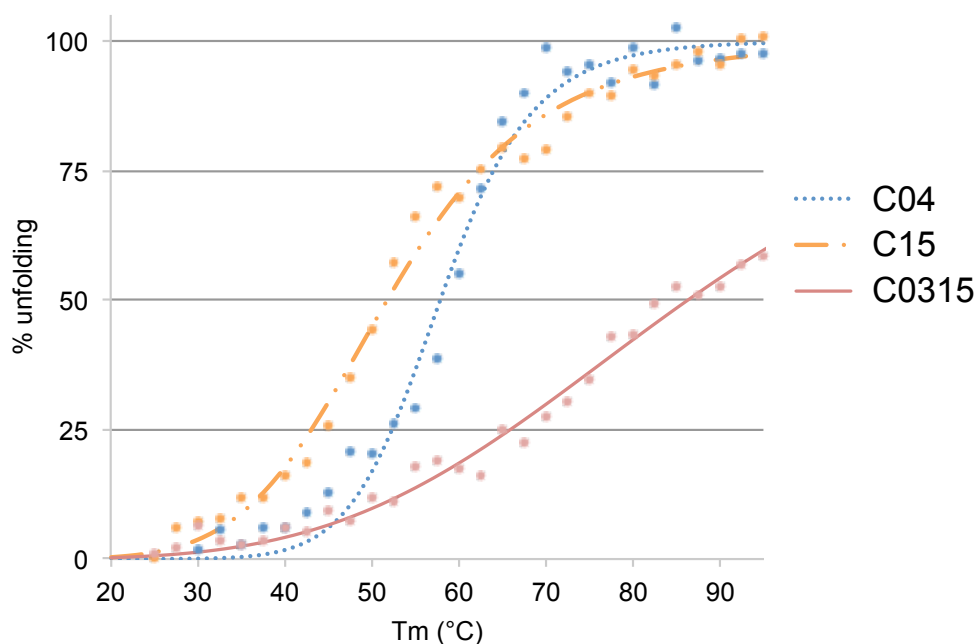


**Figure 8.3: Results from pellet “beads” and supernatant products of temperature pull-down assays, testing for thermal stability in complexes pertaining to the Residue Volume study.** The density of a single set of peptide bands in the SDS-gel was measured, and this was plotted as a function of the incubation temperature. The red line “50% Unfolded” represents the halfway point between the highest and lowest band intensities. The intersection point between the peptide band density and the “50% Unfolded” line is effectively the melting temperature ( $T_m$ ) determined using this methodology. Of the three “Improvement Study” complexes, only C12 showed definitive evidence of assembly, whilst no conclusion was reached for C14 when viewing the native gels (**Figure 7.7**). The results from the beads pull-down assay of C12 (**a**) shows a plateau between 4-26°C, followed by an unexpected increase in peptide at 45°C, which subsequently sharply decreases and remains low and stable between 55-85°C. The  $T_m$  is estimated as ~51-52°C. The supernatant results (**b**) show the more characteristic sigmoidal behaviour of a protein melt, with a steady increase between 26-75°C, and a higher estimate for  $T_m$  at ~54°C. The pull-down for C14 is proof that the complex does indeed assemble, since a measurable peptide signal is only possible if the complex initially formed successfully on the SNAP-25-linked beads. The C14 beads (**c**) gave an unexpected pattern of thermostability. The results from the beads product of the pull-down should show a steady decrease in peptide band density with temperature, however here peptide band density instead increases with temperature. The  $T_m$  was measured at ~45°C. The supernatant results (**d**) showed an approximately sigmoidal shaped melt curve, with a  $T_m$  of ~53°C. Of the three “Compensation Study” complexes, only C15 showed definitive evidence of successful assembly in the native gels, whilst no conclusion was reached for C0304. No measurable peptide signal could be achieved in either the beads or supernatant products of the C0304 pull-down, so it was concluded that C0304 does not assemble. The results from the beads pull-down of C15 (**e**) showed a very sharp decrease in peptide band density from 4-45°C, and a  $T_m$  of 22-23°C. The results from the supernatant (**f**) contradict the beads, showing a relatively stable (with the exception of a spike at 26°C) increase in peptide density, and  $T_m$  of ~63-64°C. Densitometry analysis was performed on an Odyssey CLx scanner (Li-Cor Biosciences).

(a) Melting curves obtained using CD spectroscopy for native complex (C04) and compensation complexes C15 and C0315

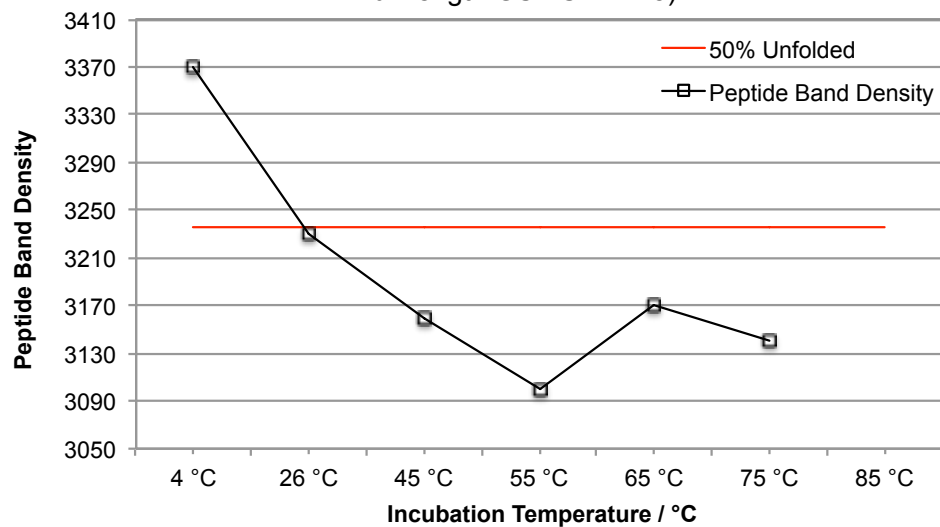


(b) Table summarising melting temperatures ( $T_m$ ) for complexes shown in graph (a), as well as standard error and  $R^2$  of the curve fitting.

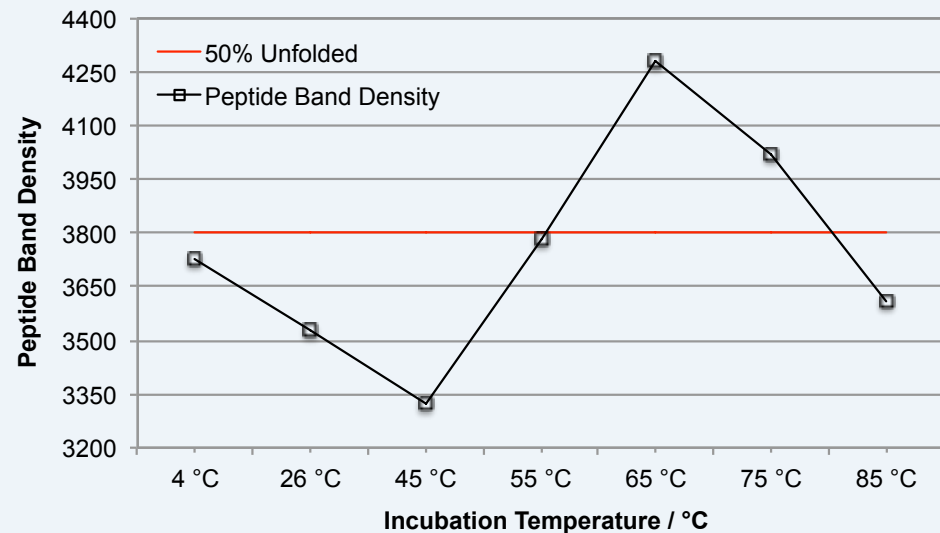
Complex		C04	C15	C0315
C.I.	$T_m$ (°C)	58	52	86
	+ (95)	2.44	2.89	
	- (95)	2.70	2.01	12.48
	$R^2$	0.987	0.992	0.985

**Figure 8.4: Results from SRCD testing for thermal stability in complexes pertaining to the Compensation study.** The CD spectra show the results of an SRCD thermal melting experiment pertaining to the complexes involved in the Compensation study, C04, C15 and C0315. CD signal was measured at 222 nm (alpha-helical trough) over a temperature range of 20-95°C (a), and the traces were recalculated as 100% change from start of the melt to the end. The curves shown are four-parametric sigmoidal curves fitted using non-linear least squares method (Kemmer and Keller, 2010). A summary table of the melting temperatures ( $T_m$ ), 95% confidence intervals (C.I.) and  $R^2$ , which is indicative of the level of correlation in the curve fitting (measured at -1 to 1, with 1 being maximum positive correlation) is shown in (b). The results show that C15, the destabilised peptide complex containing mutated Brev2-15\_34ST, which was expected to present steric hindrance with syntaxin, had slightly lower stability than the control C04 (drop in melting temperature of 6°C). C0315, the rescued “compensated” complex, has a melting temperature of 86°C, indicating that not only does it assemble, it also presents a dramatic increase in stability compared to the destabilised, and native complexes (C15 and C04 respectively). This is consistent with our expectations, and proves the TRV volume conservation strategy laid out in **section 6.1.1.2**. Synchrotron Radiation Circular Dichroism (SRCD) was performed using a nitrogen-flushed Module X end-station spectrophotometer at B23 Synchrotron Radiation CD Beamline at the Diamond Light Source, Oxfordshire, UK. Dr. Enrico Ferrari (University of Lincoln), Dr Giuliano Siligardi (Diamond UK) and Dr Mikhail Soloviev (RHUL) are acknowledged for their contribution towards the experiments, including providing the recombinant full-length protein (EF), setting up the SRCD spectrometer (GS) and experimental design (EF, MS) which ultimately generated the data in this figure.

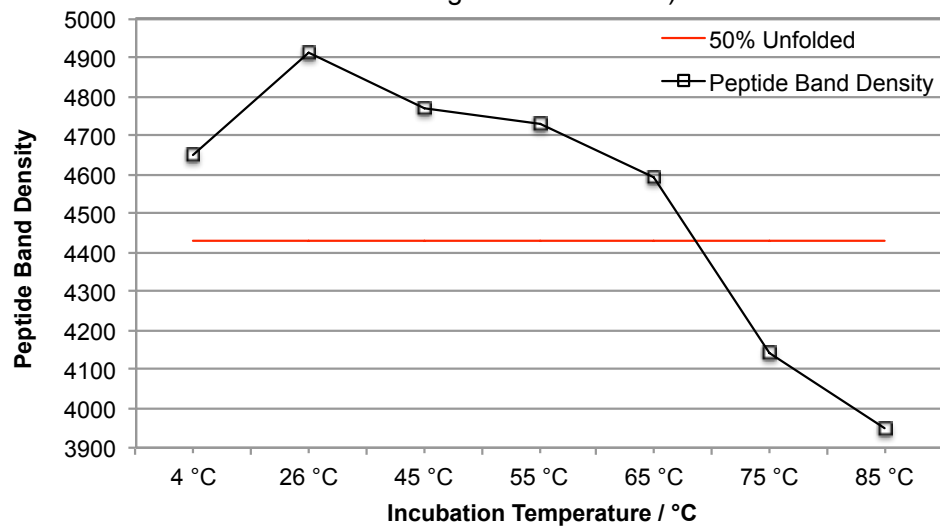
(a) **Pulldown (beads) C09** (Synt1-01\_34, Brev2-09\_34ST and full-length GST-SNAP25)



(c) **Pulldown (supernatant) C09** (Synt1-01\_34, Brev2-09\_34ST and full-length GST-SNAP25)



(b) **Pulldown (beads) C08** (Synt1-01\_34, Brev2-08\_34ST and full-length GST-SNAP25)



(d) **Pulldown (supernatant) C10** (Synt1-01\_34, Brev2-10\_34ST and full-length GST-SNAP25)

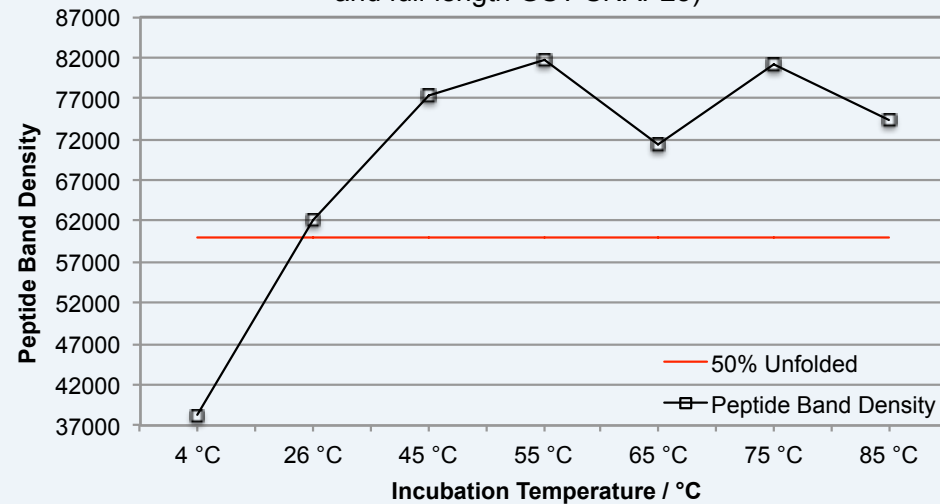
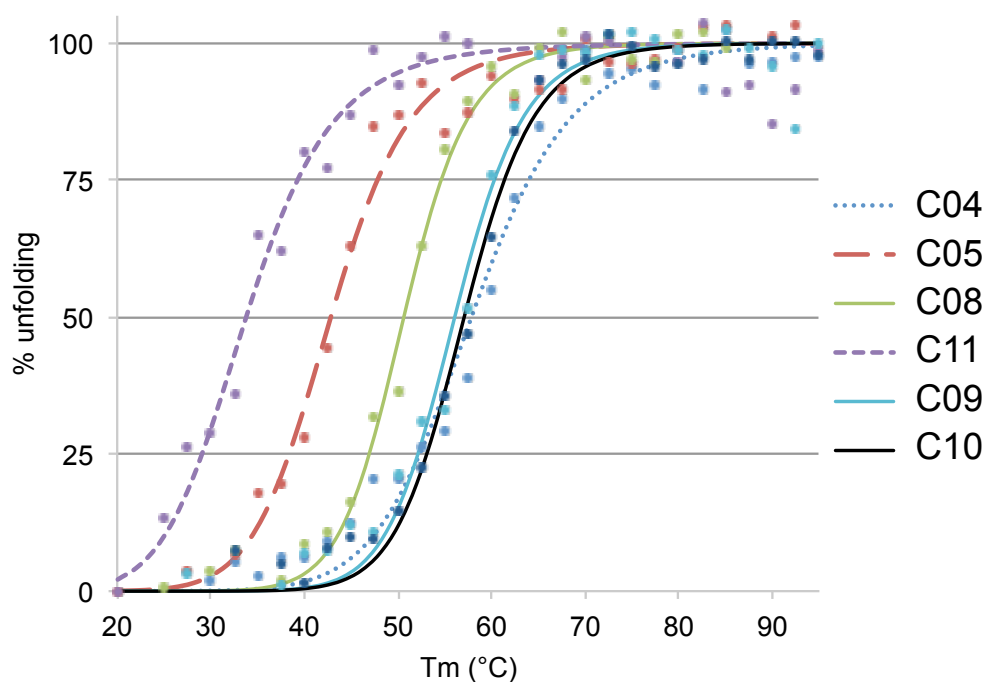


**Figure 8.5: Results from pellet “beads” and supernatant products of temperature pull-down assays, testing for thermal stability in complexes pertaining to the Salt Bridge study.** The density of a single set of peptide bands in the SDS-gel was measured, and this was plotted as a function of the incubation temperature. The red line “50% Unfolded” represents the halfway point between the highest and lowest band intensities. The intersection point between the peptide band density and the “50% Unfolded” line is effectively the melting temperature ( $T_m$ ) determined using this methodology. All four complexes were shown to assemble in the native gels (**Figure 7.7**), however only C08, C09 and C10 showed any evidence of complex assembly in the form of peptide retention on beads or peptide release into supernatant, in the pull-down assays. Complex C09 was the only complex to yield a measurable amount of peptide in both the beads and supernatant products of the pull-down. The results from the beads (**a**) shows a sharp decrease in stability from 4°C, and a  $T_m$  of ~25-26°C. The expected results from a supernatant product should be such that the amount of peptide at low temperatures remains low and steadily increases with temperature as the complex disassembles. Therefore, the beads and supernatant results should reinforce one another. This is not the case of C09 supernatant (**c**), which shows an initial decrease in peptide from 4-45°C, followed by a sharp increase to 65°C, then a decrease from this point onwards. The  $T_m$  from the supernatant product is shown to be ~55°C, substantially higher than the beads. The results for C08 beads (**b**) show relatively strong thermostability until ~65°C, and a  $T_m$  of ~69°C, whilst the results for C10 supernatant (**d**) show very weak thermostability with a  $T_m$  of ~26°C. Densitometry analysis was performed on an Odyssey CLx scanner (Li-Cor Biosciences).



(a) Melting curves obtained using CD spectroscopy for native complexes, and complexes in the Salt Bridge study

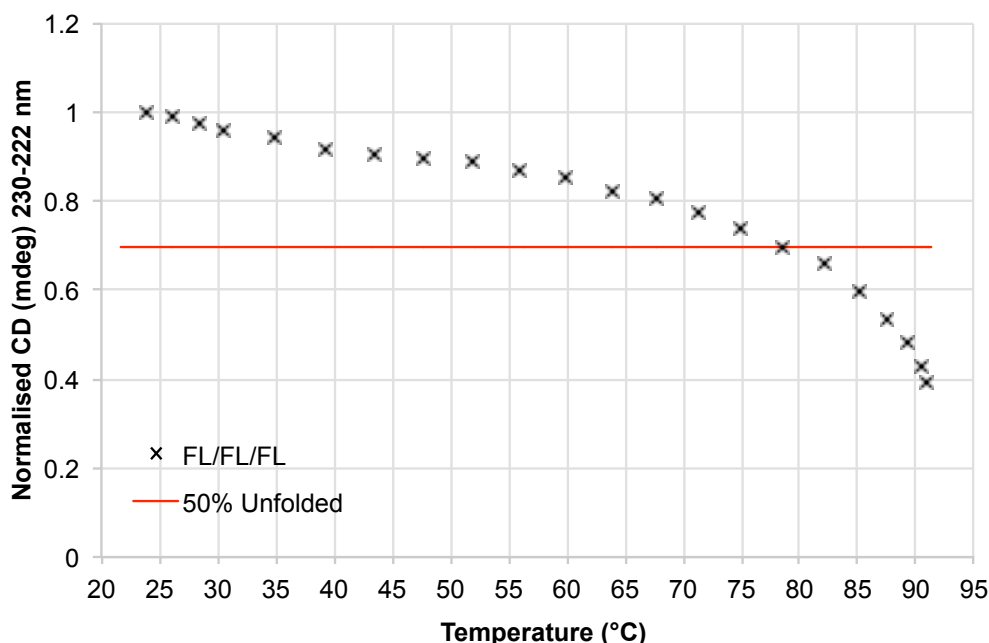


(b) Table summarising melting temperatures ( $T_m$ ) for complexes shown in graph (a), as well as standard error and  $R^2$  of the curve fitting.

Complex		C04	C05	C08	C11	C09	C10
C.I.	$T_m$ (°C)	58	43	51	34	56	57
	+ (95)	2.44	2.27	1.24	3.17	1.71	1.22
	- (95)	2.70	1.60	1.33	2.05	2.21	1.49
	$R^2$	0.987	0.985	0.992	0.967	0.986	0.994

**Figure 8.6: Results from SRCD testing for thermal stability in complexes pertaining to the Salt Bridge study.** The CD spectra show the results of an SRCD thermal melting experiment pertaining to the complexes involved in the Salt Bridge study, C04, C08, C09, C10, and C11. It also shows the results from thermal melting of C05 (27-length VAMP in otherwise native complex). CD signal was measured at 222 nm (alpha-helical trough) over a temperature range of 20-95°C (a), and the traces were recalculated as 100% change from start of the melt to the end. The curves shown are four-parametric sigmoidal curves fitted using non-linear least squares method (Kemmer and Keller, 2010). A summary table of the melting temperatures ( $T_m$ ), 95% confidence intervals (C.I.) and  $R^2$ , which is indicative of the level of correlation in the curve fitting (measured at -1 to 1, with 1 being maximum positive correlation) is shown in (b). The results are consistent with our expectations (outlined in section 6.2.1.2) as: C08 has been mutated such that it has lost one potential salt bridge, and the drop in  $T_m$  compared to the control C04 indicates a drop in stability; and C11 has been mutated to lose three potential salt bridges, and there is a substantial loss in stability (24 °C difference). There are minor differences in samples C09 and C10 – each of these contain mutations intended to break 1 potential salt bridge, and so these results may indicate that these salt bridges have little or no bearing on the structural stability of the complex. Synchrotron Radiation Circular Dichroism (SRCD) was performed using a nitrogen-flushed Module X end-station spectrophotometer at B23 Synchrotron Radiation CD Beamline at the Diamond Light Source, Oxfordshire, UK. Dr. Enrico Ferrari (University of Lincoln), Dr Giuliano Siligardi (Diamond UK) and Dr Mikhail Soloviev (RHUL) are acknowledged for their contribution towards the experiments, including providing the recombinant full-length protein (EF), setting up the SRCD spectrometer (GS) and experimental design (EF, MS) which ultimately generated the data in this figure.

(a) Thermal melt of full-length SNARE complex – FL/FL/FL



(b) Thermal melt of SNARE complex with full-length SNAP-25, full-length syntaxin and truncated synaptobrevin (length 34) – FL/FL/34

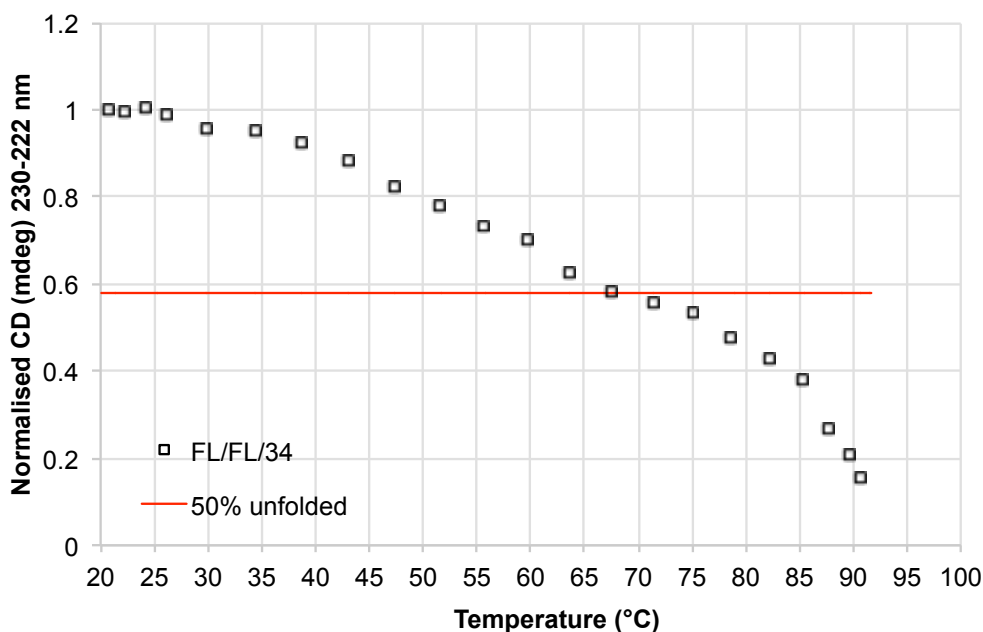
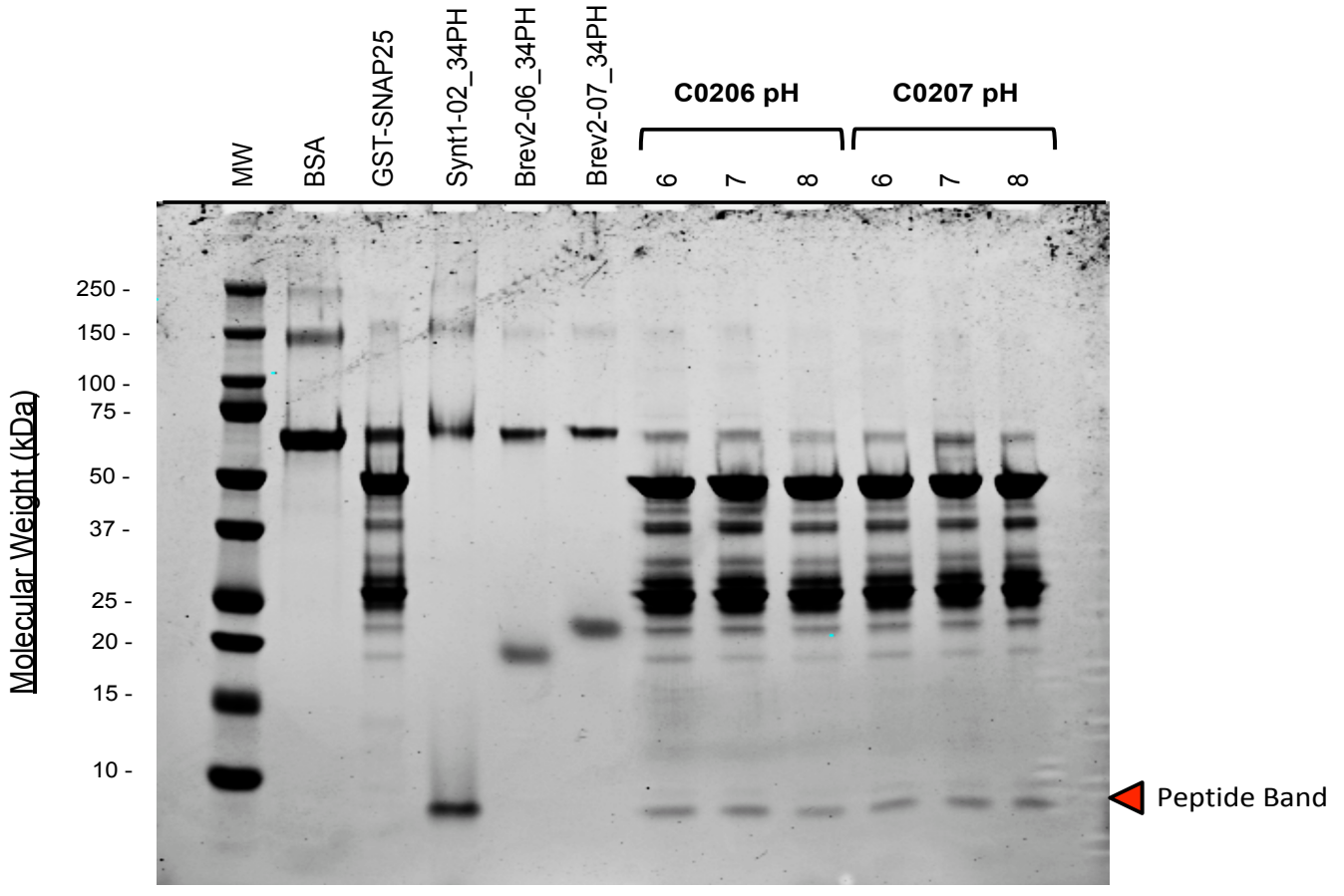


**Figure 8.7: Circular dichroism (CD) signal as a function of temperature for full-length, and partially truncated SNARE complexes.** CD signal was averaged over the alpha-helical trough (222-230 nm), and these values were normalised and plotted as a function of the incubation temperature to generate the thermal melt graphs in this figure. The red line represents 50% of unfolded complex (i.e. the melting temperature –  $T_m$ ). Graph (a) shows the thermal melt behaviour of a full-length SNARE complex (FL/FL/FL). The  $T_m$  of this complex is shown to be  $\sim 79^\circ\text{C}$ , consistent with the data obtained using synchrotron radiation CD (SRCD) in **Figure 6.1**. Graph (b) shows the thermal melt behaviour of the partially truncated SNARE complex which contains a full-length SNAP-25 and syntaxin, but a truncated synaptobrevin peptide of length 34 aa (Brev2-04\_34). The  $T_m$  of this complex is shown to be  $\sim 67\text{-}71^\circ\text{C}$ , which is reasonably consistent with the data obtained using SRCD. All spectra shown here have undergone HEPES background subtraction, and were averaged over a window length of 5 values to improve the signal-to-noise ratio. Circular Dichroism was performed using a nitrogen-flushed PiStar-180 CD stopped-flow spectrometer at University of Lincoln, UK. Elina Dosadina is acknowledged for her guidance in using the instrument, and Dr. Enrico Ferrari (University of Lincoln) is acknowledged for arranging access to instrument, contributing towards the experimental design and providing the recombinant full-length proteins.

Example of Pull-down pH Assay:

GST-C0206/C0207 pH Assay pull-down **beads** SDS-PAGE gel



4-20% gradient TruPage precast SDS-gel (Sigma) with Precision Plus Protein Dual color standards molecular weight (MW) ladder (Biorad).

All complex samples (C0206/C0207) were incubated for 1 h at RT in Potassium Phosphate buffer (10 mM) prepared at the pH specified.

**Figure 8.8: Example of a typical SDS-gel containing the results of a pull-down assay which tests for pH-sensitivity in the complexes pertaining to the pH-sensitivity study.** This particular gel shows the results of the pH pull-down assay of complexes C0206 and C0207. Complexes were assembled on glutathione agarose beads linked to GST-SNAP25 fusion protein. After thorough washing, the complexes were incubated in potassium phosphate buffer (10 mM) prepared at the pH 6, 7, 8, as specified in the gel lanes “C0206 pH” and “C0207 pH”. After thorough washing, the complex mixture was denatured with heat and reduced with 2-mercaptoethanol in order to liberate the remaining protein and peptides from the beads. There are many extraneous bands in the complex lanes (“C0206” and “C0207”) because the glutathione-agarose-GST-SNAP25 beads are impure, and contain all the cell lysate products alongside GST-SNAP25 immobilised on the beads. GST-SNAP-25 band was identified at ~ 50 kDa. Densitometry analysis of the coomassie-stained gel was then performed on the peptide band corresponding to syntaxin, since this is the most easily identifiable peptide from the complexes. Gels were scanned, and analysis was conducted on an Odyssey CLx scanner (Li-Cor Biosciences).

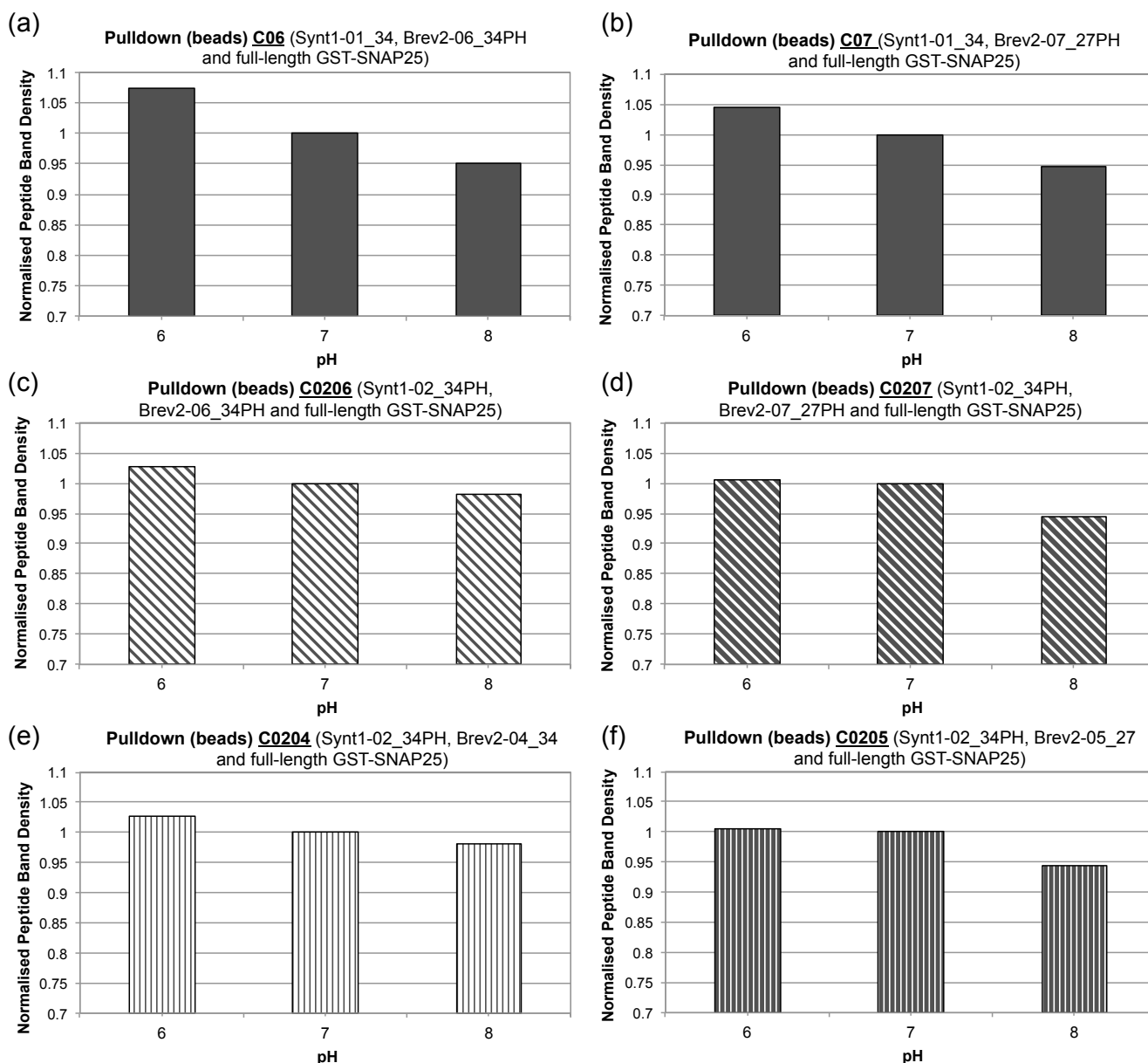
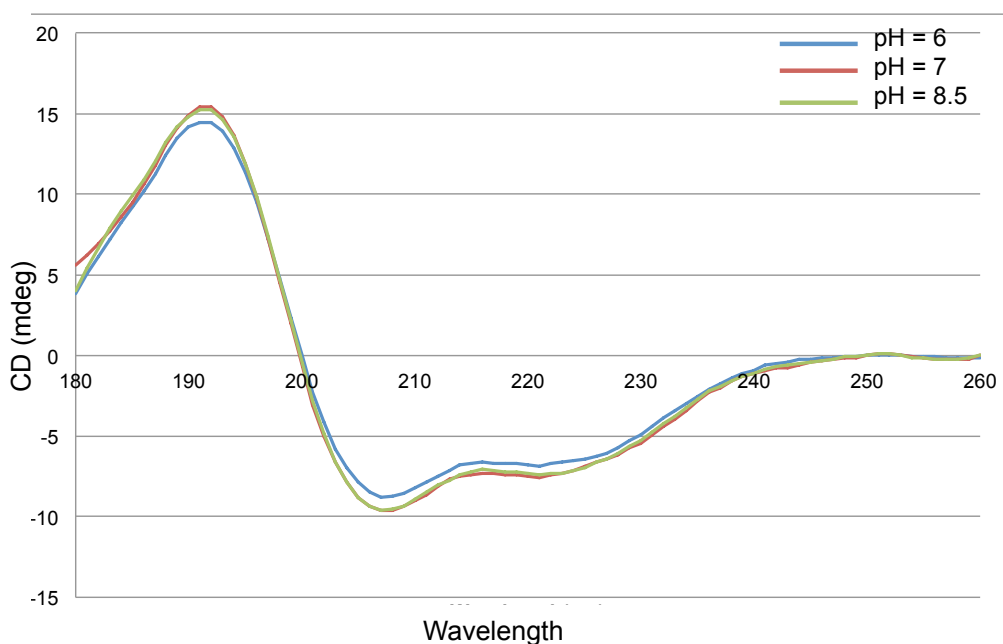


**Figure 8.9: Results from the pull-down assays testing for pH-sensitivity in the complexes pertaining to the pH-sensitivity study.** The peptides in the pH-sensitivity study contain histidine mutations at key positively charged sites. It was expected that these mutations should impart pH-sensitivity onto the complexes, such that at pH 6 (the pH at which histidine is positive), the complex assembly should be unaffected, and any increase in pH should have a negative impact on assembly, by breaking the salt bridges that the positively charged sites were originally part of. For each complex mixture, the density of the syntaxin peptide bands was measured, and then the absolute density at each pH was normalised against the value obtained at pH 7, then normalised against native SNARE controls C04 for complexes C06, C0206, C0204; and C05 for complexes C07, C0207, and C0205. Inherent weaknesses in the pull-down methodology resulted in the possibility arising of non-specific interactions, which may have interfered with SNARE complex formation, and have rendered the results inconclusive. Although all complexes showed a negative correlation between increasing pH and the normalised peptide band density, the differences between the data points are near negligible, and so they are very difficult to interpret definitively. We have used the insights gained from this experiment to inform the experimental method for an SRCD experiment involving C04, C06 and C0206 in **Figures 8.10** and **8.11**. Densitometry analysis was performed on an Odyssey CLx scanner (Li-Cor Biosciences).

(a) pH-sensitivity of re-engineered complex C04 (containing full length SNAP-25 + Synt1-01-34 + Brev2-04-34)



(b) pH-sensitivity of re-engineered complex C0206 (containing full length SNAP-25 + Synt1-02-34PH + Brev2-06-34PH)

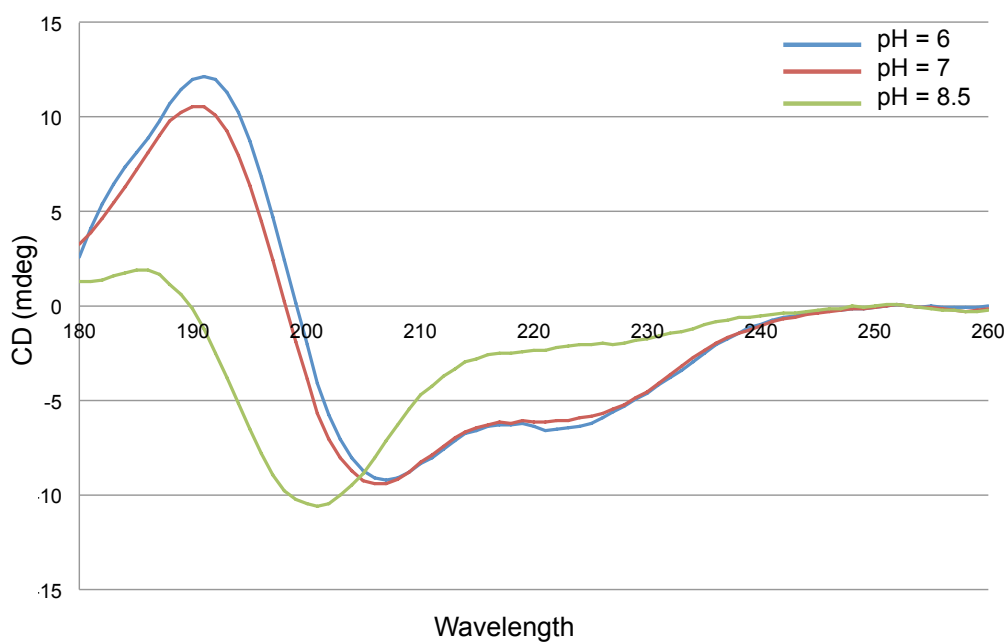
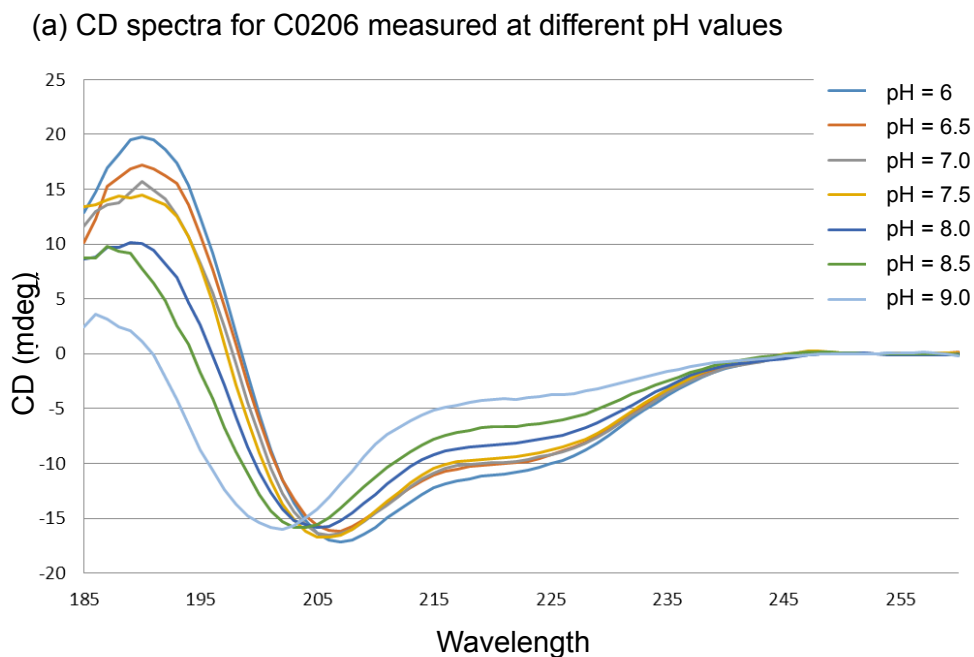


**Figure 8.10: Typical SRCD responses to pH by re-engineered complexes C04 and C0206.** These particular CD spectra show the results of a SRCD experiment where native complex C04 (a) and re-engineered complex C0206 (b) were studied under three different pH conditions. In both panels the blue trace is the CD measured at pH 6, dark red at pH 7 and light green at pH 8.5. The difference in the CD spectra recorded at pH 8.5 clearly shows that the engineered complex lacks alpha-helical content and unfolds at pH 8.5 (indicated by lack of trough at 220 nm), but the native complex remains stable (indicated by no change in the secondary structure). Synchrotron Radiation Circular Dichroism (SRCD) was performed using a nitrogen-flushed Module X end-station spectrophotometer at B23 Synchrotron Radiation CD Beamline at the Diamond Light Source, Oxfordshire, UK. Dr. Enrico Ferrari (University of Lincoln), Dr Giuliano Siligardi (Diamond UK) and Dr Mikhail Soloviev (RHUL) are acknowledged for their contribution towards the experiments, including providing the recombinant full-length protein (EF), setting up the SRCD spectrometer (GS) and experimental design (EF, MS) which ultimately generated the data in this figure.



(b) Summary of pH-sensitivity CD experiments for C04, C06, C0206

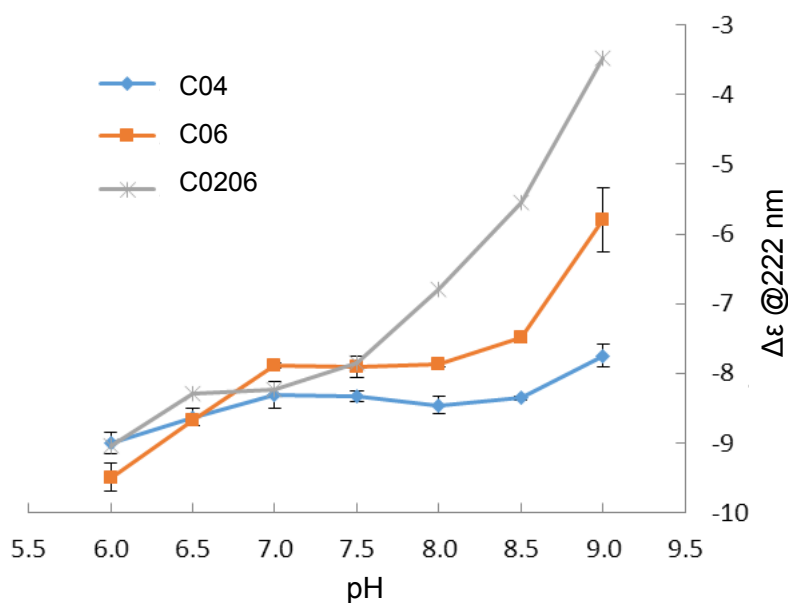
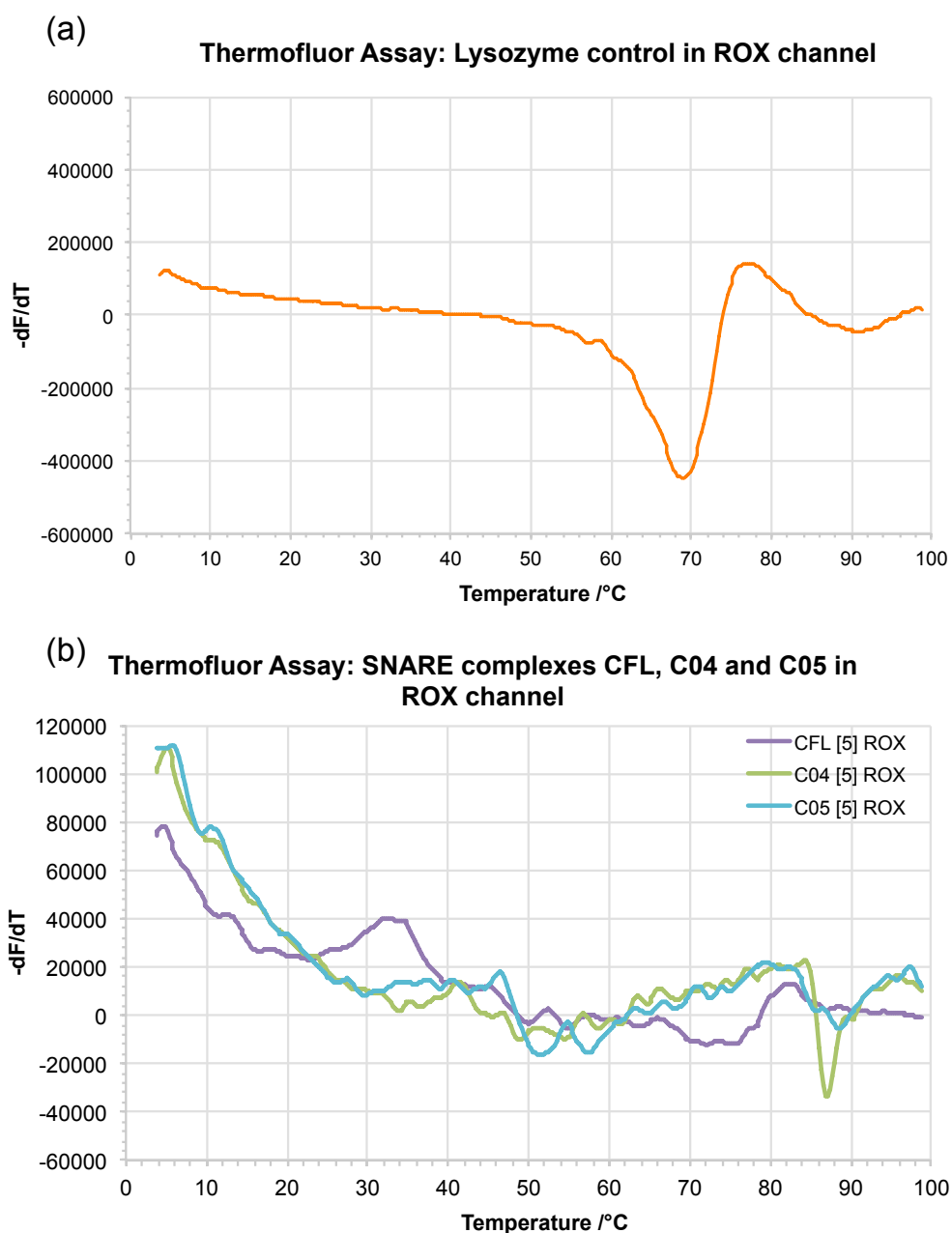


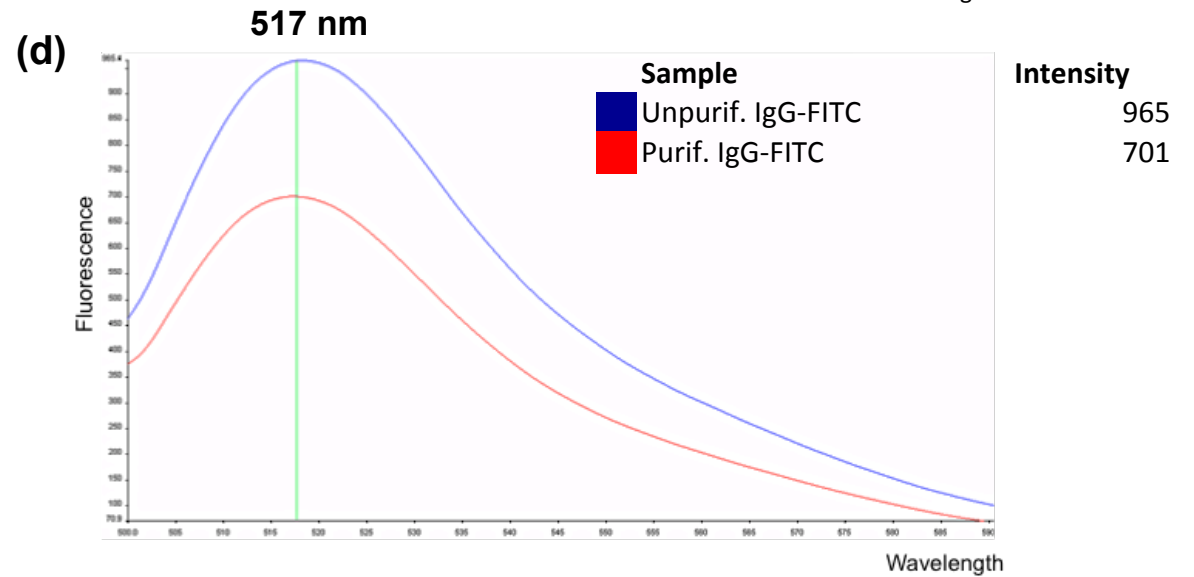
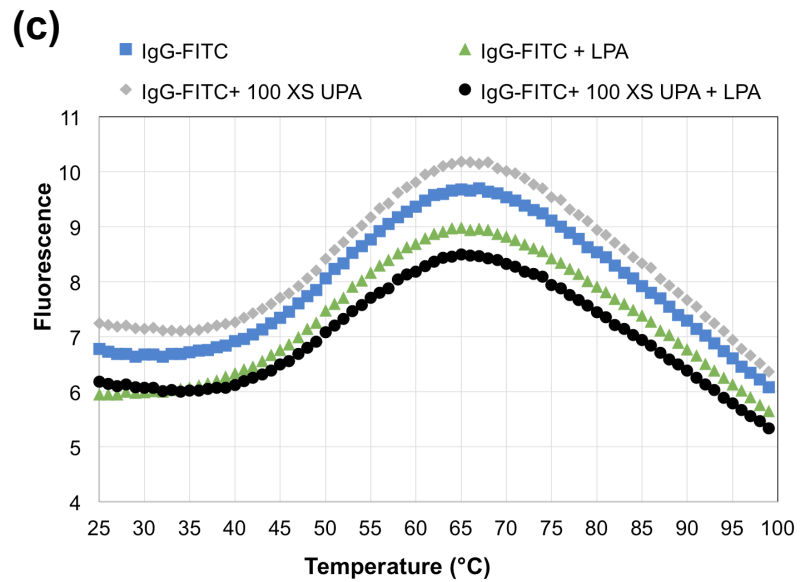
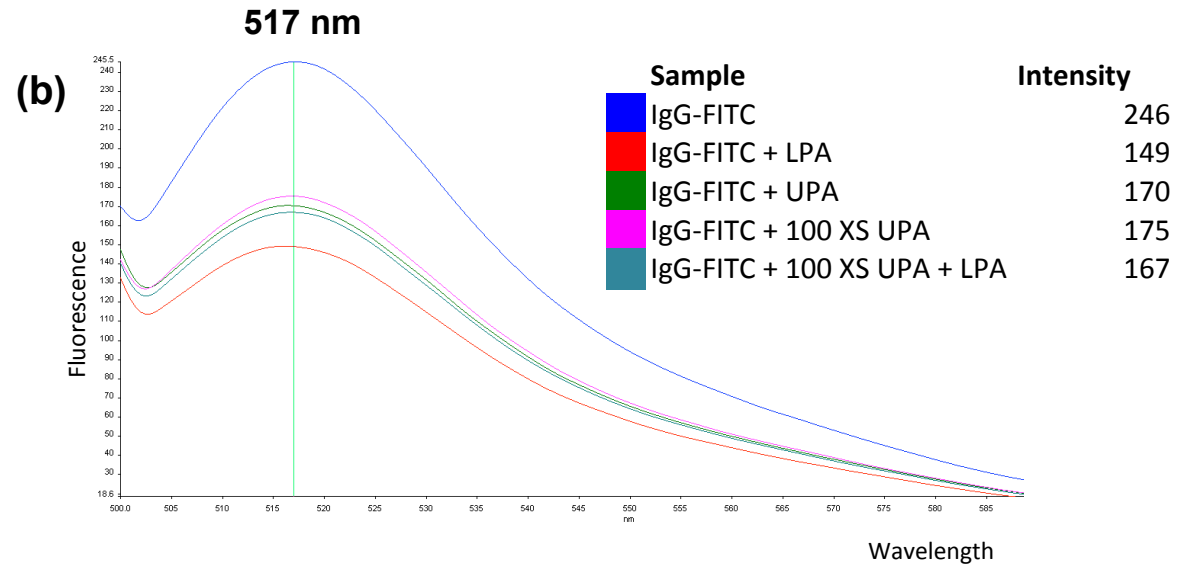
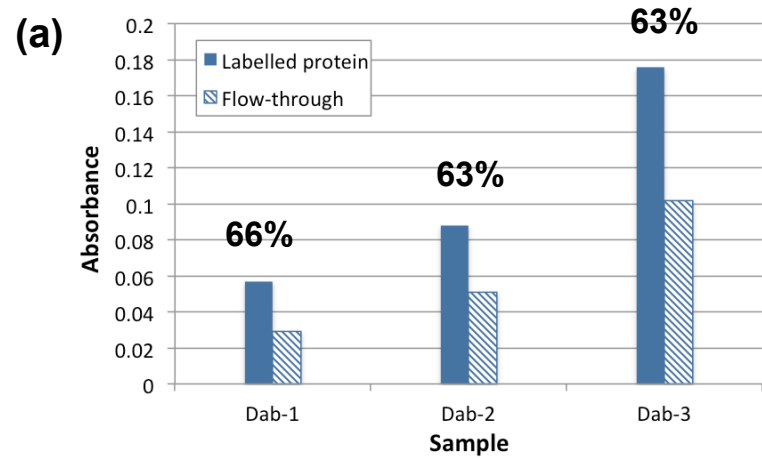
**Figure 8.11: Summary of pH response curves measured for three typical complexes C04, C06 and C0206.**

The CD spectra show the results of an SRCD experiment wherein C04, C06 and C0206 were studied under three different pH conditions. The detailed CD spectra for C0206 were measured under different pH in (a). The change in secondary structure, moving from coiled coil to random coil, in C0206 as pH increases is clearly demonstrated in this panel. A summary of the data for all three complexes can be seen in (b). CD signal was measured at constant temperature at 222 nm (alpha-helical trough), and these values were plotted as a function of pH. The data points are indicative of the mean of three individual CD spectra scans at each of the conditions tested, with error bars indicating +/- standard error. Differential pH sensitivity is revealed between pH 7.0 – 9.0 in (b). Here all complexes are shown to be stable at pH values up to 7.0, but past this point C06 and C0206 show substantial unfolding. Synchrotron Radiation Circular Dichroism (SRCD) was performed using a nitrogen-flushed Module X end-station spectrophotometer at B23 Synchrotron Radiation CD Beamline at the Diamond Light Source, Oxfordshire, UK. Dr. Enrico Ferrari (University of Lincoln), Dr Giuliano Siligardi (Diamond UK) and Dr Mikhail Soloviev (RHUL) are acknowledged for their contribution towards the experiments, including providing the recombinant full-length protein (EF), setting up the SRCD spectrometer (GS) and experimental design (EF, MS) which ultimately generated the data in this figure.

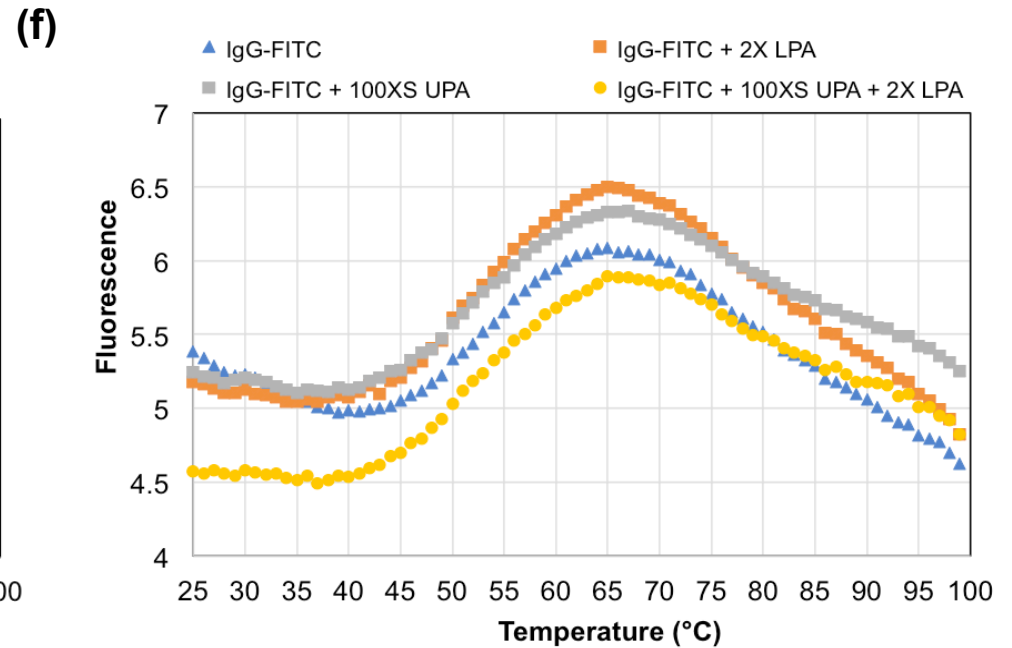
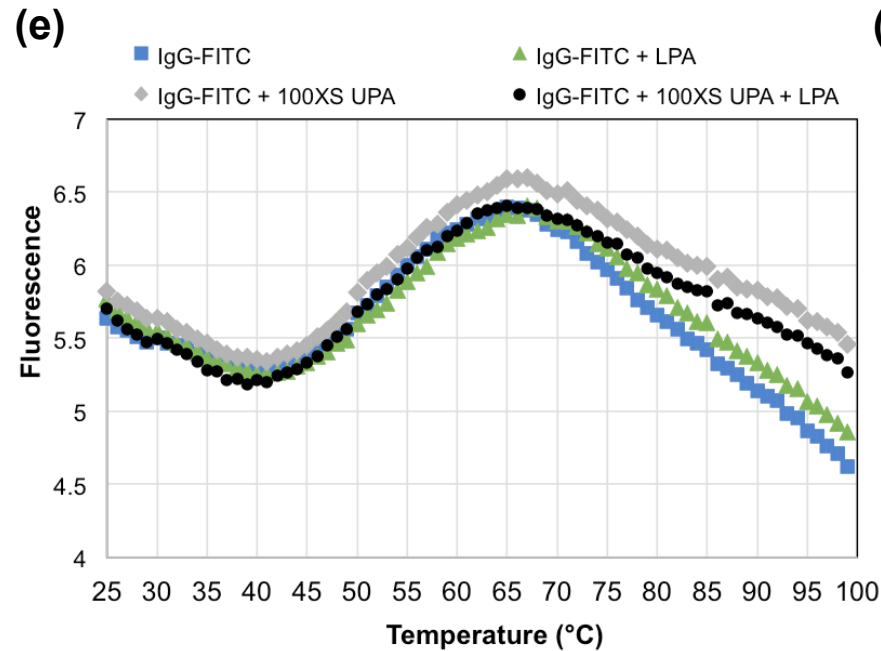
## 14. Appendix



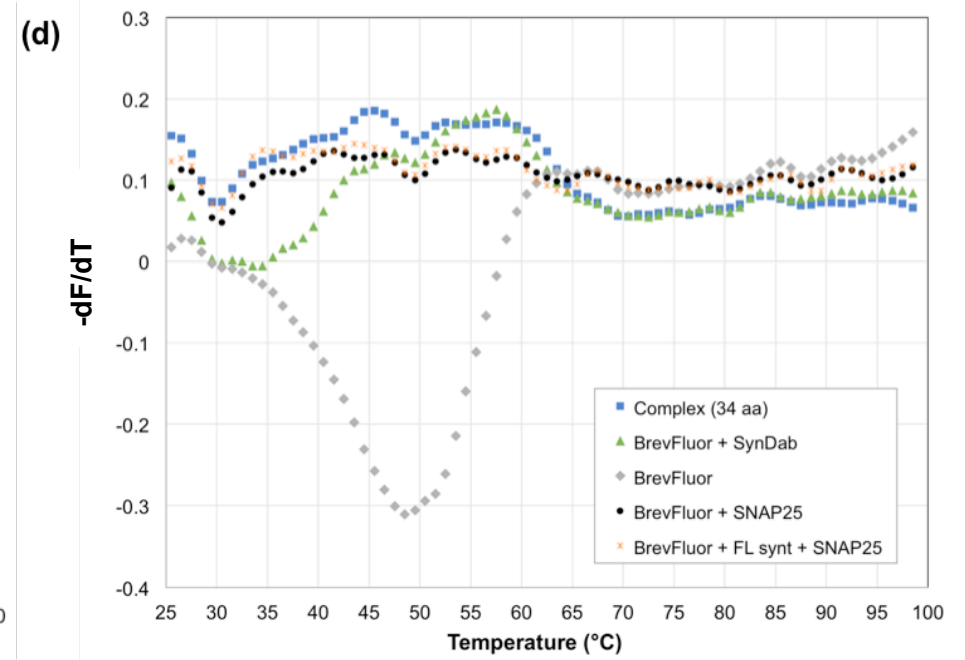
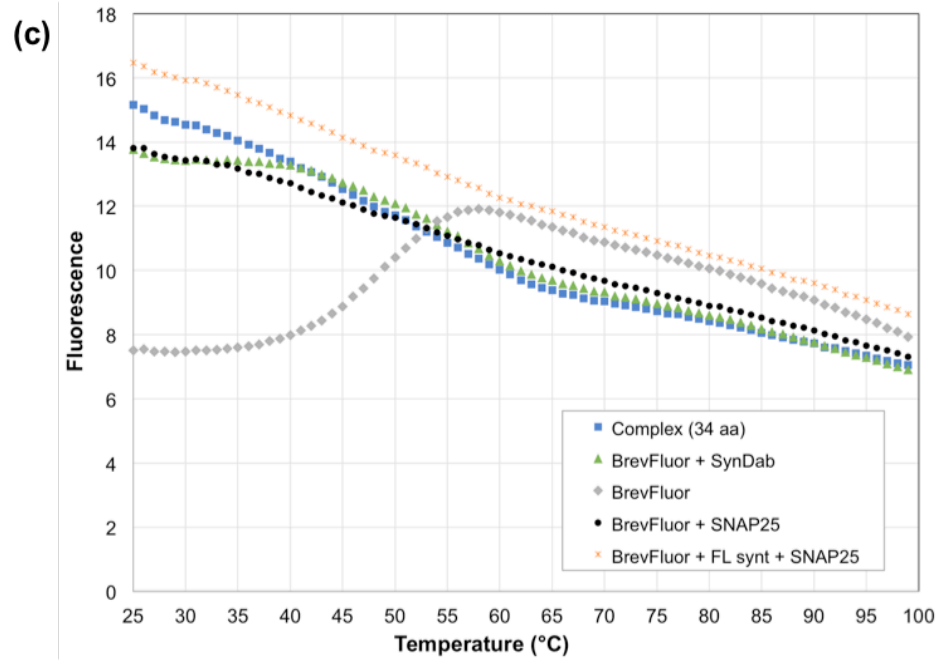
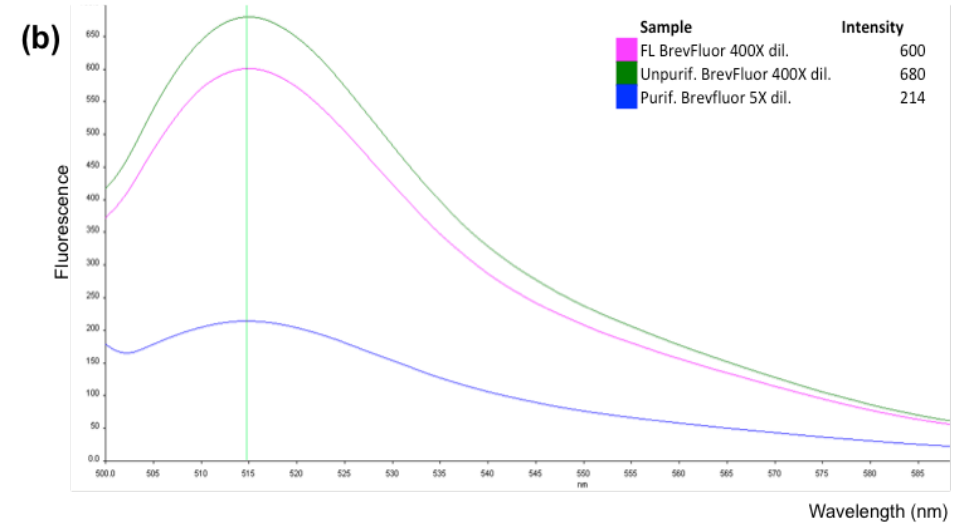
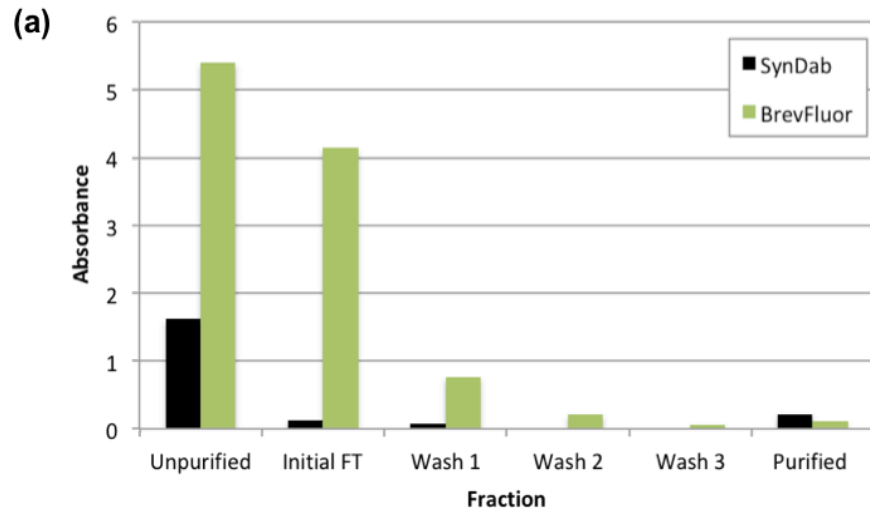
**Appendix 14.1: Differentiated thermal melt profiles, from the ROX channel (excitation 586 nm, emission 610/616 nm), of SNARE complexes (all 5  $\mu$ M) including CFL (full-length SNARE complex), C04 (SNARE complex containing truncated Synt1-01\_34 and Brev2-04\_34), C05 (SNARE complex containing truncated Synt1-01\_34 and Brev2-05\_27), and control lysozyme (0.1 mg/mL). All samples contain 10X SYPRO Orange, SNARE complexes were prepared in buffer (18 mM HEPES, 90 mM NaCl, 0.1% OG), and the control lysozyme was in 0.03X PBS. A clear strong trough was present in the control at its expected melting temperature  $\sim$ 69°C. The signals for the SNARE complexes were averaged over a window of five [5] values, however despite this the SNARE complexes still show very low signal to noise ratio, and there are no appreciable troughs that could be indicative of a melting temperature for complex disassembly. Thermofluor assay was conducted on a StepOnePlus Real-Time PCR system (Thermo Fisher Scientific), and data was normalised and differentiated by the StepOnePlus software. Elina Dosadina is acknowledged for her contribution towards optimising the conditions for the control lysozyme, which ultimately were used for the SNARE complexes also.**







**Appendix 14.2: Outcomes from Protein A labelling, fluorescent emission of IgG-FITC in the presence of labelled Protein A, high-resolution melts of IgG-FITC in the presence of labelled Protein A, and how it differs when commercial IgG-FITC is purified beforehand.** Protein A was labelled with the quencher Dabcyl in the ratios: 12-fold excess Dabcyl (Dab-1), 30-fold excess Dabcyl (Dab-2), and 90-fold excess Dabcyl (Dab-3). Assuming no loss of dabcyl in the filtration units, and assuming that the total absorbance (i.e. absorbance of labelled protein plus absorbance of flow-through for each “Dab” sample – seen in (a)) is equivalent to the total amount of Dabcyl used in the initial labelling reaction, the efficiency of labelling on average is approximately  $64\% \pm 2$ . The efficiency of IgG-Protein A binding on FRET quenching is demonstrated in (b), where it can be seen in the emission spectra that as expected, the greatest quenching occurs with labelled Protein A (IgG-FITC + LPA), with a percentage of FITC quenching  $\sim 39\%$ . The controls with unlabelled Protein A (IgG-FITC + UPA, IgG-FITC + 100 XS UPA), also demonstrate quenching, which although is  $\sim 9\%$  less than the labelled Protein A, it is still substantially high. Results from the high-resolution melt (HRM) using real-time qPCR (c) were not as promising. All samples, including IgG-FITC in the presence of unlabelled protein A (IgG-FITC + UPA) showed the same signal, with similar intensity. It became clear that FITC was overpowering the signal, and the only phenomenon being observed was FITC behaviour as a function of temperature. The commercial IgG-FITC was purified using a Micro Bio-Spin 30 column, and its resultant emission spectrum demonstrated a reduction in fluorescence of  $\sim 27\%$ , indicating that the sample was impure (d). The HRM was repeated with purified IgG-FITC using the same conditions as previously (e), and also doubling the amount of labelled Protein A (f). There was very little difference compared to the unpurified IgG-FITC HRM (c), and the controls containing unlabelled Protein A still showed no difference compared to the sample containing labelled Protein A, so FRET was not observed.



**Appendix 14.3: Results from the high-resolution melt of the labelled peptide complex and controls.** Graph (a) shows the absorbance measurements of fractions obtained during labelled-peptide purification. According to this data, there was approximately 13% incorporation of Dabcyl in “SynDab”, and ~2% incorporation of fluorescein in “BrevFluor”. Purification was successful with no Dabcyl detected from Wash 2 onwards, and minor amounts of fluorescein detected in Wash 3. Graph (b) shows the fluorescent emission measurements of selected fractions obtained from BrevFluor purification. The graph shows emission of unpurified BrevFluor (400-fold dilution); flow-through BrevFluor (400-fold dilution) and purified BrevFluor (5-fold dilution). According to this data, there was approximately 0.4% incorporation of fluorescein in “BrevFluor”, which is in line with absorbance data. The data obtained from the high-resolution melt of the labelled peptide complex, and the associated controls, is presented in graphs (c) and (d). Graph (c) shows the raw unprocessed data, whilst graph (d) shows the first derivative of this data. The labelled peptide complex (blue) shows a similar trend to all the controls (except BrevFluor) of fluorescence decreasing at a steady rate as temperature increases. BrevFluor alone (grey) shows the FRET trend we were expecting to observe with the complex. It’s worth noting that this trend was observed in the labelled Protein A and IgG studies too, and so it’s highly likely we are just observing the behaviour of fluorescein as a function of temperature. Both the complex and the control BrevFluor + SynDab contain the same amount of SynDab, and differ only at the very start of the run (temp <40C). Overall there is no meaningful interpretation for what is being observed in these graphs, and it is clear the method requires more optimisation before it will be possible to observe melting of complexes.